# *Ab Initio* STM and STS Simulations on Magnetic and Nonmagnetic Metallic Surfaces

Alexey Dick

Paderborn 2008

# *Ab Initio* STM and STS Simulations on Magnetic and Nonmagnetic Metallic Surfaces

Dissertation
zur Erlangung des akademischen Grades
*Doktor der Naturwissenschaften (Dr. rer. nat.)*
vorgelegt dem
Department Physik der Fakultät für Naturwissenschaften
an der Universität Paderborn

Alexey Dick

| Promotionskommission | |
|---|---|
| Vorsitzender | Prof. Dr. phil. Klaus Lischka |
| Gutachter | Prof. Dr. rer. nat. Wolf Gero Schmidt |
| Gutachter | Prof. Dr. rer. nat. Jörg Neugebauer |
| Beisitzer | Universitätsdozent Dr. rer. nat. Uwe Gerstmann |


| | |
|---|---|
| Tag der Einreichung: | 21 Dezember 2007 |
| Tag der mündlichen Prüfung: | 14 April 2008 |

*Моей семье...*
*To my family...*

# Acknowledgements

This years-long work would have never been completed and made to its current state without collective efforts of a considerable number of people, which I wish to acknowledge at the beginning of this thesis.

First of all, I would like to express my most sincere thanks to Prof. Dr. Jörg Neugebauer for giving me an excellent opportunity and creating the best possible atmosphere and environment to perform this work. Jörg introduced me into the field of computational condensed-matter physics and, despite of an exponentially increasing waterfall of new duties and responsibilities, was always able to find enough time for me and my problems. Only because of such a strong continuous support, Jörg's fruitful suggestions and his careful guidance through my whole doctoral research I was able to complete this work.

An enormous impact on the content and results of this work was made by Prof. Dr. Nacho Pascual and Prof. Dr. Karsten Horn from the FHI, who have performed STM experiments on Ag(110) surfaces, and by Prof. Dr. Arthur R. Smith from the Ohio University, who provided us with his results on the $Mn_3N_2(010)$ surface. Since this thesis is to a major extend a result of the tight collaboration with these experimental groups, my gratitude to these people is tremendous. Without the constant exchange of ideas and fruitful discussions the right understanding and interpretation of the STM experiments would hardly have been possible, and I thank Nacho, Karsten and Arthur for their indispensable help.

I would also like to thank the director of the Theory Department of the Fritz-Haber-Institute (FHI) Prof. Dr. Matthias Scheffler for giving me the opportunity to join the FHI and to participate in the highly stimulating and encouraging research there. I wish to express my appreciation to all the people I met and got to know there, for their standing willingness to help and to keep the friendly and creative environment in the department. My special thanks goes to Martin Fuchs and Prof. Dr. Peter Kratzer, who were always open to my questions and helped me in understanding concepts behind pseudopotentials and density functional theory.

I am also thankful to all members of the Computational Materials Design department, where I have finished and written-up my thesis, for building a warm and constructive atmosphere. I would like to explicitly thank Sixten Boeck, to whom I am much indebted for his ever standing support in

all aspects of the PhD studentship, particularly for showing me an effective way to use and develop the S/PHI/nX software. I also thank Dr. Tilmann Hickel for proofreading the final draft of the thesis and making a great deal of valuable suggestions, as well as for translating the preface of my thesis to German.

My infinite thanks to my wife Tatjana and to my two small daughters Tanja and Anja for their standing patience, support and understanding. I am also deeply grateful to all other members of my big family: my parents Tatjana and Vladimir, my grandparents Tamara (in memoriam) and Pavel, Evgenia and Alexey, and to my brother Pavel and my sister-in-law Xenia for their encouragement and faith.

# Preface

An unambiguous understanding and control of the surfaces, of atoms or molecules positioned on a surface, and of their interaction with the environment is critical for an efficient development and engineering of future solid-state technology. One of the most celebrated experimental techniques to study surface properties with down to single-atom resolution is the scanning tunneling microscopy (STM), awarded with the Nobel Prize in 1986. The interpretation of the STM experiments is, however, frequently cumbersome because STM superimposes contributions from the surface topography and its electronic structure. Fortunately, modern *ab initio* methods like the Density Functional Theory (DFT) are capable to provide an accurate theoretical description of surface properties, and can be used to get a detailed understanding of STM experiments. Consequently, most state-of-the-art STM studies are joined efforts of experimental and theoretical groups.

The aim of this work was to provide an in-depth understanding of a new generation of scanning tunneling microscopy experiments, performed employing different regimes of the STM: the spectroscopy-mode (the so-called Fourier Transformed STM, FT-STM), and the spin-sensitive mode (the so-called spin-polarized STM, SP-STM). In the present thesis *ab initio* tools will be proposed that are based on DFT calculations to theoretically predict and analyze such types of the STM. All STM-relevant schemes were implemented into the multiscale library S/PHI/nX. These methods are general and can be applied to accurately predict and analyze STM images on various magnetic and nonmagnetic metallic surfaces.

The first part of this thesis focusses on the simulation of FT-STM, the mode that allows to probe local dispersion properties of the electrons at the surface. In order to provide the theoretical counterpart of the experimental FT-STM spectra we have introduced a new implicit approach that is derived from Tersoff-Hamann theory of the STM. Specifically, treating surface imperfections (that are necessary in FT-STM experiments) as ideally reflecting objects gave rise to a dramatic reduction of the computational complexity, since it requires explicit *ab initio* calculations only for the smallest (chemical) unit cell of the ideal unperturbed surface. The importance of an accurate description of surface wavefunctions at $5-15$ Å above the surface as well as the spurious quantum-size effects have been discussed in detail together with approaches to obtain converged FT-STM images. We applied our method to FT-STM experiments performed on Ag(110) surfaces. The

resulting simulated FT-STM spectra are in excellent agreement with experimental data, and allow a complete interpretation even of specific experimental details. In particular, we have for the first time shown that STM, in contrast to common believe, is able to detect dynamic properties of the bulk electrons. The physical effect underlying this phenomenon was explained in detail.

In the second part of the thesis we discuss the modeling of the spin-resolved STM, the mode that allows to characterize the magnetic structure of a surface. As a case system we studied here the magnetically-ordered transition-metal nitride surface $Mn_3N_2(010)$. Because SP-STM experiments did not allow a conclusive understanding of the surface structure, we have first employed *ab initio* thermodynamics to figure out the most stable magnetic and atomic configuration of the surface that are consistent with experiments. To simulate SP-STM images on the most stable $Mn_3N_2(010)$ surface we have employed the spin-generalized transfer-Hamiltonian formalism, assuming that the tip wavefunctions have dominant radial symmetry ($s$-like tip). It was found that a real-space description of the vacuum region is essential in our case, and this method has been implemented into S/PHI/nX. The theoretical results have been found in excellent agreement with the measured profiles and allowed to resolve all open questions of the experiment, providing an in-depth understanding of all major effects such as the magnetic contrast reversal and the influence of the STM-tip on the measured profiles.

In summary, in this thesis we developed an approach for *ab initio* simulations of the FT-STM and SP-STM experiments, and applied it to a number of hitherto unsolved problems in recently reported STM experiments performed on magnetic and nonmagnetic surfaces. Most parts of the work presented here have been done in close collaboration with experimental groups from the Fritz-Haber-Institut der Max-Planck-Gesellschaft in Berlin and the Ohio University in USA.

# Zusammenfassung

Um eine effiziente Entwicklung und Prozessierung zukünftiger Festkörpertechnologien voranzutreiben, sind ein klares Verständnis und eine gezielte Optimierung von Oberflächen, auf der Oberfläche befindlichen Atome und Moleküle und deren Wechselwirkung mit der Umgebung notwendige Voraussetzungen. Die Rastertunnelmikroskopie (STM), im Jahre 1986 mit dem Nobelpreis bedacht, stellt eine der bekanntesten Techniken zur Untersuchung von Oberflächeneigenschaften mit atomarer Auflösungen dar. Die Interpretation der STM Experimente ist jedoch meist aufwendig, da STM eine Überlagerung der Beiträge der Oberflächentopographie und der elektronischen Struktur detektiert. Heute bieten moderne *ab initio* Methoden wie die Dichtefunktionaltheorie (DFT) die Möglichkeit einer genauen theoretischen Beschreibung von Oberflächeneigenschaften. Sie können daher für ein detailiertes Verständnis von STM Experimenten herangezogen werden. Dementsprechend sind moderne STM Untersuchung immer das Ergebnis gemeinsamer Anstrengungen von experimentellen und theoretischen Gruppen.

Das Ziel der vorliegenden Arbeit ist es, ein tiefgehendes Verständnis und theoretisch fundierte Simulationsmethode einer neuen Generation von Rastertunnelmikroskopie-Experimenten zu liefern. Der Fokus liegt dabei auf der Verwendung zweier verschieder STM-Moden: dem Spektroskopie-Modus (sogenanntes Fourier transformiertes STM, FT-STM) und dem Spin-sensitiven Modus (sogenanntes Spin-polarisiertes STM, SP-STM). Um diese STM-Operationstechniken theoretisch vorhersagen und analysieren zu können, haben wir verschiedene auf der DFT basierende *ab initio* Verfahren entwickelt. Alle STM-relevanten Verfahren wurden in die Multiskalen-Bibliothek S/PHI/nX integriert. Die verwendeten Methoden sind allgemeingültig und können auf beliebige Materialsysteme angewandt werden, um STM Bilder verschiedener magnetischer und nichtmagnetischer metallischer Oberflächen präzise vorherzusagen und zu analysieren.

Der erste Teil dieser Dissertation konzentriert sich auf die Simulation von FT-STM, also der Mode, die die Abbildung der lokalen Dispersionseigenschaften von Elektronen auf der Oberfläche erlaubt. Um das theoretische Gegenstück zu den experimentellen FT-STM Spektren zu gewinnen, haben wir einen neuen impliziten Zugang vorgestellt, der auf der Tersoff-Hamann-Theorie beruht: Der dabei vorgeschlagene Ansatz, der Behandlung von Oberflächenfehlern (die notwendigerweise in FT-STM-Experimenten auftreten) als ideal reflektierende Objekte führt zu einer dramatischen

Reduzierung des Rechenaufwandes, da sich dadurch die expliziten *ab initio* Rechnungen nur auf die kleinste (chemische) Elementarzelle der idealen, ungestörten Oberfläche beschränken. Die Bedeutung einer genauen Behandlung der Oberflächen-Wellenfunktionen 5-15 Å oberhalb der Oberfläche sowie von spurious Quanten-size Effekten zur Erzielung konvergierten FT-STM Abbildungen werde im Detail diskutiert. Wir haben unsere Methode auf FT-STM Experiment, die an Ag(110) Oberflächen durchgeführt wurden, angewandt. Die mit diese Methode simulierte FT-STM Spektren sind in ausgezeichneter Übereinstimmung mit den experimentellen Daten und ermöglichen eine detalierte Interpretation. Insbesondere haben wir erstmalig zeigen können, dass STM in der Lage ist, dynamische Eigenschaften von Elektronen im Volumenmaterial zu erfassen. Der physikalische Effekt, auf dem dieses Phänomen beruht, wurde im Detail erklärt.

Im zweiten Teil dieser Dissertation haben wir die Modellierung von Spin-aufgelöstem STM diskutiert. Diese Modus erlaubt die Charakterisierung der magnetischen Struktur der Oberfläche. Als Beispielsystem haben wir magnetisch geordnete Oberflächen des Übergangsmetall-Nitrids $Mn_3N_2$ (010) untersucht. Da die SP-STM Experimente kein schlüssiges Verständnis der Oberflächenstruktur erlaubten, haben wir zunächst *ab initio* Thermodynamik verwendet, um die stabilsten magnetischen und atomaren Konfigurationen der Oberfläche herauszufinden, die mit dem Experiment in Übereinstimmung waren. Um die SP-STM Abbildungen der stabilsten $Mn_3N_2$(010) Oberfläche zu simulieren, haben wir den Spin-verallgemeinerten Transfer-Hamiltonian Formalismus angewandt. Dieser geht von der Annahme aus, dass die Wellenfunktion der STM-Spitze in erster Linie radialen Charakter hat ($s$-artige Spitze). Wir haben festgestellt, dass die Beschreibung der Vakuumregion im Realraum in unserem Fall essentiell ist, und diese Methode wurde in S/PHI/nX eingebaut. Die theoretischen Ergebnisse sind in exzellenter Übereinstimmung mit den gemessenen Profilen waren, und erlauben daher ein tiefgreifendes Verständnis aller wichtigen Effekte, wie der magnetischen Kontrastumkehr und des Einflusses der STM-Spitze auf die gemessenen Daten.

Zusammenfassend wird in dieser Dissertation ein *ab initio* Zugang zur Simulation von FT-STM und SP-STM Experimenten entwickelt und auf verschiedene bislang ungelöste Probleme aktuelle STM Experimente an magnetischen und nichtmagnetischen Oberflächen angewandt. Ein Großteil der hier vorgestellten Ergebnisse wurden in enger Zusammenarbeit mit experimentellen Gruppen am Fritz-Haber-Institut der MPG in Berlin und an der Ohio Universität in der USA gewonnen.

# Contents

# Chapter 1

# Introduction

## 1.1 Importance of the scanning tunneling microscopy for modern solid state physics

At present the constantly continuing miniaturization of electronic devices has reached a point, where the typical feature size of the active region may be as small as several Angströms, i.e. it may consist of several tens or even single atoms only. At this scale the nanosized devices can be built on the basis of low-dimensional objects like, e.g., discrete atoms, monoatomic chains or compact atomic islands, corresponding to zero-, one-, and two-dimensional quantum objects. Such nanometric systems can be employed to construct molecular magnets, atomic spin devices, logic gates, quantum size computers, single-electron transistors *etc.*

The electronic properties of nanosized objects are significantly different from those in bulk material. Quantum effects may strongly modify properties of matter like "color", reactivity, magnetic or dipolar moment, *etc.* A detailed insight into novel electronic properties and into the interplay between structure and electronic properties of such devices is critical for developing efficient nanosize electronics. Surfaces form an ideal playground to build up and to study properties of such nanosized objects. Moreover, such objects are used to control/enhance surface catalytic activity or specific aspects of crystal growth and are an active field of research.

The demand for a detailed understanding and characterization of the surface at the nanoscale requires adequate experimental and theoretical tools that are able to address the desired properties, including magnetic, structural, electronic, and transport phenomena. The requisite accuracy of these methods must be high enough to get to the bottom of the problem, i.e. to explicitly characterize material properties on the atomic scale.

The modern key experimental tools for studying the electronic structure of surfaces can be divided into area-averaging and scanning-probe techniques. The area-averaging methods such as, e.g., angle resolved (inverse) photoemission spectroscopy (AR(I)PES), electron energy loss spectroscopy, infrared reflection-absorbtion spectroscopy, inherently average the measured electronic

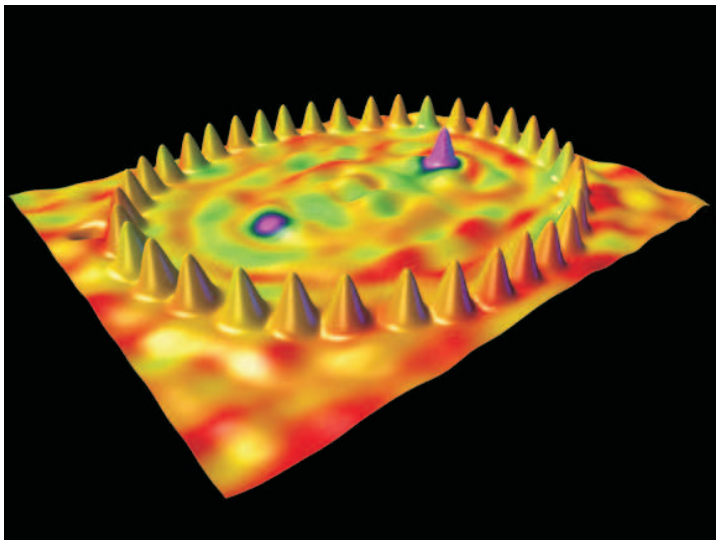

Figure 1.1: "Quantum mirage" effect observed with a scanning tunneling microscope (STM) in a quantum corral. When a magnetic cobalt atom (purple peak in the upper right) is placed at a focus point of the elliptical corral, some of its properties (the Kondo resonance [3]) also appear at the other focus (the purple spot in the lower left) where no atoms exist. This effect has the potential to enable data transfer within future nanoscale electronic circuits so small that conventional wires do not work. The corral consists of 36 cobalt atoms placed on a copper (111) surface. The STM is used to position these atoms. Figure is a courtesy of IBM Research.

properties over surface areas of $\sim$1 mm$^2$. These methods, therefore, cannot be employed to explore electronic properties of atomic-size objects. In contrast to area-averaging methods, the local-probe techniques such as tunneling microscopy (spectroscopy) (STM(S)) provide a unique possibility to probe the electronic structure with spatial resolution down to the single atom.

The STM was introduced by Gerd Binnig and Heinrich Rohrer in 1981 [1, 2], and is one of the most celebrated scanning-probe microscopy tools nowadays. The operating principle of the STM is based on a quantum tunneling of electrons between the surface of interest and the STM tip that occurs when the tip is placed several Angström above the surface and a tip-surface voltage (so-called bias voltage) is applied. The STM measures (in the topographic regime) the variation of the bias and the tunneling current as the tip is scanned along the surface, from which information about the surface properties can be derived.

The invention of the STM had a great impact on surface science, and has essentially revolutionized this field. Initially used for a three-dimensional imaging of atomic surfaces (see, e.g., Figs. 1.2-1.3), during the last decades this technique has developed into an ubiquitous experimental tool to study a vast range of phenomena in many disciplines of condensed matter physics, chemistry and biology, with an atomic resolution. The ability of the STM to investigate the fundamental relationship between the nanostructure and the nanophysical properties of materials determines the high impact of the STM not only on scientific research, but also on nanotechnology. This technique therefore contributes to the exploration and the benefit from quantum phenomenology in the ultimate limit of miniaturization.

The discovery of the "quantum mirage" effect is one of the famous examples that illustrates

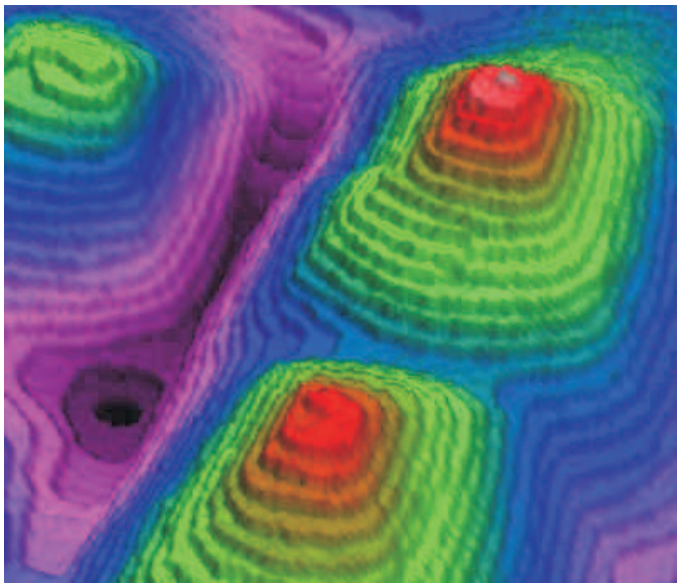

Figure 1.2: Nanometer-scale morphology of the spiral-like structures observed with scanning tunneling microscope. The spirals appear during molecular beam epitaxy of a GaSb film on a GaAs(001) surface. They grow around threading dislocations, that are caused by the film's 7% lattice mismatch with the substrate. Each threading dislocation creates a 0.3 nm-height spiraling "step" where it emerges at the surface. From Refs. [29, 30].

the abilities of the STM. In 2000, a group of researches from the IBM Almaden Research Center used the STM to construct atom-by-atom an elliptical ring consisting of 36 cobalt atoms, a so-called quantum corral (see Fig. 1.1 and Ref. [3]). By positioning a single cobalt atom at one of the two focus points of the quantum corral, it was shown that some of the atom properties suddenly appear at the other focus, where no atoms exist (Fig. 1.1). It was suggested that this effect, called "quantum mirage", may lead to an efficient way of data transfer that enables drastic miniaturization of future atomic-scale circuits and electronic devices.

The range of problems being addressed by the STM is large and is continuing to grow [4]. Here, we mention only major application fields of the modern STM. These include, e.g., investigations on the surface topography (Figs. 1.3-1.2), control and characterization of thin film and nanosized objects growth [5–7], measurements of adhesion and strength of individual chemical bonds, electronic and vibrational properties [8], dielectric and magnetic properties [9–17], as well as electron dynamics [6, 7, 18]. Lately, the STM has been applied to isolate reaction intermediates [19], to study the binding of molecules to surfaces [20], or to study biological samples such as e.g. freeze-dried DNA [21]. The STM has proven to be of indispensable help for the experimental research on high-temperature superconductors [22, 23], or for the identification of the most catalytically active surface sites [24]. In the spectroscopic regime, the STM allows to probe the local electronic structure of surfaces, to visualize a single molecular orbital of complex nanoobjects like, e.g., a $C_{60}$ molecule [25], or to probe vibrational properties of fullerene-cages in the inelastic regime [8]. Recently, the STM has been applied to study properties of nanotubes and novel nanosized devices, such as nanotube junctions/molecular electronic devices [26, 27], or molecular switches [28].

As discussed before, the STM is capable not only to probe surface properties, but could be also used to manipulate the positions of individual atoms [31] (see Fig. 1.1). This has been first shown

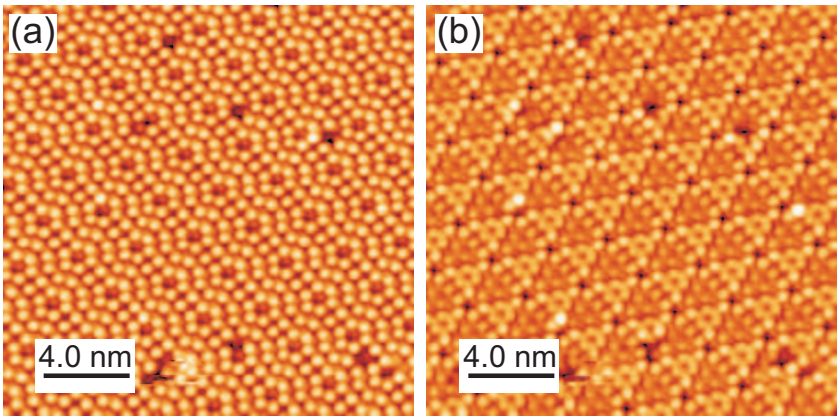


Figure 1.3: Atomically-resolved STM relief imaging electronic properties of a Si(111) surface. (a) The unoccupied and (b) occupied electronic states are probed at a bias voltage of +1.0 V and -1.0 V, respectively. The surface shows a 7×7 reconstruction pattern, described by the so-called dimer-adatom-stacking fault (DAS) model [35]. Figures taken from Ref. [36].

by Donald Eigler and Erhard Schweizer already in 1990 [20]. Since then, the STM is also used to design and construct artificial atomic structures atom-by-atom, and to study and/or control the properties of such objects. These can be, e.g., quantum corals, that can be used to study dynamical properties of electrons (Fig. 1.1 and Refs. [3, 6, 7]), or the fabrication of the so-called molecular cascades [32], that could be used to create the world-smallest logical circuits. Very recently, the STM was used to induce rolling of the so-called nanowheels along a copper surface [33, 34], the first steps towards a construction of nanomachines.

## 1.2 Necessity of an STM theory

While early research in the STM field often took experimental results at face value, many seemingly paradoxical results have now taught experimentalists to be cautious and even skeptical when confronted with STM images [4]. Despite the STM is capable to provide images that are very reminiscent to those obtained with an optical microscope (see, e.g., figures 1.1-1.3), an STM image contains *merged* effects of topography and electronic structure, causing a highly nontrivial relationship between the measured STM voltage and current, and the physical environment they reveal. As an example, in Fig. 1.3 we show an atomically-resolved STM image of the famous 7×7 reconstructed Si(111) surface that was the first reported great success of the STM [1, 2]. Although the STM experiments show seemingly simple images that could be interpreted as atomic maps, the actual surface structure could not be resolved from the STM experiments alone, and has been later achieved with the help of high resolution transmission electron microscopy [35]. Such a situation holds in most cases, i.e. the results of the STM experiments must be supported either by other experiments, or by an accurate theoretical modeling in order to get an unambiguous understanding of the STM images, and, consequently, of the surface properties being studied. The

experimental clarification of STM experiments, however, is typically not feasible, since STM is in many cases a unique experimental tool. Therefore, the theoretical description of the STM becomes an indispensable part of state-of-the-art STM studies.

Since STM images essentially depend on the electronic properties of a studied sample, an adequate theoretical model of the STM must rely on an explicit description of the electronic structure. Such a description is provided by modern *ab initio*[1] electronic structure theories. The development of such theories went in parallel with the development of the STM. Nowadays, electronic structure calculations have reached a level, where the same quantities that are being measured within STM can be simulated with a high level of accuracy. Consequently, it is highly desirable to interpret STM micrographs on the basis of *ab initio* calculations that allow an in-depth analysis and understanding of the experiments. Not the least, because the novel STM experiments become increasingly complex and are applied to study new physical phenomena, it is of extreme importance to verify the limits and applicability of the existing STM models. In case when existing approaches are not capable of an adequate description of the STM experiments, new models should be developed and applied.

## 1.3 Aim of this work

In this study we investigate to what extend *ab initio* simulations can contribute to an understanding of recent state-of-the-art STM experiments. We have concentrated on two fundamental problems of the STM: the study of the electron dynamics at surfaces, and the detailed characterization of the surface magnetic structure. In collaboration with two experimental groups we have selected two material systems which are particularly suited for these purposes. The main objective pursued in this work is to get an in-depth understanding of the STM experiments performed by our collaborators. For this purpose, we needed to develop several reliable theoretical tools and implement them into our multiscale simulation library S/PHI/nX [37, 38].

The dynamic properties of electrons (their dispersion) at the surfaces can be studied employing the so-called Fourier-Transformed STM (FT-STM). This technique is mostly used to study the properties of surface electrons, i.e., of electrons that do not penetrate deep into the substrate. The contribution due to bulk electrons that are essentially localized away from the surface, is typically assumed to be unimportant and is neglected. Therefore, one aim of our study is to identify, if bulk electrons indeed do not play a significant role in FT-STM experiments, and consequently cannot be studied with this technique. For this purpose our collaborators at the Fritz-Haber-Institut in Berlin have performed a set of FT-STM measurements on a terraced Ag(110) surface. In these experiments, the dispersion of a weak signal behaving similar to a surface electronic state has been observed. The origin of this signal, however, was not well understood, but it was assumed that

[1]The Latin term *ab initio*, translated as "from the beginning", indicates that the theory does not have any adjustable parameter that could be fitted to experiment. All parameters in an *ab initio* theory are based on the fundamental physical constants such as, e.g., electron charge, electrons mass, speed of light *etc.*

it is due to the bulk electrons. A theoretical confirmation of this assumption is highly desirable, being the first proof that the range of physical phenomena accessible with the STM technique can be extended to studying *local dynamical properties of bulk electrons*. Such a message is of great importance for the STM community and for fundamental surface science research. It is, therefore, one aim of the present work, to provide an *ab initio* justification of the assumption regarding bulk electrons has to be justified theoretically and, in case it is valid, to propose a comprehensive interpretation for the observed phenomenon.

Regarding the surface magnetism, we have focused our study on an in-depth understanding of the spin-polarized STM (SP-STM) experiments recently performed by our collaborators from Ohio University in USA on magnetically-ordered transition-metal nitride surfaces. The choice of the studied materials is stimulated by their primary technological interest, in view of the potential application to spin-based electronics and data-storage. On a $Mn_3N_2(010)$ surface SP-STM experiments allowed for the first time a *simultaneous* detection of both nonmagnetic *and* magnetic surface profiles. An in-face interpretation of these profiles, however, does not allow an unambiguous understanding of the actual surface properties, including both atomic and magnetic structure. It was not clear, e.g., whether all nitrogen atoms remained at the surface or have desorbed into the surrounding atmosphere. There were also no conclusive explanation of the surface magnetic ordering: whether it remains unchanged when compared with that in the bulk, or undergoes a sudden change (so-called magnetic surface reconstruction). Furthermore, a fundamental question how much an SP-STM image is affected by an STM tip needed to be clarified. Within this work we wanted to developed and apply a reliable theoretical tool for modeling SP-STM experiments in order to resolve these problems.

We shall start this work with a short description of the basic theoretical STM model employed in this study, given in chapter 2. The used STM model is based on the density functional theory (DFT) calculations. The DFT allows us to accurately describe the atomic geometry, the electronic structure, and the energetics of the surfaces without using any parameter that could be fitted to experiment, i.e. to perform STM simulations *ab initio*.

In chapter 3, we present a new computationally efficient approach for simulating FT-STM spectra in the constant-current mode of the STM. Here, the electron dynamics is detected by measuring standing wave patterns created due to electron scattering on surface imperfections. The model is applied to the particular case of Ag(110), with a detailed explanation of the experimental STM spectra and their correlation with surface electronic properties. A generalization of the results to other metallic surfaces is given.

In chapter 4, we perform SP-STM simulations on the $Mn_3N_2(010)$ surface, starting with a determination of the most stable surface structure by means of *ab initio* thermodynamics. The STM simulations are then performed on these surfaces, with a comparison of the simulated spectra to the corresponding experimental data. The effects of the STM tip on the simulated SP-STM images is discussed, with an in-depth explanation of the detected SP-STM maps in terms of the

electronic properties of the studied surface.

Finally, the results of this study are summarized in chapter 5.

# Chapter 2

# *Ab initio* Methods

Within the last decades computational methods have revolutionized the world of material science. Although the theoretical concepts behind these methods are well known since decades, only now the evolution of the computers let us to apply these methods to problems relevant for practical applications, such as modeling of the STM.

In this chapter we survey the theoretical methods used in this study for the simulation of STM experiments. We restrict ourselves solely to *ab initio* theoretical approaches. The term *ab initio* means that the mathematical approximations to the full M-particle Schrödinger equation are constructed without any adjustable parameter that can be fitted to reproduce experimental data.

This chapter is divided into two partitions. In the first part (sections 2.1-2.5) we briefly describe the *ab initio* approach to solid state physics, with emphasize on the most common *ab initio* method - density functional theory (DFT). The second part (sections 2.6-2.6.2) is based on results provided by the DFT, and describes the theoretical method used for STM simulations.

## 2.1 The many-body problem

A fundamental description of the chemical and physical properties of materials requires a quantum-mechanical treatment of the many-particle (many-body) system consisting of nuclei and electrons. Despite its complexity such an approach provides the most accurate description of the material properties.

Both the time-evolution and properties of the many-body system are completely defined by the corresponding many-body Hamiltonian, that contains the full information regarding the fundamental interactions between the constituent particles. Assuming that the Hamiltonian is a well defined operator, the complete description of the many-body system at any given time $t$ can be obtained by solving the time-dependent Schrödinger equation, that has been proposed by Erwin Schrödinger in 1925 [39]. In most cases, however, one is concerned with atoms and molecules without time-dependent interactions, and the time-dependent Schrödinger equation can be replaced by the time

independent one:

$$H(\{\mathbf{x}_i\},\{\mathbf{R}_I\})\Phi_\nu(\{\mathbf{x}_i\},\{\mathbf{R}_I\}) = E_\nu\Phi_\nu(\{\mathbf{x}_i\},\{\mathbf{R}_I\}). \tag{2.1}$$

Equation (2.1) describes the eigenvalue problem of the Hamiltonian $H(\{\mathbf{x}_i\},\{\mathbf{R}_I\})$, with the total energy of the system $E_\mu$ as eigenvalue, and the corresponding many-body wavefunction $\Phi_\nu(\{\mathbf{x}_i\},\{\mathbf{R}_I\})$ as eigenfunction. All properties of the system in a given state $\nu$ are explicitly characterized by the many-body wavefunction $\Phi_\nu(\{\mathbf{x}_i\},\{\mathbf{R}_I\})$, where the $\{\mathbf{R}_I\}$ are the spatial coordinates of the nuclei and the $\{\mathbf{x}_i\} = \{(\mathbf{r}_i,\sigma_i)\}$ are the generalized coordinates of the electrons, that contain both the spatial $\{\mathbf{r}_i\}$ and the spin $\{\sigma_i\}$ degrees of freedom. The explicit dependence on the spin degrees of freedom $\sigma_i = (\uparrow,\downarrow)$ has to be introduced in Eq. (2.1) additionally, in contrast to a fully-relativistic treatment (Dirac theory) where the electron spin arises naturally as one of the system properties. The subscript $\nu$ emphasizes that for each given set of coordinates $(\{\mathbf{x}_i\},\{\mathbf{R}_I\})$ there exists a set of possible solutions $\{\Phi_\nu\}$ that correspond to a set of possible system energies $\{E_\nu\}$.

Assuming that the relativistic effects are negligible[1] and that there are no external electric or magnetic fields acting on the system, the Hamiltonian of a system comprised of L nuclei and N electrons is written as[2]:

$$H(\{\mathbf{x}_i\},\{\mathbf{R}_I\}) = \underbrace{-\frac{1}{2}\sum_{i=1}^{N}\nabla_i^2}_{T^{\mathrm{e}}(\{\mathbf{x}_i\})} \underbrace{-\frac{1}{2}\sum_{I=1}^{L}\frac{1}{m_I}\nabla_I^2}_{T^{\mathrm{n}}(\{\mathbf{R}_I\})} \underbrace{-\sum_{i=1}^{N}\sum_{I=1}^{L}\frac{Z_I}{|\mathbf{r}_{iI}|}}_{V^{\mathrm{en}}(\{\mathbf{x}_i\},\{\mathbf{R}_I\})} + \underbrace{\sum_{i=1}^{N}\sum_{j>i}^{N}\frac{1}{|\mathbf{r}_{ij}|}}_{V^{\mathrm{ee}}(\{\mathbf{x}_i\})} + \underbrace{\sum_{I=1}^{L}\sum_{J>I}^{L}\frac{Z_I Z_J}{|\mathbf{R}_{IJ}|}}_{V^{\mathrm{nn}}(\{\mathbf{R}_I\})}. \tag{2.2}$$

In Eq. (2.2) atomic units ($m_e = \hbar = e = 1$, where $m_e$ and $e$ are the charge and rest mass of electron) are used. The Hamiltonian in Eq. (2.2) treats both nuclei and electrons as classical point-charges, with $Z_I$ and $m_I$ being the atomic number and mass of the $I$-th nucleus. $\nabla_\alpha^2$ is the Laplacian acting on particle $\alpha$, $|\mathbf{r}_{iI}| = |\mathbf{r}_i - \mathbf{R}_I|$, $|\mathbf{r}_{ij}| = |\mathbf{r}_i - \mathbf{r}_j|$, and $|\mathbf{R}_{IJ}| = |\mathbf{R}_I - \mathbf{R}_J|$ are the distances between electron $i$ and nuclei $I$, between two electrons with indices $i$ and $j$, and between two nuclei with indices $I$ and $J$, respectively. The Hamiltonian in Eq. (2.2) consists of five parts. The first and the second term correspond to the kinetic-energy operators, $T^{\mathrm{e}}$ and $T^{\mathrm{n}}$, for electrons and nuclei. The third term, $V^{\mathrm{en}}$, corresponds to the electron-nucleus Coulomb attraction. The

[1] This assumption generally applies to species with atomic numbers less than 40 and to valence electrons of heavier species. The validity of this assumption should be justified in each specific case when the core-electrons of heavy species are studied. The latter is due to the high degree of electronic localization, that results in the large kinetic energy of the core-electrons [40]. In our study we account for the relativistic effects by using a scalar-relativistic kinetic energy operator (the non-relativistic operator is shown in Eq. (2.2) for the sake of simplicity) [41] and averaging over the spin-orbit coupling term, as is commonly done in most applications (see, e.g., Refs. [42, 43] and Sec. 2.5).

[2] This form of the Hamiltonian is also referred to as Coulomb Hamiltonian. In addition to the assumption of zero external electromagnetic fields, the Coulomb Hamiltonian does not account for the spin-related effects like spin-orbit or spin-spin coupling. These terms can be added, however, on demand when the spin-dependencies cannot be averaged out (see Sec. 2.6.3 for spin-systems, and Ref. [40]).

fourth and the last term, $V^{\mathrm{ee}}$ and $V^{\mathrm{nn}}$, describe the Coulomb repulsion between the electrons resp. between the nuclei.

Eq. (2.2) can be rewritten in compact form as:

$$H(\{\mathbf{x}_i\},\{\mathbf{R}_I\}) = T^{\mathrm{e}}(\{\mathbf{x}_i\}) + T^{\mathrm{n}}(\{\mathbf{R}_I\}) + V^{\mathrm{en}}(\{\mathbf{x}_i\},\{\mathbf{R}_I\}) + V^{\mathrm{ee}}(\{\mathbf{x}_i\}) + V^{\mathrm{nn}}(\{\mathbf{R}_I\}). \tag{2.3}$$

Although the Hamiltonian in Eq. (2.3) is known, it is generally too complex to be solved for realistic many-body systems[3]. Indeed, the many-body wavefunction in Eq. (2.1) depends on the $M = 4N + 3L$ independent system variables, where $3N + 3L$ degrees of freedom result from the spatial coordinates, and $M$ degrees of freedom from the electron spin-coordinates. In condensed matter physics $M$ is of the order of Avogadro's constant $N_{\mathrm{A}} = 6.022 \times 10^{23}$ particles per cubic centimeter. The huge dimensionality of the problem and the many-body nature of equations (2.1)-(2.3) makes a numerically exact solution practically impossible and at the same time even undesired, since the many-body wavefunction $\Phi_\nu$ is a much too complicated object if one aims to understand and predict material properties.

It is clear (i) that the solution of Eq. (2.1) for realistic systems can be obtained only numerically and (ii) that such a solution cannot be made without approximations. The hierarchy of approximations that allow a numerical solution of the many-body Schrödinger equation without sacrificing it's physical content is described in the following chapters.

## 2.2 Born-Oppenheimer Approximation

One of the major simplifications to Eq. (2.1) was suggested in 1927 by Born and Oppenheimer [44], who proposed a separation in the time scale of processes involving electrons and nuclei.

The validity of such a separation is based on the mass-ratio $m_{\mathrm{I}}/m_e$ of the electrons and nuclei, that is already $\sim 2000$ for a single proton, and is $\sim 10^5$ for heavier elements. This implies that assuming thermal equilibrium between electrons and nuclei (the same average kinetic energy per substituent particle), electrons are typically $10^2$ to $10^3$ times faster than the nuclei. Hence, one supposes that electrons respond on the nuclei motion almost instantaneously, and recognize the actual configuration of the ions as an essentially stationary external potential to which electrons adjust by adopting the state of the lowest energy [45]. This allows to decouple the nuclear and electronic motion, and perform calculations of the electronic structure separately from a calculation of the ionic motion.

For each fixed nuclei configuration $\{\mathbf{R}_I\}$ one defines the electronic Hamiltonian as[4]:

[3] In fact, the solution of Eq. (2.1) in the closed form can be derived only for two mutually interacting particles like the proton-electron structure of the hydrogen atom.

[4] Sometimes it is assumed that electronic Hamiltonian contains electrostatic nuclear-nuclear interactions (see, e.g.

$$H^{\mathrm{e}}(\{\mathbf{x}_i\},\{\mathbf{R}_I\}) = T^{\mathrm{e}}(\{\mathbf{x}_i\}) + V^{\mathrm{ne}}(\{\mathbf{x}_i\},\{\mathbf{R}_I\}) + V^{\mathrm{ee}}(\{\mathbf{x}_i\}). \tag{2.4}$$

The corresponding possible stationary solutions $\Psi_\nu$ and energy eigenvalues $E^{\mathrm{e}}_\nu$ for the electronic subsystem are obtained by solving the time-independent Schrödinger equation for electrons experiencing the potential of the static array of nuclei:

$$H^{\mathrm{e}}(\{\mathbf{R}_I\})\Psi_\nu(\{\mathbf{x}_i\},\{\mathbf{R}_I\}) = E^{\mathrm{e}}_\nu(\{\mathbf{R}_I\})\Psi_\nu(\{\mathbf{x}_i\},\{\mathbf{R}_I\}). \tag{2.5}$$

The Hamiltonian in Eqs. (2.4)-(2.5), as well as the corresponding solutions of the Schödinger equation (2.5), depend on the nuclei positions $\{\mathbf{R}_I\}$ parametrically. For a given nuclei configuration, the $\Psi_\nu$ form a complete basis set, that can be used to expand the solution of Eq. (2.1) in the form:

$$\Phi_\eta(\{\mathbf{x}_i\},\{\mathbf{R}_I\}) = \sum_\nu \Lambda_{\eta\nu}(\{\mathbf{R}_I\})\Psi_\nu(\{\mathbf{x}_i\},\{\mathbf{R}_I\}), \tag{2.6}$$

with expansion coefficients $\Lambda(\{\mathbf{R}_I\})$ that depend on the ion configuration $\{\mathbf{R}_I\}$. The whole problem for the nuclei-electron many-body Hamiltonian then reads as:

$$(T^{\mathrm{n}} + H^{\mathrm{e}} + V^{\mathrm{nn}})\Phi_\eta(\{\mathbf{x}_i\},\{\mathbf{R}_I\}) = E_\eta\Phi_\eta(\{\mathbf{x}_i\},\{\mathbf{R}_I\}). \tag{2.7}$$

Substituting Eq. (2.6) into Eq. (2.7) and eliminating the electron coordinates in the obtained expression (for details see e.g. Refs. [45, 47]) one gets the following Hamiltonian describing the motion of the nuclei:

$$\left[T^{\mathrm{n}} + E^{\mathrm{e}}_\mu + V^{\mathrm{nn}} - \sum_\nu \sum_{I=1}^{L} \frac{1}{2m_I}\left(\langle\Psi_\eta|\nabla_I^2|\Psi_\nu\rangle + 2\langle\Psi_\eta|\nabla_I|\Psi_\nu\rangle\nabla_I\right)\right]\Lambda_{\eta\mu} = E^{\mathrm{n}}_\eta\Lambda_{\eta\mu}. \tag{2.8}$$

The fourth term in the ionic Hamiltonian is due to the coupling of the nuclei motion with the electronic subsystem, the so-called electron-phonon coupling. This term is essential e.g. in the field of the superconductivity, for studying Jahn-Teller distortions, Peierls instabilities, Kohn anomalies, and high-energy atom-surface collisions [48]. In most other cases, however, the electron-phonon matrix elements are small enough that the mass-arguments hold: due to the comparably large nuclear masses in the denominator of the electron-phonon coupling term these interactions can be neglected altogether. Neglecting the electron-phonon coupling in Eq. (2.8) is known as the Born-Oppenheimer approximation. The corresponding ionic Hamiltonian is written as:

Ref. [46]), that does not affect neither derivation nor conclusions of this section.

$$\left[ T^{\mathrm{n}}(\{\mathbf{R}_I\}) + \underbrace{E^{\mathrm{e}}_{\mu}(\{\mathbf{R}_I\}) + V^{\mathrm{nn}}(\{\mathbf{R}_I\})}_{E^{\mathrm{BOS}}_{\mu}(\{\mathbf{R}_I\})} \right] \Lambda_{\eta\mu}(\{\mathbf{R}_I\}) = E^{\mathrm{n}}_{\eta} \Lambda_{\eta\mu}(\{\mathbf{R}_I\}). \tag{2.9}$$

According to Eq. (2.9) the nuclei experience the potential $E^{\mathrm{BOS}}_{\mu} = E^{\mathrm{e}}_{\mu}(\{\mathbf{R}_I\}) + V^{\mathrm{nn}}(\{\mathbf{R}_I\})$, called Born-Oppenheimer surface, that is due to the electrostatic nuclear-nuclear repulsion and the total energy of the electronic subsystem. Eq. (2.9) implies, therefore, that the nuclei move on a potential energy surface derived from the solution of the electronic problem for each static configuration.

In this study we do not deal with systems requiring inclusion of electron-phonon or spin-phonon coupling, and can safely employ the Born-Oppenheimer approximation. We concentrate, therefore, on the solution of the electronic Schrödinger equation for a given positions of nuclei.

## 2.3 Solving electronic Schrödinger equation

Despite the fact that the Born-Oppenheimer approximation significantly simplifies the original many-body problem, the solution of the electronic Hamiltonian, except for the simplest cases, is possible only numerically and by introducing further approximations. There are essentially two conceptually different techniques to solve the electronic Schrödinger equation: the wavefunction-based theory (quantum chemistry and quantum Monte Carlo methods) and the electron-density based methods (density functional theory). Both approaches are introduced in the following sections in some detail, with special attention to the electronic exchange and correlation effects.

Since electronic structure calculations for surfaces are dominated by density functional theory methods, this section is mostly focused on this method. The section starts with an introduction of an important quantum mechanical principle - the Rayleigh-Ritz variational principle - that provides a straightforward scheme to find a numerical solution for the ground-state properties of the electronic Schrödinger equation, that is heavily used in nearly all modern quantum mechanical studies.

### 2.3.1 The Rayleigh-Ritz variational principle

The Rayleigh-Ritz variational principle [46, 49] provides the basis for the most contemporary numerical calculations on the electronic Schrödinger equation (Eq. (2.5)). The principle holds, however, for any system described by a known Hamiltonian, i.e. it also applies to Eq. (2.1).

According to this principle, the expectation value of a known Hamiltonian, calculated using *any* trial wavefunction $\Psi_{\mathrm{trial}}$ is always greater than or equal to the true ground state energy $E_0$:

$$E[\Psi_{\mathrm{trial}}] \equiv \frac{\langle \Psi_{\mathrm{trial}} | H^{\mathrm{e}} | \Psi_{\mathrm{trial}} \rangle}{\langle \Psi_{\mathrm{trial}} | \Psi_{\mathrm{trial}} \rangle} \geq E_0. \tag{2.10}$$

Here, $E_0$ is the system energy obtained by a full minimization of the functional $E[\Psi]$ with respect to all allowed $N$-electron wavefunctions, that gives the true ground state $\Psi_0$ and energy $E_0 = E[\Psi_0]$:

$$E_0 = \min_{\Psi} E[\Psi]. \tag{2.11}$$

The variational principle allows to reformulate the Schrödinger equation (Eq. (2.5)) in completely equivalent form:

$$\delta[\langle\Psi|H^{\mathrm{e}}|\Psi\rangle - E\langle\Psi|\Psi\rangle] = 0. \tag{2.12}$$

Here, the total energy of the system $E$ enters as a Lagrange multiplier that guarantees a proper normalization of the final solution $\Psi$. The true ground state is obtained by solving Eq. (2.12), that allows a search of the true ground-state wavefunction $\Psi$ for a given Hamiltonian $H^{\mathrm{e}}$ starting with an arbitrary guess for $\Psi$.

### 2.3.2 Wavefunction-based theories

Wavefunction-based methods solve the electronic Schrödinger equation by focusing on the full many-body wavefunction $\Psi$. It is either calculated directly or for larger systems by using perturbation theory or a statistical sampling. The set of wavefunction-based methods includes quantum chemistry and quantum Monte Carlo techniques. These methods target on a very high accuracy, as needed, e.g., to understand the details of chemical reactions (chemical accuracy 1 kcal/mol). The wavefunction-based methods are only briefly described here. A more detailed discussion of these methods can be found elsewhere (see e.g. Ref. [46] and references therein).

The fundamental quantum chemistry approach is the Hartree-Fock approximation (HF) [50, 51]. In frame of HF theory the many-body problem is transformed into an equivalent single-particle problem by approximating the electronic wavefunction by a Slater determinant of single wavefunctions:

$$\Psi_{\mathrm{HF}}(\{\mathbf{x}_i\}) = \frac{1}{\sqrt{N!}} \begin{vmatrix} \psi_1(\mathbf{x}_1) & \psi_2(\mathbf{x}_1) & ... & \psi_N(\mathbf{x}_1) \\ \psi_1(\mathbf{x}_2) & \psi_2(\mathbf{x}_2) & ... & \psi_N(\mathbf{x}_2) \\ \vdots & \vdots & & \vdots \\ \psi_1(\mathbf{x}_N) & \psi_2(\mathbf{x}_N) & ... & \psi_N(\mathbf{x}_N) \end{vmatrix} \tag{2.13}$$

$$= \frac{1}{\sqrt{N!}} \det[\psi_1\psi_2...\psi_N]. \tag{2.14}$$

Here, $\psi_i(\mathbf{x}_j)$ is the $i$-th single-particle wavefunction that depends both on the spatial coordinate $\mathbf{r}_j$ and the spin $\sigma_j$. $\psi_i(\mathbf{x}_j) \equiv \psi_{i\sigma_j}(\mathbf{r}_j)$ form an orthogonal basis set ($\langle\psi_i|\psi_j\rangle = \delta_{ij}$) and are the

solutions of the Hartree-Fock equation. The Hartree-Fock equation is derived by applying the variational principle to the many-body Hamiltonian (Eq. (2.4)) with the Hartree-Fock ansatz for the many-body wavefunction (Eq. (2.14)) to get the ground-state solution for $\Psi_{\mathrm{HF}}$:

$$\left[-\frac{1}{2}\nabla^2 + \underbrace{V^{\mathrm{en}}(\mathbf{r}) + V^{\mathrm{H}}(\mathbf{r}) + V^{\mathrm{x}}_{i\sigma_j}(\mathbf{r})}_{V^{\mathrm{HF}}_{i\sigma_j}(\mathbf{r})}\right] \psi_{i\sigma_j}(\mathbf{r}) = \varepsilon_{i\sigma_j}\psi_{i\sigma_j}(\mathbf{r}). \tag{2.15}$$

From Eqs. (2.14)-(2.15) it is clear that the Hartree-Fock theory corresponds to a mean-field approximation: the one-particle Schrödinger equation is solved for an electron embedded in the electrostatic field $V^{\mathrm{HF}}_{i\sigma_j}(\mathbf{r})$ due to all electrons, i.e. the original many-body problem is mapped onto a system of noninteracting electrons. The effective electrostatic potential $V^{\mathrm{HF}}_{i\sigma_j}(\mathbf{r})$ in Eq. (2.15) consists of three parts. The first term, $V^{\mathrm{en}}(\mathbf{r})$, accounts for electrostatic interaction between electron and the nuclei. The second term, the Hartree potential $V^{\mathrm{H}}(\mathbf{r})$, is the electrostatic potential of all electrons. The third term $V^{\mathrm{x}}_{i\sigma_j}(\mathbf{r})$, called the exchange term, fully accounts for the correlated motion of electrons with the same spin, and appears due to an antisymmetry requirement for the wavefunction $\Psi_{\mathrm{HF}}$ that is incorporated in the Hartree-Fock method in order to fulfil the Pauli principle (see, e.g. Ref. [46] for details).

The Hartree-Fock ansatz does not allow, however, to calculate the true ground state properties, because it completely neglects the correlated motion of electrons with opposite spin. Due to this correlation the total energy of the system can be further reduced if these electrons are also avoiding each other [46]. This additional effect that is not captured in the Hartree-Fock theory is defined as *electron correlation*, and the energy difference between the exact and the Hartree-Fock energy is defined as *electron correlation energy*[5]. Although the electronic correlation energy is typically a rather small contribution to the total energy it cannot be neglected, if one is interested, e.g., in a reliable description of the chemical bond formation.

In order to improve the original Hartree-Fock approach, more involved theories have been developed, that treat the electron correlation at various levels of sophistication [52–57]. These methods can be divided into two categories, the single-reference and the multiple-reference methods. The single-reference methods start with a solution of the Hartree-Fock Hamiltonian and introduce correlation effects by including virtually excited states, that are derived from the Hartree-Fock Slater determinant. The most popular single-reference methods are the second/fourth order perturbation theory by Møller and Plesset (MP2/MP4) [52], as well as configuration interaction (CI) [54] and coupled cluster (CC) [55] approaches. The single-reference methods are known to produce accurate results in the vicinity of equilibrium configurations, but are no longer adequate to describe, e.g., the bond-breaking process. In these cases one needs the multiple-reference methods,

[5]The distinction between exchange and electron correlation is to some extend artificial, because the Hartree-Fock exchange is in principle also a correlation effect (so-called Pauli correlation). It is commonly agreed, however, that the term *correlation* is used for all the contributions that are not accounted for in the HF theory.

like multiconfigurational self-consistent field (MCSCF) or complete active space SCF (CASSCF) techniques [53, 56], that expand the many-body wavefunction as a sum of Slater determinants corresponding to different configurations of the system.

Quantum chemistry methods allow for a systematic improvement in the description of the electron correlation. This is a very attractive property of these methods, that has to be paid, however, by enormous computational efforts. This limits the maximum system size to typically 10-20 atoms, which is often not sufficient to model realistic solid-state systems. Consequently, the quantum chemistry methods are mostly used to theoretically study atoms and molecules.

Another wavefunction-based approach is the quantum Monte Carlo technique (QMC), that allows to obtain very accurate ground-state properties for weakly correlated systems [58]. QMC exhibits a favorable scaling of computational costs with system size when compared to conventional quantum chemistry methods, and can be consequently applied to calculate correlated properties of large molecules or even solid systems, where quantum chemistry methods are extremely difficult to apply. QMC is based on a statistical sampling of the many-body wavefunction $\Psi$, i.e. is an explicit many-body method that includes the electron correlations from the outset. The use of QMC has been greatly hampered over the last decades by a combination of insufficient computer power and inefficient computer techniques. Only recently remarkable progress has been made in development of efficient and accurate QMC algorithms, and first applications to surface science problems have been carried out [46].

An alternative more efficient scheme for solving the electronic Schrödinger equation is given by the density functional theory, that is described in the next section. It is noteworthy, that although the DFT originates mainly from solid state physics, this method becomes more popular also in the quantum chemistry [59].

### 2.3.3 Density functional theory

Density functional theory (DFT) is an alternative approach to solve the electronic Hamiltonian $H^{\mathrm{e}}$ by shifting the attention from the complex many-body wavefunction $\Psi(\{\mathbf{x}_i\})$ to physical observables, most notably to the electron density $n(\mathbf{r})$ and the total energy of the electronic system $E$. The electron density $n(\mathbf{r})$ determines the probability to find an electron in a volume $d\mathbf{r}$ around an arbitrary spatial position $\mathbf{r}$, and is related to the many-body wavefunction $\Psi(\{\mathbf{x}_i\})$ as [59]:

$$n(\mathbf{r}) = \langle\Psi| \sum_{i}^{N} \delta(\mathbf{r} - \mathbf{r}_i)|\Psi\rangle, \tag{2.16}$$

Eq. (2.16) can be rewritten explicitly as [59]:

$$n(\mathbf{r}) \equiv n(\mathbf{r}_1) = N \int ... \int |\Psi(\{\mathbf{x}_i\})|^2 d\sigma_1 d\mathbf{x}_2 ... d\mathbf{x}_{N_{\mathrm{e}}}. \tag{2.17}$$

It is obvious from Eqs. (2.16)-(2.17) that treating the electron density as a basic variable is

more attractive than an explicit calculations on the many-body wavefunction $\Psi(\{\mathbf{x}_i\})$, mostly due to the drastic reduction in degrees of freedom. Indeed, while $\Psi(\{\mathbf{x}_i\})$ depends on $3N$ spatial coordinates, the electron density is a function of only three coordinates ($\mathbf{r} = (x, y, z)$)[6]. Despite the fact that the electron density is a much simpler object as compared to the complex many-body wavefunction, DFT allows an exact formulation of the original many-body problem in terms of the electron density.

In what follows, we introduce below the fundamental concepts of the DFT, starting from the simple predecessor of this theory, the Thomas-Fermi approximation.

#### 2.3.3.1 The Thomas-Fermi model

In 1927, Thomas and Fermi [60–62] suggested the very first approach for solving the electronic Schrödinger equation using the electron density $n(\mathbf{r})$. In their model the total energy of a system was formulated as a functional of the electron density as:

$$E_{\mathrm{TF}}[n(\mathbf{r})] = \frac{3}{10}\left(3\pi^2\right)^{\frac{2}{3}} \int n^{\frac{5}{3}}(\mathbf{r})d\mathbf{r} - \sum_{I=1}^{L} Z_I \int \frac{n(\mathbf{r})}{\mathbf{r}} d\mathbf{r} + \frac{1}{2}\int\int \frac{n(\mathbf{r})n(\mathbf{r}')}{|\mathbf{r}-\mathbf{r}'|} d\mathbf{r}d\mathbf{r}'. \tag{2.18}$$

Here, the exchange and correlation effects are neglected, and interactions between constituent particles are taken into consideration only classically via electron-nuclei attraction (second term in Eq. (2.18)) and electron-electron repulsion (third term in Eq. (2.18)). The first term in Eq. (2.18) is the famous Thomas-Fermi kinetic energy functional, that is a rough approximation to the true many-body kinetic energy. The Thomas-Fermi kinetic energy functional is derived from the kinetic energy density for a homogeneous gas of noninteracting electrons.

The ground state density $n_0(\mathbf{r})$ for a given configuration of nuclei and number of electrons $N$ is then calculated *assuming* (i.e. without any proof) that for the ground state of the system the electron density minimizes the functional $E_{\mathrm{TF}}[n(\mathbf{r})]$, under the constraint of keeping the number of electrons in the system constant:

$$\int n(\mathbf{r})d\mathbf{r} = N. \tag{2.19}$$

The application of the Thomas-Fermi approach to realistic systems elucidated significant deficiencies of the method. Among other, no molecular binding to form molecules and solids was predicted by the Thomas-Fermi theory. Even for isolated molecules the results are not satisfactory, revealing no shell structure of atoms, and consequently predicting a shrinkage of the atom size with increasing the atomic number $Z$ [40]. The largest source of errors in the Thomas-Fermi theory is the use of the free-electron approximation for the kinetic energy, which should be replaced by a better functional [63].

[6] The spin degrees of freedom are discussed in Sec. 2.6.3.

Because of the essentially inaccurate results, the ideas of the Thomas-Fermi theory were for a long time viewed as oversimplifications that are not suitable for quantitative predictions. The situation changed 40 years later with the proof of the Hohenberg-Kohn theorems, that justified the use of the electron density as fundamental variable to describe the electronic Hamilton operator.

#### 2.3.3.2 The Hohenberg-Kohn theorems

In 1964 Hohenberg and Kohn have formulated two theorems that legitimized the use of the electron density $n(\mathbf{r})$ as the basic variable in solving the electronic Schrödinger equation, and formally became a foundation of the modern DFT [64].

To introduce the Hohenberg-Kohn theorems, let us consider the general case of $N$ interacting electrons moving in an external potential $\upsilon^{\text{ext}}$, that can arise, e.g., due to the electron-nuclei interactions (but is not necessary restricted to this case). The Hamiltonian of such a system is written as:

$$H^{\text{e}} = T^{\text{e}} + V^{\text{ee}} + \upsilon^{\text{ext}}. \tag{2.20}$$

Here, $T^{\text{e}}$ is the kinetic energy operator and $V^{\text{ee}}$ corresponds to the electron-electron Coulomb repulsion (defined in Eq. (2.2)). The first Hohenberg-Kohn theorem states that the external potential $\upsilon^{\text{ext}}$ is determined, within a trivial additive constant, by the ground-state electron density $n_0(\mathbf{r})$[7]. By definition (see Eq. (2.2)), the $T^{\text{e}}$ kinetic energy and $V^{\text{ee}}$ electron-electron interaction operators depend only on the total number of electrons in the system, that in turn can be also derived from the electron density (see Eq. (2.19)). The ground-state electron density, therefore, completely determines the full Hamiltonian $H^{\text{e}}$ and all quantities that can be derived from it, e.g., the electronic excitation spectrum and/or any quantum mechanical observable of the system $O$:

$$n_0(\mathbf{r}) \rightarrow \left\{ \begin{matrix} \upsilon^{\text{ext}}(\mathbf{r}) \\ N \end{matrix} \right\} \rightarrow H^{\text{e}} \rightarrow \Psi \rightarrow \langle \Psi | O | \Psi \rangle. \tag{2.21}$$

From the first Hohenberg-Kohn theorem it follows that the total energy of the electronic system, as one of the observables, is completely defined by the ground-state charge density. The total energy of the system can be formulated therefore as a functional of the electron density as:

$$E[n(\mathbf{r})] = F[n(\mathbf{r})] + \int n(\mathbf{r}) \upsilon^{\text{ext}}(\mathbf{r}) d\mathbf{r}. \tag{2.22}$$

Here, the functional $F$ does not depend on the external potential and is therefore universal, i.e. is the same for all systems described by the Schrödinger equation (Eq. (2.5)). It is defined as [59, 63]:

[7] In case of a non-degenerate ground-state, there is even a one-to-one correspondence between $\upsilon^{\text{ext}}(\mathbf{r})$ and $n(\mathbf{r})$, i.e. $n_0(\mathbf{r}) \rightleftarrows \upsilon^{\text{ext}}(\mathbf{r})$.

$$F[n(\mathbf{r})] = \min_{\Psi \to n(\mathbf{r})} \langle \Psi | \left( T^{\mathrm{e}} + V^{\mathrm{ee}} \right) | \Psi \rangle = T^{\mathrm{e}}[n(\mathbf{r})] + V^{\mathrm{ee}}[n(\mathbf{r})]. \tag{2.23}$$

Here, the functional $F[n(\mathbf{r})]$ is further split into two independent contributions, the kinetic energy functional $T^{\mathrm{e}}[n(\mathbf{r})]$ and the electron-electron interactions term $V^{\mathrm{ee}}[n(\mathbf{r})]$. The functional $F[n]$ searches all $\Psi$ that yield the input electron density $n(\mathbf{r})$ (not necessary the ground-state density) and then delivers the minimum expectation value for operator $(T^{\mathrm{e}} + V^{\mathrm{ee}})$. The above definition of the functional $F$ can be derived, e.g., from the total energy expressed in terms of a mixed $\Psi$/electron-density representation:

$$E = \langle \Psi | H^{\mathrm{e}} | \Psi \rangle = \langle \Psi | \left( T^{\mathrm{e}} + V^{\mathrm{ee}} \right) | \Psi \rangle + \int n(\mathbf{r}) \upsilon^{\mathrm{ext}}(\mathbf{r}) d\mathbf{r}, \tag{2.24}$$

and applying the Rayleigh-Ritz minimum-energy principle for the ground-state.

Eq. (2.22) would provide an *exact* solution of the many-body electronic Hamiltonian, if the universal functional $F$ was known *exactly*. Unfortunately, the explicit form of the functionals in Eq. (2.24) is unknown.

The second Hohenberg-Kohn theorem is essentially the energy variational principle (see Sec. 2.3.1) formulated for the minimization of the total energy with respect to the electron density $n(\mathbf{r})$. Assuming that the electron density is well behaved, i.e. that $n(\mathbf{r}) \geq 0$ and Eq. (2.19) holds, the total energy of electronic system is always greater or equal to the true ground state total energy $E_0$:

$$E[n_{\mathrm{trial}}(\mathbf{r})] \geq E_0 = E[n_0(\mathbf{r})]. \tag{2.25}$$

The minimum of the energy functional $E[n]$ corresponds to the true ground state energy, that is defined by the corresponding ground state electron density $n_0(\mathbf{r})$:

$$E_0 = \min_n E[n]. \tag{2.26}$$

The variational principle for electron density is analogous to variational principle for wavefunctions, and provides justification of the variational principle employed without any proof in the Thomas-Fermi theory (see Sec. 2.3.3.1).

The second Hohenberg-Kohn theorem provides a straightforward way to solve the electronic Schrödinger equation by virtue of Eq. (2.26) under the constraint of a constant number of electrons $N$ (cf. Eq. (2.19)), which results in the Euler-Lagrange equation:

$$\delta \left( E[n(\mathbf{r})] - \mu \left[ \int n(\mathbf{r}) d\mathbf{r} - N \right] \right) = 0. \tag{2.27}$$

Here, the Lagrange multiplier $\mu$ physically corresponds to chemical potential of electrons.

As mentioned above, the Hohenberg-Kohn theorems provide the firm basis of modern DFT, because they allow to solve the many-body electronic Schrödinger equation *exactly*, if the explicit

expression for the universal functional $F[n]$ is known. Unfortunately, the problem of constructing such an expression is not solved up to now and is likely never will be solved. In the next section we present a state-of-the-art method of handling the functional $F[n]$ as provided by the Kohn-Sham theory.

#### 2.3.3.3 The Kohn-Sham equations

Despite of the fact that the Hohenberg-Kohn theorems significantly simplify the many-electron problem by shifting the focus from the many-body wavefunction $\Psi$ to the much simpler electron density $n(\mathbf{r})$, the density-based theory seems to be rather abstract and of minor use due to the unknown form of the universal functional $F[n(\mathbf{r})]$ (see previous section). Thomas-Fermi model and related approaches tried to construct explicit forms for $F[n]$ resulting in equations that involve the electron density alone, but were not able to go beyond the crude level of approximations [59]. In 1965, about a year after the introduction of the Hohenberg-Kohn theorems, Kohn and Sham [65] proposed a practical way to evaluate the universal functional $F[n(\mathbf{r})]$, that is of major importance for modern density functional theory.

Kohn and Sham proposed a route to calculate a part of the universal functional $F[n]$, the kinetic energy contribution $T^{\mathrm{e}}[n]$ (see Eq. (2.23)), approximately but with a good accuracy, leaving the small residual corrections that are handled separately. According to the approach of Kohn and Sham, this is accomplished via the introduction of a fictitious auxiliary noninteracting electron system that moves in some effective external potential $V^{\mathrm{eff}}(\mathbf{r})$. The corresponding single-electron Hamiltonian is $H^{\mathrm{s}} = T^{\mathrm{s}} + V^{\mathrm{eff}}$. The effective potential is constructed in such a way, that the electron density of the auxiliary non-interacting system equals the density of the interacting system of interest [63]. In other words, Kohn and Sham assumed that the following relation holds:

$$H^{\mathrm{s}} \rightarrow n^{\mathrm{s}}(\mathbf{r}) \stackrel{!}{\equiv} n(\mathbf{r}) \leftarrow H^{\mathrm{e}}. \tag{2.28}$$

There is no formal proof that Eq. (2.28) can always be fulfilled, i.e. that the electron density of an arbitrary interacting many-electron system can be always mapped onto the electron density of some noninteracting many-electron system. Nevertheless, the vast amount of DFT calculations that have been performed during the last forty years have shown that the Kohn assumption (Eq. (2.28)) nicely performs for *studied* realistic systems (which is not a proof that Eq. (2.28) holds for *all* systems). Condition (2.28) implies that $T^{\mathrm{s}}[n^{\mathrm{s}}] \equiv T^{\mathrm{s}}[n]$, and allows to recast the universal functional $F[n]$ in terms of the kinetic energy functional $T^{\mathrm{s}}[n]$ for a system of noninteracting electrons as:

$$F[n] = T^{\mathrm{s}}[n] + J[n] + E^{\mathrm{xc}}[n]. \tag{2.29}$$

Here, one introduces $J[n]$ as the repulsive energy due to the classical electrostatic electron-electron interaction (Hartree term):

$$J[n(\mathbf{r})] = \frac{1}{2}\int\int \frac{n(\mathbf{r})n(\mathbf{r}')}{|\mathbf{r}-\mathbf{r}'|}d\mathbf{r}d\mathbf{r}'. \tag{2.30}$$

The remaining part in Eq. (2.29) is the so-called exchange-correlation energy of a system of interacting particles, that contains the difference in the kinetic energy between the real, interacting system, and the artificial noninteracting counterpart as well as the nonclassical part of the electron-electron repulsion ($E^{\mathrm{ncl}}[n] = V^{\mathrm{ee}}[n] - J[n]$):

$$E^{\mathrm{xc}}[n] \equiv T^{\mathrm{e}}[n] - T^{\mathrm{s}}[n] + V^{\mathrm{ee}}[n] - J[n]. \tag{2.31}$$

Although the functional $F[n]$, reformulated according to Eq. (2.29), is still unknown, the two major energy contributions $T^{\mathrm{s}}[n]$ and $J[n]$ can now be calculated *exactly*. All unknown terms are now merged into the exchange-correlation energy, that is presumably small compared to $T^{\mathrm{e}}[n]$ and $J[n]$, if one assumes that the nonclassical electrostatic energy is small, and recalls that $T^{\mathrm{e}}$ and $T^{\mathrm{s}}$ are of comparable magnitude. The expression for $T^{\mathrm{s}}[n]$ has a particularly simple form, if one requests the auxiliary single-particle wavefunctions $\varphi_i$ to be orthonormalized[8]:

$$T^{\mathrm{s}}[n(\mathbf{r})] = -\frac{1}{2}\langle\varphi_i|\sum_{i=1}^{N}\nabla_i^2|\varphi_i\rangle. \tag{2.32}$$

Here, $i$ denotes both the spin as well as the spatial quantum numbers, and the sum runs over $N$ lowest (occupied) eigenstates $\varphi_i$ to respect the Pauli principle. The wavefunctions $\varphi_i$ are obtained by solving the single-particle Schrödinger equation with Hamilton operator $H^{\mathrm{s}}$:

$$\left[-\frac{1}{2}\nabla^2 + V^{\mathrm{eff}}(\mathbf{r})\right]\varphi_i = \epsilon_i\varphi_i. \tag{2.33}$$

Kohn and Sham have derived the explicit form of the effective potential $V^{\mathrm{eff}}(\mathbf{r})$ by applying the variational principle (second Hohenberg-Kohn theorem, Eq. (2.26)) to the functional $F[n]$ as given by Eq. (2.29). The minimization of $F[n]$ is performed in the space of single-particle wavefunctions $\varphi_i$ (implicitly in the space of the corresponding electron density $n = n[\{\varphi_i\}]$), employing the

[8]The many-body kinetic energy operator for the electronic subsystem is written as (see Eq. (2.2)):

$$T^{\mathrm{e}} = -\frac{1}{2}\sum_{i=1}^{N}\nabla_i^2.$$

The many-particle ground-state wavefunction for a system of *noninteracting* electrons can be exactly expressed in form of the single Slater determinant, that ensures the antisymmetry of the wavefunction with respect to the permutation of two electrons [59]:

$$\Psi = \frac{1}{\sqrt{N!}}\det[\varphi_1\varphi_2...\varphi_N],$$

where the $\varphi_i$ are the $N$ lowest single-particle wavefunctions that form an orthonormal basis set ($\langle\varphi_i|\varphi_j\rangle = \delta_{ij}$). The orthonormality constraint for auxiliary orbitals $\varphi_i$ is the crucial point in the Kohn-Sham theory, because otherwise the particularly simple expressions for kinetic energy $T = \langle\Psi|T^{\mathrm{s}}|\Psi\rangle$, given by Eq. (2.33), and electron density $n(\mathbf{r})$ of the noninteracting electrons, given by Eq. (2.36) respectively, would not hold.

constraint of an orthonormalization for $\varphi_i$. The details of the derivation can be found elsewhere (see, e.g., Ref. [59]).

The Kohn-Sham effective potential $V^{\text{eff}}(\mathbf{r})$ consists of the external potential $V^{\text{ext}}(\mathbf{r})$, the classical Coulomb repulsive potential, and the exchange-correlation potential $V^{\text{xc}}(\mathbf{r})$:

$$V^{\text{eff}}(\mathbf{r}) = V^{\text{ext}}(\mathbf{r}) + \int \frac{n(\mathbf{r}')}{|\mathbf{r}-\mathbf{r}'|} d\mathbf{r}' + V^{\text{xc}}(\mathbf{r}). \tag{2.34}$$

The first two terms in Eq. (2.34) are explicitly known. The remaining term, the exchange-correlation potential $V^{\text{xc}}(\mathbf{r})$, is defined as the functional derivative of the exchange-correlation energy $E^{\text{xc}}[n(\mathbf{r})]$:

$$V^{\text{xc}} = \frac{\delta E^{\text{xc}}[n(\mathbf{r})]}{\delta n(\mathbf{r})}. \tag{2.35}$$

Finally, because the electron density of the noninteracting electrons is by definition equal to the real electron density (Eq. (2.28)), the true electron density can be expressed in terms of the Kohn-Sham orbitals $\varphi_i$ as:

$$n(\mathbf{r}) = \sum_{i=1}^{N} |\varphi_i(\mathbf{r})|^2 . \tag{2.36}$$

Equations (2.33)-(2.36) are the celebrated Kohn-Sham equations, that provide the advantage of calculating the dominant part of the true kinetic energy functional $T^{\text{e}}[n]$ *indirectly* (using $N$ auxiliary one-particle wavefunctions), but *exactly*. Solely the exchange-correlation functional $V^{\text{xc}}[n(\mathbf{r})]$ in the Kohn-Sham theory remains unknown. The Kohn-Sham theory is exact (assuming that condition (2.28) holds), and would provide the exact electron density $n(\mathbf{r})$ and total energy of the interacting electrons $E$, if $V^{\text{xc}}[n(\mathbf{r})]$ were known exactly. Unfortunately, the explicit form of the exchange-correlation functional has not been found so far, and it is likely that it does not exist. Consequently, finding a good approximation for the exchange-correlation functional $V^{\text{xc}}[n]$ is still one of the greatest challenges in modern DFT. Some of the basic ideas of constructing reliable approximations of $V^{\text{xc}}[n]$ are outlined in the next section.

It should be noted, that the effective potential $V^{\text{eff}}$ depends on the electron density via (2.34), and at the same time the electron density $n(\mathbf{r})$ depends on the effective potential via (2.29) and (2.36), as sketched below:

$$H^{\text{s}}[n(\mathbf{r})] \rightarrow \{\varphi_i\} \rightarrow n(\mathbf{r}) \rightarrow H^{\text{s}}[n(\mathbf{r})]. \tag{2.37}$$

Therefore, the Kohn-Sham equations have to be solved *selfconsistently*, i.e. requiring that the output electron density $n$ equals the electron density used to construct the Hamilton operator $H^{\text{s}}[n]$. In practice, the selfconsistent solution is found iteratively, starting with some guess for the density, $n_{\text{guess}}(\mathbf{r})$, and improving $n(\mathbf{r})$ in each iteration, until selfconsistency is reached.

#### 2.3.3.4 Exchange-correlation functionals

As pointed out in the previous section, the exchange-correlation functional $V^{\mathrm{xc}}[n(\mathbf{r})]$ is the only unsettled contribution in the Kohn-Sham theory that is not known exactly and therefore requires an approximate treatment. Finding an accurate approximation for $E^{\mathrm{xc}}[n(\mathbf{r})]$ and improving existing exchange-correlation functionals is an ever ongoing work in density functional theory.

The simplest, and most commonly used approximation for the exchange-correlation functional is the local-density approximation (LDA), that was first proposed by Kohn and Sham in 1965 [65]. The LDA is derived from an infinite system of interacting electrons that experience a uniform external potential, the so-called homogeneous electron gas model. The LDA functional assumes that the per-electron exchange-correlation energy at every point in space $\mathbf{r}$ is equal to the per-electron exchange-correlation energy of a homogeneous electron gas with density $n = n(\mathbf{r})$. The LDA functional is consequently local in the sense that the electron xc-energy at any point in space is a function of the electron density at that point only:

$$E^{\mathrm{xc}}_{\mathrm{LDA}}[n(\mathbf{r})] = \int n(\mathbf{r})\epsilon^{\mathrm{xc}}\left(n(\mathbf{r})\right) d\mathbf{r}. \tag{2.38}$$

Here, $\epsilon^{\mathrm{xc}}(n(\mathbf{r}))$ is the exchange-correlation energy per-electron of the homogeneous electron gas with electron density $n = n(\mathbf{r})$. $\epsilon^{\mathrm{xc}}(n(\mathbf{r}))$ can be split into an independent exchange and correlation contributions as:

$$\epsilon^{\mathrm{xc}}(n(\mathbf{r})) = \epsilon^{\mathrm{x}}(n(\mathbf{r})) + \epsilon^{\mathrm{c}}(n(\mathbf{r})), \tag{2.39}$$

where the exact expression for exchange part is derived analytically from the Hartree-Fock theory (see e.g. Sec. 2.3.2):

$$\epsilon^{\mathrm{x}}(n(\mathbf{r})) = -\frac{3}{4}\sqrt[3]{\frac{3n(\mathbf{r})}{\pi}}. \tag{2.40}$$

For the remaining correlation part $\epsilon^{\mathrm{c}}(n(\mathbf{r}))$ in Eq. (2.39) there is no explicit expression, but there are highly accurate quantum Monte Carlo simulations (see Sec. 2.3.2) for the homogeneous electron gas [66], that are merged into $\epsilon^{\mathrm{c}}(n(\mathbf{r}))$ via a parameterized expression [67].

Although the LDA appears to be a crude approximation for realistic systems that yields exact results only for homogeneous electron gas, it is widely used (particularly in solid-state physics) and often provides astonishingly good results [68]. Typically the results obtained with LDA become worse with increasing inhomogeneity of the system, which is particularly the case for atoms and molecules. For bulk materials the LDA shows the tendency to overestimate the strength of the chemical bonds, leading to overestimated binding energies and underestimated equilibrium volumes. Nevertheless, the LDA is the backbone of essentially all currently used exchange-correlation functionals.

The obvious shortcoming of the LDA is that it ignores the nonlocality of the true exchange-

correlation functional, i.e. it does not account for complete electron density $n(\mathbf{r})$, but rather treats the exchange-correlation energy at any point in space independent from the neighborhood. The performance of the LDA can be consistently improved by constructing a xc-functional that depends not only on the *local* electron density, but also includes information regarding the surrounding electron density (ideally of the whole electron density). Such extension of the LDA can be obtained, e.g., by superimposing the local density $n(\mathbf{r})$ with a local gradient of the electron density $|\nabla n(\mathbf{r})|$ at each point $\mathbf{r}$, i.e. including information about the local inhomogeneity of the electron density. Such an approach is known as generalized gradient approximation (GGA), that is formally expressed as:

$$E_{\mathrm{GGA}}^{\mathrm{xc}}[n(\mathbf{r})] = \int n(\mathbf{r})\epsilon^{\mathrm{xc}}\left[n(\mathbf{r}), |\nabla n(\mathbf{r})|\right] d\mathbf{r}. \tag{2.41}$$

The functional is usually divided into an exchange and correlation part, which are expanded separately. Several approximations have been proposed for a parametrization of the GGA functional, as for example those by Becke [69] (exchange part) and Perdew [70] (correlation part), Becke [69] (exchange part) and Lee-Yang-Parr [71] (correlation part), Perdew and Wang [72], or by Perdew, Burke, and Ernzehof [73]. For many solids, GGA was found to correct the LDA-overbinding problem and significantly improve the cohesive energies for solids. GGA also provides a better description of the activation energy barriers in chemical reactions. On the other hand, GGA tends to underestimate the strength of the chemical bonds, yielding to an increased bond lengths and subsequently a decrease in the bulk moduli [74].

The errors introduced by an approximate exchange-correlation functional cannot be generally quantified. For this reasoning some of the calculations in this work have been repeated employing LDA and GGA functionals. A comparison of the different results obtained by using different xc-functionals is then used as an estimate of the uncertainty arising from the approximate treatment of the exchange-correlation functional.

#### 2.3.3.5 Generalization of the DFT for spin systems

Up to now, magnetic interactions were not explicitly included into the electronic Hamiltonian, i.e. it was assumed that the external potential $V^{\mathrm{ext}}$ experienced by the electrons is scalar. For such systems, it has been shown that there is an intimate correlation between the electron density $n$ and scalar potential $V^{\mathrm{ext}}$, that results in the spin-compensated DFT, described in sections 2.3.3.2-2.3.3.4.

In 1972 Barth and Hedin have generalized the concepts of DFT to spin-polarized systems [75], where the usual scalar external potential $v^{\mathrm{ext}}$ is superimposed with a contribution due to an external magnetic field $\mathbf{B}$. The resulting spin-density functional theory is exceedingly important not only for systems in presence of a magnetic field, but also for spin systems with $\mathbf{B}(\mathbf{r}) = 0$. In the later case, the improved spin-dependent exchange-correlation functionals embeds more information regarding electron-electron interactions [59], leading to a more accurate description of the system.

The electronic Hamilton operator in the presence of a magnetic field $\mathbf{B}(\mathbf{r})$ and a scalar external field $v^{\text{ext}}(\mathbf{r})$ for a given nuclei configuration $\{\mathbf{R}_I\}$ can be written as [59][9]:

$$H^{\text{e}}(\{\mathbf{x}_i\},\{\mathbf{R}_I\}) = T^{\text{e}}(\{\mathbf{x}_i\}) + V^{\text{ee}}(\{\mathbf{x}_i\}) + \underbrace{v^{\text{ext}}(\mathbf{r}) + 2\mu_{\text{B}}\sum_i^N \mathbf{B}(\mathbf{r})\cdot\mathbf{s}_i}_{\boldsymbol{v}^{\text{ext}}}. \tag{2.42}$$

Here, $\mu_{\text{B}}$ is the Bohr magneton, and $\mathbf{s}_i$ is the electron spin angular momentum vector for the $i$th electron. The explicit form of the kinetic energy operator $T^{\text{e}}$, electron-electron interaction operator $V^{\text{ee}}$, and electron-nuclei interaction operator $V^{\text{en}}$ is defined in Eq. (2.2). Compared to the spin-averaged formulation of the electronic Hamiltonian (Eq. (2.20)), the external potential in Eq. (2.42) is now a vector field that depends on the spatial orientation of spins.

Barth and Hedin have shown that the Hohenberg-Kohn theory (Sec. 2.3.3.2) can be extended to a spin-polarized system described by Hamiltonian (2.42), employing the electron density $n(\mathbf{r})$ (scalar) and the magnetization density $\mathbf{m}(\mathbf{r})$ (vector) as basic variables. The electron density is defined exactly as in case of the spin-compensated Hamiltonian as:

$$n(\mathbf{r}) = \langle\Psi|\sum_i^N \delta(\mathbf{r}-\mathbf{r}_i)|\Psi\rangle, \tag{2.43}$$

and the magnetization density is defined as:

$$\mathbf{m}(\mathbf{r}) = -2\mu_{\text{B}}\langle\Psi|\sum_i^N \mathbf{s}_i\delta(\mathbf{r}-\mathbf{r}_i)|\Psi\rangle. \tag{2.44}$$

The first spin-generalized Hohenberg-Kohn theorem states that the external potential $\boldsymbol{v}^{\text{ext}}(\mathbf{r})$ is determined by the ground-state electron density $n(\mathbf{r})$ and the ground-state magnetization density $\mathbf{m}(\mathbf{r})$ of the system. In contrast to the nonmagnetic case, where the functional was defined uniquely up to a trivial additive constant, the uniqueness of the external potential is not guaranteed in the spin-polarized case, and is possible only up to the additive functional that depends on the magnetization density (for details see Ref. [76]). This was first shown by Barth and Hedin [75]. Later, Capelle and Vignale [77], as well as Eschrig and Pickett [78], have proven that such an ambiguity is true in general. In 2004, Kohn *et al.* [76] estimated the practical consequence of such ambiguities for the spin-density functional theory, and concluded that they do not affect the validity of the Hohenberg-Kohn theory for nondegenerate ground states that are currently practiced [76]. This implies that the Hamiltonian $H^{\text{e}}$, the corresponding many-particle wavefunction $\Psi$, and the expectation value of some operator $O$ are completely defined by the basic variables $n$ and $\mathbf{m}$. This can be schematically shown as (compare with the corresponding spin-averaged Eq. (2.21)):

[9]This definition of the Hamiltonian provides only a partial description of the magnetic interactions, and neglects the spin interactions with the orbital angular momentum (spin-orbit coupling) and magnetic interactions between electrons (spin-spin interactions). An extension of the DFT for these magnetic interactions is described elsewhere [40, 59].

$$\left\{ \begin{matrix} n_0(\mathbf{r}) \\ \mathbf{m}_0(\mathbf{r}) \end{matrix} \right\} \rightarrow \left\{ \begin{matrix} \boldsymbol{\upsilon}^{\mathrm{ext}}(\mathbf{r}) \\ N \end{matrix} \right\} \rightarrow H^{\mathrm{e}} \rightarrow \Psi \rightarrow \langle \Psi | O | \Psi \rangle. \tag{2.45}$$

In complete analogy to the spin-averaged case, the total energy of the system $E = \langle \Psi | H^{\mathrm{e}} | \Psi \rangle$ can be expressed as:

$$E[n(\mathbf{r}), \mathbf{m}(\mathbf{r})] = F[n(\mathbf{r}), \mathbf{m}(\mathbf{r})] + \int \upsilon^{\mathrm{ext}}(\mathbf{r}) n(\mathbf{r}) d\mathbf{r} - \int \mathbf{B}(\mathbf{r}) \cdot \mathbf{m}(\mathbf{r}) d\mathbf{r}, \tag{2.46}$$

where $F$ is a universal functional that does not depend on the external potentials, and is defined as [59]:

$$F[n(\mathbf{r}), \mathbf{m}(\mathbf{r})] = \min_{\Psi \rightarrow n(\mathbf{r}), \mathbf{m}(\mathbf{r})} \langle \Psi | T^{\mathrm{e}} + V^{\mathrm{ee}} | \Psi \rangle. \tag{2.47}$$

The second spin-generalized Hohenberg-Kohn theorem states that the total energy of the spin-polarized electronic system is always greater or equal to the true ground state total energy $E_0$:

$$E[n_{\mathrm{trial}}(\mathbf{r}), \mathbf{m}_{\mathrm{trial}}(\mathrm{r})] \geq E_0 = E[n_0(\mathbf{r}), \mathbf{m}_0(\mathrm{r})]. \tag{2.48}$$

Equations (2.45)-(2.48) for spin-polarized system are complete analogous of the corresponding spin-averaged equations (2.21)-(2.26), with the distinction that in the spin-polarized case the system is defined by four independent variables (scalar electron density and vector magnetization density) at each point in space, while in the spin-averaged case by only a single scalar variable (electron density).

In alternative formulation, the electron and magnetization densities can be composed into the so-called $2 \times 2$ spin-density matrix $\underline{n}(\mathbf{r})$ as:

$$\underline{n}(\mathbf{r}) = \frac{1}{2} \left( n(\mathbf{r}) \underline{\mathrm{I}} + \underline{\boldsymbol{\sigma}} \cdot \mathbf{m}(\mathbf{r}) \right) = \frac{1}{2} \begin{pmatrix} n(\mathbf{r}) + m_z(\mathbf{r}) & m_x(\mathbf{r}) - \mathrm{i}\, m_y(\mathbf{r}) \\ m_x(\mathbf{r}) + \mathrm{i}\, m_y(\mathbf{r}) & n(\mathbf{r}) - m_z(\mathbf{r}) \end{pmatrix}. \tag{2.49}$$

Here, $\boldsymbol{\sigma}$ is the vector of the $2 \times 2$ Pauli matrices, $\underline{\mathrm{I}}$ is the $2 \times 2$ unity matrix, and i is the imaginary unit. The density matrix must fulfil the condition that the total number of electrons is conserved:

$$\sum_{\alpha} \int n_{\alpha\alpha}(\mathbf{r}) d\mathbf{r} = N. \tag{2.50}$$

Applying the original arguments of Kohn and Sham, Barth and Hedin [75] derived the spin-generalized Kohn-Sham equations using the spin-density matrix $\underline{n}(\mathbf{r})$ as the basic system variable:

$$\left[ \left( -\frac{1}{2} \nabla^2 + \sum_{\alpha} \frac{n_{\alpha\alpha}(\mathbf{r}')}{|\mathbf{r} - \mathbf{r}'|} d\mathbf{r}' \right) \underline{\mathrm{I}} + \underline{V}^{\mathrm{ext}}(\mathbf{r}) + \frac{\delta E^{\mathrm{xc}}}{\delta \underline{n}(\mathbf{r})} \right] \begin{pmatrix} \varphi_i^{\uparrow}(\mathbf{r}) \\ \varphi_i^{\downarrow}(\mathbf{r}) \end{pmatrix} = \epsilon_i \begin{pmatrix} \varphi_i^{\uparrow}(\mathbf{r}) \\ \varphi_i^{\downarrow}(\mathbf{r}) \end{pmatrix}. \tag{2.51}$$

Here, $\underline{V}^{\mathrm{ext}}(\mathbf{r})$ is the external potential $2 \times 2$ matrix corresponding to the spin-density $\underline{n}(\mathbf{r})$, and

the exchange-correlation potential is now also a $2 \times 2$ matrix[10]. Arrows $\uparrow, \downarrow$ indicate the spin-up and spin-down electrons, respectively. Finally, the density matrix can be written in terms of the Kohn-Sham wavefunctions as:

$$n_{\alpha\beta}(\mathbf{r}) = \sum_{i}^{\text{occ}} \varphi_i^{*\alpha}(\mathbf{r})\varphi_i^{\beta}(\mathbf{r}), \tag{2.52}$$

where $\alpha, \beta = \uparrow, \downarrow$, and the summation is performed over occupied single-electron eigenstates.

Within the spin-generalized formalism given by Eqs. (2.42)-(2.52), the non-collinear magnetic structures can be described in the framework of density functional theory [40, 63]. In many applications, for instance in ferromagnetic, ferrimagnetic and antiferromagnetic solids (that is of interest in this study), the quantization axis is not spatially dependent, and a common magnetization axis exists for all atoms. The $z$-axis can then be chosen globally along the direction of the magnetic field, that has the simplifying consequence that the energy and other physical observables are functionals of the electron density and of the magnitude of the magnetization density $m(\mathbf{r}) = |\mathbf{m}(\mathbf{r})|$ rather than of the vector $\mathbf{m}(\mathbf{r})$ [40]. For collinear spin systems the potential matrices in Eq. (2.51) as well as the spin-density matrix reduce to a diagonal form and can be decoupled into a system of Kohn-Sham equations for spin-up and spin-down electrons:

$$\begin{cases} \left[-\frac{1}{2}\nabla^2 + V^{\text{H}}(\mathbf{r}) + V^{\text{ext}}(\mathbf{r}) + B_z(\mathbf{r}) + V_{\uparrow}^{\text{xc}}(\mathbf{r})\right] \varphi_i^{\uparrow}(\mathbf{r}) = \epsilon_i^{\uparrow}\varphi_i^{\uparrow}(\mathbf{r}), \\ \left[-\frac{1}{2}\nabla^2 + V^{\text{H}}(\mathbf{r}) + V^{\text{ext}}(\mathbf{r}) - B_z(\mathbf{r}) + V_{\downarrow}^{\text{xc}}(\mathbf{r})\right] \varphi_i^{\downarrow}(\mathbf{r}) = \epsilon_i^{\downarrow}\varphi_i^{\downarrow}(\mathbf{r}). \end{cases} \tag{2.53}$$

Equations (2.53) are coupled via the Hartree potential $V^{\text{H}}(\mathbf{r}) = \int \frac{n(\mathbf{r})}{|\mathbf{r}-\mathbf{r}'|} d\mathbf{r}'$ that depends on the electron density $n(\mathbf{r})$, and via the exchange-correlation functional that can have different values for two spin directions even without an external magnetic fields:

$$V_{\uparrow,\downarrow}^{\text{xc}}(\mathbf{r}) = \frac{\delta E^{\text{xc}}[n^{\uparrow}(\mathbf{r}), n^{\downarrow}(\mathbf{r})]}{\delta n^{\uparrow,\downarrow}(\mathbf{r})}. \tag{2.54}$$

$n^{\uparrow,\downarrow}(\mathbf{r})$ in equations ((2.62)-(2.63)) are the spin-up and spin-down electron densities, that can be written as:

$$n^{\uparrow,\downarrow}(\mathbf{r}) = \sum_{i}^{\text{occ}} |\varphi_i^{\uparrow,\downarrow}(\text{r})|^2, \quad n(\mathbf{r}) = n^{\uparrow}(\mathbf{r}) + n^{\downarrow}(\mathbf{r}), \quad m(\mathbf{r}) = n^{\uparrow}(\mathbf{r}) - n^{\downarrow}(\mathbf{r}). \tag{2.55}$$

[10]Similarly to the definition of the spin-density matrix (2.49), the potential matrices can be written in terms of a scalar potential and magnetic field:

$$\underline{V}^{\text{ext}}(\mathbf{r}) = V^{\text{ext}}(\mathbf{r})\underline{\text{I}} + \mu_{\text{B}}\, \underline{\boldsymbol{\sigma}} \cdot \mathbf{B}(\mathbf{r}),$$

and

$$\underline{V}^{\text{xc}}(\mathbf{r}) = V^{\text{xc}}(\mathbf{r})\underline{\text{I}} + \mu_{\text{B}}\, \underline{\boldsymbol{\sigma}} \cdot \mathbf{B}^{\text{xc}}(\mathbf{r}).$$

From these equations it follows, that even in the absence of an external magnetic field $\mathbf{B}$ there might exist an exchange-correlation field $\mathbf{B}^{\text{xc}}$ that yields nonzero magnetization density.

Similar to the spin-compensated Kohn-Sham theory, the spin-polarized Kohn-Sham equations (2.49)-(2.52) provide an exact solution of the many-electron Hamiltonian, if the explicit form of the spin-dependent exchange-correlation functional $\underline{V}^{\mathrm{xc}}(\mathbf{r})$ is known. To treat the unknown $\underline{V}^{\mathrm{xc}}(\mathbf{r})$, approximative spin exchange-correlation functionals have been developed. Similar to the nonspin case, approximate xc-functionals include the local spin-density approximation (LSDA) [67, 75, 79], which depend locally on the spin-up and spin-down densities, and spin-generalized GGA functionals [73, 80, 81] for spin polarized systems. A detailed discussion of these functionals is presented elsewhere [40, 59, 63].

## 2.4 The plane wave DFT

### 2.4.1 DFT for periodic crystals

The density functional theory allows to map the problem of interacting electrons onto a physically completely equivalent system comprised of noninteracting electrons moving in an effective Kohn-Sham potential. Applied to realistic solids, the DFT still faces the formidable task of handling about $10^{23}$ nuclei and $10^{23} - 10^{25}$ electrons per cubic centimeter. The Kohn-Sham wavefunction must be calculated for each electron in the system, and, since each electronic wavefunction extends over the entire solid, the basis set required to expand each wavefunction is immense, that makes a practical solution of the Kohn-Sham problem impossible [82]. For crystalline solids, however, the dimensionality of the many-electron system can be drastically reduced when employing the translational periodicity that is intrinsic for this class of matter.

In a crystalline solid the electrons move in a periodic external potential $V^{\mathrm{ext}}(\mathbf{r})$, that is created by the periodically arranged array of nuclei that reflects the symmetry of the crystal[11]:

$$V^{\mathrm{ext}}(\mathbf{r}+\mathbf{R}) = V^{\mathrm{ext}}(\mathbf{r}). \tag{2.56}$$

Here, $\mathbf{R} = n_1\mathbf{a}_1 + n_2\mathbf{a}_2 + n_3\mathbf{a}_3$ is the translational lattice vector, $\mathbf{a}_i$ are the unit cell vectors of the crystal (primitive vectors), and $n_i$ are integers. Eq. (2.56) implies that also the corresponding Kohn-Sham Hamiltonian obeys translational invariance. According to Bloch's theorem, the electronic wavefunctions resulting from a Schrödinger equation with a periodic Hamiltonian are described by a product of a wavelike part and a function, that exhibits the periodicity of the crystal:

$$\varphi_{i\mathbf{k}}(\mathbf{r}) = \exp[\mathrm{i}\mathbf{k}\cdot\mathbf{r}]u_{i\mathbf{k}}(\mathbf{r}). \tag{2.57}$$

Here, $i$ is the band index, $\mathbf{k}$ is the vector[12] that lies within the unit cell of the reciprocal lattice $\mathbf{G}$

[11] A detailed discussion on types of crystal symmetries as well as on the real-space and corresponding reciprocal-space lattices can be found e.g. in Ref. [83].

[12] The $\mathbf{k}$-point in Eq. (2.57), also known as the quasimomentum, can be regarded as a quantum number that appears due to the translational periodicity of the crystal. The number and reciprocal-space coordinates of the allowed $\mathbf{k}$-points in Eq. (2.57) depend on the macroscopic size of the solid. The density of the $\mathbf{k}$-points in the first Brillouin

(so-called first Brillouin zone):

$$\mathbf{G} = m_1\mathbf{b}_1 + m_2\mathbf{b}_2 + m_3\mathbf{b}_3, \tag{2.58}$$

where $m_i$ are integers. The reciprocal lattice is associated with the real-space lattice $\mathbf{R}$ as:

$$\mathbf{a}_i \cdot \mathbf{b}_j = 2\pi\delta_{ij}. \tag{2.59}$$

$u_{i\mathbf{k}}(\mathbf{r})$ in Eq. (2.57) is the cell-periodic part:

$$u_{i\mathbf{k}}(\mathbf{r} + \mathbf{R}) = u_{i\mathbf{k}}(\mathbf{r}). \tag{2.60}$$

Since the electronic Hamiltonian $H^{\mathrm{s}}(\mathbf{r})$, the corresponding wavefunctions $\varphi_i(\mathbf{r})$, and consequently all physical observables obey the periodicity of the crystal, it is sufficient to solve the single-particle Schrödinger equation only within the real-space unit cell that is spanned by the primitive vectors $\mathbf{a}_i$. This drastically reduces the system size that has to be treated explicitly from the whole crystal to it's simplest "construction brick", the unit cell. For an infinite periodic crystal, Bloch's theorem exactly reformulates the problem of an infinite number of electrons occupying a finite number of electronic states in an infinite crystal to the equivalent task of calculating a finite number of electrons located in a finite unit cell, but at an infinite number of **k**-points. Although formally both tasks are equivalent, the numerical treatment of the infinite number of **k**-points is by far more advantageous. Indeed, since the electron density is calculated as a sum over all occupied one-particle electron states, the electron density is written as:

$$n(\mathbf{r}) = \sum_i^{\mathrm{occ}} |\varphi_i(\mathbf{r})|^2 = \frac{1}{\Omega_{\mathrm{BZ}}} \sum_i^{\mathrm{occ}} \int_{\mathrm{BZ}} |\varphi_{i\mathbf{k}}(\mathbf{r})|^2 d\mathbf{k}. \tag{2.61}$$

Here, $\Omega_{\mathrm{BZ}}$ is the volume of the first Brillouin zone that ensures a proper normalization of the single-particle wavefunctions $\varphi_{i\mathbf{k}}(\mathbf{r})$. Because the electronic wavefunctions at vicinal **k**-points are almost identical (i.e. wavefunctions are smooth functions in the reciprocal space [82]), it is possible to represent the electronic wavefunctions that originate from some volume in the **k**-space by the single wavefunction from this volume. The integral (2.61) can be safely approximated therefore by a weighted sum over special **k**-points:

$$n(\mathbf{r}) = \sum_i^{\mathrm{occ}} \sum_j^{N_{\mathbf{k}}} w_j |\varphi_{i\mathbf{k}_j}(\mathbf{r})|^2, \tag{2.62}$$

where $N_{\mathbf{k}}$ is the number of special **k**-points, $w_j$ is the weight assigned to each special **k**-point $\mathbf{k}_j$. Due to the normalization constraint of the wavefunctions the following condition must be fulfilled:

zone is proportional to the volume of the crystal; for infinite crystals all **k**-points from the first BZ are allowed [83].

$$\sum_{j}^{N_{\mathbf{k}}} w_j = 1. \tag{2.63}$$

Obviously, choosing a dense enough mesh of the special **k**-points the integral in Eq. (2.61) can be accurately approximated. The error introduced by using a discrete **k**-point set can be systematically decreased by increasing the density of the mesh, and should be one of the objectives of convergence tests. It should be noted, however, that the total energy of the system is not variational with respect to the density of the special **k**-points, implying that the total energy does not necessarily decrease by increasing the number of **k**-points.

Several methods of calculating the charge density on a discrete **k**-point mesh have been developed [84, 85]. In this work we use the scheme proposed by Monkhorst and Pack [85]. The application of this scheme ensures a homogeneous distribution of the sampled **k**-points over the whole first Brillouin zone with rows and columns of **k**-points running parallel to the reciprocal lattice vectors $\mathbf{b}_i$. According to the idea of Monkhorst and Pack, the first Brillouin zone is tiled by small polyhedra having the same shape as the first Brillouin zone itself, where the number of tiles along the $\mathbf{b}_1$, $\mathbf{b}_2$, and $\mathbf{b}_3$ are specified by so-called folding parameters. Each tile is then sampled with a set of **k**-points (called *special* **k**-points), which relative coordinates within each tile are fixed. Additional information regarding the **k**-point sampling used in this work can be found in the manuals of the used codes [37, 38, 86, 87].

It should be also noted, that the point group symmetries of the crystal under investigation might reduce the number of the symmetry-inequivalent **k**-points. The remaining **k**-points occupy only a part of the first Brillouin zone, the so-called irreducible first Brillouin zone. The set of the reduced **k**-points that remains after application of the symmetry operators is frequently referred to as irreducible **k**-point set.

### 2.4.2 Describing nonperiodic systems with periodic boundary conditions

In contrast to bulk crystals that are periodic in three dimensions, there is a vast variety of physical objects and structures that do not obey 3D-translational periodicity, but are of high importance for computational material science. Such objects include, e.g., surfaces, points defects, dislocations, quantum dots, atoms, and molecules. In this study we are concerned with crystal surfaces, that are periodic in the surface plane only; the periodicity of the crystal along the surface normal vanishes due to the presence of the nonsymmetric bulk-surface-vacuum interface, as shown on Fig. 2.1(a).

In order to fully exploit the advantages provided by Bloch's theorem, a system with three-dimensional periodicity is required. Thus the structure of interest has to be cast into a three-dimensional periodicity, that is accomplished by a so-called supercell approach [46].

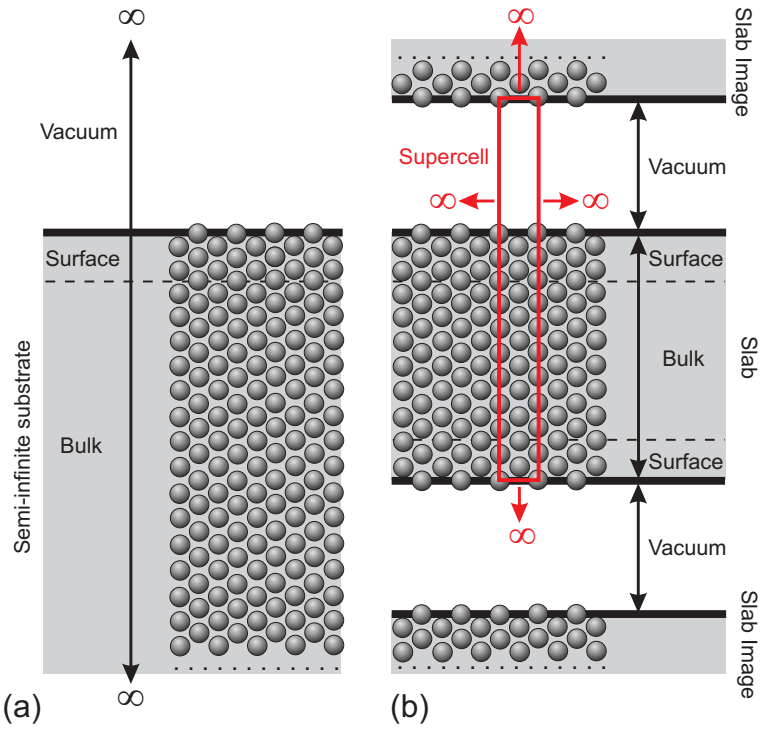


Figure 2.1: Comparison of (a) an ideal two-dimensional crystal surface with (b) the corresponding slab model. While the ideal surface is formed by a semi-infinite substrate and by a semi-infinite vacuum, the surface within the supercell approach rests on a finite-sized slab and vacuum. The supercell is periodic in all three spatial dimensions.

Within the supercell approach[13], both the semi-infinite substrate supporting the surface, and the semi-infinite vacuum above the surface, are truncated at a certain distance by planes parallel to the surface of interest (Fig. 2.1(b)). The resulting slab-vacuum geometry fits into a supercell that is periodic in all three spatial dimensions. Hence, the surface is represented by an infinite array of slabs, that are periodic in the surface plane, and separated by a vacuum region in the direction perpendicular to the surface.

The above described truncation procedure results in the presence of an artificial surface below and above (at the bottom of the slab image) the surface of interest, as shown on Fig. 2.1(b). This may lead to spurious interactions between these surfaces through the vacuum and/or through the slab regions. Therefore, a numerical convergence with respect to the vacuum and slab thickness of all relevant surface properties has to be ensured.

### 2.4.3 Planewave representation of the Kohn-Sham wavefunctions

The application of periodic boundary conditions reduces the problem of solving the Kohn-Sham equations (2.31)-(2.36) for an infinite number of electrons to the equivalent problem of solving the Kohn-Sham equations for a finite number of electrons at an infinite number of **k**-points. This leads to the expression of Bloch's type (2.57) for the single-electron wavefunction $\varphi_{i\mathbf{k}}(\mathbf{r})$, where the unknown lattice-periodic part $u_{i\mathbf{k}}(\mathbf{r})$ has to be determined by solving the Kohn-Sham equations.

[13]Here we focus on the description of the crystalline surfaces; the generalization to other low-dimensional structures is straightforward.

In principle, it is possible to find a purely numerical solution for $u_{i\mathbf{k}}(\mathbf{r})$. In practice, however, most applications of DFT use an expansion of $u_{i\mathbf{k}}(\mathbf{r})$ into basis functions[14] $\phi_i$:

$$u_{i\mathbf{k}} = \sum_{j=1}^{N_{\text{set}}} c_j^{i\mathbf{k}} \phi_j. \tag{2.64}$$

Solution of the Kohn-Sham equation is then reduced to the unknown coefficients $c_j^{i\mathbf{k}}$. In practice, the expansion in Eq. (2.64) has to be truncated as early as possible to achieve a better computational efficiency. At the same time, the Hilbert space spanned by the basis set $\phi_i$ should ideally be equal to the Hilbert space of the real solution. Finding better basis sets that provide a reasonable compromise between these two requirements is a subject of ongoing research in DFT.

Bloch's theorem suggests the natural expansion of the cell-periodic part in Eqs. (2.60),(2.64) to be a Fourier series with planewaves that obey the periodicity of the crystal. This implies that the wavevectors of these planewaves are reciprocal lattice vectors of the system:

$$u_{i\mathbf{k}}(\mathbf{r}) = \sum_{\mathbf{G}} c_{i,\mathbf{k}+\mathbf{G}} \exp[\mathrm{i}\mathbf{G}\cdot\mathbf{r}]. \tag{2.65}$$

The major advantage of this basis set is the fact that it is *in principle* complete, i.e. it allows to span the whole Hilbert space of the system. The plane-wave basis set also allows straightforward calculations of the forces that are acting on the nuclei by virtue of the Hellmann-Feyman theorem (for details see e.g. Refs. [47, 82, 88]).

Combining equations (2.57) and (2.65) one can finally derive the expression for the single-particle Kohn-Sham wavefunction in the periodic potential as:

$$\varphi_{i\mathbf{k}}(\mathbf{r}) = \sum_{\mathbf{G}} c_{i,\mathbf{k}+\mathbf{G}} \exp[\mathrm{i}(\mathbf{k}+\mathbf{G})\cdot\mathbf{r}]. \tag{2.66}$$

Expression (2.66) is the expansion of a Kohn-Sham orbital in the basis set of plane waves. Using such an expression for the single-particle wavefunction, the Kohn-Sham equation (2.33) is written as:

$$\sum_{\mathbf{G}'} \left[ -\frac{1}{2}|\mathbf{k}+\mathbf{G}|^2 \delta_{\mathbf{G}\mathbf{G}'} + V^{\text{eff}}(\mathbf{G},\mathbf{G}') \right] c_{i,\mathbf{k}+\mathbf{G}'} = \epsilon_{i\mathbf{k}}\, c_{i,\mathbf{k}+\mathbf{G}}. \tag{2.67}$$

In this form, the kinetic energy operator is diagonal in $\mathbf{G}$-space, and the external potential is described in terms of its Fourier transforms. For each $\mathbf{k}$-point the unknown expansion coefficients $c_{i,\mathbf{k}+\mathbf{G}'}$ in Eq. (2.67) are obtained by diagonalizing Hamiltonian matrix $H^{\text{s}}_{\mathbf{k}+\mathbf{G},\mathbf{k}+\mathbf{G}'}$ given by the bracket in Eq. (2.67).

In principle, an infinite plane-wave basis set is required to expand the electronic wavefunctions

[14] In principle, one can also relax the requirement of periodic boundary conditions and apply Eq. (2.64) to expand the Kohn-Sham orbital $\varphi_i$.

$\varphi_{i\mathbf{k}}(\mathbf{r})$. This results in an infinite size of the Hamiltonian matrix $H^{\mathrm{s}}_{\mathbf{k}+\mathbf{G},\mathbf{k}+\mathbf{G}'}$. The coefficients $c_{i,\mathbf{k}+\mathbf{G}}$ of the planewaves with small kinetic energy $T^{\mathrm{s}} = 1/2|\mathbf{k}+\mathbf{G}|^2$ are typically more important than those with large kinetic energy [82]. This allows to truncate the planewave basis set, and to include only those planewaves with a kinetic energy less than some particular value, called the cutoff energy:

$$\frac{1}{2}|\mathbf{k}+\mathbf{G}|^2 \leq E_{\mathrm{cutoff}}. \tag{2.68}$$

Obviously, the truncation (2.68) leads to an error in the computed total energy. Similar to the **k**-point sampling, the magnitude of this error is well-controllable, and is subject to convergence tests. An increase of $E_{\mathrm{cutoff}}$ leads to a consistently improved description of the Kohn-Sham wavefunctions, that smoothly approaches the real ground state wavefunctions. For this reason the quality of the planewave basis set obeys the variational principle (2.26), i.e. an increase of the cutoff energy $E_{\mathrm{cutoff}}$ necessarily leads to a decrease of the total energy.

The actual choice of the cutoff energy, and consequently the computational complexity of the problem, is system dependent. For most of the systems, an enormous basis set size is required to provide an acceptable resolution of the strong wavefunction oscillations in the vicinity of the nuclei cores [89]. This is severe problem for most systems of interest, but it can be overcome by the use of a pseudopotential approach, as discussed in the next section.

## 2.5 Electron-nuclei interactions: pseudopotentials approach

The external potential $V^{\mathrm{ext}}(\mathbf{r})$ experienced by noninteracting Kohn-Sham particles (see equation (2.34)) is essentially the superposition of the nuclear Coulomb potentials:

$$V^{\mathrm{ext}}(\mathbf{r}) = -\sum_{I=1}^{L} \frac{Z_I}{|\mathbf{R}_I - \mathbf{r}|}. \tag{2.69}$$

The single-particle wavefunctions in such a singular external potential are either strongly localized in the vicinity of the nuclei, and/or rapidly oscillate in this region. This effect is induced by the orthogonality of the wavefunctions $\varphi_i$ to the energetically lower Kohn-Sham orbitals. In the planewave representation, the accurate description of such wavefunctions requires a prohibitively large number of planewaves, what limits the practical application of the planewave expansion to small systems only. For most systems of interest, however, the planewave Hamiltonian $H^{\mathrm{s}}_{\mathbf{k}+\mathbf{G},\mathbf{k}+\mathbf{G}'}$ becomes intractably large, and an explicit treatment of all electrons in the system is computationally not feasible.

For a planewave approach to be of practical use, the true nuclei-electron Coulomb potential $V^{\mathrm{ext}}(\mathbf{r})$ has to be replaced with a so-called pseudopotential $V^{\mathrm{ps}}(\mathbf{r})$. It is constructed such that it significantly reduces the complexity of the problem, but nevertheless captures all essential proper-

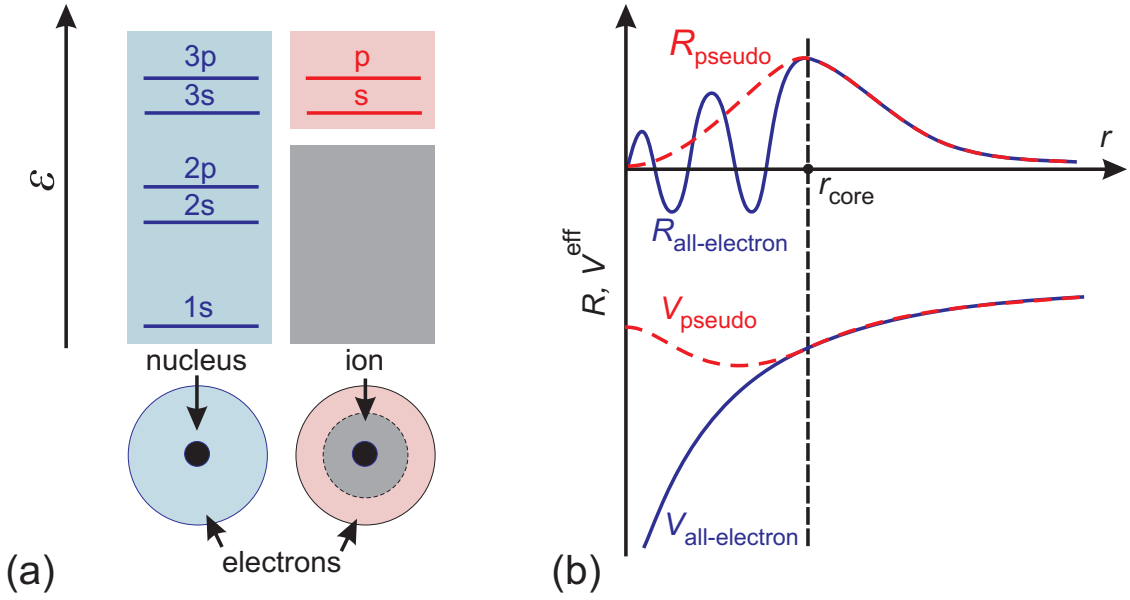


Figure 2.2: (a) Comparison of a schematic all-electron atom and corresponding energy spectrum with that of a pseudoatom. (b) Schematic comparison between all-electron (solid blue lines) and its corresponding pseudopotential (dashed red lines) wavefunctions and Coulomb potentials for an isolated atom. Only radial dependencies are shown.

ties of the true external potential $V^{\text{ext}}(\mathbf{r})$. The basic idea of pseudopotential theory is to distinguish the valence and core electrons, and to treat them on a different level of accuracy. The physical motivation of such a distinction is the fact, that most physical and chemical properties of crystals and molecules depend to a very good approximation only on the distribution of the valence electrons[15]. The core electrons are strongly localized around the nucleus and their wavefunctions overlap only very little with the core electron wavefunctions stemming from neighboring nuclei [40]. The core electrons, therefore, do not take part in the chemical bonding (at least explicitly), and the distribution of the core wavefunctions basically does not change when the atoms are placed in a different chemical environment. It is thus justified to assume that the core electrons are inert and always remain in the same state as they are in the isolated atom. This assumption is the so-called frozen core approximation [90], that provides a number of advantages.

First, the frozen-core approximation allows to merge the core electrons with the nucleus, and recast the Kohn-Sham equations in terms of such ions (nucleus plus core electrons). This implies that now less electrons have to be treated explicitly, and consequently less eigenstates of the Kohn-Sham equation have to be calculated, as shown on Fig. 2.2(a). Second, the total energy scale is largely reduced when the core electrons are removed from the calculations, which makes the

[15]Formally, the valence electrons are those that occupy the outermost nonclosed shell of an atom. Other electrons located on the closed inner shells are referred to as core electrons. In practice, however, the distinction between the valence and core electrons is more complicated, and is based upon a comparison of the electron energies, the distribution of the electron densities, and the impact of the electrons on the chemical bonding [74].

calculation of energy differences between atomic configurations numerically much more stable [40].

Within the frozen-core approximation, the valence electrons experience the rigid ionic core potential, but the valence wavefunctions still have to maintain their nodal structure in order to be orthogonal to the core states. Consequently, the planewave representation of such wavefunctions still requires a huge size of the basis set. The valence wavefunctions are, however, strongly oscillating only in the vicinity of the nucleus, and are rather smooth outside of the ionic core region, where the chemical bonding mostly occurs. It is, therefore, practical to replace the ionic core potential by a pseudopotential which will lead to nodeless valence wavefunctions inside of the core region and provide an exact description of the valence wavefunctions outside this core. The resulting pseudo wavefunction is much softer that the original one, and thus can be accurately represented by a fairly small set of planewaves (Fig. 2.2(b)).

In practice, pseudopotentials are constructed from *ab initio* all-electron calculations for isolated atoms, for which the Kohn-Sham effective potential $V^{\text{eff}}$ is written as:

$$V^{\text{eff}}[n;\mathbf{r}] = V^{\text{ext}}(\mathbf{r}) + V^{\text{H}}[n;\mathbf{r}] + V^{\text{xc}}[n;\mathbf{r}], \tag{2.70}$$

where the external potential is written as $V^{\text{ext}}(\mathbf{r}) = -Z/|\mathbf{r}|$. Due to the spherical symmetry of the external potential, it is meaningful to recast the wavefunctions in spherical coordinates as:

$$\varphi_i(\mathbf{r}) \equiv \varphi_{nlm}(\mathbf{r}) = r^{-1} R_{nl}(r) \cdot Y_{lm}(\Omega_{\mathbf{r}}). \tag{2.71}$$

Here, $\mathbf{r} = (r, \Omega_{\mathbf{r}})$, where $\Omega_{\mathbf{r}}$ is the body angle in direction $\mathbf{r}$. In turn, $\Omega_{\mathbf{r}} = (\theta_{\mathbf{r}}, \phi_{\mathbf{r}})$, with $\theta_{\mathbf{r}}$ and $\phi_{\mathbf{r}}$ being the polar and azimuthal angles. Employing ansatz (2.71), the Schrödinger equation splits into two independent parts, for the radial functions $R_{nl}(r)$ and azimuthal functions $Y_{lm}$, respectively. The $Y_{lm}$ are obtained by solving the angular equation:

$$-\left[\frac{1}{\sin\theta_{\mathbf{r}}}\frac{\partial}{\partial\theta_{\mathbf{r}}}\left(\sin\theta_{\mathbf{r}}\frac{\partial Y_{lm}(\Omega_{\mathbf{r}})}{\partial\theta_{\mathbf{r}}}\right) + \frac{1}{\sin^2\theta_{\mathbf{r}}}\frac{\partial^2 Y_{lm}(\Omega_{\mathbf{r}})}{\partial\phi_{\mathbf{r}}^2}\right] = l(l+1)Y_{lm}(\Omega_{\mathbf{r}}), \tag{2.72}$$

and the radial equation for the radial part[16]:

$$\left[-\frac{1}{2}\frac{d^2}{dr^2} + \frac{l(l+1)}{2r^2} + V^{\text{eff}}[n;r]\right] R_{nl}(r) = \epsilon_{nl} R_{nl}(r). \tag{2.73}$$

The solution of the Kohn-Sham equation is thus reduces to a one-dimensional radial equation (2.73), that can be integrated numerically. Eq. (2.73) is solved for a given atomic configuration, the so-called reference configuration, specified by occupation numbers for each electronic shell (typically the ground state configuration). Having obtained the all-electron potential and valence state wavefunctions, the pseudopotential is derived from these data. The aimed pseudopotential

[16]Here, for the sake of simplicity, we show the non-relativistic Schrödinger equation. In practice, however, particular for heavy species, one solves a scalar-relativistic Schrödinger equation, that includes the kinematic relativistic terms (the mass-velocity and Darwin terms). The spin-orbit coupling terms are commonly averaged over [43].

should replace the effective all-electron potential within a given sphere[17] with radius $r_{\text{core}}^{l}$ by a much weaker potential that provides a nodeless ground state wavefunction $R_l^{\text{ps}}$ with the same energy eigenvalue as the original all-electron state $R_{nl}(r)$:

$$\epsilon_l^{\text{ps}} \equiv \epsilon_{nl}. \tag{2.74}$$

The principal quantum number $n$ for pseudopotential eigenvalues is omitted since the pseudo wavefunctions are restricted to valence orbitals only. The second constraint applied on pseudopotential is the exact match of the all-electron and pseudo wavefunctions outside the sphere (see Fig. 2.2(b)). This implies that:

$$R_l^{\text{ps}}(r) = R_{nl}(r) \quad \text{for} \quad r > r_{\text{core}}^{l}, \tag{2.75}$$

and

$$\frac{d}{dr}R_l^{\text{ps}}(r) = \frac{d}{dr}R_{nl}(r) \quad \text{for} \quad r > r_{\text{core}}^{l}. \tag{2.76}$$

The wavefunction $R_{nl}(r)$ is substituted by an arbitrary smooth nodeless function within the core-sphere. Conditions (2.74)-(2.76) ensure that the effective potential experienced by the pseudo valence electrons is *exactly* the same as the one experienced by the corresponding valence electrons in an all-electron calculations. The intermediate, so-called screened pseudopotential, is obtained by a simple inversion of the radial non-relativistic Schrödinger equation for a pseudo atom:

$$\left[-\frac{1}{2}\frac{d^2}{dr^2} + \frac{l(l+1)}{2r^2} + V_l^{(\text{ps,scr})}[n;r]\right] R_l^{\text{ps}}(r) = \epsilon_l^{\text{ps}} R_l^{\text{ps}}(r). \tag{2.77}$$

It becomes a valid mathematical operation due to the nodeless structure of the pseudo wavefunction $R_l^{\text{ps}}(r)$. The pseudopotential components that correspond to the inversion of the Schrödinger equation (2.77) are written as:

$$V_l^{(\text{ps,scr})}(r) = \epsilon_l^{\text{ps}} - \frac{l(l+1)}{2r^2} + \frac{1}{2V_l^{\text{ps}}(r)} \cdot \frac{d^2}{dr^2}V_l^{\text{ps}}(r). \tag{2.78}$$

By construction, the screened pseudopotential becomes identical to the all-electron potential for $r > r_{\text{core}}^{l}$. Since the effective all-electron potential is a functional of the total electron density $n = n_{\text{core}} + n_{\text{val}}$, the screened pseudopotential also depends on the interactions between valence electrons, between core electrons, and between valence and core electrons. These additional terms due to the valence electrons screen the actual ionic potential, that by virtue of the frozen-core approximation should be independent on the environment where it is placed to, i.e. on the state of the valence electrons.

[17] Equation (2.73) implies that the effective potential in the radial equation depends on the angular quantum number $l$. Consequently, each atomic $l$-shell has to be treated independently.

The ionic pseudopotential is determined by subtracting from the screened pseudopotential the electrostatic and exchange-correlation screening contributions due to the valence electrons as:

$$V_l^{\rm ps}(r) = V_l^{\rm (ps,scr)}(r) - V^{\rm H}[n^{\rm ps};r] - V^{\rm xc}[n^{\rm ps};r]. \tag{2.79}$$

Here, $n^{\rm ps}(r)$ is the valence electron density evaluated from the atomic pseudo wavefunctions, taking the same occupancies as for the all-electron valence states. The terms $V^{\rm H}[n^{\rm ps};r]$ and $V^{\rm xc}[n^{\rm ps};r]$ in Eq. (2.79) refer to the electrostatic and the exchange-correlation interactions between valence electrons only. Eq. (2.79) is derived recalling that the Hartree potential is a linear functional in the density ($V^{\rm H}[n^{\rm core}(r)+n^{\rm val}(r)] = V^{\rm H}[n^{\rm core}(r)]+V^{\rm H}[n^{\rm val}(r)]$), and assuming that the same holds for exchange-correlation interactions. Although the true $V^{\rm xc}$ is a nonlinear functional of the total electron density, such a "linearization" of the core-valence contributions is a usual and adequate approximation for calculations within both LDA and GGA [65, 91, 92]. In some cases, however, like for alkali metal atoms or within the spin-density functional theory, an explicit account of the core-valence nonlinearity of $V^{\rm xc}$ is required. The nonlinearity of the exchange-correlation functional is restored by including the so-called nonlinear core correction. When this correction is included, the ionic pseudopotential $V_l^{\rm ps}(r)$ is redefined as:

$$V_l^{\rm ps}(r) = V_l^{\rm (ps,scr)}(r) - V^{\rm H}[n^{\rm ps};r] - V^{\rm xc}[n^{\rm ps}+n^{\rm core};r]. \tag{2.80}$$

Here, $n^{\rm core}$ is the core electron density. In practice, it is sufficient to exchange the true core density $n^{\rm core}$ with the so-called partial core density $\widetilde{n}^{\rm core}$ that reproduces the full core density outside a chosen cutoff radius $r^{\rm nlc}$, but is a smoother function inside. Such a substitution enables a more efficient treatment of the core density with planewave basis set.

Since the ionic pseudopotential depends on the angular momentum $l$ (see Eqs. (2.79)-(2.80)), the full pseudopotential for an atom has to be a nonlocal operator. One can express this as follows:

$$\hat{V}^{\rm ps} = \sum_{l=0}^{l_{\rm max}} V_l^{\rm ps}(r)\hat{P}_l, \tag{2.81}$$

where $l_{\rm max}$ is the highest value of the angular momentum, for which a pseudopotential has been generated. $\hat{P}_l$ is a projection operator which picks out the $l$-th angular momentum component from the subsequent wavefunction[18]. By this construction, it is guaranteed that when the full potential operator $\hat{V}^{\rm ps}$ is applied to a general wavefunction, each angular momentum component of the wavefunction experiences only the corresponding part $V_l^{\rm ps}(r)$ of the potential [40]. In order to reduce the computational effort, expression (2.82) can be reformulated as:

[18]Specific form of the projection operator $\hat{P}_l$, as well as details on a computationally efficient implementation of the projection operator are given elsewhere [43, 74, 88].

$$\hat{V}^{\mathrm{ps}} = V_{\mathrm{loc}}(r) + \sum_{l=0}^{l_{\max}} \delta V_l^{\mathrm{ps}}(r)\hat{P}_l, \tag{2.82}$$

where $\delta V_l^{\mathrm{ps}}(r) = V_l^{\mathrm{ps}}(r) - V_{\mathrm{loc}}(r)$, and $V_{\mathrm{loc}}(r)$ is the local part of the potential $\hat{V}^{\mathrm{ps}}$. The latter is typically taken as one of the $l$-dependent components $V_{\mathrm{loc}}(r) = V^{\mathrm{ps}}_{l=l_{\mathrm{loc}}}(r)$. The number of projections in Eq. (2.82) is reduced most, if one picks the $l_{\mathrm{loc}} = l_{\max}$ component as the local potential. It should be noted, that the potentials $\delta V_l^{\mathrm{ps}}(r)$ are essentially localized within the core region, and vanish outside of the core. Therefore, the pseudopotential (2.82) should in principle correctly reproduce the scattering properties also in the higher angular momentum channels with $l > l_{\max}$. This is also due to the high centrifugal barrier $l(l+1)/r^2$ (see Eq. (2.73)), that repels high $l$-electrons to a region where all pseudopotentials behave as $Z/r$.

Finally, the total energy for an arbitrary system expressed with pseudopotential reads as:

$$E[n^{\mathrm{ps}}] = \sum_{i}^{\mathrm{occ}} \langle\varphi_i|\hat{T} + \hat{V}^{\mathrm{ps}}|\varphi_i\rangle + E^{\mathrm{H}}[n^{\mathrm{ps}}] + E^{\mathrm{xc}}[n^{\mathrm{ps}}], \tag{2.83}$$

or, if the nonlinear core correction is included, as:

$$E[n^{\mathrm{ps}}] = \sum_{i}^{\mathrm{occ}} \langle\varphi_i|\hat{T} + \hat{V}^{\mathrm{ps}}|\varphi_i\rangle + E^{\mathrm{H}}[n^{\mathrm{ps}}] + E^{\mathrm{xc}}[n^{\mathrm{ps}} + n^{\mathrm{core}}]. \tag{2.84}$$

Up to this point we have outlined the general approach for constructing the pseudopotential, without specifying how to choose the pseudo wavefunction within the core region. In fact, there is a large degree of freedom to setup the pseudo wavefunction there, and over the last decades many different recipes have been published [93–101]. All proposed schemes try to balance the best compromise between the two contradicting objectives, namely, (i) the computational effectiveness of the pseudopotential, and (ii) the transferability of the pseudopotential. The requirement of the transferability is crucial, since by construction the pseudopotential *exactly* reproduces the all-electron calculations only for a given reference atomic configuration. However, if the chemical environment of the atom changes, the eigenstates will shift to slightly different energies. Therefore, for a pseudopotential to be useful, it has to be able to reproduce the all-electron potential over an energy range that can be spanned by atomic eigenstates in realistic systems (e.g. over the whole width of the valence band in crystalline solids). The wider this energy range, the more "transferable" to other chemical environments is the pseudopotential [40].

In the present study we use the norm-conserving type of pseudopotential (generated employing the scheme proposed by Troullier and Martins [99]), for which the normalization constraint is applied to the pseudo orbitals, implying that they include the same amount of electron density inside the core region as their all-electron counterpart:

$$\int_0^{r_{\text{core}}^l} |R_l^{\text{ps}}(r)|^2 dr = \int_0^{r_{\text{core}}^l} |R_{nl}(r)|^2 dr. \tag{2.85}$$

Condition (2.85) guarantees, that the norm-conserving pseudopotential obeys the requirement of transferability [40, 43, 102].

The other goal of a use of pseudopotential is the reduction of the number of planewaves necessary for the expansion of the pseudo wavefunctions, i.e. to be as "soft" as possible. Both properties, the transferability and softness, are closely related to the cutoff radii $r_{\text{core}}^l$ and compete with each other: a low cutoff radius yields a pseudopotential which reduces the difference between the all-electron and the pseudo atom. A larger cutoff radius makes the pseudopotential softer. This implies that in practice one has to find a compromise between the two requirements. We note, that the actual value of the cutoff radius $r_{\text{core}}^l$ is bounded within some interval $(r_{\text{min}}^l, r_{\text{max}}^l)$. The lower limit $r_{\text{min}}^l$ is dictated by the position of the outermost node of the corresponding valence all-electron wavefunction, and is due to the requirement of a nodeless pseudo wavefunction. The upper limit $r_{\text{max}}^l$ is given by half the distance to the next nearest atom in the configuration for which pseudopotential needs to be applied. Otherwise an accurate description of the chemical bonds between the two atoms may not be guaranteed.

## 2.6 Modeling of the tunneling current in the STM

The operating principle of STM is conceptually simple, and is based upon the detection of a current $I_{\text{tunnel}}$ that is due to electrons tunneling through the vacuum barrier separating the STM tip and the surface of interest. A sketch of the STM is shown on figure 2.3. When the tip is placed sufficiently far away from the surface, the surface and the tip do not interact with each other, the tip-vacuum-surface system splits into two independent tip-vacuum and surface-vacuum subsystems, and no tunneling of electrons occurs (Fig. 2.3(a)). When the tip-surface separation is shrunk down to several tens of angstrom, the two subsystems become weakly coupled, and electrons can tunnel from the surface to the tip and vice versa. Treating the tip-vacuum-surface system as thermodynamically closed, the tunneling continues until the thermodynamic equilibrium between the two subsystems is established, implying that the Fermi energy of the surface and of the tip become aligned (equivalent to saying that the chemical potentials of the electrons in both subsystems are equal). The resulting net tunneling current between the tip and the surface is then settled down to zero, although there might appear an electrical field within the tunneling junction (Fig. 2.3(b)).

Applying external voltage between the tip and the surface (so-called bias voltage) shifts the Fermi energy of one lead (surface or tip) relative to that of the other lead, i.e. pushes the system away from the equilibrium (Fig. 2.3(c)). The quantum mechanical tunneling between the leads is then dominated by electrons tunneling from the subsystem with the higher Fermi level, that

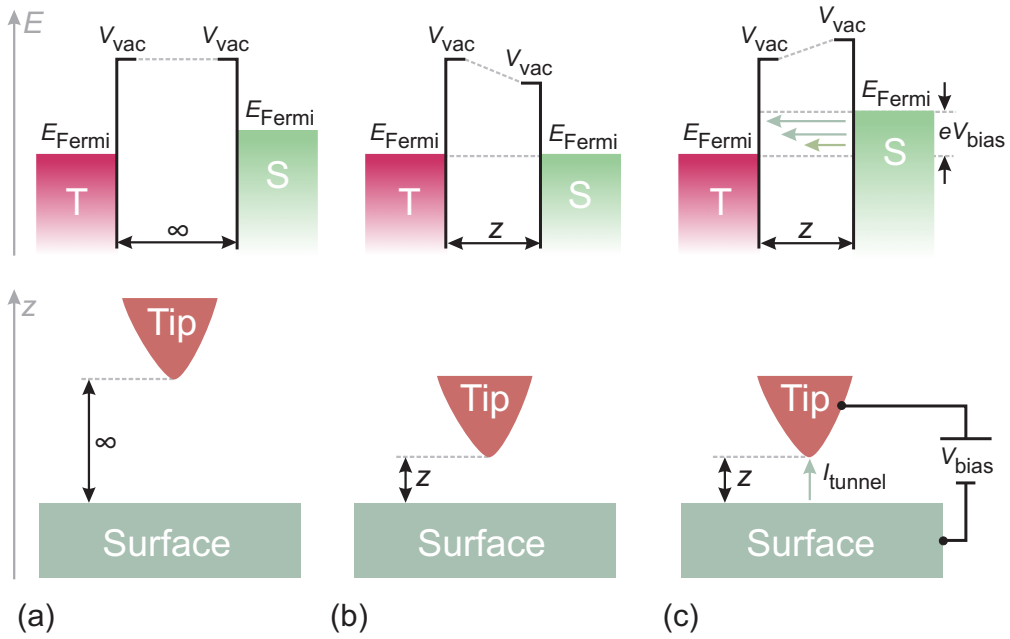


Figure 2.3: One-dimensional sketch of the operational principle of the STM. (a) At large tip-surface separations the tip and the surface do not interact and can be treated independently. (b) Tip and surface are in intimate contact (tip-surface separation is less than several tens of angstrom). The net tunneling current is zero, implying that the Fermi energies of the tip and of the surface are aligned. (c) A bias voltage $V_{\text{bias}}$ is applied between the tip and the surface, leading to a tunneling of electrons from the surface towards the tip, i.e. to a tunneling current $I_{\text{tunnel}}$. The upper row of figures sketches the electronic structure, the lower row the real-space configuration of the STM setup.

results into a nonzero net tunneling current flowing between the electrodes. The direction of the current is defined by the sign of the bias voltage[19] $V_{\text{bias}}$. Typically, the STM operates slow enough that for each spatial position of the tip $\mathbf{R}_{\text{tip}}$ and bias voltage $V_{\text{bias}}$, the system relaxes to a steady state (not equilibrium), characterized by the tunneling current $I_{\text{tunnel}}$. The STM records the modulation of the current $I_{\text{tunnel}}$ versus the spatial position of the tip (topographic regime), and/or versus the applied bias voltage (spectroscopic regime). Obviously, the realistic tunneling is highly influenced by the tip-surface distance, the chemical compositions of the tip and of the surface, the electronic properties of both subsystems, the chemical interactions between the surface and tip atoms, and the electrostatic interaction of the surface and the tip [4]. Assuming, however, that the tip properties do not change during the experiment and that the tip is only weakly coupled to the surface, the lateral/bias variation of the tunneling current can be linked to corresponding laterally/energetically-resolved properties of the surface.

It is clear from the discussion presented above, that an accurate modeling of the tunneling

[19]By convention, the net tunneling current due to electrons ejected from the tip towards the surface corresponds to a positive bias voltage.

current is the key objective for a theoretical analysis of STM. It is also obvious, that STM models should be based on an explicit description of the tip and surface electronic properties. A number of theoretical methods for calculating the tunneling current have been developed over a few decades, being different in the theoretical complexity and accuracy. A complete survey of all methods is given by Briggs and Fisher [103], and by Hofer *et al.* [4]. Here, we outline the three main approaches used up to date. In decreasing order of theoretical complexity, the methods are: (i) the Keldysh-Green's-function approach [104], (ii) the scattering or Landauer-Büttiker approach [105], and (iii) the transfer Hamiltonian or Bardeen approach [106].

The most complete treatment of the full STM Hamiltonian is achieved on basis of a nonequilibrium Green's-function formalism [104], that explicitly describes the coupled tip-vacuum-surface system in the steady state. The full Green's-function of the Keldysh approach includes all inelastic processes, spin flips, and multiple scattering events, making this method the most accurate today. The inclusion of such a wide range of interactions hinders, however, a merging of this method with a high quality *ab initio* description of the Hamiltonian. Consequently, the main drawback of the method is the computational cost, which has to be reduced by an introduction of severe approximations in the description of the tip and the surface properties.

The neglect of electron interactions inside the vacuum barrier reduces the Keldysh method to the Landauer-Büttiker approach. The latter calculates the conductance of the vacuum barrier as a ratio of the transmission probability and the scattering probability, i.e. treating the STM current as an electron scattering problem. The advantage of the Landauer-Büttiker approach is its mathematical rigor and its flexibility in including different boundary conditions of the STM leads. Moreover, it accounts for interference effects between separate conductance channels. The main disadvantage of this method is, however, its practical limitation to a tight-binding approach to describe the tip and surface electronic structures. The choice of tight-binding models is triggered by a significant speed up of the calculations, but might simultaneously lead to a poor description of electronic properties. Specifically, even if the parameters for the tight binding model are taken from *ab initio* simulations, the localized basis set used in the tight-binding model usually disagrees with the decay characteristics of the tunneling current found in the experiments [4].

It should be noted, that the Keldysh-Green's-function and the Landauer-Büttiker approaches are essential when a complete treatment of the electron transport through the whole tip-vacuum-surface system is necessary [103], e.g., when a point contact between the tip and the surface is formed or when the tunneling is more rapid than some other part of the electron transport. In most cases, however, it is sufficient to assume a weak coupling between the tip and the surface, and to treat both subsystems independently. Such a treatment of the STM is derived on basis of perturbation theory, and is referred to as the transfer Hamiltonian approach. This method is the most widely used approach for STM modeling nowadays. The major advantages provided by the perturbative treatment are (i) the possibility to describe the realistic tip and the surface with DFT accuracy, and (ii) the intuitive interpretation of the STM experiments in terms of the electronic

properties of the subsystems.

In this study we perform an analysis of STM experiments combining density functional theory with the transfer Hamiltonian formalism, as discussed in more detail in the next section.

### 2.6.1 The transfer Hamiltonian formalism

The most extensively used tool to model the tunneling junction in STM is the time-dependent perturbation approach of Bardeen, that is sufficiently simple for treating most realistic cases, and has been successfully used to describe a wide variety of effects [106, 107]. Bardeen's idea is to substitute the Schrödinger equation of the combined system with that of two separate subsystems (for a tip and for a surface), for which the exact solution is obtained by solving the corresponding stationary Schrödinger equations. With an adequate description of the isolated subsystems, Bardeen approximated the rates of the individual electron transfer events across the tunneling barrier using time-dependent perturbation theory.

According to Bardeen, the total effective potential[20] $V^{\text{eff}}$ of the tip-vacuum-surface system under applied bias voltage $V_{\text{bias}}$ is defined as the sum of the two potentials of the tip-vacuum and surface-vacuum subsystems:

$$V^{\text{eff}}(\mathbf{r}) = V_{\text{s}}^{\text{eff}}(\mathbf{r}) + V_{\text{t}}^{\text{eff}}(\mathbf{r}), \tag{2.86}$$

where $V_{\text{s(t)}}^{\text{eff}}$ is the potential of the surface (tip) subsystem, with the separation surface $\Sigma$ being located between the tip and the surface (Fig. 2.4). The effective potentials in Eq. (2.86) are chosen such, that the tip potential $V_{\text{t}}^{\text{eff}}$ is identical to the total potential $V^{\text{eff}}$ everywhere in the region $\Omega_{\text{t}}$ occupied by the tip subsystem, implying that:

$$V_{\text{t}}^{\text{eff}}(\mathbf{r}) = 0 \text{ in } \Omega_{\text{s}}, \quad V_{\text{s}}^{\text{eff}}(\mathbf{r}) = 0 \text{ in } \Omega_{\text{t}}. \tag{2.87}$$

The condition given by Eq. (2.87) is necessary to reduce the error of the perturbation treatment used in the transfer Hamiltonian method, i.e. to ensure that the first-order perturbation theory provides a meaningful approximation to the exact tunneling current [107, 108]. Using subsystem potentials as defined in Eqs. (2.86)-(2.87), the electronic structure of the tip and surface are considered now independently rather than as parts of the STM, solving the corresponding Hamiltonians:

$$(T + V_{\text{s}}^{\text{eff}})\varphi_{\nu}^{\text{s}} = \epsilon_{\nu}^{\text{s}}\varphi_{\nu}^{\text{s}}, \tag{2.88}$$

and

$$(T + V_{\text{t}}^{\text{eff}})\varphi_{\mu}^{\text{t}} = \epsilon_{\mu}^{\text{t}}\varphi_{\mu}^{\text{t}}. \tag{2.89}$$

[20] We discuss here the single-particle representation of the Bardeen's theory, although in his original report the many-body problem was considered [106].

Here, $\varphi_\mu^{\mathrm{t}}$ and $\varphi_\nu^{\mathrm{s}}$ are unperturbed electron states of the tip and the surface, that are called "tip states" and "surface states", respectively. The tunneling current is the result of the electron transfer from the tip states to the surface states and vice versa under the influence of the STM Hamiltonian, that can be written as:

$$H^{\mathrm{s}} = H_{\mathrm{s}}^{\mathrm{s}} + V_{\mathrm{t}}^{\mathrm{eff}} = T + V_{\mathrm{s}}^{\mathrm{eff}} + V_{\mathrm{t}}^{\mathrm{eff}}. \tag{2.90}$$

The solutions of the complete STM system defined by (2.90) are constructed from the eigenfunctions of the unperturbed constituent subsystems. Assuming that the tip and the surface in STM behave like two weakly coupled systems, and that it is therefore reasonable to perform perturbation theory in this coupling [103], the evolution of the isolated subsystems into a coupled STM is evaluated employing first-order time-dependent perturbation theory. The tip potential is considered then as adiabatic time-dependent perturbation to an isolated surface.

Specifically, following the ansatz of perturbation theory, it is assumed that the total wavefunction of the STM system evolves with time from a pure unperturbed surface wavefunction $\varphi_\nu^{\mathrm{s}}$ (tip perturbation at time $t = 0$ is switched off) to a wavefunction $\varphi(t)$ that can be expressed as a superposition of $\varphi_\nu^{\mathrm{s}}$ and all bound single-particle tip states $\varphi_\mu^{\mathrm{t}}$:

$$\varphi(t) = \mathrm{e}^{-\mathrm{i}t\epsilon_\nu^{\mathrm{s}}}\varphi_\nu^{\mathrm{s}} + \sum_\mu a_\mu(t)\varphi_\mu^{\mathrm{t}}. \tag{2.91}$$

Here, the first term is the time evolution governed by the surface Hamiltonian (2.88), and $a_\mu(t)$ are unknown expansion coefficients, which need to be approximated[21]. The coefficients $a_\mu(t)$ are calculated from the time-dependent Schrödinger equation that describes the evolution of the system from an isolated surface to a coupled STM system, assuming that tunneling is weak.

For a single event, the probability of an electron initially in the surface state $\varphi_\nu^{\mathrm{s}}$ to "scatter into" the tip state $\varphi_\mu^{\mathrm{t}}$ under the influence of the STM Hamiltonian (2.90) is given by $|\langle\varphi_\mu^{\mathrm{t}}|\varphi(t)\rangle|^2$. Assuming that the tip and surface states are nearly orthogonal allows to approximate the transition probability $|\langle\varphi_\mu^{\mathrm{t}}|\varphi(t)\rangle|^2$ by the expansion coefficients $|a_\mu(t)|^2$ [109], and to write the scattering rate $\varphi_\nu^{\mathrm{s}} \to \varphi_\mu^{\mathrm{t}}$ as[22]:

$$\varpi_{\mu\nu} = 2\pi|M_{\mu\nu}|^2\delta\left(\epsilon_\mu^{\mathrm{t}} - \epsilon_\nu^{\mathrm{s}}\right), \tag{2.92}$$

where $M_{\mu\nu}$ is the so-called tunneling matrix element:

$$M_{\mu\nu} = \langle\varphi_\mu^{\mathrm{t}}|V_{\mathrm{t}}^{\mathrm{eff}}|\varphi_\nu^{\mathrm{s}}\rangle. \tag{2.93}$$

[21] The expansion coefficients in Eq. (2.92) are $a_\mu(t) = \langle\varphi_\mu^{\mathrm{t}}|\varphi(t) - \mathrm{e}^{-\mathrm{i}t\epsilon_\nu^{\mathrm{s}}}\varphi_\nu^{\mathrm{s}}\rangle$, so that $\sum a_\mu(t)\mathrm{t}_\mu$ is the projection of $\varphi(t) - \mathrm{e}^{-\mathrm{i}t\epsilon_\nu^{\mathrm{s}}}\varphi_\nu^{\mathrm{s}}$ onto the space spanned by the bound states of the tip. Since the tip's bound states do not span the whole Hilbert space of solutions, equation (2.92) is only an approximate [109].

[22] For details on the derivation see, e.g., Refs. [108, 109].

Since the tip potential is set to zero everywhere outside $\Omega_t$, the integral in Eq. (2.93) is evaluated only inside of the tip-subsystem volume. The tunneling current due to the single scattering event is proportional to the transition probability rate, $I_{\mu\nu} \sim e\varpi_{\mu\nu}$, where $e$ is the electron charge. The term $\delta(\epsilon^t_\mu - \epsilon^s_\nu)$ reflects the conservation of the electron energy during the tunneling process, i.e. the equation (2.92) describes the elementary process of elastic tunneling.

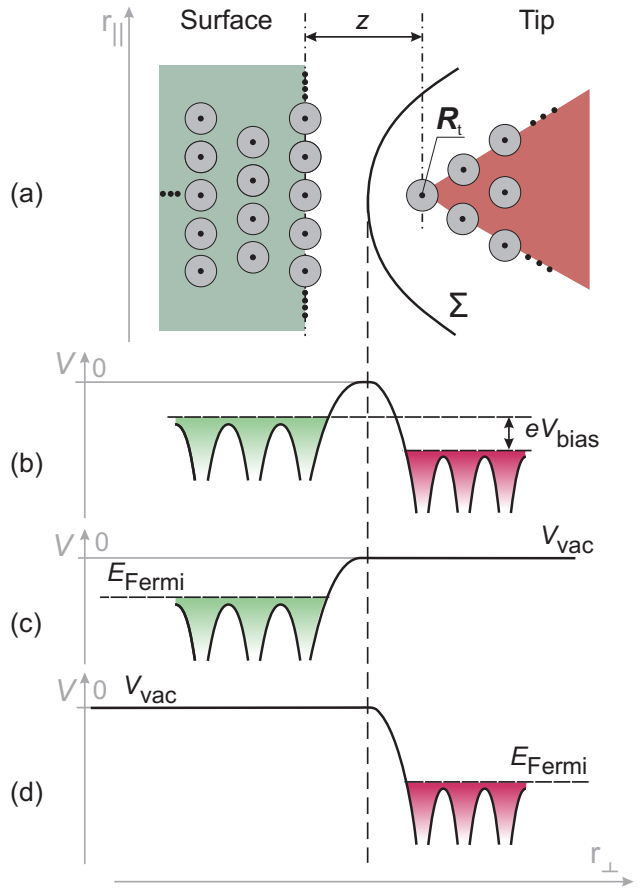


Figure 2.4: Schematics of the perturbation approach to quantum electron transmission. (a) Geometry of the STM setup. A separation surface $\Sigma$ between the tip and the surface subsystems is drawn. The precise location and shape of $\Sigma$ is not crucial. (b) The $(x, y)$-averaged (with $z$ being normal to the surface plane) effective potential of the tip-vacuum-surface system under a bias voltage $V_{\text{bias}}$. (c) and (d): the $(x, y)$-averaged effective potentials of the surface in absence of the tip, and of the tip in absence of the surface, respectively.

To compute the final expression for the total tunneling current one has to sum over all possible scattering events. Within Bardeen's theory it is assumed, that both subsystems are very large, each of them incorporates its own electron reservoir of virtually unlimited capacity, for then the tunneling does not affect the density of electronic states. In other words, it is assumed that (i) the tunneling probabilities for the tip and surface are independent of each other and do not change despite of the tunneling, and (ii) the tip and the surface are each in thermodynamic equilibrium.

These assumptions imply that the occupation $f$ of each single-particle eigenstate with energy $\epsilon$ (relative to the Fermi level) obeys Fermi-Dirac statistics:

$$f(\epsilon) = \frac{1}{1 + \exp\left[\frac{\epsilon}{k_{\mathrm{B}}T}\right]}. \tag{2.94}$$

Obviously, electrons can tunnel only from the occupied states to empty ones. In the steady state of the STM under applied bias $V_{\mathrm{bias}}$, the net tunneling current is a superposition of the two opposite tunneling currents, that are due to electron transport from the occupied tip state into unoccupied surface states (see Fig. 2.4):

$$I_{\mathrm{t}\to\mathrm{s}} = 4\pi \sum_{\mu\nu} f(\epsilon^{\mathrm{t}}_{\mu} - E^{\mathrm{t}}_{\mathrm{Fermi}}) \left[1 - f(\epsilon^{\mathrm{s}}_{\nu} - E^{\mathrm{s}}_{\mathrm{Fermi}})\right] |M_{\mu\nu}|^2 \delta\left(\epsilon^{\mathrm{t}}_{\mu} - \epsilon^{\mathrm{s}}_{\nu} - eV_{\mathrm{bias}}\right), \tag{2.95}$$

and the opposite current due to electrons hopping from the occupied surface states into empty tip states:

$$I_{\mathrm{s}\to\mathrm{t}} = 4\pi \sum_{\mu\nu} f(\epsilon^{\mathrm{s}}_{\mu} - E^{\mathrm{s}}_{\mathrm{Fermi}}) \left[1 - f(\epsilon^{\mathrm{t}}_{\nu} - E^{\mathrm{t}}_{\mathrm{Fermi}})\right] |M_{\mu\nu}|^2 \delta\left(\epsilon^{\mathrm{t}}_{\mu} - \epsilon^{\mathrm{s}}_{\nu} - eV_{\mathrm{bias}}\right). \tag{2.96}$$

The summation over all scattering events provides the expression for the net tunneling current:

$$I = 4\pi \sum_{\mu\nu} \left[f(\epsilon^{\mathrm{s}}_{\mu} - E^{\mathrm{s}}_{\mathrm{Fermi}}) - f(\epsilon^{\mathrm{t}}_{\nu} - E^{\mathrm{t}}_{\mathrm{Fermi}})\right] |M_{\mu\nu}|^2 \delta\left(\epsilon^{\mathrm{t}}_{\mu} - \epsilon^{\mathrm{s}}_{\nu} - eV_{\mathrm{bias}}\right). \tag{2.97}$$

The summation over discrete eigenstates in Eq. (2.97) is conventionally reformulated into an energy integral over the density of electronic states[23] $n(E)$:

$$\begin{aligned} I = 4\pi \int dE \left[f(E^{\mathrm{s}}_{\mathrm{Fermi}} - eV_{\mathrm{bias}} + E) - f(E^{\mathrm{t}}_{\mathrm{Fermi}} + E)\right] \\ \times n^{\mathrm{t}}(E^{\mathrm{s}}_{\mathrm{Fermi}} - eV_{\mathrm{bias}} + E) n^{\mathrm{s}}(E^{\mathrm{t}}_{\mathrm{Fermi}} + E) \\ \times \left|M(E^{\mathrm{t}}_{\mathrm{Fermi}} + E, E^{\mathrm{s}}_{\mathrm{Fermi}} - eV_{\mathrm{bias}} + E)\right|^2. \end{aligned} \tag{2.98}$$

Equation (2.98) formally couples the electronic structures of the tip and the surface, expressed in terms of the corresponding density of states $n(E)$. The spatial dependence of the tunneling current is completely incorporated into the tunneling matrix element $M_{\mu\nu}$. For practical purposes, $M_{\mu\nu}$ is converted from the integral over volume $\Omega_{\mathrm{t}}$ into a surface integral over the separation surface $\Sigma$ as [4, 107–109]:

[23] The density of states $n$ (DOS) is defined as the number of electronic states $N$ available in the energy interval $(E, E + \Delta E)$:

$$N(E, \Delta E) = \int_{E}^{E+\Delta E} n(E')dE'.$$

For more details see Sec. A.3.

$$M_{\mu\nu} = -\frac{1}{2m}\int_{\Sigma} d\mathbf{S}\cdot\left(\varphi_{\nu}^{\mathrm{t}\,*}\nabla\varphi_{\mu}^{\mathrm{s}} - \varphi_{\mu}^{\mathrm{s}}\nabla\varphi_{\nu}^{\mathrm{t}\,*}\right), \tag{2.99}$$

where the precise location of the separation surface $\Sigma$ is not critical.

The major advantage provided by Bardeen's treatment is the expression of the tunneling current via the wavefunctions of the bare surface and tip, i.e. without knowledge of the full Hamiltonian and the full many-particle wavefunctions. Although Bardeen's current formula (2.98) is derived employing a number of assumptions, Pendry *et al.* [110] showed that it is an approximation to the most exact nonequlilibrium Green's-function formula when an interface between the tip and surface can be found where the density of states is small. The predictions of the original Bardeen's theory are considered to be trustworthy when the tip and surface are sufficiently far apart (typically, above $\sim 5$ Å from a metal surface), and when the vacuum barrier is reasonably high (more that $\sim 1.5$ eV above the tunneling channel [111])[24].

Bardeen's theory also applies within the range of chemical forces between the tip and the surface, that become essential when the STM tip comes close to the surface. In contrast to the original derivation, however, the correct tunneling matrix elements should accommodate now the tip effects, e.g., (i) account for the actual electrostatic potential profile in the tip-vacuum-surface system, and (ii) include the movement of the tip and surface atoms due to tip-surface interactions.

A solution of the problem (i) has been proposed by Chen, who suggested to use tip and surface potentials $V_{\mathrm{t}}^{\mathrm{eff}}$ and $V_{\mathrm{s}}^{\mathrm{eff}}$ not equal to that of the free surface and tip as in the original transfer-Hamiltonian theory (see Refs. [107, 112] for details). Chen has shown that his choice of unperturbed potentials minimizes the error introduced by neglecting the higher terms in the perturbation theories. The so-called modified Bardeen's approach (MBA) of Chen accounts for a modification of the tip and the surface wavefunctions when the vacuum barrier collapses (e.g. when the tip comes too close to the surface), or when these wavefunctions are modified due to a finite electric field between the STM leads. For normal tip-surface distances (5-10 Å), however, the original and modified Bardeen's approaches provide essentially identical results.

The modification of the tip/surface local atomic structures at low tip-surface separations have been studied e.g. by Hofer *et al.* for an Fe(100) surface [113]. They concluded that, employing modified Bardeen's tunneling matrix elements calculated for modified atomic geometries provides qualitative agreement with experimental STM images even when the tip-surface difference is as low as 4 Å.

Eqs. (2.98)-(2.99) of Bardeen's theory for the STM allow to calculate the tunneling current for

[24] In cases when the vacuum potential is not flat, i.e. when there is an electrical field between the tip and the surface (caused by a finite bias voltage, and/or due to different work functions of the metallic leads), the tunneling matrix elements become dependent on the interface position $\Sigma$. Hörmandinger [111] has shown, that using the original Bardeen's approach with an interface midway between the tip and surface provides a reasonable approximation even for a barrier with electric field (see discussion in Ref. [111]). Another approach for treating nonzero electric fields in vacuum was proposed by Chen [107, 112], who suggested to calculate matrix elements using *modified* wavefunctions (see discussion in Refs. [107, 112] and in the text).

known tip and surface structures. While the surface is generally a well-defined object in the STM, much less is known about the atomic scale properties of the tips. Therefore, more or less educated guesses should be and are made regarding the structure of the tip. Several authors calculated the tunneling matrix elements $M_{\mu\nu}$ explicitly using various tip models, from an atom adsorbed onto a jellium surface [114, 115], to little pyramids of tungsten atoms [116, 117], to tungsten surfaces with protruding atoms or clusters [118].

### 2.6.2 The Tersoff-Hamann approximation

In most studies the electronic properties of the STM tip are not calculated *ab initio*, but introduced via simpler tip-models. The Tersoff-Hamann approximation to the tunneling current is the celebrated and the most widely used method for a theoretical understanding of STM images [119]. The method was proposed in 1985, and is derived from the perturbation theory of Bardeen (see Sec. 2.6.1) assuming a specific tip structure. Specifically, Tersoff and Hamann have assumed, that (i) perturbation theory for the tip-surface interaction is appropriate, i.e. Bardeen's equations hold; (ii) there exists a region between the tip and the surface within which the potential is equal to its vacuum value, and (iii) the predominant tip state involved in the tunneling is a $s$-like (spherically symmetric) state.

Assumptions (ii) and (iii) allow to express the tip wavefunction within the region of the vacuum potential in the asymptotic spherical form as:

$$\varphi_\nu^{\mathrm{t}}(\mathbf{r}) = C\frac{e^{-\kappa|\mathbf{r}-\mathbf{R}_{\mathrm{t}}|}}{\kappa|\mathbf{r}-\mathbf{R}_{\mathrm{t}}|}, \quad \text{for} \quad |\mathbf{r}-\mathbf{R}_{\mathrm{t}}| \neq 0, \tag{2.100}$$

where $\mathbf{R}_{\mathrm{t}}$ is the center of the tip curvature with radius $r_{\mathrm{t}}$, as shown in Fig. 2.5. $\kappa = \sqrt{2m|\phi|}$ is the minimum inverse decay length for wavefunctions in vacuum, where $\phi$ is the work function (for simplicity assumed to be equal for both tip- and surface-subsystems). $C$ is a normalization parameter[25] that guarantees a matching of the wavefunction (2.100) to the unknown tip wavefunction on the boundary between the tip and vacuum potential, and is determined by the tip geometry, the detailed electronic structure, and the tip-vacuum boundary condition [108, 119].

Placing the separation surface $\Sigma$ in the vacuum region where the tip and the surface potentials equal the vacuum potential, enables one to perform the integration of the tunneling matrix element (2.99) explicitly. Expanding both the surface and the tip wavefunctions into a completely general Fourier-series (plane waves), in the limit of low temperatures, Tersoff and Hamann have shown that:

$$M_{\mu\nu} = -\frac{2\pi C}{\kappa}\varphi_\mu^{\mathrm{s}}(\mathbf{R}_{\mathrm{t}}). \tag{2.101}$$

[25] In the original paper by Tersoff and Hamann $C$ is defined as $C = \Omega_{\mathrm{t}}^{-1/2} c_{\mathrm{t}} \kappa r_{\mathrm{t}} \exp[\kappa r_{\mathrm{t}}]$, where the parameter $c_{\mathrm{t}}$ is of the order of 1, and is used for normalization.

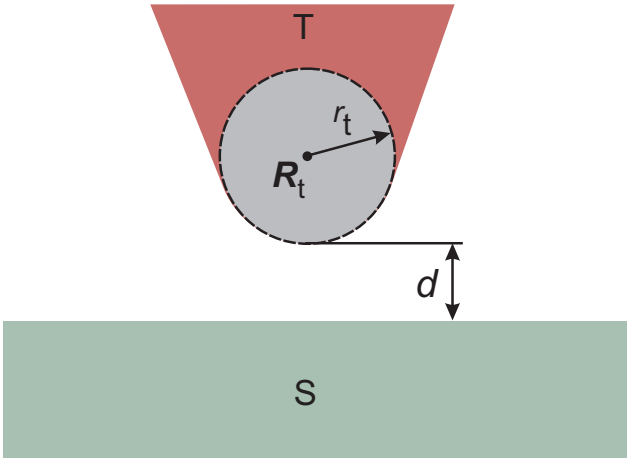


Figure 2.5: Schematic picture of the tunneling geometry within the Tersoff-Hamann picture. The STM tip has an arbitrary shape, but the tip apex is assumed to be locally spherical with a radius of curvature $r_t$. The center of the sphere at the top of the tip is labeled $\mathbf{R}_\mathrm{t}$, the nearest distance between the tip and the surface is $d$.

According to Tersoff and Hamann, the tunneling matrix element $M$ is proportional to the surface wavefunction at the center $\mathbf{R}_\mathrm{t}$ of the tip apex-atom if the tip electronic structure can be described via $s$-like atomic orbitals.

Substituting Eq. (2.101) into Eq. (2.98), and assuming that the density of tip states is essentially constant within the tunneling energies, i.e. $n^\mathrm{t}(E) = \mathrm{const}$, results in the Tersoff-Hamann expression for the tunneling current:

$$I(\mathbf{R}_\mathrm{t}, V_\mathrm{bias}) = \frac{16\pi^3 C^2}{\kappa^2} n^\mathrm{t} \int_0^{eV_\mathrm{bias}} dE \;\; n^\mathrm{s}(\mathbf{R}_\mathrm{t}, E^\mathrm{s}_\mathrm{Fermi} + E), \tag{2.102}$$

where $n^\mathrm{s}(\mathbf{R}, E)$ is the *local* density of states (LDOS) for the surface, defined as:

$$n^\mathrm{s}(\mathbf{R}, E) = \sum_\mu \left|\varphi^\mathrm{s}_\mu(\mathbf{R})\right|^2 \delta(E - \epsilon_\mu). \tag{2.103}$$

The absolute value of the tunneling current (2.102) is not well defined, because the information regarding the tip orbitals, merged into parameter $C$ in Eq. (2.102), is not known. However, since the unknown prefactor is independent of the spatial position of the tip and of the applied bias, the modulation of the tunneling current is proportional to that of the surface LDOS integrated over the energy range $(E^\mathrm{s}_\mathrm{Fermi}, E^\mathrm{s}_\mathrm{Fermi} + eV_\mathrm{bias})$:

$$I(\mathbf{R}_\mathrm{t}, V_\mathrm{bias}) \propto \int_0^{eV_\mathrm{bias}} dE \;\; n^\mathrm{s}(\mathbf{R}_\mathrm{t}, E^\mathrm{s}_\mathrm{Fermi} + E). \tag{2.104}$$

This information is sufficient to simulate STM images, both in the constant-current regime ($I(\mathbf{R}_\mathrm{t}, V_\mathrm{bias}) = \mathrm{const}$) and in the constant-height regime ($\mathbf{R}_\mathrm{t} = \mathrm{const}$). A major advantage of the

Tersoff-Hamann theory is the particular simplicity of the tunneling current, that allows a straightforward interpretation of the STM experiments in terms of the electronic density of the surface alone, disregarding the presence of the STM tip. In many standard situations, e.g. in research on molecular adsorption or surface reconstructions, the model provides a reliable qualitative picture of the surface topography, even though it does not generally reproduce the observed corrugation values [4].

The requirement of a flat vacuum potential (ii) limits the applicability of the Tersoff-Hamann theory to low bias voltages (compared to the work functions of the leads), and to tips and surfaces with similar work functions (with difference less than 1 eV according to Ref. [119]). Hofer *et al.* judges the Tersoff-Hamann model to be reliable for interpreting images of surface structures whose feature size is well above the typical length scale of electron states of the STM tip, provided that there are no substantial chemical interactions between the surface and the tip [4]. Tersoff-Hamann theory is thus deemed adequate for images whose feature size is well above 1 or 2 Å, when these images are produced at a large enough tip-surface distance (larger than 5-6 Å for metal surfaces) [109].

In conclusion we note, that the Tersoff-Hamann model may be unable to account for atomic-resolution features on an STM image due to the spherical approximation for the tip wavefunctions. When using better tip models (like, e.g., the "derivative rule" proposed by Chen, who extended the Tersoff-Hamann theory to $p$- and $d$-type atomic orbitals [107, 112, 120, 121]) the atomic resolution can be well reproduced within Bardeen's view on STM.

### 2.6.3 Spin-generalized transfer-Hamiltonian formalism

When the STM experiments are performed on a magnetic surface and the tip potential is spin-dependent (e.g., when magnetic tips are employed or by virtue of the spin-dependent scattering/absorption due to a spin-orbit coupling) the tunneling current is modulated by the spin-structures of the tip and surface. For a system without interaction between the magnetic tip and the surface, i.e. when the vacuum barrier is so wide that it is essentially nonpenetratable, the tip (surface) stationary electronic states are eigenstates of the Hamiltonian:

$$H^{\mathrm{s}}_{\mathrm{t(s)}} = T + \ \boldsymbol{h}_{\mathrm{t(s)}} \cdot \boldsymbol{\sigma}. \tag{2.105}$$

Here, $\boldsymbol{h}_{\mathrm{t(s)}}$ is a 2×2 Hermitian matrix that acts on the spin degree of freedom of an electron, and $\boldsymbol{\sigma} = (\sigma_x, \sigma_y, \sigma_z)$ are the Pauli spin matrices.

The solution of Eq. (2.105) is known and is a two component spinor. Choosing the quantization axis $z$ of a tip (surface) collinear with $\boldsymbol{h}_{\mathrm{t(s)}}$ the tip (surface) spinor can be expressed as two independent eigenvectors denoted as $\Psi^{\mathrm{t(s)}}_{\mu\uparrow}$ and $\Psi^{\mathrm{t(s)}}_{\mu\downarrow}$:

$$\Psi^{\mathrm{t(s)}}_{\mu\uparrow}(\mathbf{r}) = \varphi^{\mathrm{t(s)}}_{\mu\uparrow}(\mathbf{r})\chi_{\uparrow} \qquad \text{and} \qquad \Psi^{\mathrm{t(s)}}_{\mu\downarrow}(\mathbf{r}) = \varphi^{\mathrm{t(s)}}_{\mu\downarrow}(\mathbf{r})\chi_{\downarrow}, \tag{2.106}$$

where

$$\chi_\uparrow = \begin{pmatrix} 1 \\ 0 \end{pmatrix} \qquad \text{and} \qquad \chi_\downarrow = \begin{pmatrix} 0 \\ 1 \end{pmatrix} \tag{2.107}$$

are eigenvectors of the $\sigma_z$ Pauli matrix, and $\psi^{\mathrm{t(s)}}_{\mu\uparrow(\downarrow)}(\mathbf{r})$ are functions describing the spatial dependence of the spinor components [122].

Now we assume that the width of the tunneling junction is reduced such that the tip and the surface can interact with each other via a low rate electron tunneling. Assuming that the tunneling is spin-conserving (i.e. the tip potential is diagonal in spin space), it is possible to employ first order perturbation theory in complete analogy to the nonmagnetic case (see Sec. 2.6.1) and to show that the tunneling current between the magnetic tip and the surface can be expressed as:

$$I(V_{\mathrm{bias}}) = 2\pi \sum_{\substack{\mu\nu \\ \sigma\sigma'}} \left[ f(\epsilon^{\mathrm{s}}_{\mu\sigma} - E^{\mathrm{s}}_{\mathrm{Fermi}}) - f(\epsilon^{\mathrm{t}}_{\nu\sigma'} - E^{\mathrm{t}}_{\mathrm{F}}) \right] \left| M^{\sigma\sigma'}_{\mu\nu} \right|^2 \delta(\epsilon^{\mathrm{t}}_{\nu\sigma'} - \epsilon^{\mathrm{s}}_{\mu\sigma} - eV_{\mathrm{bias}}). \tag{2.108}$$

Here, $M^{\sigma\sigma'}_{\mu\nu}$ is the tunneling matrix element that is equal to the probability of an electron to tunnel from the tip state $\Psi^{\mathrm{t}}_{\mu\sigma}$ into the surface state $\Psi^{\mathrm{s}}_{\nu\sigma'}$:

$$M^{\sigma\sigma'}_{\mu\nu} = \langle \Psi^{\mathrm{t}}_{\mu\sigma} | U_{\mathrm{t}} | \Psi^{\mathrm{s}}_{\nu\sigma'} \rangle. \tag{2.109}$$

Since the tip and the surface are no longer independent, the wavefunctions in Eq. (2.109) should correspond to the same quantization axis of a joined tip-barrier-sample system $\mathbf{e}^{\mathrm{tbs}}_M$. Solutions given by Eq. (2.106) hold, therefore, only when both the tip and the surface are collinear magnets with coinciding directions of magnetization, i.e. when $\mathbf{e}^{\mathrm{tbs}}_M = \mathbf{e}^{\mathrm{t}}_M = \mathbf{e}^{\mathrm{s}}_M$. In general, however, the quantization axis of the tip is not aligned in parallel to that of the surface ($\mathbf{e}^{\mathrm{t}}_M \neq \mathbf{e}^{\mathrm{s}}_M$) since both the tip and the sample may possess a variety of different magnetic structures, including noncollinear configurations.

For $\mathbf{e}^{\mathrm{t}}_M \neq \mathbf{e}^{\mathrm{s}}_M$ we take the $z$-axis of the tip-barrier-sample system along $\boldsymbol{h}_{\mathrm{t}}$ and assume that $\boldsymbol{h}_{\mathrm{s}}$ is tilted by an angle $\theta$ with respect to this direction. In this geometry:

$$H^{\mathrm{s}}_{\mathrm{t}} = T - h_{\mathrm{t}}\sigma_z = T - h_{\mathrm{t}} \begin{pmatrix} 1 & 0 \\ 0 & -1 \end{pmatrix}, \tag{2.110}$$

and

$$H_{\mathrm{s}} = T - h_{\mathrm{s}}[\cos(\theta)\sigma_z - \sin(\theta)\sigma_y] = T - h_{\mathrm{s}} \begin{pmatrix} \cos(\theta) & -\mathrm{i}\sin(\theta) \\ \mathrm{i}\sin(\theta) & -\cos(\theta) \end{pmatrix}. \tag{2.111}$$

The solutions of the tip Hamiltonian (Eq. (2.110)) are given by Eq. (2.106), while for the surface the corresponding spinors are obtained by using the spinor transformation [122]:

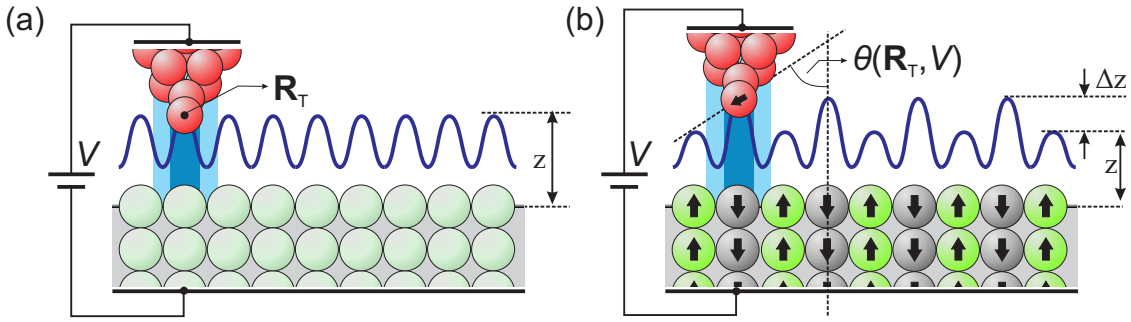


Figure 2.6: Comparison of (a) conventional spin-averaged STM with (b) spin-polarized STM in the constant-current mode. Within the framework of the Tersoff-Hamann model the tunneling current in the nonmagnetic STM is proportional to the surface LDOS at the tip-apex position $\mathbf{R}_\mathrm{T}$. When the tip is magnetized the tunneling current is additionally modulated by a magnetic contribution, that depends on the surface magnetic LDOS and the angle $\theta\,(\mathbf{R}_\mathrm{T}, V)$ between the magnetization direction of the tip and the surface at $\mathbf{R}_\mathrm{T}$.

$$\Psi^\mathrm{s}_{\mu\uparrow} = \varphi^\mathrm{s}_{\mu\uparrow} \begin{pmatrix} \cos\left(\frac{\theta}{2}\right) \\ \mathrm{i}\sin\left(\frac{\theta}{2}\right) \end{pmatrix} \qquad \text{and} \qquad \Psi^\mathrm{s}_{\mu\downarrow} = \varphi^\mathrm{s}_{\mu\downarrow} \begin{pmatrix} \sin\left(\frac{\theta}{2}\right) \\ -\mathrm{i}\cos\left(\frac{\theta}{2}\right) \end{pmatrix}. \tag{2.112}$$

Similar to the nonmagnetic case (Sec. 2.6.2) we introduce assumptions regarding the particular structure of the magnetic tip, expanding the tip wavefunctions into its spherical-harmonic components and taking into account only the spherically symmetric ($s$-state) part:

$$\varphi^\mathrm{t}_{\nu\sigma}(\mathbf{r}) = C_\sigma \frac{e^{-\kappa_\sigma|\mathbf{r}-\mathbf{R}_\mathrm{t}|}}{\kappa_\sigma|\mathbf{r}-\mathbf{R}_\mathrm{t}|}, \tag{2.113}$$

where $\sigma = \uparrow, \downarrow$ denotes the spin index, and $\mathbf{R}_\mathrm{t}$ is the position of the tip apex atom. We assume that the spin-up and spin-down $s$-wave states can be characterized by the same decay constant $\kappa = \kappa_\sigma$ and the same normalization coefficient $C = C_\sigma$. The tunneling matrix can be expressed as:

$$M_{\mu\nu}(\mathbf{R}_\mathrm{t}) = -\frac{2\pi C}{\kappa} \begin{pmatrix} \varphi^\mathrm{s}_{\mu\uparrow}(\mathbf{R}_\mathrm{t})\cos(\frac{\theta(\mathbf{R}_\mathrm{t})}{2}) & \varphi^\mathrm{s}_{\mu\downarrow}(\mathbf{R}_\mathrm{t})\sin(\frac{\theta(\mathbf{R}_\mathrm{t})}{2}) \\ \mathrm{i}\varphi^\mathrm{s}_{\mu\uparrow}(\mathbf{R}_\mathrm{t})\sin(\frac{\theta(\mathbf{R}_\mathrm{t})}{2}) & -\mathrm{i}\varphi^\mathrm{s}_{\mu\downarrow}(\mathbf{R}_\mathrm{t})\cos(\frac{\theta(\mathbf{R}_\mathrm{t})}{2}) \end{pmatrix}, \tag{2.114}$$

where $\theta(\mathbf{R}_\mathrm{t})$ denotes the angle between the magnetization direction of the tip and the sample at $\mathbf{R}_\mathrm{t}$. Inserting the matrix elements of Eq. (2.114) into Eq. (2.108) leads to:

$$\begin{aligned} I(\mathbf{R}_\mathrm{t}, V_\mathrm{bias}) &= I_0(\mathbf{R}_\mathrm{t}, V_\mathrm{bias}) + I_M(\mathbf{R}_\mathrm{t}, V_\mathrm{bias}, \theta(\mathbf{R}_\mathrm{t})) \\ &= \frac{4\pi^3 C^2}{\kappa^2} \int dE g_v(E)[n^\mathrm{t}(E - eV_\mathrm{bias})n^\mathrm{s}(\mathbf{R}_\mathrm{t}, E) + \mathbf{m}^\mathrm{t}(E - eV_\mathrm{bias}) \cdot \mathbf{m}^\mathrm{s}(\mathbf{R}_\mathrm{t}, E)]. \end{aligned} \tag{2.115}$$

Here, $g_v(E) = f(E - E_\mathrm{F}) - f(E - E_\mathrm{F} - eV_\mathrm{bias})$ and we have introduced the local magnetization

density of the surface states:

$$\mathbf{m}^{\mathrm{s}}(\mathbf{R}_{\mathrm{t}}, E) = \sum_{\mu} \delta(E - \epsilon_{\mu}) \Psi_{\mu}^{\mathrm{s}\dagger}(\mathbf{R}_{\mathrm{t}}) \boldsymbol{\sigma} \Psi_{\mu}^{\mathrm{s}}(\mathbf{R}_{\mathrm{t}}). \tag{2.116}$$

Analogously, the LDOS of the sample $n^{\mathrm{s}}(\mathbf{R}_{\mathrm{t}}, E)$ is defined by Eq. (2.116), replacing the Pauli's spin matrix $\boldsymbol{\sigma}$ by the unit matrix. $n^{\mathrm{t}}(E)$ and $\mathbf{m}^{\mathrm{t}}(E)$ are the energy-dependent DOS and magnetic DOS of the tip, defined as:

$$n^{\mathrm{t}}(E) = n_{\uparrow}^{\mathrm{t}}(E) + n_{\downarrow}^{\mathrm{t}}(E) \tag{2.117}$$

and

$$\mathbf{m}^{\mathrm{t}}(E) = \mathbf{e}_{M}^{\mathrm{t}}(n_{\uparrow}^{\mathrm{t}}(E) - n_{\downarrow}^{\mathrm{t}}(E)). \tag{2.118}$$

Eq. (2.115) states that the tunneling current can be separated into a nonmagnetic part $I_0$ that depends on the LDOS of the sample at the position of the tip apex $\mathbf{R}_{\mathrm{t}}$ and a spin-polarized contribution $I_M$ given by the projection of the local magnetization DOS of the surface onto the magnetization direction of the tip [123]. The spin-polarized STM thus images the local degree of spin polarization at the position of tip apex, a result analogous to that by Tersoff and Hamann for normal STM.

When the tip and the surface are collinear magnets, Eq. (2.115) can be simplified to:

$$I(\theta, \mathbf{R}_{\mathrm{t}}, V_{\mathrm{bias}}) \propto \int dE g_v(E) [n^{\mathrm{t}}(E - eV_{\mathrm{bias}}) n^{\mathrm{s}}(\mathbf{R}_{\mathrm{t}}, E) + m^{\mathrm{t}}(E - eV_{\mathrm{bias}}) m^{\mathrm{s}}(\mathbf{R}_{\mathrm{t}}, E) \cos(\theta)]. \tag{2.119}$$

Here, $\theta(\mathbf{R}_{\mathrm{t}}) = \mathrm{const}$ is the angle between the magnetization axis of the tip $\mathbf{e}_{M}^{\mathrm{t}}$ and that of the surface $\mathbf{e}_{M}^{\mathrm{s}}$. Surface LDOS and local magnetization DOS are obtained from the spin-up and spin-down constituents as:

$$n^{\mathrm{s}}(\mathbf{R}_{\mathrm{t}}, E) = n_{\uparrow}^{\mathrm{s}}(\mathbf{R}_{\mathrm{t}}, E) + n_{\downarrow}^{\mathrm{s}}(\mathbf{R}_{\mathrm{t}}, E), \tag{2.120}$$

and

$$\mathbf{m}^{\mathrm{s}}(\mathbf{R}_{\mathrm{t}}, E) = \mathbf{e}_{M}^{\mathrm{s}}(n_{\uparrow}^{\mathrm{s}}(\mathbf{R}_{\mathrm{t}}, E) - n_{\downarrow}^{\mathrm{s}}(\mathbf{R}_{\mathrm{t}}, E)), \tag{2.121}$$

where the surface LDOS of the spin-up or spin-down character is defined as:

$$n_{\sigma}^{\mathrm{s}}(\mathbf{R}_{\mathrm{t}}, E) = \sum_{\mu} \delta(E - \epsilon_{\mu\sigma}) \psi_{\mu\sigma}^{\mathrm{s}\dagger}(\mathbf{R}_{\mathrm{t}}) \psi_{\mu\sigma}^{\mathrm{s}}(\mathbf{R}_{\mathrm{t}}). \tag{2.122}$$

# Chapter 3

# Probing the dynamics of bulk electrons with STM

An in-depth understanding of the surface properties is a key for successful evolution of the modern technology based on the condensed matter physics. The surface properties, that include various contributions including atomic, electronic, magnetic and vibronic parts, are crucial for, e.g., construction of the effective state-of-the-art catalysts, or in development of the electronic technology with ambition to bring the devices onto atomic scale, i.e. to regime when devices would consist of several tens or even single atoms. Clearly, an unambiguous understanding and control over electronic properties of such nanosize devices and objects is crucial. Since the nanosized objects of interest conventionally rest on a surface, they are necessarily electronically coupled to it. It is equally essential, therefore, to study both the properties of such objects and the properties of the surface on which the object resides. In turn, since the surface is also coupled to the bulk of the substrate that supports the surface, an accurate characterization of surface properties should include properties of both the surface and the bulk electrons.

STM is an indispensable experimental tool to study properties of the surfaces, including the corresponding electronic structure, *locally*, i.e. with spatial resolution of several Angström (see Sec. 3.1). So far, however, most STM studies on the surface electronic structure conceal the effect of bulk electrons, interpreting the measured STM images in terms of the surface electrons only.

Recently, the dispersion of surface electrons was studied in a set of Fourier-Transformed STM (FT-STM) experiments performed on terraced noble metal (Ag(110)) surfaces (Sec. 3.3). The experimental images showed presence of a weak signal, that behaves like a two-dimensional surface state, but is located at the edge of the projected bulk bands (BBE), where no surface states exist. The origin of this signal was not well understood, but it may be assumed that it appears due to the bulk electrons. In this case, it would be for the first time shown, that the range of the surface properties accessible by STM can be extended to the *local* dynamic properties of the bulk electrons

(their dispersion). However, the assumption regarding the origin of the detected surface-state-like signal must be verified, and an in-depth understanding of the experimental FT-STM images should be given.

Therefore, a detailed and accurate *ab initio* description of the FT-STM experiments on Ag(110) has been performed and is presented in this chapter. The theoretical analysis allowed for the first time an unambiguous proof to understand whether and why STM can be used to probe the dynamics of bulk electrons.

The chapter is organized as follows: in Sec. 3.1 a brief introduction into the current state of the STS and FT-STM are given. The few STM studies addressing the contribution of bulk states to STM are discussed in Sec. 3.2. The main outcome of recent FT-STM experiments on terraced Ag(110) surfaces that have stimulated the present theoretical research is discussed in Sec. 3.3. In Secs. 3.4-3.5 the theoretical approach for evaluating FT-STM spectra and theoretical results are presented. Conclusions and a summary of the chapter are given in Sec. 3.6.

## 3.1 Introduction into spectroscopic mode of the STM

Topographic images obtained in STM commonly depend on the tip-sample bias voltage (see, e.g. Eqs. (2.98), (2.104)). An analysis of this dependence allows to obtain spectroscopic information with atomic spatial resolution [124]. As a consequence, an increasing number of topographic STM studies are combined with scanning tunneling spectroscopy (STS) experiments, that directly measure the relation between the tunneling current and the bias voltage.

In these experiments, the current feedback loop is disengaged in order to keep the tip-sample separation fixed, and the STM tip is positioned at a known point above the surface. Using this technique, Hamers and Köhler [125] have measured the local electronic properties of atomic-sized defects on the Si(001) surface (Fig. 3.1). Feenstra *et al.* [126] have reported a similar $I(V)$ spectrum on Si(111) 2x1 surfaces, where the measured $I(V)$ spectrum showed a decrease of the surface band gap. This result allowed to deduce disorder-related surface states. Fuhr *et al.* [127] theoretically analyzed several surface point defects on $MoS_2(0001)$ surfaces. Based on these calculations they showed that different point defects result in unique $I(V)$ spectra; these spectra can therefore be used as chemical signatures of the surface point defects.

The theoretical interpretation of nearly all STS experiments is based on the transfer-Hamiltonian approach to STM (Secs. 2.6.1-2.6.2). According to this approach, the tunneling current is proportional to the *energy-integrated* surface local density of states (LDOS):

$$I(V_{\rm bias}) \sim \overline{n}^{\rm s}(\mathbf{R}_{\rm t}, V_{\rm bias}) = \int dE n^{\rm s}(\mathbf{R}_{\rm t}, E). \tag{3.1}$$

Here, the integral sweeps over all energies between the Fermi level at the surface $E_{\rm Fermi}$ and $E_{\rm Fermi} + eV_{\rm bias}$. Except for low bias voltages, therefore, measurements of the tunneling current $I(V)$ do not

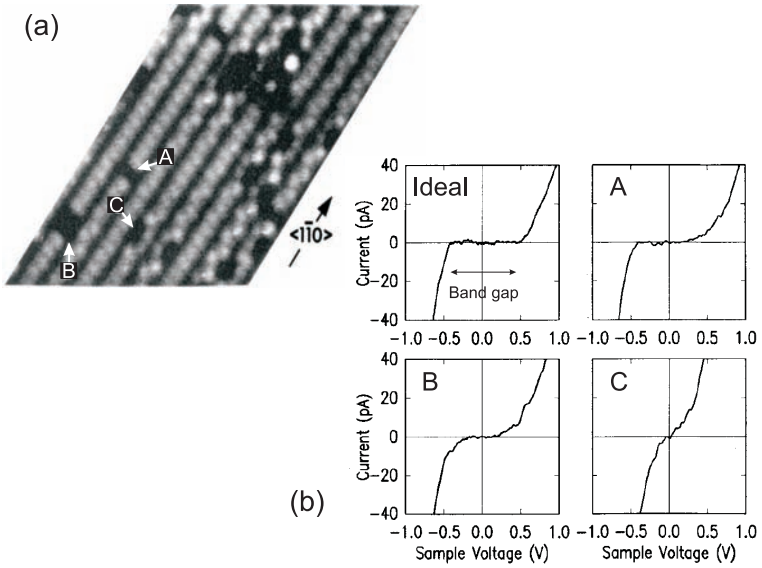


Figure 3.1: Surface band gap measured with STS. (a) Atomically resolved topographic STM image of a Si(001) surface. Different types of surface defects can be seen. (b) Tunneling $I(V)$ curves measured at an ideal surface, a type A single dimer vacancy, a type B double dimer vacancy, and a type C defect. The flat part in the I-V spectra indicates the surface band gap. Adapted from Hamers and Köhler [125].

allow to get *explicit energy-resolved* surface electronic properties as given by the surface LDOS. This severely limits the capability of the method. In fact, very limited number of STS studies are exclusively based on the $I(V)$ spectra.

In order to overcome the aforementioned deficiency, the $I(V)$ spectra are commonly supplemented by measurements of the differential tunneling conductivity $\frac{dI(V)}{dV}$, that is *roughly* proportional to the surface LDOS at the energy $E_{\mathrm{Fermi}} + eV_{\mathrm{bias}}$ (see Sec. 3.4.1):

$$\frac{dI(\mathbf{R}_{\mathrm{t}}, V_{\mathrm{bias}})}{dV_{\mathrm{bias}}} \sim n^{\mathrm{s}}(\mathbf{R}_{\mathrm{t}}, E_{\mathrm{Fermi}} + eV_{\mathrm{bias}}). \tag{3.2}$$

A $dI/dV$ spectrum can be produced either by a numerical differentiation of the measured $I(V)$ signal [128], or by direct measurements as first proposed by Binnig and Rohrer [129, 130]. In a direct measurement a small voltage oscillating with low frequency (in the range of kHz) is added on top of the constant bias voltage. The frequency of the modulation is chosen high enough to keep the tip-sample separation constant. The amplitude of the first harmonic in the resulting response modulation of the tunneling current is proportional to $dI/dV\ |_{V=V_{\mathrm{bias}}}$ and is detected with a lock-in amplification technique [4, 129–132]. It is noteworthy, that in the case of direct measurements of $dI(V)/dV$ a feedback loop can be engaged, and the differential conductance can be measured in the constant-current mode.

Measuring the dependence of $dI/dV$ versus the bias voltage became a powerful and widespread tool to characterize local energy-resolved electronic properties on both semiconducting and metallic surfaces. Becker *et al.* [131] applied this technique to the Si(111) 7x7 surface, and observed a structure in the differential conductance spectra associated with the surface states. Based on these measurements the energy difference between the surface states in the faulted and unfaulted parts of the Si(111)7x7 surface could be obtained. Similar studies on the Au(111) surface state have

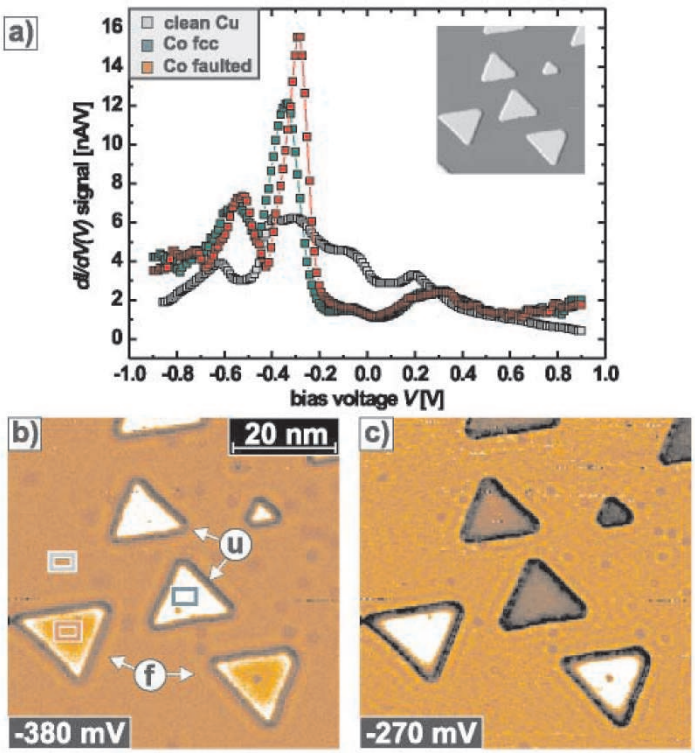


Figure 3.2: Resolution of two different types of Co-island on a Cu(111) surface obtained with STS. (a) $dI/dV$ tunneling spectra, (b)-(c) $dI/dV$ maps at voltages as indicated. The curves were averaged in the colored boxes in (b), the island types are labeled $u$ (unfaulted) and $f$ (faulted). Spectra of the two island types differ in peak energetic positions and intensities. At the voltages of maps (b)-(c), the contrasts are maximal. Inset in (a): Topographic image. After Pietzsch *et al.* [142].

been performed by Everson *et al.* [133]. These authors detected a variation in the surface state properties due to different surface potentials of the clean surface, of the monoatomic step, and of the $23 \times \sqrt{3}$ reconstructed surface. Yazdani *et al.* [134] employed low temperature STS to probe the local effects of isolated magnetic adatoms on the electronic properties of the surface of a Nb(110) superconductor.

During the last decades the STS technique has been extended, e.g., to get chemical signatures of surface point defects [127], resolve and discriminate between different surface structures [135, 136], to access dynamical properties of surface states such as their lifetimes [137, 138], and to analyze the defect induced surface electronic states [139]. By magnetizing the STM tip, STS allows to study the magnetoresistance of the tunneling junctions [140], and to characterize magnetic islands on metal surfaces [141, 142].

A work of Pietzsch and Wiesendanger [142] provides a nice example, how this technique can be used to to distinguish between two different types of triangular Co islands on a Cu(111) substrate by comparing corresponding STS spectra. Examples of their STS images are shown on Fig. 3.2. A comparison between measured $dI/dV$ spectra measured employing nonmagnetic and magnetic tips allowed to separate magnetic and structural effects, and to deduce magnetic structure and properties of the Co-islands.

A shortcoming of STM and spatially-resolved STS experiments is their inability to access a quasiparticle $\mathbf{k}_{||}$-wavevector information of the surface electrons, and thus to obtain their dispersion

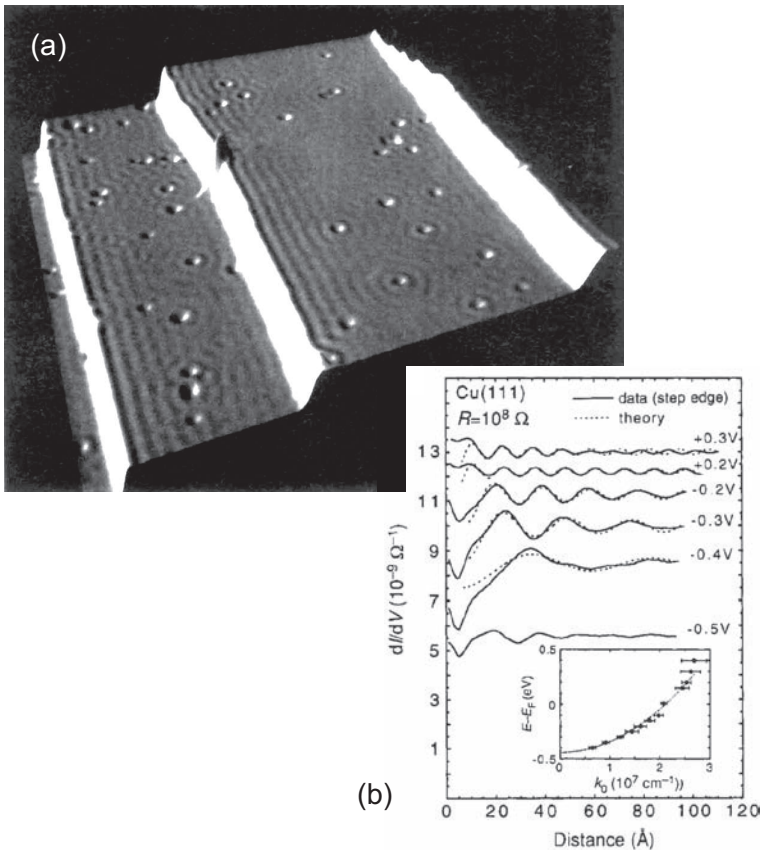


Figure 3.3: Measurements of the Cu(111) surface state dispersion obtained with the FT-STM technique. (a) Constant-current image of the Cu(111) surface. Three monoatomic steps and about 50 point defects are visible. Spatial standing electron wave patterns with a wavelength of $\sim$ 15 Å are clearly evident. (b) Solid lines: spatial dependence of $dI/dV$ standing waves, measured as a function of distance (along the upper terrace) from the step edge at different bias voltages. The inset shows the surface state dispersion obtained from the standing wave periodicity via Fourier transformation. Adapted from Crommie *et al.* [5].

relations [143]. This is due to a cancelation of the exponential prefactor $e^{i\mathbf{k}_{||}\mathbf{r}}$, that accounts for $\mathbf{k}_{||}$ dependence, when an electron $\psi_{\mathbf{k}_{||},\epsilon}(\mathbf{r}) = u_{\mathbf{k}_{||},\epsilon}(\mathbf{r}) \cdot e^{i\mathbf{k}\mathbf{r}}$ is traveling on the defect-free surface. The resulting charge density $|\psi_{\mathbf{k}_{||},\epsilon}(\mathbf{r})|^2 = |u_{\mathbf{k}_{||},\epsilon}(\mathbf{r})|^2$ lacks an explicit $\mathbf{k}_{||}$ dependency, and contains the lattice periodic part $u_{\mathbf{k}_{||},\epsilon}(\mathbf{r})$ only.

A decade ago, the pioneering work of Crommie [5] and Avouris [144, 145] resulted in a Fourier transformed STM (FT-STM), a technique that overcomes the above mentioned deficiencies of local STS and STM. FT-STM provides experimental access to the $\mathbf{k}_{||}$-dependence of surface electrons by recording $dI/dV$ standing wave patterns induced by an electronic screening of surface perturbations. Such perturbations can be created by, e.g., surface point defects [145–149], single [5, 18, 132, 144, 145, 150–155] or double [155–157] steps, artificially created quantum corrals [6, 7, 158], or subsurface defects [159]. Since oscillations in the $dI/dV$ are proportional to the corresponding oscillations in the surface LDOS (see Eq. (3.2)), the measured patterns can be explained by the dynamics of the surface electrons. When the electrons scatter from impurities, they interfere with themselves, creating a quantum-mechanical interference pattern in the form of a standing wave (see, e.g., Refs. [5, 132, 155, 157, 160]). The periodicity of the created pattern is entrained by $\mathbf{k}_{||}$ of the incoming and back-scattered electron, and can be extracted from the real-space image by Fourier transformation (see Sec. 3.4.1 and references therein).

On Fig. 3.3(a) we show electron standing waves created on terraced Cu(111) surfaces, as reported by Crommie and co-workers [5]. The periodicity of the pattern has been measured as a function of the applied bias voltage (Fig. 3.3(b)). The dispersion of the Cu(111) surface state, that is responsible for the observed oscillations, has been derived from corresponding real-space profiles (Fig. 3.3(b), inset). Since its introduction, FT-STM has been successfully applied to analyze a wide range of surface state related properties such as their lifetimes and dispersion with high accuracy. Jeandupeux and Bürgi [151–153] have measured the *local* dispersion of the surface states on Ag(111) and Cu(111) surfaces. They have performed a careful analysis of standing waves on these surfaces, and suggested a direct approach for the determination of the elastic and inelastic (via electron-electron and electron-phonon interactions) lifetimes. Similar studies on silver low-index surfaces have been reported by Vitali *et al.* [154], Li *et al.* [150] and Pascual *et al.* [132]. Hansmann and co-workers [157] have reported a local change in the dimensionality of the surface states on vicinal Cu(111) surfaces due to a local confinement to (111) terraces.

To summarize, over the last decades FT-STM has developed into unique experimental tool that allows to probe *spatially localized* surface electronic properties with high energy and wavevector resolution.

## 3.2 Bulk electronic properties measured with FT-STM

Although STM is intrinsically a surface technique, in some cases it is capable to explore properties of the underlying bulk electrons. The contribution of bulk states and thus the bulk band structure was discussed mostly for semiconductors, especially III/V compounds and superconductors [161].

In contrast to the situation in semiconductors, most of the STS experiments on metal surfaces have been explained in terms of the Shockley-like surface states, that dominate tunneling. Only a very limited number of studies demonstrated that the bulk electrons may significantly affect the tunneling on metal surfaces [162–165]. In the late eighties Kaiser and Jaklevic [164] have reported STS spectra on Au(111) and Pd(111) surfaces. Their spectroscopic data showed the presence not only of surface states, but also of bulk electrons. This has later been confirmed in a theoretical analysis of STS in the case of Pd(111) surfaces by Drakova and Doyen [162, 163]. Due to the absence of surface states and surface resonance states on Nb(110) surfaces, Koslowski *et al.* [165] were able to extract prominent features of the Nb bulk band structure, in excellent agreement with theory and photoemission spectroscopy.

Similar to STS, FT-STM experiments on metal surfaces have been almost exclusively focused on the dynamics of surface states (see Sec. 3.1 and references therein). There are two exceptions, namely studies by Petersen *et al.* [147, 166] and Hansen *et al.* [160], who discussed the possible contribution of bulk electrons in the case of Au(111), Cu(111) and NiAl(110) surfaces. In the late nineties, Petersen and co-workers [166] have employed FT-STM to obtain information on the role

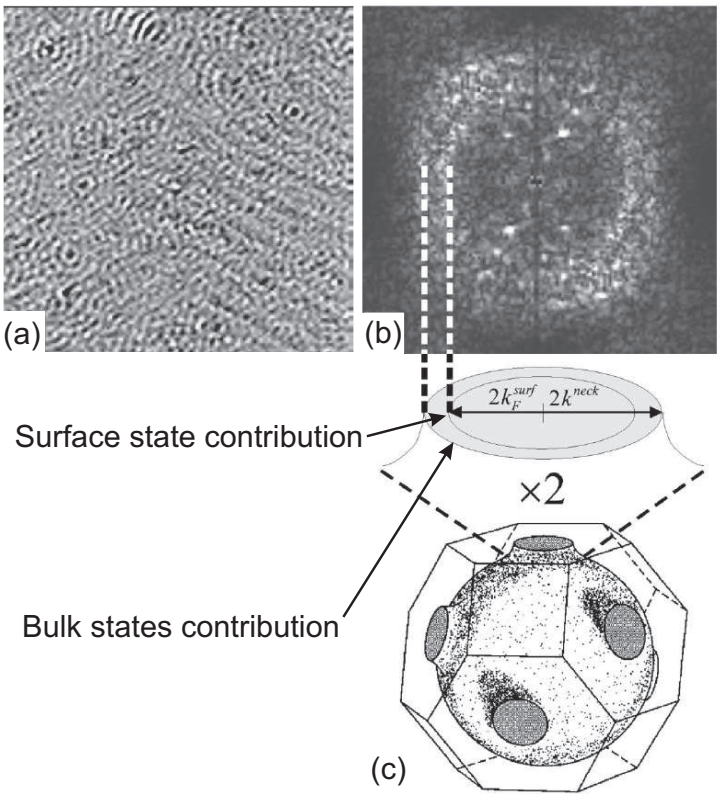


Figure 3.4: Contribution of bulk electrons to a FT-STM spectrum on Cu(111) surfaces. (a) The STM image of Au(111) had been acquired at low bias voltage and temperature $\sim 140$ K. Standing waves are visible. (b) Power spectrum of the Fourier transform of Fig. 3.4(a). Two concentric circles are visible. (c) Illustration of the origin of the two concentric circles seen in Fig. 3.4(b). Adapted from Petersen *et al.* [166].

of surface states versus bulk states in the screening of defects and step edges at the close-packed Cu and Au surfaces. The experiments were performed at extremely small bias voltages ($\sim 1$ mV), i.e. yield information on the Fermi surface of the bulk and the Fermi contour of the surface states (see e.g. Eq. (3.2)). These results showed that bulk electrons substantially contribute to the standing wave pattern formed on Au(111) and Cu(111) surfaces. From the pattern measured in the vicinity of defects the corresponding Fourier-transformed power spectrum was obtained. The spectrum revealed the presence of the edge, or 'neck', of the bulk Fermi surface, as shown on Fig. 3.4. From the radius of this neck on Fig. 3.4(b) the corresponding wavevector $k_{\mathrm{neck}} = 0.21 \pm 0.01$ Å$^{-1}$ has been obtained, which is in very good agreement with measurements of the bulk neck radius utilizing de Haas-van Alphen and magnetoacoustic effects. A similar set of experiments, but on NiAl(110) surfaces, have been performed three years later by Hansen *et al.* [160], yielding similar conclusions.

It is striking, that while the continuum of bulk electrons should contribute to the tunneling, the measured signal stems only from the edge of the bulk Fermi surface, as shown on Figs. 3.4(b-c) and 3.5. This phenomenon has been explained by Petersen [166] on the basis of the free-electron model as follows.

Let the surface wavefunctions be of the form:

$$\psi = u_{\mathbf{q}}(\mathbf{r}_{||}) \exp(-\sqrt{\alpha^2 + q^2} z), \tag{3.3}$$

where $z$ is the distance above the surface, $\mathbf{q} = \mathbf{k}_{||}$ is the component of the wavevector parallel to the surface, $u_{\mathbf{q}}(\mathbf{r}_{||})$ is the in-plane part of the wavefunction, and $\alpha^2 = 2m\phi$ with $\phi$ being the surface work function.

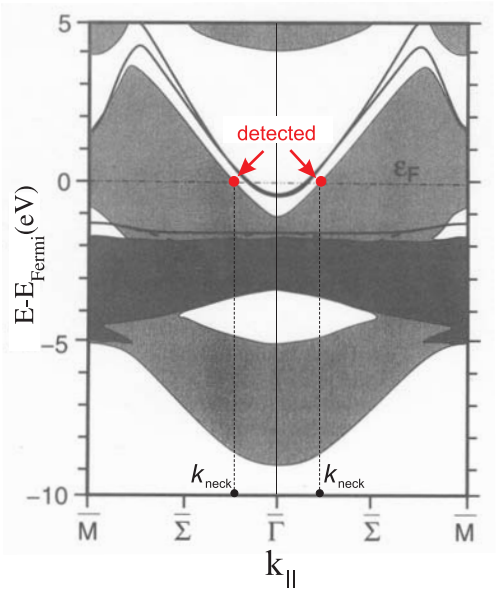


Figure 3.5: *Ab initio* surface band structure of a Cu(111) surface. Arrows indicate bulk electron states that have been detected in experiment (see Fig. 3.4(b)). The horizontal dashed line indicates the continuum of bulk electron states that contribute to the tunneling current. Image from Ref. [46].

with wavevector $k_{\text{neck}}$.

For a free-electron like bulk state, $q$ lies in the range from 0 to $k_E = \sqrt{2mE}$, since the dispersion is given by $E(k) = (q^2 + k_\perp^2)/2m$. Thus, to find the bulk contribution to the surface LDOS, one has to sum over all $q$ belonging to the energy $E$:

$$n(E, \mathbf{r}) \propto \int_0^{2\pi} \int_{k_0}^{k_E} |u_{\mathbf{q}}|^2 \exp(-2\sqrt{\alpha^2 + q^2}z) q \, dq \, d\theta. \tag{3.4}$$

For simplicity, the realistic bulk Fermi surface of Au and Cu (Fig. 3.4(c)), is modeled as a sphere with a hole in the top and the bottom. Hence, the lower integration limit $k_0$ is equal to the hole radius $k_{\text{neck}}$ (in the case of a free-electron sphere $k_0 = 0$).

The damping of the wave components with values $q$ other than $q = k_{\text{neck}}$ is explained employing Eq. (3.4) and the following arguments: (i) at the edge of the bulk bands, the sharp cutoff of the continuum of wavevectors may lead to weak net oscillations with wavevectors $k_{\text{neck}}$ and $k_E$ for $z = 0$, i.e. at the surface. (ii) Outside the surface, i.e. for $z > 0$, the exponential term in Eq. (3.4) suppresses the contribution from larger wavevectors, and the only oscillation that survives is the one with the smallest $q$, i.e. the one stemming from the bulk band edge

## 3.3 Motivation for FT-STM theory

Recently, Pascual and co-workers [132, 155, 167] have applied the FT-STM technique to study the dynamics of electrons on the terraced Ag(110) surface. An ultrahigh vacuum scanning tunneling microscope was employed at liquid helium temperature. Using lock-in amplification techniques, the tunneling differential conductivity $dI/dV$ pattern (that is correlated to the surface LDOS as discussed in Sec. 3.4.1) has been recorded at different bias voltages and distances from the terrace

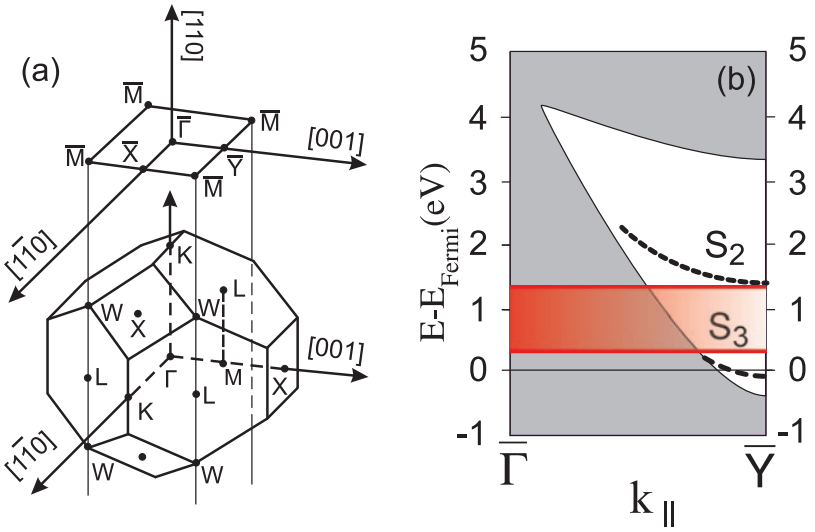


Figure 3.6: (a) Brillouin zone of a face-centered cubic crystal and its projection onto the (110) plane. (b) Surface band structure of a Ag(110) surface (only the energy- and $\mathbf{k}_{||}$-range relevant to interpret the FT-STM experiments of Pascual *et al.* [155] are shown), extracted from Refs. [132, 168–170]. In the pocket in the projected bulk band structure two surface states labeled as $S_2$ and $S_3$ exist. The red-shaded region indicates the energy window where the signal, which is located in the vicinity of the projected bulk band edge, has been probed by STM (see Figs. 3.7-3.8).

edges. The monoatomic terrace edges were oriented along [010] crystallographic axis, resulting in electron standing waves along [001] direction. The measurements were performed on a wide terrace (with width $> 150$ Å), which is sufficiently large to exclude interactions between the steps confining the terrace. In contrast to previous studies a wide range of energies between $-0.1$ eV up to $+4.5$ eV (vacuum level) relative to the Fermi level $E_{\text{Fermi}}$ has been explored.

The electronic properties of an Ag(110) surface in the range of energies and wavevectors relevant to the FT-STM are well known from angle-resolved photoemission [169–171] and *ab initio* [168] studies (Fig. 3.6). The surface-projected bulk bands form a continuum of energy states, with exception for a states-free pocket, that is centered on the edge of the surface Brillouin zone. The pocket supports two Shockley-like surface states, namely, an unoccupied surface state $S_2$, and a partially occupied surface state $S_3$. These states are located above $E_{\text{Fermi}} + 1.7$ eV and below $E_{\text{Fermi}} + 0.2$ eV respectively.

In his first study, Pascual *et al.* [132] focused on the energies above $E_{\text{Fermi}} + 1.7$ eV, that are specific for the $S_2$ surface state. Similar to previous studies (see Sec. 3.1), it has been shown that the tunneling in this energy range is dominated by the surface state. The topology of the $S_2$ state in the reciprocal space has been examined, showing unique capabilities of FT-STM to resolve surface state dynamics at energies up to the vacuum level and for wavevectors in the entire Brillouin zone. The reconstructed dispersion of the $S_2$ state is shown, e.g., on Fig. 3.7(a).

In a later study Pascual *et al.* [155] reported the unexpected presence of a weak standing wave pattern below the energy offset of $S_2$ state, as shown on Fig. 3.7(c)-(d). The measured pattern is

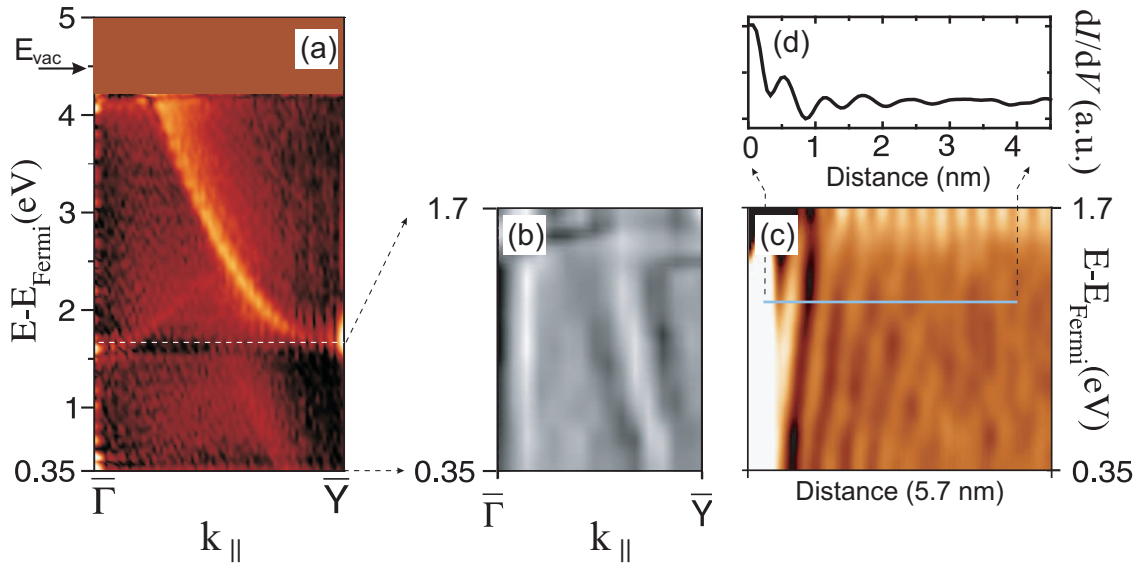


Figure 3.7: (a) Energy-resolved FT-STM spectrum of a Ag(110) surface acquired on a 150 Å wide terrace. The strong increase of the signal at $E = E_{\text{Fermi}} + 1.7$ eV is due to the onset of the Ag(110) surface state [132]. (b) Same as (a), but zoomed to the energy range below the surface state ($E_{\text{Fermi}} + 0.35$ eV, $E_{\text{Fermi}} + 1.70$ eV) (c) Real-space $dI/dV$ map corresponding to (b). The map is from the region close to a step (bright feature left) and is a function of the energy and the distance along the [001] direction. The oscillations disperse as the energy is increased. (d) The $dI/dV$ profile along the line shown in (c). Adapted from Refs. [155, 167].

energy-dependent, and disappears at energies below $E_{\text{Fermi}}+0.35$ eV. The corresponding dispersion of these electron waves in the reciprocal space is shown on Fig. 3.7(a)-(b). From the $k_{||}$-space profiles it is obvious, that the measured standing waves are created by electrons located in the vicinity of the projected bulk band edge (compare Fig. 3.7(a)-(b) and Fig. 3.6). Hence, the detected contribution to the FT-STM spectrum strongly resembles the dispersion of a, albeit weak, surface state, that essentially coincides with the edge of the projected bulk band structure (BBE).

Since the measured signal is located on top of the BBE, it is tempting to ascribe this contribution to the bulk electrons. However, due to the lower-lying surface state $S_3$, an alternative explanation exists: although, according to inverse-photoemission studies [170], $S_3$ crosses the BBE at the energy $E_{\text{Fermi}} + 0.2$ eV, an associated surface resonance may exist above this energy. Due to similar dispersion properties of the BBE and $S_3$, the surface resonance should essentially coincide with reciprocal space topology of the BBE. Similar to a surface state, the resonance electrons can scatter on surface imperfections, and become detectable by the STM tip. Since the surface resonances are less surface localized compared to surface states, they do not penetrate far into vacuum. This would explain the small magnitude of the measured signal.

However, if the measured contribution is due to a surface resonance, there should be a smooth transition from the resonance state to the corresponding $S_3$ surface state when decreasing the bias

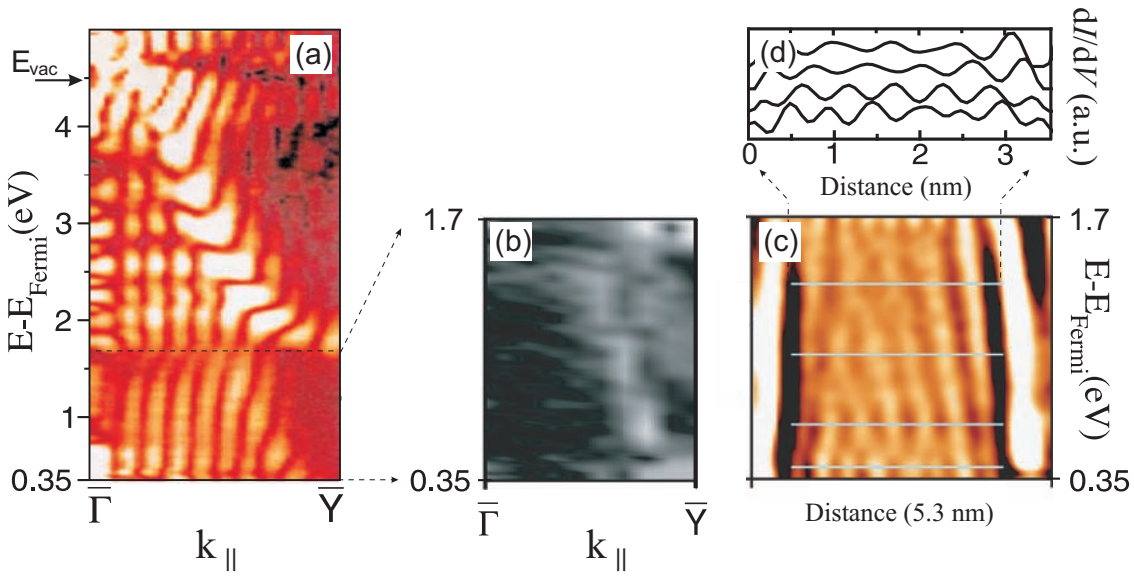


Figure 3.8: (a) Energy-resolved FT-STM spectrum of a Ag(110) surface acquired on a 36 Å wide terrace. (b) Same as (a), but zoomed to an energy range ($E_{\text{Fermi}} + 0.35$ eV, $E_{\text{Fermi}} + 1.70$ eV) with a better contrast. The signal located on top of the bulk band edge appears discretized due to quantum confinement. (c) $dI/dV$ signal as a function of energy and real-space position along the [001] direction, corresponding to (b). Two monoatomic steps appear as bright features left and right. (d) $dI/dV$ profiles along constant-energy lines shown on (c). The lines correspond to those energy values where the oscillations amplitude is larger. A decreasing integer number of nodes is found. Adapted from Refs. [155, 167].

voltage. In contrast, the measured signal vanishes below $E_{\text{Fermi}} + 0.35$ eV. The $S_3$ state shows up again 0.1 eV lower, i.e. at $E_{\text{Fermi}} + 0.25$ eV [167]. The presence of the energy gap between the $S_3$ state and the measured signal may indicate their different origin. The weak signal measured in the energy range ($E_{\text{Fermi}} + 0.35$ eV, $E_{\text{Fermi}} + 1.70$ eV) may therefore be associated with a scattering of bulk electrons on the surface. This would be the first time that the topology of the projected bulk band edge has been detected by STM.

However, assuming that that these oscillations are due to the bulk electrons, their origin is not clear. According to Petersen (see Sec. 3.2), qualitatively this effect could be accounted by a sharp cutoff of the continuum of wavevectors, that can lead to a weak oscillation with wavevector $k_{\text{BBE}}(E)$ around the scattering centers.

To verify the role of the above reasonings, the FT-STM experiments have been repeated on small confined terraces, with terrace width $\sim 36$ Å. The results are shown on Fig. 3.8.

At such small terraces, the surface electronic states may become localized, as they are confined on both sides by monoatomic steps. This gives rise to standing waves patterns with the characteristics of a particle-in-a-box behavior [156]. The patterns appear only at discrete energies, those at which the state's wavelength is commensurate with the length of the confined region. For the

case of bulk states, their surface-projected components might also be confined at small terraces. Since the surface-projected band consists of a continuous range of wavevectors, several of these may simultaneously fulfill the terrace boundary conditions, resulting in oscillations composed of a discrete number of overlapping standing waves at a certain energy, each associated with one of the harmonics fitting into the terrace resonator. Moreover, since the bulk band is now discrete due to confinement, the sharp cutoff at the BBE should not enhance the weight of the edge bulk electrons in the resulting standing wave pattern.

From Fig. 3.8(c)-(d), however, the single wavelength $dI/dV$ oscillations are found evolving with energy with discrete changes in the number of nodes. The corresponding Fourier map (Fig. 3.8(b)) reveals the shape of the standing waves in the reciprocal space. Again, similar to an one-side confined terrace, the signal is located on top of the projected bulk band edge, that appears discretized because of the confinement on the terrace. This reveals a more subtle origin for the enhancement of the $dI/dV$ oscillations in the vicinity of the BBE, rather than a sharp cutoff of the continuum bands at the edge of the projected bulk bands.

From the experiments we may conclude, that if the signal located at the BBE has a bulk origin, the edge of the projected bulk bands has an enhanced weight at the surface over the rest of the bulk states. This behavior is especially pronounced on the Ag(110) surface, where the band-edge states have *the largest* wavevector $\mathbf{k}_{||}$, i.e. possess the fastest decay into the vacuum (see Eq. (3.4)). This is in contrast to arguments of Peterson *et al.*, described in Sec. 3.2, where the enhancement of the band-edge states was ascribed to the slowest decay of the edge states due to *the smallest* value of wavevectors $\mathbf{k}_{||}$ there.

In summary, it has been recently shown in the experimental FT-STM study, that at the metal surface a weak signal behaving like a two-dimensional surface state is detected in the energy window separating the two surface states. The reciprocal space topology of the detected signal coincides with that of the projected bulk band edge. This might indicate, that it is possible to probe dynamical properties of bulk states with STM. However, the origin of the detected signal was unclear: it could be related solely to the bulk electrons, or appear due to the surface resonance. In case when the signal is a bulk-driven feature, enhancement of the edge bulk states is unclear: as pointed out above none of the previously proposed model is able to consistently explain the FT-STM data on the Ag(110) surface. Therefore, a detailed and accurate *ab initio* description of the FT-STM experiments on Ag(110) is required to understand (i) whether the measured $dI/dV$ oscillations are due to the bulk electrons, or occur due to the surface resonance. If the signal has a bulk-origin, the following problems must be solved: (ii) when and how STM can be used to probe the dynamics of bulk electrons and (iii) the superior role of edge-states over the rest of bulk electrons.

## 3.4 Theoretical treatment of the FT-STM measurements

### 3.4.1 FT-STM spectrum in the constant-current regime

The experimental FT-STM maps, like e.g., shown on Figs. 3.7(a) and 3.8(a), are based on an analysis of the bias-dependent oscillations of the $dI/dV$-signal close to scattering centers. At each bias voltage $V$, the FT-STM spectrum quantifies the magnitude of the oscillations with a wavevector $\mathbf{k}$ in the resulting $dI/dV$ standing wave pattern. Therefore, to simulate FT-STM maps it is crucial to correlate the experimentally measured differential junction conductivity $dI/dV$ with tip and surface electronic properties accessible by DFT simulations.

To do so, we start with a high-voltage extension of the Tersoff-Hamann theory (see Sec. 2.6.2 for details) as proposed by Strokbro *et al.* [172]. According to it, the tunneling current, induced by the application of a voltage $V$ between a surface and a $s$-like tip located at the position $\mathbf{R}_\mathrm{t} = (x, y, z)$, can be expressed as:

$$I\left(\mathbf{R}_\mathrm{t}, V\right) \propto \int_0^{eV} dE\, n^\mathrm{s}\left(\mathbf{R}_\mathrm{t}, V, E\right) n^\mathrm{t}\left(V, \pm(E - eV)\right). \tag{3.5}$$

Here the upper sign corresponds to a positive bias ($V > 0$), and lower signs to negative bias voltages ($V < 0$). $n^\mathrm{t}\left(V_\mathrm{bias}, E\right)$ is the tip density of states (DOS) and

$$n^\mathrm{s}\left(\mathbf{r}, V, E\right) = \int d\mathbf{k}_{||} \sum_i |\varphi_{i,\mathbf{k}_{||}}(V, \mathbf{r})|^2 \delta(E - E_\mathrm{Fermi} - \epsilon_{i,\mathbf{k}_{||}}) \tag{3.6}$$

is the surface local density of states (LDOS) at position $\mathbf{r}$ and energy $E$ in the the presence of an applied bias voltage $V$. Integration in Eq. (3.6) is performed over all wavevectors $\mathbf{k}_{||}$ from the first surface Brillouin zone (SBZ). $\varphi_{i,\mathbf{k}_{||}}(V, \mathbf{r})$ are the Bloch wavefunctions and $\epsilon_{i,\mathbf{k}_{||}}$ are the corresponding eigenvalues of a surface in the presence of an applied bias voltage $V$. The energies $E$ in Eq. (3.5) are measured with respect to the corresponding Fermi levels of the tip and of the surface, i.e., $E_\mathrm{Fermi}$ in Eq. (3.6) is the surface Fermi energy. For the further discussion it is assumed that the surface is normal to the $z$ axis and positioned at $z_\mathrm{s} = 0$. $z$ is then the tip-surface separation.

Experimentally, the exact tip properties, especially in the tip-apex region, are unknown entities, and can be even subject to modifications during the scanning process. A widely used approach is to assume the tip density of states $n^\mathrm{t}$ to be constant. Although such a simplifying assumption is not meant to be realistic [173], the agreement between the corresponding theoretical and experimental results is encouraging [111, 132, 150, 173–175].

From Eq. (3.5), neglecting the tip effects, it is straightforward to derive an expression for the tunneling differential conductivity:

$$\frac{dI(\mathbf{R}_\mathrm{t}, V)}{dV} \propto n^\mathrm{s}\left(\mathbf{R}_\mathrm{t}, V, E\right)|_{E=eV} + \int_0^{eV} dE\, \frac{d\, n^\mathrm{s}\left(\mathbf{R}_\mathrm{t}, V, E\right)}{dV}. \tag{3.7}$$

From Eq. (3.7) it is obvious that within the generalized Tersoff-Hamann model for the tunneling

current there is no simple relation between the differential conductivity $dI/dV$ and the surface local density of states $\rho_S$ due to presence of the second term in the expansion [124, 176].

The influence of the second term on the total differential conductivity $dI/dV$ has been discussed in several studies (see e.g. Refs. [111], [174], and [150]). Li and co-workers [150] have applied Eq. (3.7) to describe the electron scattering at steps on Ag(111) surfaces in the case of constant current simulations, and have found a negligible effect of the second term at the considered bias voltages. Hörmandinger [111] has applied a layer-Korringa-Kohn-Rostoker-like approach for the characterization of the surface state dispersion in case of a Cu(111) surface. By modeling surface steps as totally reflecting hard walls he demonstrated that the optimum way to obtain the dispersion relation is by measuring $dI/dV$ at a constant tip height and sufficiently far away from the step edge. These conditions ensure that the second term in Eq. (3.7) contributes to the background signal only, and that the differential conductivity closely resembles the surface LDOS as described by the first term in Eq. (3.7). As has been shown by model calculations of Li *et al.* [174], the second term dominates in the total differential conductivity at negative bias voltages. This effect severely hampers the detection of the occupied surface states. For positive bias voltages, i.e. when probing an unoccupied surface electronic structure, the effect of this term decreases with increasing voltage.

Thus, the second term in Eq. (3.7) can be neglected when the $dI/dV$ measurements are performed in regions away from steps at large positive biases. It is common to neglect the second term even in the vicinity of scatterers and at all biases [5, 6, 132, 134, 135, 145–147, 152, 157, 166, 175, 177]. Employing this assumption leads to excellent agreement of simulated and experimental profiles, indicating that the minor importance of the second term is a general phenomenon. This, together with the fact that our study on Ag(110) is based on large ($> 0.3$ eV) positive biases, allows us to safely drop the second term in Eq. (3.7).

Thus Eq. (3.7) simplifies:

$$\frac{dI(\mathbf{R}_\mathrm{t},\, V)}{dV} \propto n^\mathrm{s}\left(\mathbf{R}_\mathrm{t},\, V,\, E\right)|_{E=eV}. \tag{3.8}$$

From Eq. (3.8) it follows, that the intensity of the $dI/dV$ signal is proportional to the magnitude of the surface LDOS at the tip-apex position $\mathbf{R}_\mathrm{t}$. The standing $dI/dV$ waves, therefore, reflect the corresponding oscillations of the surface LDOS.

Eq. (3.8) has been successfully employed to simulate the electron standing wave patterns in real-space. Comparing the theoretical patterns with corresponding experimental ones it becomes possible to obtain, e.g., lifetimes of surface states [158], or to study scattering properties of steps [175] or ad-atoms from artificially created enclosed ad-atom structures (surface-corals).

Based on Eq. (3.8), FT-STM maps could be in principle simulated by fully reproducing the atomic structure (including steps or other scatterers). However, a quick estimate shows that this is computationally not feasible: the length of the surface terraces used in experiments (Sec. 3.3) is between 36 Å and more than 150 Å.

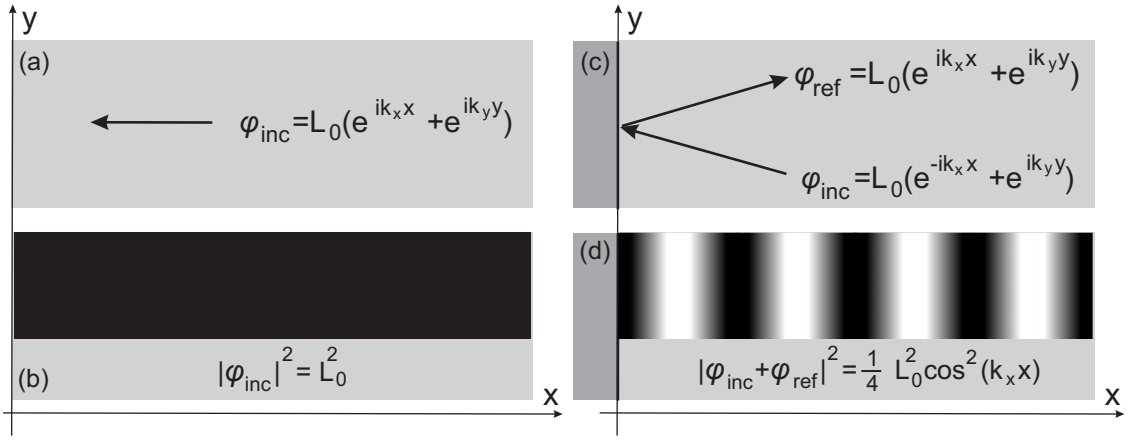


Figure 3.9: Schematics of the elastic scattering of an electron state on a straight step edge. (a) Electron $\varphi_{\text{inc}}$ propagating on the ideal surface and (b) corresponding surface LDOS. (c) Scattering of the electron $\varphi_{\text{inc}}$ on the totally reflecting step potential, that is located at $x = 0$. (d) Corresponding LDOS standing wave pattern.

We note here, that for an experimental FT-STM map the precise shape and phase of the real-space LDOS oscillations are not crucial, because these parameters are averaged during the Fourier transformation. Therefore, instead of performing an explicit evaluation of the surface LDOS for a stepped surface, we constructed a novel approach for simulating FT-STM spectrum that is based on implicit treatment of the surface scatterers. The approach is derived from Eq. (3.8) and the following assumption: the surface step potential is infinite, i.e. assumed to act on electrons as a straight hard wall[1]. Inelastic processes at steps and on terraces, such as electron-phonon and electron-electron scattering, are neglected. As discussed below, since the step scatters all states equally, the complexity of the problem reduces significantly, and it is possible to consider properties of the ideal surface only. To show this the origin of the LDOS oscillations in the vicinity of scatterers has to be briefly discussed.

The electrons that are traveling on a surface scatter elastically on the step potential, interfere with themselves, and in result form the electron standing wave pattern. To show the formation of such a standing wave due to a single Bloch electron in more detail, we consider an electron state with wavevector $\mathbf{k}_{||} = (k_x, k_y)$

$$\varphi_{i,\mathbf{k}_{||}}(\mathbf{R}_{\text{t}}, V) = u_{i,\mathbf{k}_{||}}(\mathbf{R}_{\text{t}}, V) e^{(\mathrm{i}k_x x + \mathrm{i}k_y y)}. \tag{3.9}$$

The time dependence of a Bloch state in Eq. (3.9) is not shown explicitly for the sake of simplicity. The electron $\varphi_{i,\mathbf{k}_{||}}$ is propagating along the free surface in the presence of an external

[1]The assumption of an infinite scatterer potential has been previously used to explicitly model the spatially-resolved electron standing wave patterns created by the surface states on metal surfaces [111, 132, 175]. In these studies, however, the properties of the surface states have been described employing a simplistic two-dimensional electron gas model. The contribution of the bulk electrons and of the surface resonances was completely neglected.

field, caused by the applied bias voltage $V_{\text{bias}}$ between the tip and the surface. The corresponding LDOS is:

$$n_{i,\mathbf{k}_{||}}(\mathbf{R}_{\text{t}}, V) = |u_{i,\mathbf{k}_{||}}(\mathbf{R}_{\text{t}}, V)|^2, \tag{3.10}$$

i.e. is proportional to the lattice periodic part $u_{i,\mathbf{k}_{||}}$ only. This is schematically shown on Fig. 3.9(a)-(b).

As shown on Fig. 3.9(c)-(d), the introduction of an ideally reflecting hard wall located along the $y$-axis leads to the formation of a new electron state, created by the superposition of the incoming and the reflected wave:

$$\tilde{\varphi}_{i,\mathbf{k}_{||}}(\mathbf{R}_{\text{t}}, V) = u_{i,\mathbf{k}_{||}}(\mathbf{R}_{\text{t}}, V)e^{(\mathrm{i}k_x x + \mathrm{i}k_y y)} + u_{i,\mathbf{k}_{||}}(\mathbf{R}_{\text{t}}, V)e^{(-\mathrm{i}k_x x + \mathrm{i}k_y y)} = \frac{1}{2}\, u_{i,\mathbf{k}_{||}}(\mathbf{R}_{\text{t}}, V)\cos(k_x x)e^{\mathrm{i}k_y y}. \tag{3.11}$$

The LDOS of the resulting wave is:

$$\tilde{n}_{i,\mathbf{k}}(\mathbf{R}_{\text{t}}, V) = \frac{1}{4}\, n_{i,\mathbf{k}}(\mathbf{R}_{\text{t}}, V)\, \cos^2(k_x x), \tag{3.12}$$

i.e., it is proportional to the LDOS of the free surface weighted with the $\cos^2$ function, that contains now the $\mathbf{k}_{||}$-dependence along the step-normal.

According to the Kohn-Sham theory, electrons described by the Kohn-Sham Hamiltonian (see, e.g., Sec. 2.3.3.3) are considered as *noninteracting* quasiparticles. Therefore, all electrons independently undergo an interference in a manner described above, and the resulting interference pattern will be created by a superposition of all the single-electron standing waves. At each given energy $E$, measured relative to the surface Fermi level, the corresponding LDOS is equal to:

$$\begin{aligned}\tilde{n}^{\text{s}}(\mathbf{R}_{\text{t}}, V, E) &= \int d\mathbf{k}_{||} \sum_i \tilde{n}_{i,\mathbf{k}_{||}}(\mathbf{R}_{\text{t}}, V)\delta(E - E_{\text{Fermi}} - \epsilon_{i,\mathbf{k}_{||}}) = \\ &= \frac{1}{4}\int d\mathbf{k}_{||} \sum_i n_{i,\mathbf{k}_{||}}(\mathbf{R}_{\text{t}}, V)\, \cos^2(k_x x)\, \delta(E - E_{\text{Fermi}} - \epsilon_{i,\mathbf{k}_{||}}).\end{aligned} \tag{3.13}$$

The Fourier transformation of this signal (as measured in FT-STM experiments at $E = eV$, see, e.g., Eq. (3.8)), provides the $k_x$-resolved power spectrum. The spectrum coefficients are proportional to the LDOS of the unperturbed electrons $n_{i,\mathbf{k}_{||}}$ with wavevector component $k_x$ at the tip-apex position $\mathbf{R}_{\text{t}}$. Obviously, the electronic states with high LDOS in the vacuum will dominate the measured $dI/dV$ at each given bias, and consequently will show up in the FT-STM map. Therefore, instead of having to explicitly calculate the scattering events on the steps it is sufficient to find the relative magnitudes of the $k_x$- and energy-resolved LDOS of the ideal defect-free surface.

In case of Ag(110) surfaces (Sec. 3.3), the steps are oriented along the [010] crystallographic axis. The standing waves are created normal to the step edge, i.e., along the [001] direction. By

analogy with Eq. (3.6), the $k_{[001]}$-resolved surface LDOS is introduced as:

$$n^{\mathrm{s}}(k_{[001]}, \mathbf{R}_{\mathrm{t}}, V, E) = \int d\mathbf{k'}_{||} \sum_i |\varphi_{i,\mathbf{k'}_{||}}(V, \mathbf{R}_{\mathrm{t}})|^2 \, \delta(E - E_{\mathrm{Fermi}} - \epsilon_{i,\mathbf{k'}_{||}}) \, \delta(k_{[001]} - k'_{[001]}), \qquad (3.14)$$

The $k_{[001]}$-resolved contribution to the $dI/dV$ signal is (compare with Eq. (3.8)):

$$\frac{dI(k_{[001]}, \mathbf{R}_{\mathrm{t}}, V)}{dV} \propto n^{\mathrm{s}}\left(k_{[001]}, \mathbf{R}_{\mathrm{t}}, V, E\right)|_{E=eV}. \qquad (3.15)$$

The total $dI/dV$ signal is obtained by integrating all $k_{[001]}$ from the first surface Brillouin zone:

$$\frac{dI(\mathbf{R}_{\mathrm{t}}, V)}{dV} = \int dk_{[001]} \, \frac{dI(k_{[001]}, \mathbf{R}_{\mathrm{t}}, V)}{dV}. \qquad (3.16)$$

Obviously, the surface LDOS $n^{\mathrm{s}}(k_{[001]}, \mathbf{R}_{\mathrm{t}}, V, E)$ depends not only on the tip-surface distance $z$, but also on the in-plane coordinates $(x, y)$. To get the single estimate of the LDOS magnitude corresponding to bias voltage $V$ and wavevector $k_{[001]}$, the $(x, y)$-averaging over the surface corrugation is performed. It is important to note, that at sufficiently large biases and distances $z$ to the surface, the surface corrugation $z(x, y)$ is essentially flat, since a large number of electrons with different wavevectors contribute to the tunneling, and the averaging is performed over planes parallel to the surface. Employing the averaging over the surface unit cell, the final $k_{[001]}$- and bias-voltage resolved theoretical FT-STM map is calculated according to:

$$\eta(k_{[001]}, V) = \int dx \, dy \;\; n_{\mathrm{s}}(k_{[001]}, \mathbf{R}_{\mathrm{t}}, V, E)|_{E=eV}, \qquad (3.17)$$

where the tip-surface separation $z$ at each bias voltage $V$, entering Eq. (3.17), is determined by the condition of a constant tunneling current:

$$I(\mathbf{R}_{\mathrm{t}}, V) = \int_0^{eV} dE \, n^{\mathrm{s}}(\mathbf{R}_{\mathrm{t}}, V, E) = \mathrm{const}. \qquad (3.18)$$

From Eqs. (3.17)-(3.18) the FT-STM maps can be calculated on the basis of the ideal-surface LDOS without an explicit inclusion of surface imperfections. This allows a dramatic reduction in the complexity of the problem: instead of having to use huge supercells to describe terraced surfaces the new approach allows to restrict on the (much smaller) unit cell of a perfect surface.

We concentrate now on the practical evaluation of the surface LDOS $n^{\mathrm{s}}(k_{[001]}, \mathbf{R}_{\mathrm{t}}, V, E)$, entering Eq. (3.17). An explicit evaluation of the surface LDOS $n^{\mathrm{s}}$ in the presence of an external electrical field (caused by application of the bias voltage $V$) is principally possible, but makes the method computationally rather demanding. Alternatively, an interpolation between wavefunctions, calculated at extreme biases can be employed, as was done, e.g., by Strokbro and Grey [172]. However, employing the transfer-Hamiltonian formalism, which is the basis of the Tersoff-Hamann theory (see Secs. 2.6.1-2.6.2), Lang [178] has shown that when the bias energies are small compared

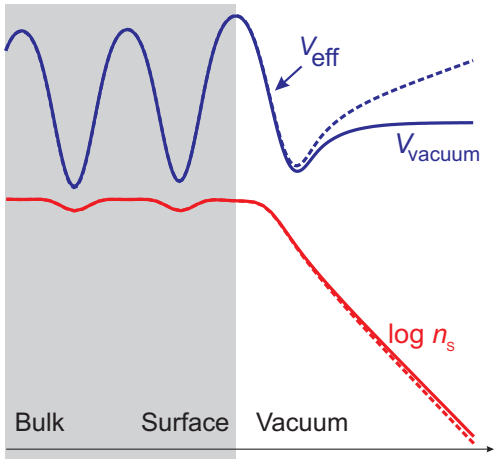


Figure 3.10: Sketch of the approximation used in calculating the surface LDOS in the presence of an external electric field. The solid blue line mimics the effective potential, that corresponds to a zero external electric field. The dashed line mimics a realistic potential. The field is assumed to be homogeneous in the vacuum region and the potential has therefore trapezoidal shape. The solid and dashed $n_s$ are the surface charge densities, corresponding to the described effective potentials.

to the surface work function, the external electrical field does not significantly affect the tunneling current. In his study, Lang has used the approximate shape of the tunneling barrier corresponding to a zero external field. The error introduced by neglecting the external field was as small as 2% for a bias $\sim 1$ eV, a surface work function $\sim 4$ eV and a tip-surface separations $z \sim 6$ Å. In the case of the Ag(110) surface the features we are interested in are at biases at and below 1.7 eV (see Sec. 3.3). The surface work function for a Ag(110) surface is $\sim$4.5 eV [179, 180]. These values are close to the corresponding values in the Lang study. It is therefore safe to neglect the effect of the external electrical field, and to employ the surface wavefunctions calculated in the zero external field (Fig. 3.10). Based on this argument Eqs. (3.17)-(3.18) can be modified accordingly:

$$\eta(k_{[001]}, V) = \int dx\, dy \;\; n^{\mathrm{s}}(k_{[001]}, \mathbf{r}, 0, E)|_{E=eV}, \tag{3.19}$$

and

$$I(\mathbf{r}, V) = \int_0^{eV} dE\, n^{\mathrm{s}}(\mathbf{r}, 0, E) = \text{const}, \tag{3.20}$$

respectively.

The constant current regime of the STM is realized by changing the tip-sample separation when the bias voltage changes. In the case of an Ag(110) surface, and assuming that the STM tip at zero bias is positioned at $z \sim 5$ Å above the surface, the tip-surface separation increases to $z \sim 12$ Å at a bias voltage of 4.5 V. As shown in App. A.2, the common planewave basis set fails at distances beyond $\zeta_{max} \cong 5$ Å above the surface. In order to overcome this limitation the exact asymptotic

decay of the surface wavefunctions at large tip-surface separations can be obtained by projecting the wavefunctions from the planewave basis onto a real-space basis. The real-space approach, described in detail in Sec. 4.3.1, is essential when *the shape* of the STM profiles at large tip-sample separations is required. A transformation to a real-space basis is not needed for the calculation of the FT-STM coefficients: these coefficients are calculated by averaging over the surface unit cell (see Eq. (3.17)). Thus, the precise real-space shape of the STM profiles is not essential: the magnitude of the calculated FT-STM coefficients is determined by the $(x, y)$-averaged protrusion of the surface wavefunctions into the vacuum. We make use of this condition and construct in the following a *qualitatively* accurate description of the FT-STM spectrum without employing the real-space approach. Specifically, it is possible to reformulate Eqs. (3.19)-(3.20) in a way, that the surface LDOS entering these equations are evaluated at the distances $\zeta$ ($\zeta$ is the distance from the surface along the surface normal; $\zeta = 0$ corresponds to a surface plane) reliably described within the planewave basis set, i.e. at $\zeta < \zeta_{\max}$, for all biases.

To show this, for each surface Bloch wavefunction $\varphi_{i\mathbf{k}_{||}}$ with a given wavevector $\mathbf{k}$ and band-index $i$ the corresponding LDOS $n_{i\mathbf{k}_{||}}(z)$ at any tip-surface separation $z$ is represented as:

$$n_{i\mathbf{k}_{||}}(z) = T_{i\mathbf{k}_{||}}(z-\zeta)\, n_{i\mathbf{k}_{||}}(\zeta). \tag{3.21}$$

To simplify Eq. (3.21) and the following equations the $(x, y)$ dependencies of all quantities are taken into account, but not explicitly written. The function $T_{i\mathbf{k}_{||}}(z-\zeta)$ in Eq. (3.21), referred to as the vacuum transmission coefficient, completely accounts for the change in the single-state LDOS $n_{i\mathbf{k}_{||}}(z)$ when the tip-surface separation is changed from $\zeta$ to $z$. We assume that $\zeta < z$, i.e., the vacuum transmission coefficient accounts for the decay of the surface LDOS at tip-surface distances larger than $\zeta$.

Since there are no restrictions regarding the choice of the distance $\zeta$, it can be taken from the region where the surface LDOS is still accurately described. Eq. (3.21), however, does not directly allow the evaluation of the FT-STM spectrum because the specific shape of the transmission coefficient $T_{i\mathbf{k}_{||}}(z-\zeta)$ is generally an unknown function of the wavevector $\mathbf{k}_{||}$, the electron energy $\epsilon_{i\mathbf{k}_{||}}$, the electronic nature of the electronic state, and the lateral coordinates $(x, y)$.

To simplify the problem, it is assumed that the transmission coefficient is essentially independent on the electronic eigenstates, and depends only on the tip-surface separation $z$, i.e.:

$$T_{i\mathbf{k}_{||}}(z-\zeta) \approx \tilde{T}(z-\zeta), \tag{3.22}$$

and

$$n_{i\mathbf{k}_{||}}(z) \approx \tilde{T}(z-\zeta)\, n_{i\mathbf{k}_{||}}(\zeta). \tag{3.23}$$

Substituting Eqs. (3.21)-(3.22) into, e.g., Eq. (3.20) results in a new expression for the tunneling

current, that in contrast to Eq. (3.20) requires the evaluation of the surface LDOS at distances $\zeta$ instead of $z$:

$$I(z,V) = \tilde{T}(z-\zeta)\int_0^{eV} dE\, n^{\mathrm{s}}(\zeta,0,E) = \text{const}, \tag{3.24}$$

The transmission coefficient $\tilde{T}(z-\zeta)$ in Eq. (3.24) is still an unknown function. It can be calculated numerically, however, employing the conditions (i) of a constant tunneling current and (ii) recalling that by definition $\tilde{T}(0)=1$. Specifically, assuming that the distance $\zeta$ corresponds to some bias voltage $V_\zeta$, condition (i) implies that:

$$I(z(V),V) = I(\zeta(V_\zeta),V_\zeta). \tag{3.25}$$

Employing condition (ii) in Eq. (3.24) the right-hand side of Eq. (3.25) can be calculated exactly:

$$I(\zeta(V_\zeta),V_\zeta) = \int_0^{eV_\zeta} dE\, n^{\mathrm{s}}\left(\zeta,\,0,\,E\right). \tag{3.26}$$

Substituting Eqs. (3.24) and (3.26) into Eq. (3.25) allows to rewrite it as:

$$\tilde{T}(z(V)-\zeta)\int_0^{eV} dE\, n^{\mathrm{s}}(\zeta,0,E) = \int_0^{eV_\zeta} dE\, n^{\mathrm{s}}\left(\zeta,\,0,\,E\right). \tag{3.27}$$

Since the integrals in Eq. (3.27) are known entities that can be evaluated at any given bias $V$, it is straightforward to rearrange Eq. (3.27) and numerically sample the transmission coefficient $\tilde{T}(z(V)-\zeta)$ as:

$$\tilde{T}(z(V)-\zeta) = \frac{\int_0^{eV_\zeta} dE\, n^{\mathrm{s}}\left(\zeta,\,0,\,E\right)}{\int_0^{eV} dE\, n^{\mathrm{s}}\left(\zeta,\,0,\,E\right)}, \tag{3.28}$$

Using Eq. (3.23) with a known transmission coefficient $\tilde{T}(z(V)-\zeta)$, one is able to reformulate Eq. (3.17), and to calculate the final FT-STM as:

$$\eta(k_{[001]},V) = \int dx\,dy\;\; \tilde{T}(\mathbf{r}(V)-\mathbf{R})\;\; n^{\mathrm{s}}(k_{[001]},\mathbf{R},0,E)|_{E=eV}, \tag{3.29}$$

where the $(x,y)$-dependencies are restored, i.e. $\mathbf{r}=(x,y,z)$ and $\mathbf{R}=(x,y,\zeta)$.

Eq. (3.29) is computationally advantageous over Eq. (3.19) because the surface LDOS in Eq. (3.29) is evaluated at a distance $\zeta$ above the surface, that can be chosen from the accurately described vacuum region. In the specific case of a Ag(110) surface the planewave basis set fails to provide an accurate description of the surface LDOS beyond $\zeta_{\max} \cong 5$ Å (App. A.2), i.e $\zeta$ must fulfil the condition $\zeta < \zeta_{\max}$.

There exists also a similar condition for a minimum value of $\zeta$, i.e. $\zeta > \zeta_{\min}$. It is needed to ensure that the assumption of an eigenstate independent transmission coefficient $\tilde{T}$ (see Eq. (3.23)) holds and does not significantly affect the calculated FT-STM spectrum (see Eq. (3.29)).

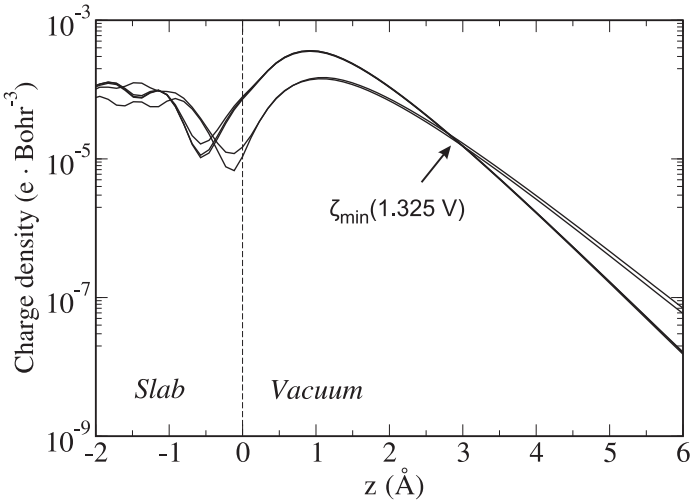


Figure 3.11: Decay of the $(x, y)$-averaged surface LDOS (Eq. (3.6)) into the vacuum. Contributions of the electronic states from the energy interval ($E_{\text{Fermi}} + 1.30$ eV, $E_{\text{Fermi}} + 1.35$ eV) are shown. The z-axis is normal to the surface. The surface plane is at $z = 0$ Å. The slab is 15 atomic layers thick.

The value of the $\zeta_{\text{min}}$ is specific for each surface and depends on the range of bias-voltages that should be covered. To estimate the critical distance $\zeta_{\text{min}}$ we analyzed the decay of the surface LDOS into the vacuum, as presented below for the specific case of the Ag(110) surface.

On Fig. 3.11 the $(x, y)$-averaged surface LDOS corresponding to the electronic states from the energy interval ($E_{\text{Fermi}}$+1.30 eV, $E_{\text{Fermi}}$+1.35 eV) are shown[2]. Considering thermal smearing, these LDOS define the magnitude of the FT-STM coefficients $\eta(k_{[001]}, V)$ at the bias energy $E \sim E_{\text{Fermi}} +$ 1.325 eV (see Eq. (3.29)). From Fig. 3.11 it is clear that the surface single-state LDOS exponentially decays at distances larger than $z \sim 2$ Å above the surface, and the decay speed is essentially constant for each LDOS. Noteworthy, that the *relative order* of these surface LDOS, and consequently of the corresponding FT-STM coefficients $\eta$, does significantly depend on the tip-surface distance $z$. The predominant LDOS contribution is exchanged at the distance $\zeta_{\text{min}}(V) = 3$ Å. If Eq. (3.29) is applied with $\zeta < \zeta_{\text{min}}(V)$, the method will fail to predict the change of the leading contribution at $\zeta_{\text{min}}$ (see Eq. (3.21)). The situation is remarkably different when $\zeta > \zeta_{\text{min}}(V)$. The relative order of the electronic states is not affected anymore by an increase of the distance $z$, and the application of Eq. (3.29) modifies only the weights of the corresponding LDOS. Qualitatively, however, the obtained FT-STM profile remains correct.

The value of $\zeta_{\text{min}}$ has been obtained by performing a search of the $\zeta_{\text{min}}(V)$ at all bias-voltages

[2]In case of a Ag(110) surface the transmission coefficient $\tilde{T}(\mathbf{r} - \mathbf{R})$ is essentially homogeneous over $(x, y)$-coordinates. At biases above 0.35 eV and below the energy offset of the $S_2$ surface state the maximum deviation from the averaged value is less than 4%, and does not exceed 30% at all biases up to the surface work function. It is justified, therefore, to move the transmission coefficient out of the integral sign in Eq. (3.29), and to analyze the $(x, y)$-averaged decay of the surface LDOS.

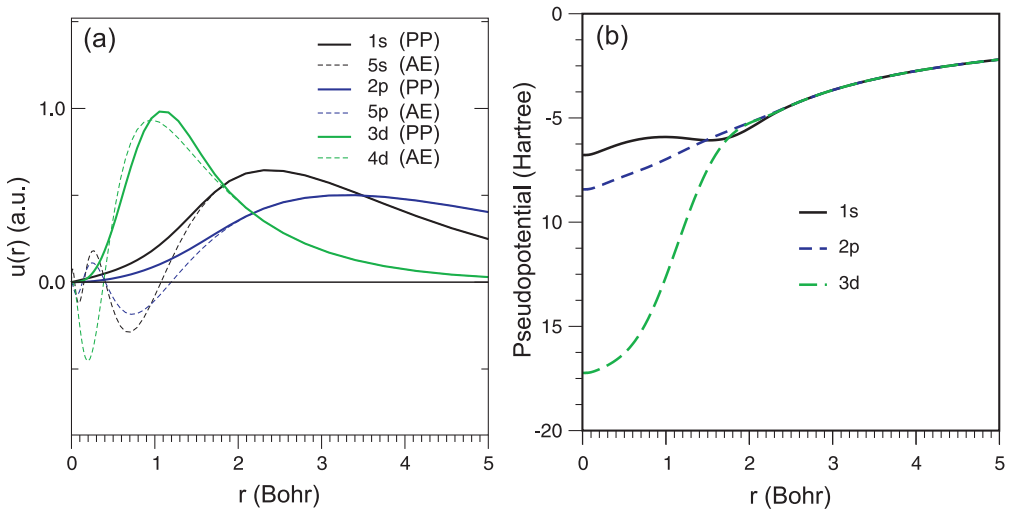


Figure 3.12: Radial part of (a) the all-electron and pseudopotential wavefunctions and (b) the ionic pseudopotential calculated for an isolated silver atom. The pseudopotential is generated employing a neutral configuration with (10,1,0) electrons on ($4d$,$5s$,$5p$) orbitals for bounded $4d$ and $5s$ shells, and an ionized configuration with (9,0.75,0.25) electrons on ($4d$,$5s$,$5p$) orbitals for unbounded $5p$ shells. LDA exchange-correlation is employed, cutoff radii of the pseudopotential are $r_s^{\rm ps} = 2.42$ Bohr, $r_p^{\rm ps} = 2.62$ Bohr, $r_d^{\rm ps} = 2.42$ Bohr.

of interest, and taking the maximum value of the critical tip-surface separation, i.e. $\zeta_{\rm min} = \max\{\zeta_{\rm min}(V)\}$.

In case of a Ag(110) surface and biases spanning energies between $E_{\rm Fermi}+0.35$ eV and $E_{\rm Fermi}+4.50$ eV, a $\zeta_{\rm min}$ of 3 Å was found. On the other hand, the planewave basis results in the restricted description of the vacuum, are reliable only up to $\zeta_{\rm max} \sim 5$ Å. Hence, the $\zeta$ employed in Eq. (3.29) has to lie in the region 3 Å$< \zeta <$ 5 Å. The value of $\zeta$ used in the actual simulations is discussed in Sec. 3.4.2.

### 3.4.2 Details of the FT-STM spectrum simulations on Ag(110) surfaces

The electronic and atomic structural properties of a Ag(110) surface are calculated employing *ab initio* planewave pseudopotential density functional theory (see Ch. 2) within the LDA parametrization for the exchange-correlation functional (see Sec. 2.3.3.4). For Ag a Troullier-Martins pseudopotential with the $4d$, $5s$ and $5p$ orbitals treated as valence is used (Fig. 3.12). Specifically, the pseudopotentials for bounded $4d$ and $5s$ orbitals are generated for a neutral atom, i.e. with (10,1,0) electrons located on the ($4d$,$5s$,$5p$) shells, respectively. The pseudopotentials for the unbounded $5p$ orbital are generated for an ionized atom with (9,0.75,0.25) electrons located on the ($4d$,$5s$,$5p$) shells, respectively. In both cases the cutoff radii $r_s^{\rm ps}$=2.42 Bohr, $r_p^{\rm ps}$=2.62 Bohr and $r_d^{\rm ps}$=2.42 Bohr are used. No nonlinear core-correction is used.

A convergence with respect to the lattice constant and the bulk modulus is obtained at a

planewave energy cutoff of 50 Ry and 20(slab) and 30(bulk) **k**-points in the irreducible wedge of the first Brillouin zone, correspondingly.

The calculated at $T = 0$ K lattice constant $a_0$, bulk modulus $B$, and pressure derivative of the bulk modulus $\partial B/\partial P$ (see App. A.4) are 4.05 Å, 1.29 MBar and 5.62, respectively. The theoretical values agree well with previous *ab initio* calculations [181, 182], and are in a excellent agreement with low-temperature experimental data ($a_0 = 4.08$ Å [183], B=1.09 MBar [184]).

The surface is modeled within the repeated slab geometry (Sec. 2.4.2). Slabs of different thicknesses ranging from 2 up to 22 atomic layers and separated by a vacuum region of $\sim 14$ Å are used.

The clean Ag(110) surface exhibits a relaxation typical for metallic surfaces and does not show a reconstruction as found e.g. for the $5d$ noble metals where for (110) surface a well-known 'missing-row' reconstruction is found [185]. In order to check the magnitude of the surface relaxation we have performed slab calculations with a 9 atomic layer thick slab and where we allow for a full relaxation of the first 4 atomic layers. We have found an oscillatory relaxation pattern, that is commensurable with the simple Smoluchowski smoothing picture [186]. The relaxation is very short-ranged and essentially localized in the first two surface layers, in agreement with previous experimental and theoretical studies [187]. The calculated change of the interlayer spacing is $\Delta d_{12} = -7.8\%$ and $\Delta d_{23} = +4.0\%$. The third and fourth layer position are practically unchanged with $\Delta d_{34} = -0.1\%$ and $\Delta d_{45} = +0.1\%$ respectively, where $\Delta d_{ij}$ indicates the percentage change of the interlayer spacing between layers $i$ and $j$ from that of the bulk.

The surface relaxation has very little effect on the surface electronic properties, e.g., the energy position of the surface states changes by less than 0.05 eV. Consequently, the FT-STM spectra calculated employing relaxed and non-relaxed Ag(110) surfaces are essentially identical (App. A.1). Therefore, for the in-depth analysis in Sec. 3.5 a non-relaxed surface is used.

All *ab initio* FT-STM spectra are calculated according to Eq. (3.29). In the constant-current STM mode the actual distance $\zeta$ in Eq. (3.29) depends on the lateral position of the tip above the surface, given by $(x, y)$ coordinates. We have compared FT-STM spectra obtained under the condition of a constant distance $\zeta\,(x,\, y) = 4$ Å with those acquired under constant tunneling current, i.e. for $I\,(\zeta\,(x,\, y)\,,\, V) = \text{const}$, with an average distance $\overline{\zeta}\,(x,\, y) = 4$ Å. The corrugation magnitude in the latter case never exceeded 0.1 Å, and both approaches provide essentially identical results. Constant $\zeta\,(x,\, y) = 4$ Å is therefore used in simulations of the FT-STM spectra.

Since the experimentally detected electron standing waves show no modulation along the $[1\bar{1}0]$ crystal axis we conclude that only $\mathbf{k}_{||} = \big(0,\, k_{[001]}\big)$, i.e. the $\bar{\Gamma}\bar{\mathrm{Y}}$ band structure path, is probed by the STM tip. We first focus therefore on a detailed analysis of the FT-STM spectrum restricting ourself to this $\mathbf{k}_{||}$-point path. According to Eqs. (3.14) and (3.17), however, all $\mathbf{k}_{||}$ components effectively contribute to the total differential conductivity and consequently should be resolved in the experiment. The modification of the spectrum due to an inclusion of the entire surface Brillouin zone is then discussed in Sec. 3.5.3.1.

## 3.5 Results

### 3.5.1 Electronic properties of bulk Ag

Silver in its ground state is a face-centered cubic crystal [183] that belongs to the class of paramagnetic $d$-metals. The electronic properties of such metals are qualitatively well understood in the frame of the so called $d$-band model [46]. According to the model the electronic structure consists of a relatively localized band of $d$-electrons below the Fermi energy, while the metal character is realized via strongly overlapping $sp$-electrons that are homogeneously smeared above and below the Fermi level.

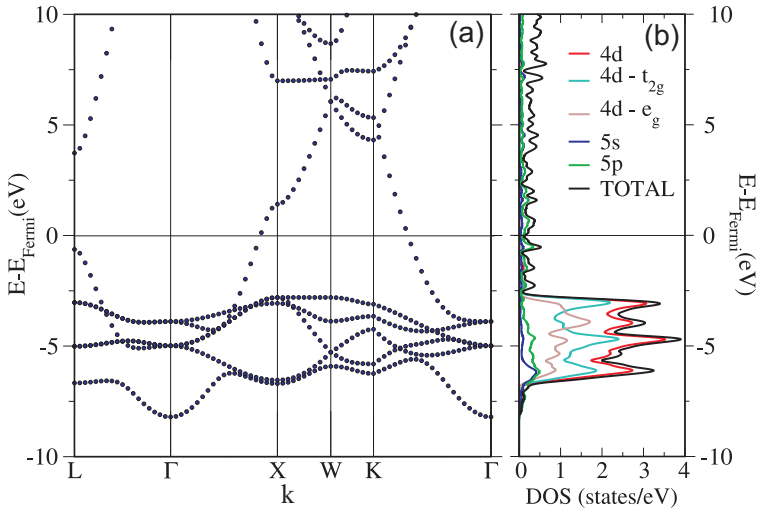


Figure 3.13: (a) Calculated *ab initio* bulk band structure of the Ag crystal in its ground state. The bulk Brillouin zone is shown on Figs. 3.6(a) and 3.14(b). (b) Density of one-particle states projected onto $4d$, $5s$ and $5p$ atomic orbitals of an Ag atom from the fcc-lattice.

The calculated bulk band electronic structure together with the corresponding density of the one-particle states are shown on Fig. 3.13. The *ab initio* electronic properties of bulk silver are a completely commensurate with $d$-band model: the major part of $d$-electrons is located in the energy window ($E_{\text{Fermi}} - 7.0$ eV, $E_{\text{Fermi}} - 2.5$ eV). Moreover, since the fcc-crystal possesses octahedral symmetry $O_h$ the $d$-states split into higher lying double-degenerate states with $e_g$-symmetry ($d_{z^2}$ and $d_{x^2-y^2}$) and lower-lying triple-degenerate states with $t_{2g}$ symmetry ($d_{xy}$, $d_{yz}$ and $d_{xz}$) (Fig. 3.13(b)), in agreement with Crystal Field theory [188].

The present study is focused on the contribution of the bulk electrons to the electronic structure of Ag(110) surfaces. While explicit surface calculations are required to get the shape of the bulk wavefunctions in the surface vicinity, the energetic spectrum of the allowed bulk states contributing to a particular surface can be readily obtained from the bulk calculations, as discussed below.

When the periodic crystal is cleaved to create a surface the translational periodicity along the surface normal breaks. The three-dimensional bulk Brillouin zone (BBZ) collapses into the two-

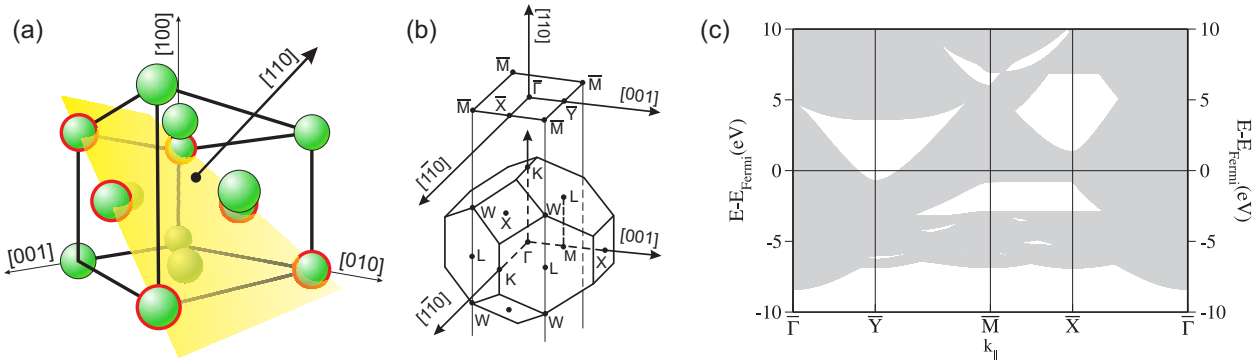


Figure 3.14: (a) Cleaving an fcc-crystal along the (110) plane (shown in yellow) leads to the appearance of two (110) surfaces. (b) Projection of the first bulk Brillouin zone onto a (110) plane results in the two-dimensional first surface Brillouin zone. The positions of the high symmetry points are shown. (c) *Ab initio* bulk band structure of an Ag projected onto a (110) plane. White regions (pockets) are forbidden for bulk states.

dimensional surface Brillouin zone, and the normal-to-surface component of the bulk **k**-vectors ceases to be a valid quantum number (see Fig. 3.14(b)). The solutions of the Hamiltonian in this case are the planewaves traveling along the surface with wavevectors $\mathbf{k}_{||}$.

For a surface supported by the semi-infinite substrate the bulk electrons are affected by the surface potential only in the surface vicinity, where they are scattered back into the bulk. Away from the surface the bulk electronic properties remain essentially unaffected since the effect of the surface potential is infinitesimally small there. The eigenspectrum of bulk electrons, therefore, does not depend on the surface and it is feasible to directly map the spectrum from the first bulk Brillouin zone onto the first surface Brillouin zone. The mapping is performed by integrating the bulk eigenspectrum over the normal-to-surface component $k_{\perp}$, since for a surface Hamiltonian with a given $\mathbf{k}_{||}$ all bulk states with different $k_{\perp}$ are still physically valid stationary solutions. Such a mapping procedure is known as *projection* of the bulk electronic bands onto a particular surface plane. The resulting electronic structure stemming from the bulk electrons is known as the projected bulk band structure.

The calculated bulk band structure of Ag being projected onto a (110) plane is shown on Fig. 3.14(c). The projected bands form a continuum of allowed states (shown in grey) with the exception of forbidden regions, referred to as pockets in the projected bulk band structure. We focus on the bulk properties in the experimentally relevant $\overline{\Gamma Y}$ range of the $\mathbf{k}_{||}$-points and energies close to the Fermi level, as shown in Fig. 3.15(a). To highlight the internal structure of the projected bulk bands (shown in grey) a set of *discretized* projected bulk bands is shown as well. The discretized spectrum is obtained by restricting $k_{[110]} \in$ BBZ to a discrete set of equidistantly spaced values, that sample the whole BBZ. Such an artificial discretization mimics a limited bulk description that arises due to a finite slab thickness (see, e.g., discussion in Sec. 3.5.4.1).

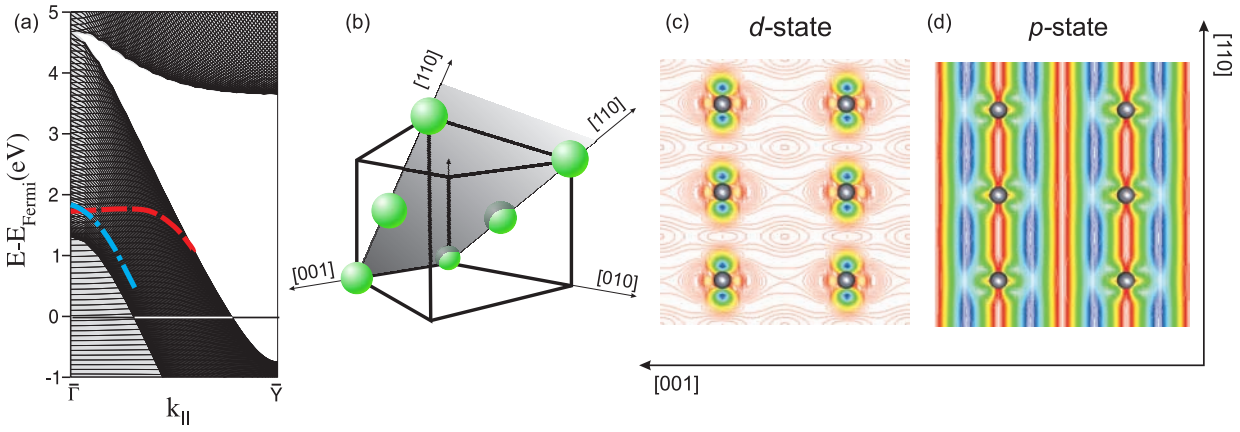


Figure 3.15: (a) Projected bulk band structure for the Ag(110) surface. Only experimentally relevant energies ($E_{\text{Fermi}} - 1$ eV,$E_{\text{Fermi}} + 5$ eV) and along the $\overline{\Gamma} - \overline{\text{Y}}$ $\mathbf{k}_{||}$-path are shown. One-particle bulk states corresponding to a discrete set of equidistantly spaced $k_{[110]}$-points are shown as thin solid lines to highlight the structure of the continuum projected bands; the continuum is shown in grey color. Two types of bulk states contribute to the projected bulk band structure: $d_{z^2}$-like states (the shape of one of these states is highlighted by a dashed red curve) and $p_x$-like states (highlighted as dash-dotted blue curve). (b) The grey-shaded region indicates the (001) plane of the fcc-crystal. (c) and (d) show the contour plots of the partial charge densities corresponding to the $d_{z^2}$ and $p_x$-like one-particle states (shown in (c)) in the (001) plane. Atoms lying in the selected plane are shown as dark balls. Blue (red) color corresponds to regions with high (low) electron density.

The analysis of the projected bulk band structure (Fig. 3.15(a)) reveals the existence of two different types of bulk states, with $d_{z^2}$ and $p_x$-character correspondingly[3]. The orbital character of these states have been obtained by projecting the corresponding eigenfunctions $\varphi_{i\mathbf{k}}$ onto the atomic pseudoorbitals $\mu$:

$$|\varphi_{i\mathbf{k}}\rangle = \sum_{\mu} |\mu\rangle \langle\mu| \varphi_{i\mathbf{k}}\rangle \,, \tag{3.30}$$

and analyzing the magnitude of the expansion coefficients $\langle\mu| \varphi_{i\mathbf{k}}\rangle$.

In order to give a more intuitive description of the bulk electronic structure, the contour plots of the partial charge density corresponding to $d_{z^2}$ and $p_x$ states are shown in Fig. 3.15(c)-(d). As follows from these figures, the spatial overlap of the $d_{z^2}$-states along the [001] direction is dramatically lower when compared to $p_x$-states. The different localization of the eigenstates causes a substantially different dispersive behavior: while the highly localized $d_{z^2}$-states are essentially dispersionless along the [001]-direction, the dispersion of the $p_x$-states there is pronounced and exceeds 5 eV (Fig. 3.15(a)).

[3]The appearance of bulk $d$-states above the Fermi energy does not contradict the $d$-band model discussed in the beginning of this chapter. The dominant part of $d$-electrons is localized below the Fermi level (Fig. 3.14(b)). The $d$-states discussed here are due to the non-negligible fraction of $d$-states (about two orders of magnitude smaller compared to the major contribution of $d$-states) that is even present well above the Fermi level.

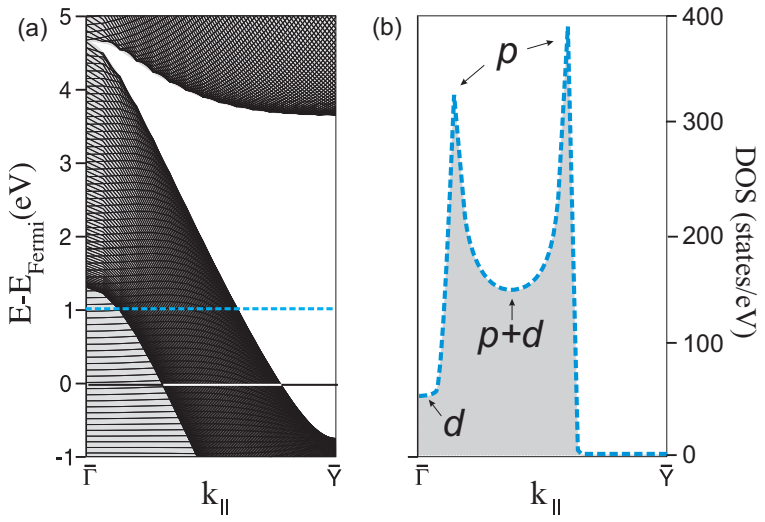


Figure 3.16: (a) Projected bulk band structure for the Ag(110) surface. Only the experimentally relevant energies ($E_{\text{Fermi}} - 1.0$ eV, $E_{\text{Fermi}} + 5.0$ eV) and the $\overline{\Gamma} - \overline{\text{Y}}$ $\mathbf{k}_{||}$-path are shown. (b) Density of the bulk states along the $\overline{\Gamma} - \overline{Y}$ $\mathbf{k}_{||}$-path at $E = E_{\text{Fermi}} + 1.0$ eV. Two peaks of the projected DOS are clearly distinguishable.

It is worth to mention, that the essentially flat $d_{z^2}$-states change their electronic character when approaching the edge of the projected bulk bands (BBE) and become $p$-like at the edge. This is manifested by a strong alteration of the $d$-band dispersion behavior close to the bulk band edge (Fig. 3.15(a)).

On Fig. 3.16 the density of the projected bulk states (DOS) as a function of the $\mathbf{k}_{||}$-vector is shown. Since the $d$-states are essentially flat along the $\overline{\Gamma\text{Y}}$ direction the corresponding DOS is a constant value. In contrast, the highly dispersive $p$-states form a band, which shows at the band edges a strong increase. For a case shown on Fig. 3.16(b) the DOS peaks appear at $k = 0.15$ $\overline{\text{Y}}$ and $k = 0.6$ $\overline{\text{Y}}$, i.e. the DOS enhancement occurs within the projected bulk band structure and exactly at the BBE. At the moment we simply emphasize this enhancement. The reasoning for such an accumulation of bulk states at particular regions of the projected bulk band structure and its importance for FT-STM are discussed in detail in Sec. 3.5.5.

### 3.5.2 Electronic properties of Ag(110) surfaces

In the presence of a surface new electronic states that are forbidden in the bulk may become allowed. These are so-called surface states and surface resonances [46]. In order to identify these states and to get the complete band structure of a Ag(110) surface we have performed explicit surface calculations with a slab having 22 atomic layers.

The calculated surface band structure (Fig. 3.17(c)) is in excellent agreement with previously reported experimental data (inverse photoemission spectra) [170], showing the presence of $S_2$-$S_4$

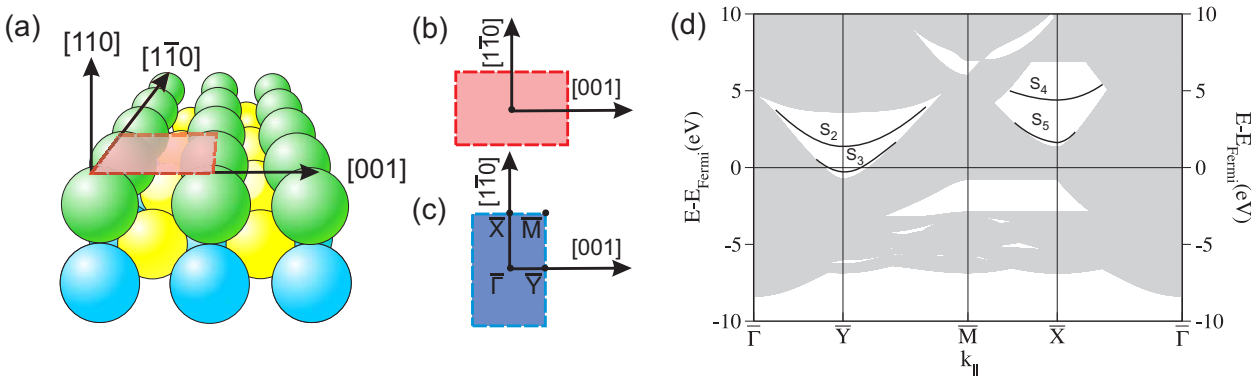


Figure 3.17: (a) Schematic view of the atomic structure of the fcc (110) surface. The primitive unit cell is shown in red. (b) Primitive unit cell of the (110) surface and (c) the corresponding first surface Brillouin zone with high-symmetry $\mathbf{k}_{||}$-points. (d) Calculated surface band structure. Breaking of the translational periodicity along the surface normal allows for new electronic states, shown as solid lines (surface resonances are not shown). The notation of the surface states is chosen according to Refs. [169, 170].

surface states, centered at $\overline{\mathrm{Y}}$ ($S_2$ and $S_3$ states) and $\overline{\mathrm{X}}$ ($S_4$ state), respectively. The appearance of surface states in the middle and on the bottom of the pockets in the projected bulk band structure is a general feature of low-index surfaces of noble metals [169, 189]. The strong parabolic dispersion of both states is characteristic for *sp*-like surface states. It is noteworthy, that only the $S_3$ state crosses the Fermi level and is consequently partially occupied, while the $S_2$ and $S_4$ states remain empty at zero temperature.

In contrast to previous studies we have also found a hitherto not reported surface state located close to the bottom of the projected bulk band pocket that is centered at the $\overline{\mathrm{X}}$ $\mathbf{k}_{||}$-point. A similar surface state have been identified by Bartinski *et al.* on Cu(110) surfaces. In their study Bartinski and co-workers pointed out that additional careful investigations are needed to verify the presence of such surface state on Ag(110) surface. This was not feasible at that time [189]. We labeled the novel *sp*-derived surface state as $S_5$, in analogy with the notation used by Altmann and co-workers [170]. $S_2$-$S_5$ are crystal-induced (Shockley-type) surface states. The effective masses and energy-offsets of these surface states are summarized in Tab. 3.1.

It should be mentioned that the calculated surface properties show significant corrections compared to a previous *ab initio* theoretical study by Ho *et al.* [168], where the surface states $S_3$ and $S_5$ were not found and the position of the $S_2$ state was slightly underestimated. Since in that study only the *s* and *p* electrons were treated as valence, we conclude that an inclusion of the 4*d* electrons in the pseudopotential calculations is essential to correctly describe the electronic structure of the Ag(110) surfaces.

We focus now on the surface electronic properties that are relevant for FT-STM experiments (Sec. 3.3), i.e. at energies ($E_{\mathrm{Fermi}} + 0.35$ eV, $E_{\mathrm{Fermi}} + 5$ eV) and along the $\overline{\Gamma} - \overline{\mathrm{Y}}$ direction. The

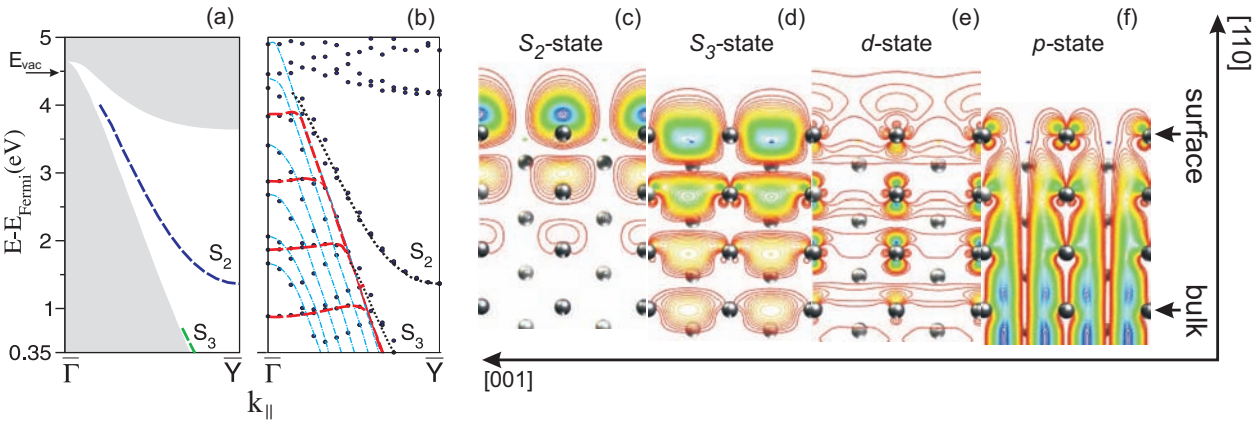


Figure 3.18: (a) Calculated band structure of the Ag(110) surface for energies ($E_{\text{Fermi}}$ + 0.35 eV, $E_{\text{Fermi}}$ + 5 eV) and along $\overline{\Gamma} - \overline{Y}$ $\mathbf{k}_{||}$. Two surface states are shown as dashed curves, the projected bulk bands are shown in grey color. (b) Band structure of a 19 atomic layers thick slab. The bulk states are discretized due to the finite slab size. $d_{z^2}$- and $p_x$-like bulk states are shown as dashed red and solid blue lines, respectively. (c)-(f) Contour plots obtained by projecting the partial charge densities onto a (001) plane for different types of electronic states. Dark and light balls represent in-plane and out-of-plane atoms accordingly. The $S_2$ and $S_3$ surface state partial charge densities are evaluated at $\overline{Y}$ ((c) and (d) frames respectively), the bulk states - at the $\overline{\Gamma}$ $\mathbf{k}_{||}$-point. The real-space shape of the $d_{z^2}$-like and $p_x$-like bulk states in the vicinity of the (110) surface ((e) and (f) frames respectively) can be directly compared with corresponding bulk contour plots (Fig. 3.15(c)-(d)).

surface electronic structure in this region is shown in Fig. 3.18(a). Similar to the analysis of the bulk states, the projection of the surface state eigenfunctions onto atomic orbitals (see Eq. (3.30)) revealed that the $S_2$-surface state has $sp_z$ atomic character, while $S_3$ has mainly $sp_x$ character. The corresponding contour plots of the surface states at $\overline{Y}$ are summarized in Fig. 3.18(c)-(d). Due to the $p_x$-character, the $S_3$ state has a high density between two neighboring surface atoms, i.e., the regions of high electron density are in anti-phase with the underlying atomic lattice. In contrast, the electron density of the $S_2$ state is high above the surface atoms, thus being in-phase with the lattice (Fig. 3.18(c)-(d)).

Another noticeable difference between the $S_2$ and $S_3$ states is a much slower decay of the $S_3$ state into the bulk of the crystal. To quantify this decay and to explore the evolution of the surface states in the vicinity of the projected bulk band edge we have plotted the charge density distribution of the surface states along the surface normal at different energies (Fig. 3.19). We note that both surface states become less surface localized when approaching the projected bulk band edge, and become bulk-like even *before* the crossing with the projected bulk band edge occurs. This effect is more pronounced for the lower lying $S_3$ surface state, since it is located barely above the edge of the projected bulk band structure. The $S_3$ state achieves the bulk-character already at $\sim E_{\text{Fermi}} + 0.5$ eV, while the $S_2$ state at $\sim E_{\text{Fermi}} + 3.7$ eV (see Fig. 3.19). Already at these energies

| State | $\left(E_{\bar{\Y}/\bar{\X}} - E_{\text{Fermi}}\right)$ /eV | $m^*/m_0$ | Method | Reference |
|---|---|---|---|---|
| $S_2$ | 1.37 | 0.6 | DFT | this work |
| | 1.7 | 0.8 | FT-STM | [132] |
| | 1.28 | 0.7 | DFT | [168] |
| | $1.6 \pm 0.2$ | $0.9 \pm 0.2$ | IPES | [169, 170] |
| | 1.65 | – | IPES | [171] |
| | $1.66 \pm 0.02$ | 0.9 | PES | [190] |
| $S_3$ | $-0.29$ | 0.2 | DFT | this work |
| | $-0.1 \pm 0.1$ | – | PES | [189] |
| | $-0.106 \pm 0.05$ | $0.26 \pm 0.02$ | PES | [190] |
| $S_4$ | 4.39 | 1.0 | DFT | this work |
| | $5.0 \pm 0.2$ | $2.0 \pm 0.4$ | IPES | [169, 170] |
| | 4.25 | $> 2.5$ | DFT | [168] |
| $S_5$ | 1.61 | 0.4 | DFT | this work |

Table 3.1: Energy positions and effective masses of the $S_2$-$S_5$ surface states. DFT, FT-STM and (I)PES stand for density functional theory, Fourier transformed scanning tunneling and (inverse) angle resolved photoemission spectroscopy, respectively.

the charge density is no longer accumulated in the surface region. This indicates an absence of surface resonances associated with the $S_2$ and $S_3$ states. To further support this conclusion we have carefully analyzed the layer charge distribution and the electronic character of the states *within* the projected bulk band region. No indication of surface resonance states could be found.

The modification of the bulk states in the vicinity of the (110) surface can be analyzed by comparing the bulk states calculated without a surface (Fig. 3.15(c)-(d)) with the respective states from slab calculations (Fig. 3.18(e)-(f)). The dispersion of the bulk states calculated within the slab (Fig. 3.18(b)) can be likewise compared with the complete spectrum of stationary eigenstates in the ideal bulk (Fig. 3.16(a)). Originally $p_x$-like bulk states get some $d_{xz}$-character at the surface, which, however, quickly vanishes when going away from the surface towards the bulk.

The $d_{z^2}$-like states are also modified due to a (110) surface potential and attain $sp_z$ character there (Fig. 3.18(e)). It is worth to mention, that the $sp_z$ character dominates over $d_{z^2}$ character for energies between $\sim -0.1$ eV and $\sim 2.8$ eV relative to the Fermi level. Outside this energy range the bulk $d_{z^2}$-states essentially conserve their native $d_{z^2}$-character at the surface layer. As has been pointed out before, the $sp_z$-character is characteristic for the $S_2$ surface state. We therefore conclude that at the surface the $d_{z^2}$-states undergoes a hybridization with the $S_2$ surface state, occurring in the energy window ($E_{\text{Fermi}} - 0.1$ eV,$E_{\text{Fermi}} + 2.8$ eV).

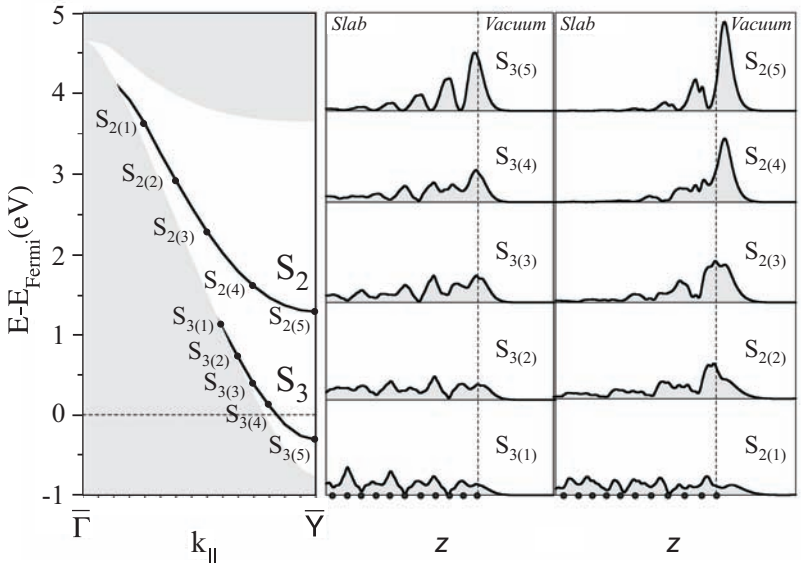


Figure 3.19: Decay of the surface states $S_2$ and $S_3$ along the $\overline{\Gamma} - \overline{\mathrm{Y}}$ $\mathbf{k}_{||}$-path. The surface band structure (left) and the corresponding layer charge distribution for $S_3$ (middle) and $S_2$ (right) states are shown. Labels show the position of the eigenstate (left) corresponding to the charge densities shown in the middle and right frames. The profiles are plotted on the same scale, with shaded circles at the bottom pictures indicating the atomic positions. The slab consists of 22 atomic layers.

### 3.5.3 Simulated FT-STM spectrum of the Ag(110) surface employing a single slab

The theoretical FT-STM spectrum has been calculated according to Eq. (3.29) for the Ag(110) surface employing a 19 atomic layers thick slab. The band structure of this slab (Fig. 3.20(a)) is compared with the corresponding simulated FT-STM spectrum in Fig. 3.20(b) and allows to identify the electronic contributions that mainly contribute to the FT-STM simulations.

Both the $S_2$ and $S_3$ surface state are clearly distinguishable in the simulated FT-STM spectrum. This is an expected result since FT-STM is intrinsically a surface sensitive tool.

The very different directionality of the bulk $p_x$- and $d_{z^2}$-states in the vicinity of the surface has noticeable consequences for FT-STM simulations. States with a $p_x$-character are strongly confined to the surface and do not extend into the vacuum. Therefore, it will be hard or even not possible to access these states by STM. This explains the absence of bulk $p_x$-contributions on the FT-STM map (Fig. 3.20(b)).

In contrast, the $d_{z^2}$-states in the surface region are formed by $s$, $p_z$ and $d_{z^2}$ orbitals (magnetic quantum number $m = 0$), i.e., their high density lobes are pointing perpendicular to the surface and are in phase with the underlying atomic lattice. This allows for an easy detection of these states. Indeed, the states are clearly visible on the simulated FT-STM spectrum. We attribute the

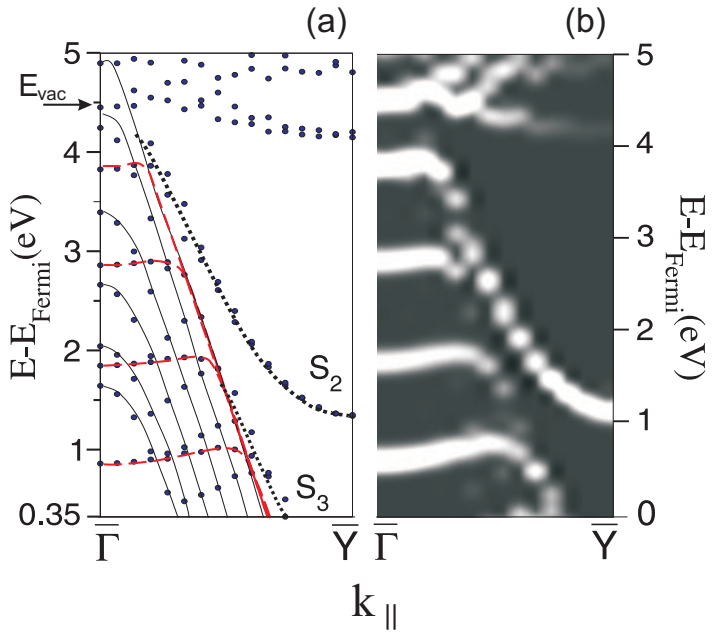


Figure 3.20: Comparison of (a) the slab band structure mimicking a Ag(110) surface with (b) the corresponding FT-STM spectrum. The FT-STM spectrum is obtained with the method described in Sec. 3.4. Dotted, dashed, and solid lines indicate surface, bulk $d$-like, and bulk $p$-like states, respectively (frame (a)). The slab is 19 atomic layers thick.

presence of the bulk $d_{z^2}$-states in the FT-STM map to (a) a hybridization of $d_{z^2}$- and $S_2$-states which becomes essential at energies below $\sim E_{\mathrm{Fermi}} + 2.8$ eV and (b) the $d_{z^2}$-directionality above this energy. It must be emphasized that at the edge of the projected bulk band the $d_{z^2}$-states smoothly disappear because they change their nature from $d_{z^2}$- to $p_x$-like. This $d$ to $p$ transition can be seen in the FT-STM spectrum as a quickly decaying tail located at the projected bulk band edge (Fig. 3.20), and will be a critical aspect for the further discussion.

It is also noticeable that the bulk $d_{z^2}$-states appear even brighter than the surface $S_2$ state. The high intensity of the bulk states is caused by quantum size effects due to the finite slab geometry (Sec. 3.5.4.1). An approach to correct the finite size effects is presented in Sec. 3.5.4.

#### 3.5.3.1 Contributions of different $k_{[1\bar{1}0]}$ components

An analysis of the real space experimental STM data reveals a lack of an electronic standing wave modulations along the $[1\bar{1}0]$ direction. Therefore, it has been commonly assumed that only $\mathbf{k}_{||} = \left(0, k_{[001]}\right)$, i.e. the $\bar{\Gamma} - \bar{\mathrm{Y}}$ band structure path, is probed. According to Eqs. (3.14) and (3.17), however, all $\mathbf{k}_{||}$ components effectively contribute to the total differential conductivity and consequently should be resolved in experiment. To clarify this, we have performed simulations of the FT-STM experiment assuming $\mathbf{k}_{||} \in \bar{\Gamma}\bar{\mathrm{Y}}$ and compared these results with FT-STM spectra where we have taken into account all $\mathbf{k}_{||}$ components from the first surface Brillouin zone (Fig. 3.21).

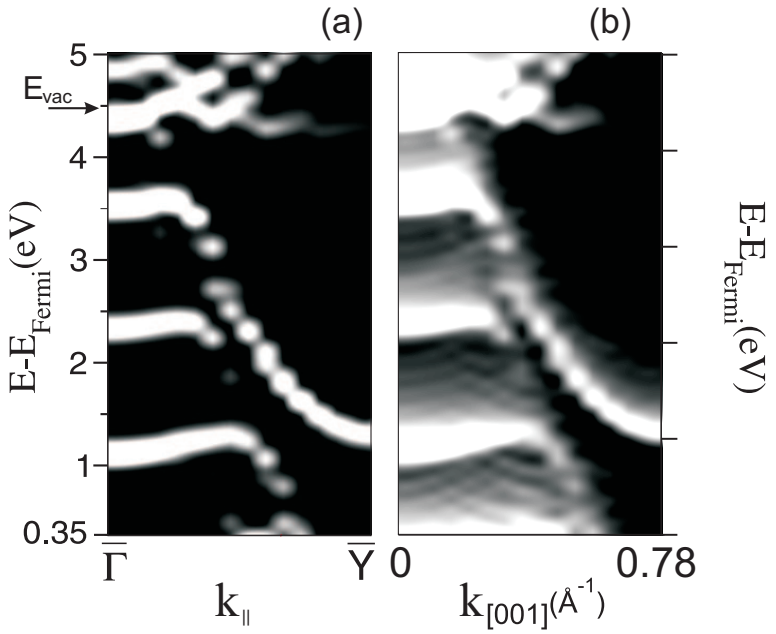


Figure 3.21: Effect of the nonzero $k_{[1\bar{1}0]}$ components on the calculated FT-STM spectrum. (a) The case with $k_{[1\bar{1}0]} = 0$ is compared with (b) the case when all $\mathbf{k}_{||}$-vectors from the first surface Brillouin zone are included. The arrow shows the theoretical vacuum level. The slab is 15 atomic layers thick.

Fig. 3.22 demonstrates a strong sensitivity of the band structure on the $k_{[1\bar{1}0]}$ component, manifested by a dramatic change in the $S_2$, $S_3$ and bulk band edge positions with when $\left|k_{[1\bar{1}0]}\right|$ increases. The simulated FT-STM spectrum (Fig. 3.21), however, does not exhibit such a strong dependence, and leaves both the surface states and the bulk edge positions unchanged. This leads to the conclusion that a major contribution to the differential conductivity stems from the $\bar{\Gamma}\bar{\mathrm{Y}}$ path, i.e. only from the $\mathbf{k}_{||}$-vectors with $k_{[1\bar{1}0]} \cong 0$. This can be understood recalling the $S_h$ mirror symmetry of the Ag(110) surface that leads to extrema of the eigenstate dispersion at $k_{[1\bar{1}0]} = 0$.

The existence of extrema results in an increase of the surface DOS at $k_{[1\bar{1}0]} \cong 0$ (see discussion in Sec. 3.5.5) and consequently explains the dominating contribution from the $\bar{\Gamma}\bar{\mathrm{Y}}$ components. At the same time, contributions with higher values of $\left|\mathbf{k}_{||}\right|$ undergo a faster damping into the vacuum (see, e.g. Eq. (3.2)). Both arguments explain why the $k_{[1\bar{1}0]} \neq 0$ contributions have only a small effect in the FT-STM simulations. However, although these contributions do not play a principal role, their effect on the corresponding FT-STM-spectra (Fig. 3.21) is noticeable and can be also observed experimentally (Fig. 3.7(a) and Fig. 3.8(a)): including the whole Brillouin zone slightly blurs out the spectra in the region of the projected bulk band structure, and adds a quickly vanishing background above the $S_2$ and $S_3$ surface states.

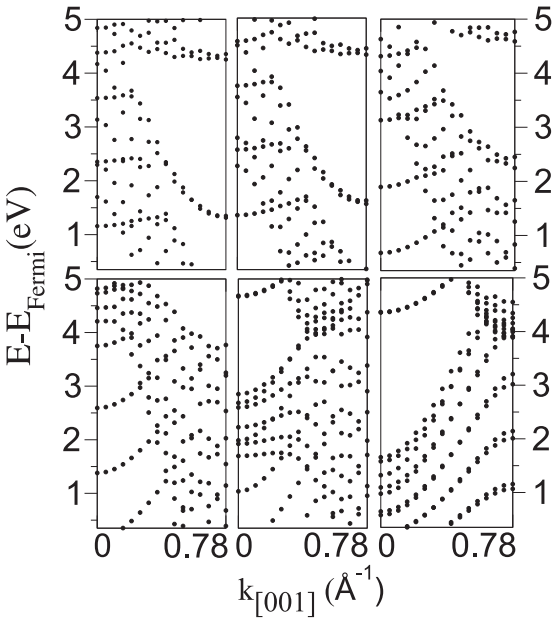


Figure 3.22: Surface band structures for different $k_{[1\bar{1}0]}$-components of the $\mathbf{k}_{||}$-vector. Figures (a)-(f) correspond to $0.0 \cdot \left|\overline{\Gamma X}\right|$, $0.2 \cdot \left|\overline{\Gamma X}\right|$, $0.4 \cdot \left|\overline{\Gamma X}\right|$, $0.6 \cdot \left|\overline{\Gamma X}\right|$, $0.8 \cdot \left|\overline{\Gamma X}\right|$, $1.0 \cdot \left|\overline{\Gamma X}\right|$ values of the $k_{[1\bar{1}0]}$ accordingly. The slab is 15 atomic layers thick.

### 3.5.4 FT-STM simulations with a continuum bulk description

As discussed in Sec. 3.3, a key problem of the current study is to identify whether and how large bulk electrons contribute to the experimental FT-STM profile. In order to perform this analysis, an accurate description of the bulk electrons is essential. As has been shown in the previous section, however, not all the bulk states are allowed in the finite size slab. As will be discussed in the following, an accurate description of the bulk electrons is generally not trivial within the slab approach.

In contrast to the realistic system, which can be considered as a surface resting on a semi-infinite substrate, the slab model contains two surfaces (Fig.2.1). The bulk part has therefore only a finite thickness, and bulk electronic wavefunctions are spatially confined between the two surfaces. This is the origin of the so-called *quantum size effect*.

Apparently, the slab boundary conditions are satisfied not for all bulk Bloch states, but for a discrete set of states commensurable with both surfaces, i.e., for states with nodal points at both surfaces. This leads to a discretization of the allowed bulk states rather than to a continuum as expected for a truly semi-infinite bulk. The origin of such a discretization is very similar to a discretization of allowed quantum states in a Fabri-Perot resonator. To show this one can, e.g., consider the simplest case of a slab with totally reflecting slab surfaces. Considering a slab with thickness $L$ the maximum number of stationary bulk states that fulfils the slab boundary conditions is:

$$N^{\max}(L) = \lfloor \frac{L\,G}{2\pi} \rfloor, \tag{3.31}$$

where $G$ is the length of the first bulk Brillouin zone along the surface normal, and $\lfloor x \rfloor$ is the floor function that return the integer part of the real number $x$.

From Eq. (3.31) it is clear that $N^{\max}(L)$ depends linearly on the slab thickness. On Fig. 3.23(b) the actual number of bulk $d$-states existing in the energy window ($E_{\text{Fermi}} - 1$ eV,$E_{\text{Fermi}} + 4$ eV) is shown as a function of the slab thickness. In agreement with Eq. (3.31) the number of stationary $d$-states is essentially a linear function of the slab thickness (the plateaus on the graph appear due to the relatively low density of bulk states).

Another drawback of the finite thickness of slabs is the distorted local density of states which significantly impacts the FT-STM analysis. Specifically, the bulk electrons are not able to travel away from the surface as they do in the case of a semi-infinite substrate, and are forced to stay in the surface vicinity due to a reflection from the second surface boundary. As a consequence, the LDOS of discretized bulk states is overestimated in the surface and vacuum regions when compared with the same bulk states on the truly semi-infinite surface.

To show this we focus on the bulk $d_{z^2}$-states that are the dominating bulk states in the FT-STM spectrum. As discussed for a case of a single slab (Sec. 3.5.3), for energies below $E_{\text{Fermi}} + 2.5$ eV these states show up in the FT-STM spectrum due to a hybridization with the surface $S_2$ state. To quantify this hybridization we have introduced the overlap integral $F$ as follows:

$$F(E_0, E_1) = \frac{2}{E_1 - E_0} \int_{E_0}^{E_1} dE\, w_{\mathbf{k}_{||}}\, G\left(E - E_{n\,\mathbf{k}_{||}}\right) \times$$
$$\times \left| \left\langle \psi_{n\,\mathbf{k}_{||}} \right| R \left| \mu_{\text{s}}^{\text{surface atom}} + \mu_{\text{p}_\text{z}}^{\text{surface atom}} \right\rangle \right|^2 . \tag{3.32}$$

Here, $w_{\mathbf{k}_{||}}$ is the relative weight of the $\mathbf{k}_{||}$ point, $\mu$ is the atomic wavefunction, $R$ is the real-space sphere that prevents an overlap with neighboring atoms, and $G\,(E)$ is a Gaussian function. The factor 2 in Eq. (3.32) accounts for the spin-degeneracy. The factor $F$ is a measure of the energy averaged overlap of the bulk bands with $s$ and $p_z$ atomic character of a surface atom, that mimics the $S_2$ surface state.

The dependence of $F$ on the slab thickness for slabs from 2 up to 22 atomic layers is presented on Fig. 3.23(a). The factor $F$ for the surface state $S_2$ is slab-independent for slab thickness more than 8 layers. This behavior is expected for a quasiparticle that does not penetrate into the bulk and is therefore not influenced by the thickness of the bulk region. More important is an essential slab-thickness independence of $F$ for bulk states. We conclude, that the pronounced appearance of bulk states at the surface is not a result of the quantum confinement. Consequently, *the energy averaged* signal stemming from the bulk region remains constant when the slab thickness is increased. In the limit of an infinite slab a nonzero bulk contribution will exist in the projected bulk band region.

Since the density of bulk states scales linearly with the slab thickness (Eq. (3.31) and Fig. 3.23(b)), while the energy-averaged bulk-signal remains constant (Fig. 3.23(a)), the intensity of each bulk state linearly decreases when increasing the slab thickness.

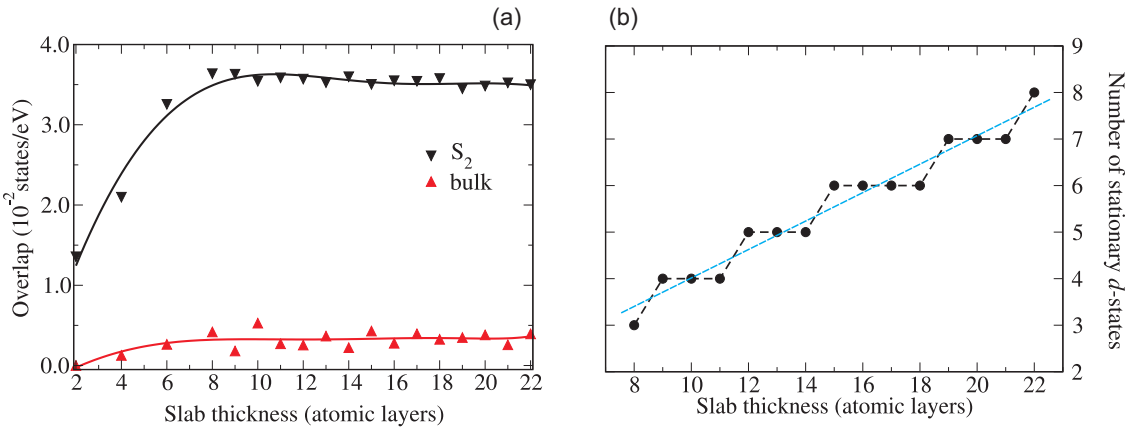


Figure 3.23: (a) Convergence of the $sp_z$ overlap integrals with respect to the slab thickness. The overlap for both the $S_2$ surface state and the bulk state with $sp_z$ atomic orbitals at the surface atoms is shown. The integrals are evaluated according to Eq. (3.32) with $E_0 = E_{\text{Fermi}} + 1.0$ eV and $E_1 = E_{\text{Fermi}} + 2.5$ eV. This choice avoids a contributions from the $S_3$ surface state. The deviation from constant values is due to noise caused by the discrete nature of the allowed bulk bands in the integration energy window. Solid lines are guides to the eye. (b) Number of discretized $d$-states (dots) in the energy window ($E_{\text{Fermi}} - 1$ eV,$E_{\text{Fermi}} + 4$ eV) versus slab thickness. The blue dashed line is a linear fit to the data-points.

The natural way to decrease the quantum size effects is to increase the slab thickness. The increase simultaneously improves both deficiencies. First, it allows more bulk states to match the slab boundary conditions. Second, the surface regions become less important, bulk electrons become less surface localized, and the overestimation of the bulk states at the surface becomes less pronounced. In the limit of an infinitely thick slab all bulk Bloch states become allowed, leading to a complete continuum description of the bulk electronic structure.

In order to obtain accurate FT-STM maps one should therefore systematically increase the slab thickness until a convergence of the theoretical FT-STM profiles is reached. Such an explicit approach is reliable, but computationally too expensive and thus generally not feasible.

In the two following sections we will introduce two alternative novel approaches for correcting finite size effects, that allow to consistently improve the description of the bulk region in the simulated FT-STM spectrum (superposition approach, Sec. 3.5.4.1), or even to get *completely* converged FT-STM maps (projected spectrum approach, Sec. 3.5.4.2).

#### 3.5.4.1 The superposition approach

In this section we propose a simple approach to overcome the effect of the finite slab size in the simulated FT-STM spectra, that we refer to as the superposition approach. The approach uses the electronic structures obtained for thin slabs with various thicknesses to construct a slab with a large effective thickness. This approach is possible, since the slab thickness does not only affect

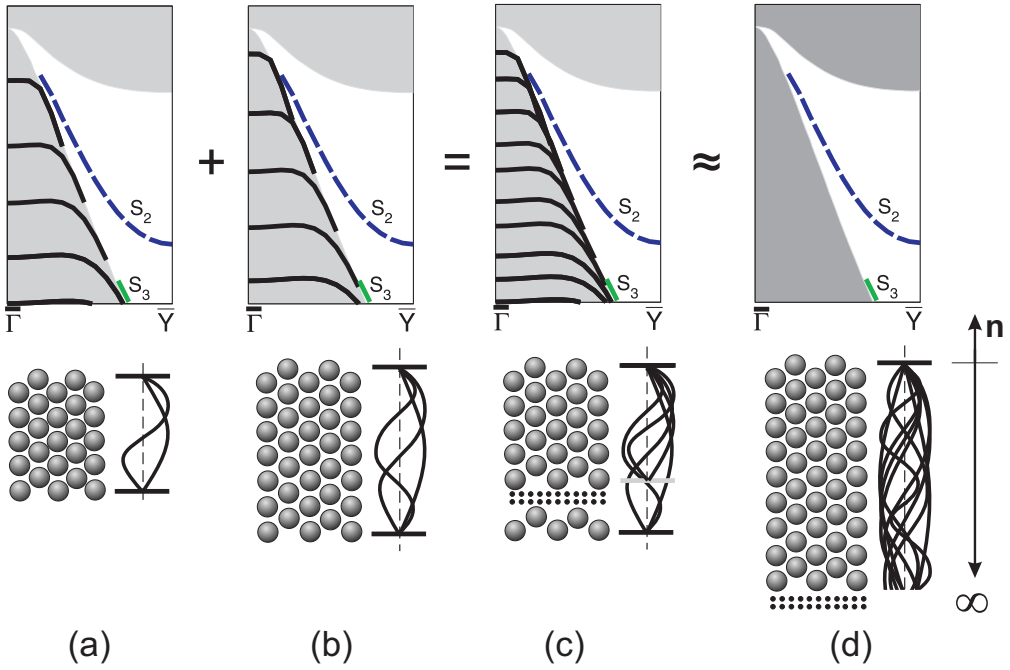


Figure 3.24: Schematic illustration of the formation of discretized bulk states within the slab geometry, and the superposition approach used to improve the bulk description. The surface electronic structure for slabs with varying thickness is shown in the upper row. The corresponding electronic bulk states are given in the lower row. The continuous spectra of the bulk states (grey-shaded regions in figures (a)-(d) upper row) is discretized due to the presence of two surfaces. (a) and (b) sketch the discretized bulk states (black solid lines) corresponding to different slab thicknesses. A superposition of the discretized states in (a) and (b) results in a slab with significantly increased effective thickness (c). This approach improves the description of the asymptotically correct projected bulk bands (d).

the number of the discretized bulk states, but also their energetic position. Thus, the various slabs project out different electronic states from the bulk continuum. Therefore, a simple superposition of the FT-STM spectra of different slabs allows to increase the number of bulk states and thus the effective slab thickness. The method is sketched in Fig. 3.24 and was found to considerably improve the description of the bulk electronic properties. Using this approach FT-STM simulations could be performed which correspond to slabs consisting of several hundred atomic layers.

Employing the superposition approach it is crucial to separate bulk, surface resonance, and surface state contributions, since each type of states possesses different slab-thickness dependencies. For sufficiently large slabs the surface states existing on both slab surfaces are well separated from each other, and the surface state contributions to the FT-STM spectrum are independent of the slab thickness. In contrast, the weight of each discretized bulk state in the vacuum region, and consequently of the FT-STM map, strongly depends on the slab thickness: increasing of the slab thickness smoothly decreases the weight of each bulk state (Sec. 3.5.4). When superimposing FT-

STM spectra corresponding to different slab thicknesses this effect must be taken into account. Specifically, one should perform a rescaling of bulk state contributions such that all superimposed bulk states are treated on the same footing and correspond to one and the same slab thickness.

The superimposed FT-STM map $\eta^{\mathrm{sup}}(k_{[001]}, V)$ is then calculated according to:

$$\eta^{\mathrm{sup}}(k_{[001]}, V) = \sum_{N=N_{\mathrm{min}}}^{N_{\mathrm{max}}} \frac{d_N}{d_{N_{\mathrm{max}}}} \frac{1}{B_N} \eta_N^{\mathrm{slab}}(k_{[001]}, V). \tag{3.33}$$

Here, $\eta_N^{\mathrm{slab}}$ is the FT-STM map obtained with a slab having a thickness of $N$ atomic layers, $N_{\mathrm{min}}/N_{\mathrm{max}}$ is the minimum/maximum slab thickness used in the superposition. $d_N$ is the number of discretized $d$-states in the energy window of interest for a slab of thickness $N$ as shown on Fig. 3.23. $B_N$ is the energy-averaged contribution of bulk states to the FT-STM spectrum for slab $N$:

$$B_N = \int_{E_0}^{E_1} dE \int_{k_0}^{k_1} dk_{[001]}\, \eta_N^{\mathrm{slab}}(k_{[001]}, E), \tag{3.34}$$

where $E_0 = E_{\mathrm{Fermi}} + 0.35$ eV, $E_1 = E_{\mathrm{Fermi}} + 3.00$ eV, $k_0 = \left|\overline{\Gamma}\right|$ and $k_1 = 0.3\left|\overline{\Gamma\mathrm{Y}}\right|$ are chosen to avoid a contributions from surface states.

In the current formulation the first fraction in the right part of Eq. (3.33) accounts for an increase of the bulk state density, while the second fraction ensures a constant intensity of the bulk contribution in the energy window of interest.[4]

We note here that the suggested approach does effectively smear the contribution of the bulk states while keeping the position of the surface states and the ratio between the surface- and bulk-driven signal unchanged.

We have employed Eqs. (3.33)-(3.34) and slabs consisting of 11-22 atomic layers to calculate the *ab initio* superimposed FT-STM spectrum. The results are shown in Fig. 3.30(a). The linear dependence of the bulk states density on the slab thickness (Fig. 3.23(b)) allows to estimate the effective thickness of a slab that would provide a comparable resolution. Such a slab would have to consist of $\sim$220 atomic layers!

Despite getting an improved description of the projected bulk bands on the FT-STM spectrum and obtaining FT-STM maps that can be readily compared with corresponding experimental data (Fig. 3.30(b)), the description of the bulk bands is still not fully complete. We therefore propose novel projected spectrum approach which allows to get a *complete* description of the projected bulk band structure thus to obtain a *complete* FT-STM map.

[4]The factor $B_N$ is required due to the limited number of $d$-states in the energy window of interest, that leads to moderate fluctuations of the energy-averaged bulk contribution (Fig. 3.23). For large slabs (and a large density of $d$-states) $B_N$ converges to a constant value.

#### 3.5.4.2 The projected spectrum approach

The key idea of the projected spectrum approach is to construct a model that accurately reproduces all available *ab initio* FT-STM spectra corresponding to different slab thicknesses and treats the slab thickness as a variable. This allows to use as input for the simulated FT-STM spectra slabs of arbitrary thickness. The parameters entering the model are solely based on (projected from) *ab initio* data.

The model is based on the reciprocal space topology of the electronic states $\alpha$, given by a function $\epsilon_\alpha(k_{[001]})$, existing in the experimentally relevant range of energies and $k_{[001]}$-vectors. To get the model FT-STM spectrum, the weighting function $w_\alpha(k_{[001]})$ is applied to each electronic state, and the resulting model FT-STM spectrum is calculated according to:

$$\eta^{\mathrm{proj}}(\mathbf{k}_{[001]}, V) = \sum_\alpha \epsilon_\alpha(k_{[001]}) \cdot w_\alpha(k_{[001]})\, G(\epsilon_\alpha(k_{[001]}) - E_{\mathrm{Fermi}} - eV), \tag{3.35}$$

where $G(E)$ is a Gaussian function[5].

Both the dispersion $\epsilon_\alpha(k)$ and the corresponding weighting function $w_\alpha(k)$ entering Eq. (3.42) are obtained from the calculated *ab initio* FT-STM spectrum and the surface electronic structure as described in the following.

Obviously, the dominating states in the FT-STM spectrum are in the first place the surface states $S_2$ and $S_3$. Their dispersions $\epsilon_\alpha^{ss}(k)$ are essentially parabola in $k$-space, and their shape is taken directly from the *ab initio* surface band structure (see Fig. 3.25(b)).

The dispersion of the $d$-states is more sophisticated: while at small values of $k$ the state is practically flat, it's shape significantly changes in the vicinity of the projected bulk band edge[6]. This dispersion behavior has a clear physical interpretation: up to a critical value of the $k$-vector the $d$-character essentially remains, resulting in a dispersionless state along $\overline{\Gamma\mathrm{Y}}$. When approaching the edge of the projected bulk bands the $d$-state starts to transform into a $p$-like state. This change of the orbital-character is manifested by a corresponding change of the dispersion. Finally, the $p$-character starts to dominate, and the dispersion of the bulk state coincides with that of the projected bulk band edge. Considering a $d$-state having an energy $E_d$ at $\overline{\Gamma}$ the corresponding model dispersion is given by:

[5]The model given by Eq. (3.35) includes all electronic states stemming from both bulk and surface. However, not all these states are equally important for the simulated FT-STM spectrum. As discussed in Sec. 3.5.3, e.g., bulk $p_x$-states do not show up in the simulated FT-STM map. In the following we focus therefore only on the quasiparticles that contribute to the FT-STM map with a weight of more that 5% compared to the maximum contribution.

[6]The finite-size effects arising in slab calculations do slightly affect the shape of the $\epsilon_\alpha^{\mathrm{bulk}}(k)$ for $d$-states (compare, e.g., Fig. 3.25(a) and (c)). In the current study $\epsilon_\alpha^{\mathrm{bulk}}(k)$ were obtained based on the compute slab band structure calculations.

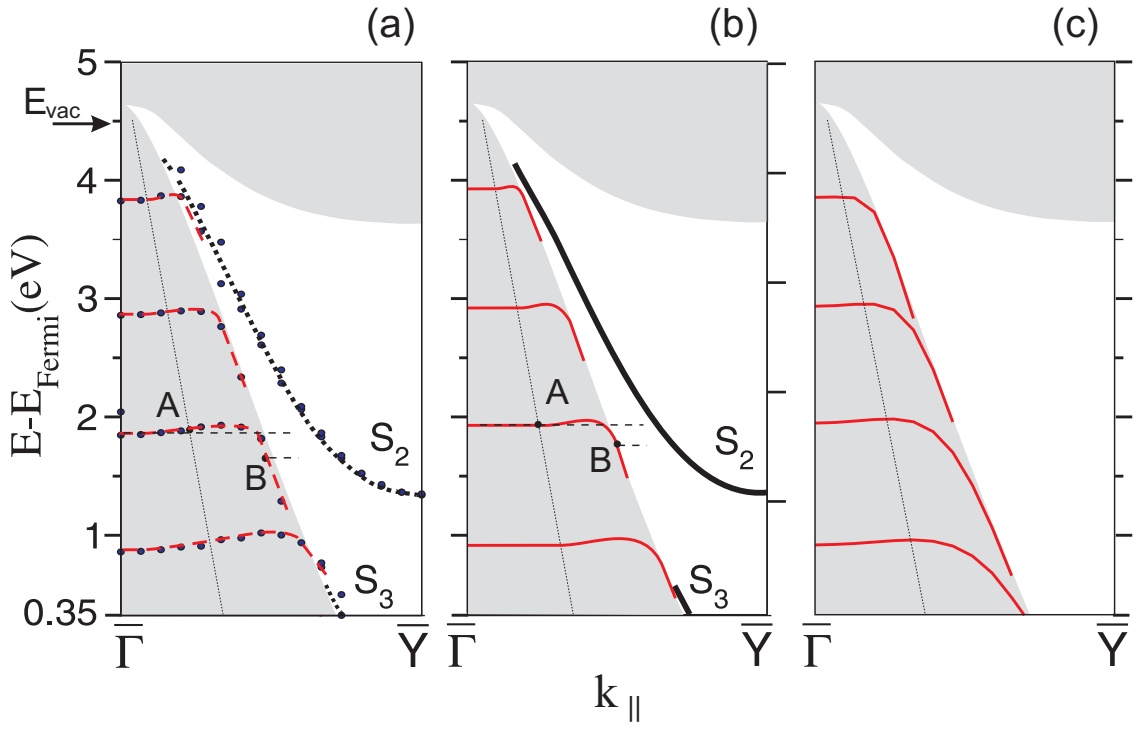


Figure 3.25: Comparison of (a) the *ab initio* surface band structure corresponding to a 19 atomic layers thick slab with (b) the corresponding projected spectrum model and (c) the relevant bulk states from the projected bulk band structure. The points were the $d$-state starts to bend (point A) and were the dispersion of the $d$-state starts to coincide with the dispersion of the projected bulk band edge (point B) are shown for one $d$-state.

$$\epsilon_{\alpha}^{\text{bulk}}(k) = \begin{cases} E_d, & (I)\ \ 0 \le k \le 0.5\ k_{BBE}(E_d), \\ I(k), & (II)\ \ 0.5\ k_{\text{BBE}}(E_d) < k < k_{\text{BBE}}(E_d - S(E_d)), \\ \epsilon_{\text{BBE}}(k), & (III)\ \ k \ge k_{\text{BBE}}(E_d - S(E_d)), \end{cases} \tag{3.36}$$

where $S(E) = -0.05 \cdot (E - E_{\text{Fermi}}) + 0.2$ eV accounts for the energy-dependent bending of the $d$-states in the vicinity of the projected bulk band edge. A geometrical interpretation of the function $S(E)$ is shown in Fig. 3.25(b): the function $S(E)$ defines the width of the energy window between the point where the $d$-state starts to bend (see, e.g., point A on Fig. 3.25(b)) and the point where the dispersion of the $d$-state starts to coincide with the edge of the projected bulk bands (see, e.g., point B on Fig. 3.25(b)). $k_{\text{BBE}}(E)$ and $\epsilon_{\text{BBE}}(k)$ in Eq. (3.36) are the dispersion relations for the projected bulk band edge (taken from the bulk calculations), and $I(k)$ is a sixth-order polynomial that interpolates between regions $(I)$ and $(III)$.

The shape of the $d$-states in **k**-space described by Eq. (3.36) is shown in Fig. 3.25(b), where it can be directly compared with the corresponding $d$-states obtained by a slab geometry (Fig. 3.25(a)) or by bulk calculations (Fig. 3.25(c)).

The weighting functions $w_\alpha(k)$ are deduced from a comparison of the FT-STM spectrum with the corresponding slab band structure. The weighting functions for $S_2$ and $S_3$ are taken to be constant up to energies $E_{\text{offset}} = E_{\text{Fermi}} + 3.8$ eV and $E_{\text{offset}} = E_{\text{Fermi}} + 0.4$ eV, correspondingly. For higher energies the weights are exponentially fading out since the surface state undergoes a smooth transition to a bulk state (see, e.g. Fig. 3.19), i.e. the $w_\alpha(k)$ for the surface states are chosen as:

$$w_\alpha^{\text{ss}}(k) = \begin{cases} 1, & \epsilon_\alpha(k) < E_{\text{offset}}, \\ \exp(-A_1^{\text{ss}}\,(\epsilon_\alpha(k) - E_{\text{offset}})^{m^{\text{ss}}}), & \epsilon_\alpha(k) \geq E_{\text{offset}}, \end{cases} \tag{3.37}$$

where parameters $A_1$ and $m$ define the speed of the fading for the $S_2$ and $S_3$ states.

We have found that in case of the bulk $d$-states the following expression for a weighting function provides an excellent agreement with an *ab initio* FT-STM spectrum:

$$w_\alpha^{\text{bulk}}(k) = \begin{cases} D(k, \epsilon_\alpha^{\text{bulk}}(k)), \\ \qquad\qquad (I)\ \ 0 \leq k \leq 0.5\ k_{\text{BBE}}(\epsilon_\alpha^{\text{bulk}}(0)), \\ \exp(-A_2|\epsilon_\alpha^{\text{bulk}}(k) - \epsilon_\alpha^{\text{bulk}}(0)|) \cdot D(k, \epsilon_\alpha^{\text{bulk}}(k)), \\ \qquad\qquad (II)\ \ 0.5\ k_{\text{BBE}}(\epsilon_\alpha^{\text{bulk}}(0)) < k < k_{\text{BBE}}(\epsilon_\alpha^{\text{bulk}}(0) - S(\epsilon_\alpha^{\text{bulk}}(0))), \\ \exp(-A_3|\epsilon_\alpha^{\text{bulk}}(k) - \epsilon_\alpha^{\text{bulk}}(0)|) \cdot D(k, \epsilon_\alpha^{\text{bulk}}(k)), \\ \qquad\qquad (III)\ \ k \geq k_{\text{BBE}}(\epsilon_\alpha^{\text{bulk}}(0) - S(\epsilon_\alpha^{\text{bulk}}(0))), \end{cases} \tag{3.38}$$

where regions $(I)$-$(III)$ are identical to those in Eq. (3.40), since $\epsilon_\alpha^{\text{bulk}}(0) \equiv E_d$ by construction (see Eq. (3.40)).

According to Eq. (3.38) the weighting function for bulk $d$-states consists of two terms. The first term, referred to as $D(k, E)$, accounts for drop in the transmissivity for a quasiparticle when its $\mathbf{k}_{||}$-component is increased. Assuming for simplicity a flat effective vacuum potential of height $E_{\text{vac}} = E_{\text{Fermi}} + \phi$ ($\phi = 4.5$ eV is the surface work function) and an $(x, y)$-independent surface wavefunction with an in-plane component of the wavevector $\mathbf{k}_{||}$, the corresponding LDOS at a distance $z$ above the surface can be written as (Eq. (3.2)):

$$LDOS(\mathbf{k}_{||}, z) = LDOS(\mathbf{k}_{||}, 0) \exp(-2\sqrt{(\alpha^2 + \mathbf{k}_{||}^2)}z), \tag{3.39}$$

where $\alpha^2 = 2m\phi/\hbar^2$, and $m$ is the free electron mass.

Since in the constant current regime $z$ depends on the applied bias voltage, we define the damping function $D(k, E)$ as:

$$D(k, E) = \frac{\exp(-2\sqrt{(\alpha^2 + k^2)}z(E))}{\exp(-2\alpha\ z(E))}, \tag{3.40}$$

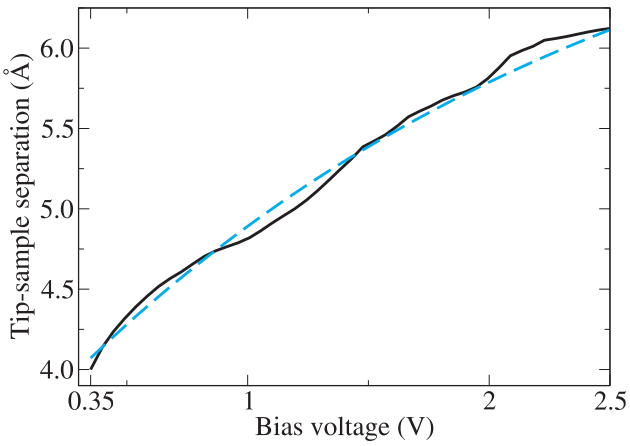


Figure 3.26: Dependence of the averaged tip-surface separation on the applied bias voltage for the Ag(110) surface. The *ab initio* curve (solid line) is obtained by superimposing corresponding curves from 2-22 atomic layer thick slabs. The blue dashed curve is a result of the exponential fitting according to Eq. (3.41) with fit parameters from Tab. 3.2. The averaged tip-surface separation at bias +0.35 V is chosen to be 4 Å.

where the denominator in Eq. (3.40) ensures that the $D$-function becomes 1 at the $\overline{\Gamma}$-point. $z(E)$ is the energy-dependent tip-surface separation that is due to the constant-current regime of the STM.

The tip-surface separation $z(E)$ in Eq. (3.40) is obtained by fitting an exponential function of the form:

$$z(E) = A_4 + A_5 \exp(A_6 \cdot E), \tag{3.41}$$

to the *ab initio* dependence obtained when the FT-STM spectrum is calculated directly employing Eq. (3.17). The comparison of the fitted and the *ab initio* $z(E)$ is shown in Fig. 3.26.

The second term in Eq. (3.41), namely, the exponential function, accounts for a change from $d$- to $p$-character close to the edge of the projected bulk bands. This transition affects the shape of the bulk states $\epsilon_\alpha^{\text{bulk}}(k)$) (regions $(II)$ and $(III)$) and introduces an additional damping to the $d$-states.

The final projected spectrum FT-STM map is then calculated as:

$$\eta^{\text{proj}}(k_{[001]}, V) = \sum_{\alpha=S_2,S_3} \epsilon_\alpha^{\text{ss}}(k_{[001]}) \cdot w_\alpha^{\text{ss}}(k_{[001]})\, G(\epsilon_\alpha^{\text{ss}}(k_{[001]}) - E_{\text{Fermi}} - eV) +$$

$$+ \frac{A_0}{N} \sum_{\alpha=1}^{N} \epsilon_\alpha^{\text{bulk}}(k_{[001]}) \cdot w_\alpha^{\text{bulk}}(k_{[001]})\, G(\epsilon_\alpha^{\text{bulk}}(k_{[001]}) - E_{\text{Fermi}} - eV), \tag{3.42}$$

where $A_0$ defines the ratio between the surface- and bulk-driven contributions, and $\frac{1}{N}$ ensures that the energy averaged contribution stemming from the bulk electrons remains constant when the

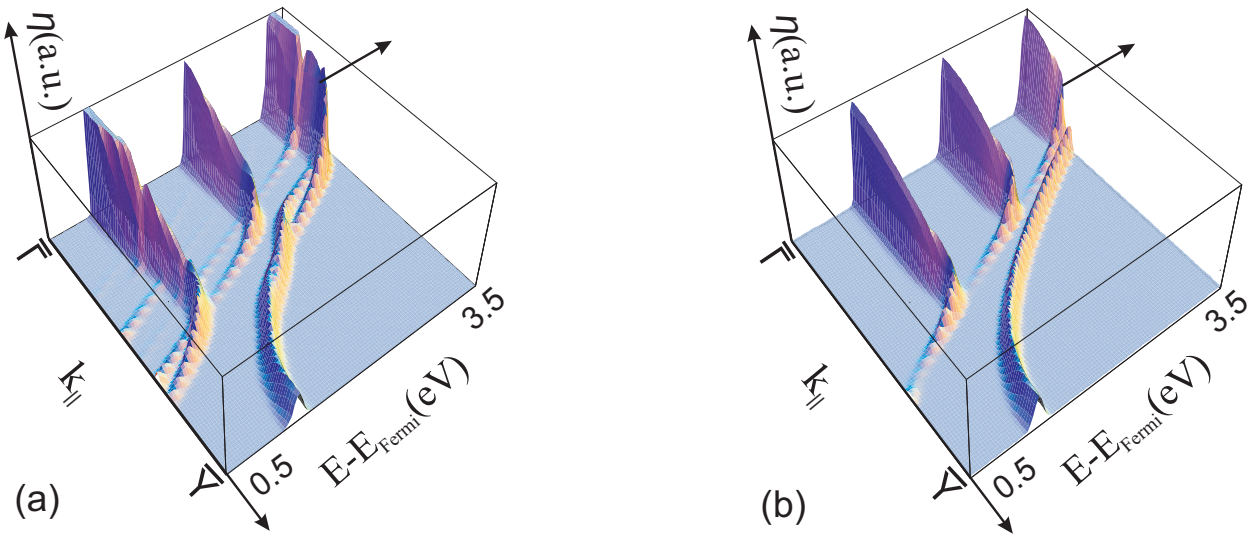


Figure 3.27: Comparison of (a) the *ab initio* FT-STM spectrum corresponding to a 15 atomic layers thick slab with (b) the FT-STM map obtained according to the projected spectrum approach.

number of bulk $d$-states $N$ is changed.[7]

To get the input parameters for the projected spectrum model we have performed a fitting to an *ab initio* FT-STM obtained for a 15 atomic layers thick slab. The resulting model FT-STM map together with the corresponding *ab initio* counterpart are shown in Fig. 3.27. The values of the fitted parameters are summarized in Tab. 3.2.

From Fig. 3.27 it is clear that the projected spectrum model captures all essential features of the *ab initio* FT-STM spectrum, like the ratio between the surface and bulk states, the shape and intensity of the contributions originating from the bulk and surface quasiparticles.

| Parameter | $A_0$ | $A_1^{S_2}$ | $A_1^{S_3}$ | $m^{S_2}$ | $m^{S_3}$ | $A_2$ | $A_3$ | $A_4$ | $A_5$ | $A_6$ |
|---|---|---|---|---|---|---|---|---|---|---|
| Value | 5.5 | 10 | 50 | 2 | 2 | 5 | 4 | 7.24 Å | 3.67 Å | -0.48 $\text{eV}^{-1}$ |

Table 3.2: Summary of the parameters defining the weighting function $w_\alpha$ in the projected model approach. Parameters are obtained by a fit to the *ab initio* FT-STM spectrum obtained for a 15 atomic layers thick slab.

To verify the accuracy and robustness of the model we have compared first the *ab initio* FT-STM spectrum calculated for a 19 atomic layers thick slab using the projected spectrum model and using identical parameters as fitted for the 15 layer slab. The resulting spectra are shown

[7] In case of the projected spectrum approach the contribution of the surface states does not depend on the number of bulk states (or, equivalently, on the modeled slab thickness). In contrast, in the superposition approach, increasing the number of bulk $d$-states by summing FT-STM maps corresponding to different slab thicknesses affects both the intensity of the bulk and surface states (Eq. (3.33)). Despite of this, the superposition and the projected spectrum approach are completely equivalent (up do a constant prefactor) because both methods keep the ratio between bulk- and surface-driven contributions to the FT-STM spectrum unchanged.

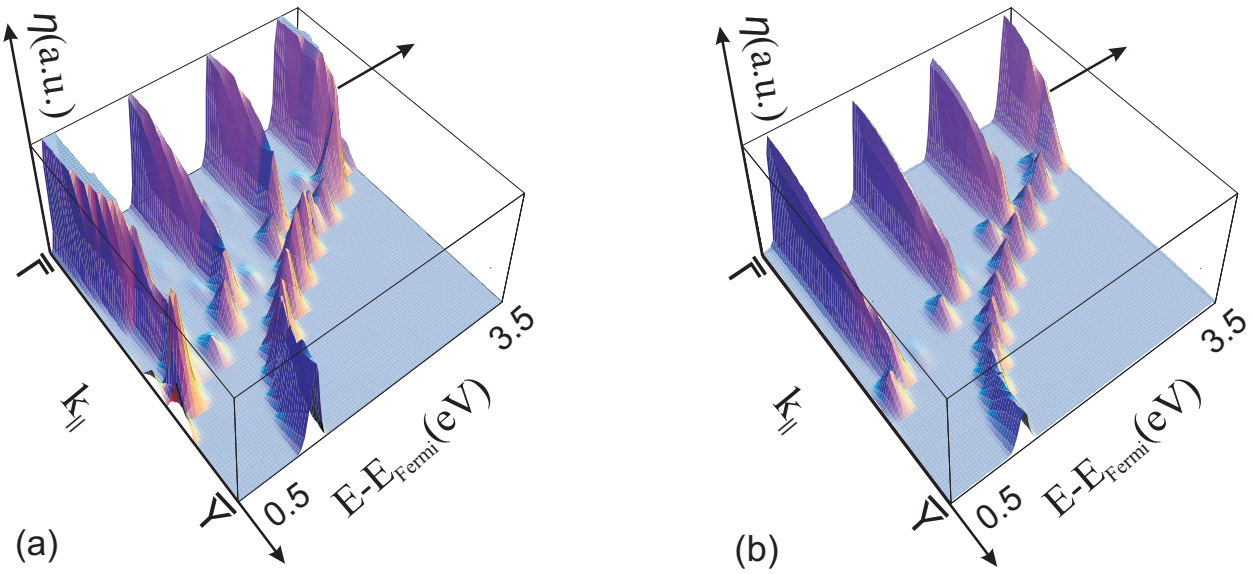


Figure 3.28: Validity check of the projected spectrum model. (a) *Ab initio* FT-STM spectrum corresponding to a 19 atomic layers thick slab is compared with (b) The FT-STM map obtained according to the projected spectrum approach. The model parameters have been taken from a slab consisting of 15 atomic layers (see Tab. 3.2).

in Fig. 3.28. The comparison reveals an excellent agreement between the two spectra in the bulk region, although the model $S_2$ state appears to be slightly underestimated compared to full *ab initio* calculation.

A further verification of the projected spectrum model is obtained by comparing with the resulting superimposed spectrum (Sec. 3.5.4.1). The corresponding spectra are shown on Fig. 3.29(a)-(b). The simulated spectra are in excellent agreement, showing essentially a homogeneous contribution due to bulk states and with a dramatic increase at the edge of the projected bulk bands.

Since the projected spectrum model accurately captures all essential features of the *ab initio* FT-STM spectrum it is possible to get *the complete* FT-STM spectrum by increasing the number of bulk states until the signal stemming from the projected bulk band region is converged. Moreover, since the projected spectrum model is computationally inexpensive, it is easy to get a dense sampling along the energy- and **k**-axises.

Since the number of the allowed bulk states is a function of the slab thickness, the model simulation corresponds to a FT-STM spectrum obtained for an virtually infinitely thick substrate. The resulting converged projected model FT-STM spectrum is shown in Fig. 3.29(c).

### 3.5.5 Discussion

The final theoretical FT-STM maps calculated employing the superposition and the projected spectrum approach are shown in Fig. 3.30(a) and (c), respectively. The corresponding surface band

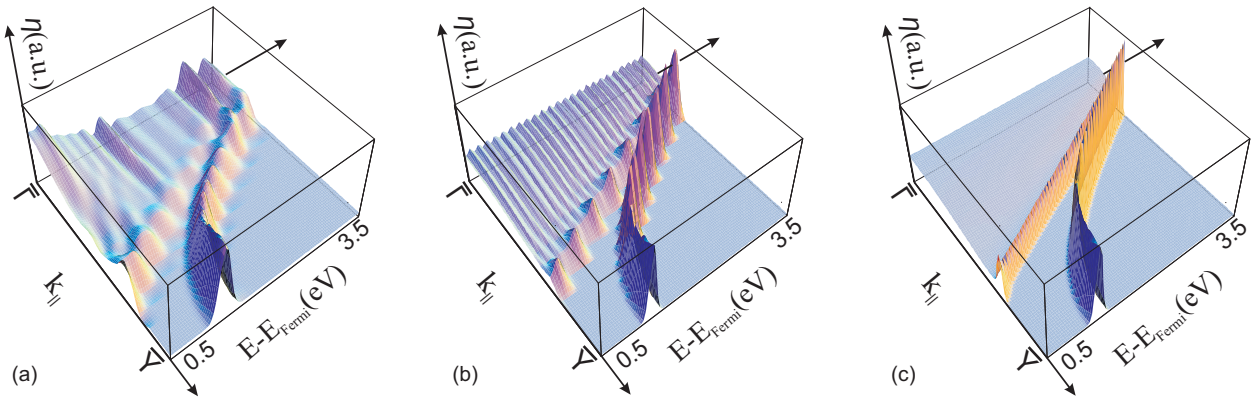


Figure 3.29: Comparison of (a) the *ab initio* FT-STM spectrum obtained according to the superposition approach with (b) the corresponding projected spectrum model. (c) Converged projected spectrum FT-STM map.

structure is drawn in Fig. 3.31(a), where for clarity only the quasiparticle states relevant for STM are shown.

The calculated data allow a consistent explanation of the experimental spectra presented in Figs. 3.7-3.8. The simulations reveal that the surface states $S_2$ and $S_3$ dominate the FT-STM spectrum, as expected for a surface sensitive tool like STM. Therefore, the relatively weak signals from bulk are completely hidden by the strong surface state signal in the energy regions where they are present and cannot be detected experimentally.

There is, however, an energy window where the surface states do not show up, i.e., between 0.5 eV and 1.37 eV above the Fermi level (*ab initio*), and between 0.25 eV and 1.7 eV (experimentally)[8]. In this energy window the nonvanishing contribution stemming from the bulk states becomes visible in STM. As discussed in Sec. 3.5.3, the appearance of the background signal in the *whole* projected bulk band region is caused by probing the continuum of the $d_{z^2}$-bulk electronic states, that extend into the vacuum and become accessible for STM tips due to a hybridization with the $S_2$ surface state.

Despite the fact the in principle the whole projected bulk band structure contributes to the FT-STM spectrum, only the part that is located at the projected bulk band edge and that behaves like a weak surface state is probed in experiments. This effect is perfectly reproduced in the simulated FT-STM maps, where the bulk contribution at the BBE possesses a kink and is therefore superior over the vicinal projected bulk region. To highlight this effect the cuts of the simulated FT-STM spectra at $E = E_{\text{Fermi}} + 1.0$ eV are presented on Fig. 3.31(d). It is noticeable, that the signal stemming from the bulk electrons exponentially decays with $k_{[110]}$, apart from the projected bulk band edge, where the intensity of the bulk signal shows an abrupt increase. Despite of the fact,

[8]Possible sources of discrepancy between the calculated and experimental energy range are (i) the approximate parametrization of the exchange-correlation functional (LDA) and (ii) the negligence of an electrical field, that might affect the position of the higher-lying surface state.

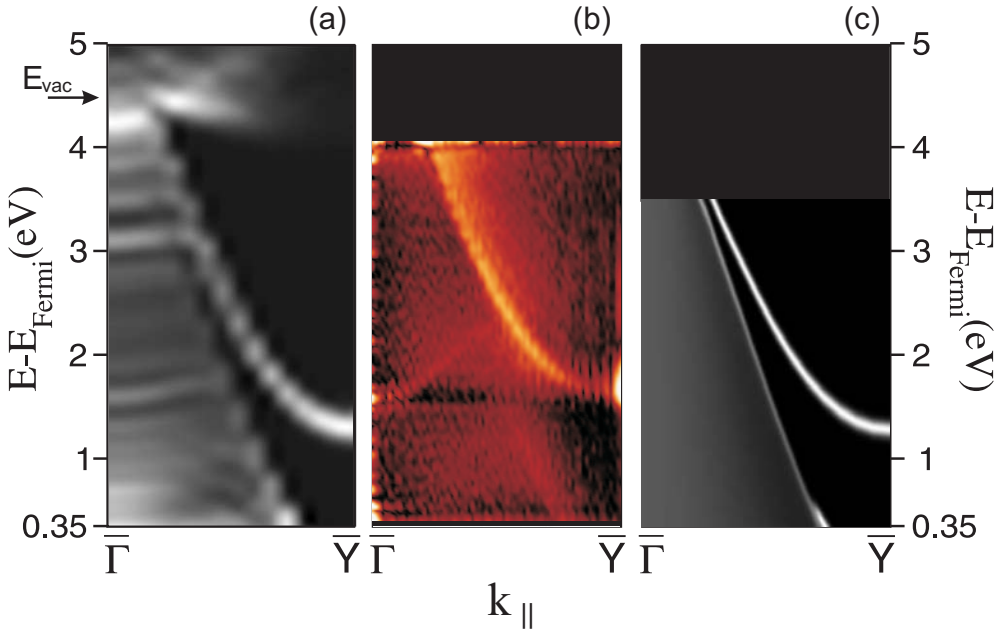


Figure 3.30: Comparison of the calculated and experimental FT-STM spectra on the Ag(110) surface. (a) Superposition approach for slabs consisting of 11-22 atomic layers. The arrow indicates the theoretical vacuum level. (b) Experimental FT-STM spectrum acquired on a one-side confined terrace (see Sec. 3.3 for details). (c) Projected-spectrum simulation corresponding to a complete description of the bulk electronic structure.

that the bulk signal in the vicinity of $\overline{\Gamma}$ is not negligible on the simulated maps, and has the same order of magnitude as the contribution from the BBE itself, the experimental accessability of these states might be complicated. This is due to (i) the large period of the standing waves with $k_{[110]}$ close to $\overline{\Gamma}$ and (ii) a superposition of different standing waves with similar intensities but slightly different $k_{[110]}$ that leads to the formation of a signal that is hardly distinguishable from the constant background, taking into account that the distances employed for recording the real-space standing waves of $dI/dV$ are relatively small. In the processing of the real-space oscillations of the $dI/dV$ signal the bulk signal from the vicinity of $\overline{\Gamma}$ is then filtered out together with a background contribution and therefore does not show up in the experimental maps shown in Figs. 3.7-3.8.

We focus now on the vicinity of the projected bulk band edge. Here, the bulk $d_{z^2}$-states undergo a transition to a $p_x$-electronic character. Due to this transition these states become more surface-localized and consequently disappear from the FT-STM spectrum. However, due to the smoothness of the transition, the $p_x$-states are nevertheless partially detectable. At the edge of the projected bulk bands the traces of the $d_{z^2}$-states overlap with each other, resulting in an increased signal there as compared with the rest of the projected bulk band structure (Fig. 3.31(d)). To highlight the origin of such an increase the line profiles from the FT-STM maps are also compared with the density of the corresponding bulk states. Obviously, the position of the peaks of the projected

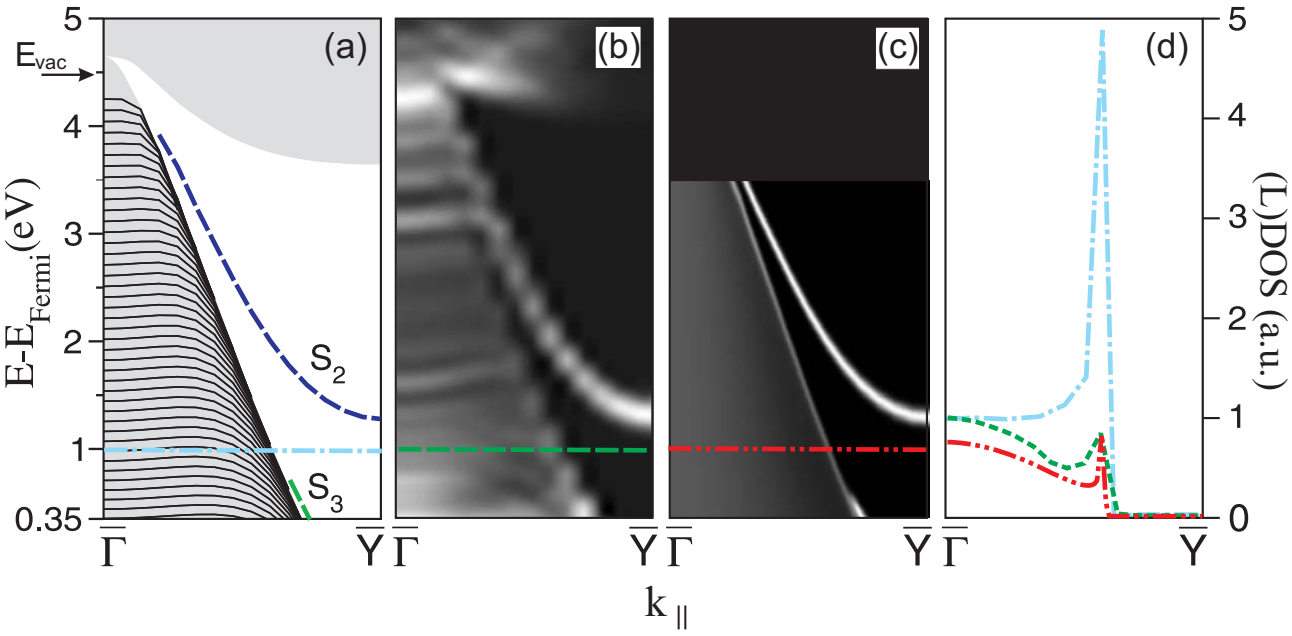


Figure 3.31: (a) Calculated surface band structure where only electronic states contributing to FT-STM are shown. Projected bulk bands (shaded area) and surface states (dashed curves) are shown. Bulk states forming the projected bulk band structure below $E = E_{\text{Fermi}} + 4$ eV are shown as thin black lines; a discrete set of bulk states is given for better visualization. (b) Simulated FT-STM map obtained by the slab-superposition approach. (c) Simulated FT-STM map obtained by the projected-spectrum approach. (d) Density of bulk states contributing to the FT-STM simulation along $k_{||}$ (dash-dotted blue line) and the corresponding FT-STM signal from (b) and (c) shown as dashed green and dash-double-dotted red line, respectively. All cuts are shown as horizontal lines on (a)-(c) and correspond to $E = E_{\text{Fermi}} + 1$ eV.

bulk DOS and of the corresponding FT-STM line-profile coincide with each other, and are located precisely at the BBE. The appearance of the BBE signal in the experimental FT-STM spectrum thus reflects the high density of bulk states there. It should be emphasized, however, that a high density of bulk states alone does not guarantee that the bulk states will be probed in the FT-STM experiments. This is because the STM tip operates at 5-10 Å above the surface, and the decay of the various different electronic states into the vacuum has to be treated explicitly. As illustration, one can compare the density of all bulk states at $E = E_{\text{Fermi}} + 1.0$ eV (Fig. 3.16(b)) with the corresponding DOS including only STM-relevant states (Fig. 3.31(d)). Below $E = E_{\text{Fermi}} + 1.3$ eV the projected bulk band structure possess two peaks in the DOS, but only one is visible for STM due to the low penetration of $p_x$-states into the vacuum.

To identify the origin of the kinks in the projected bulk DOS on Fig. 3.31(a) and (d) we analyze the **k**-space topology of the bulk states that form the (110) projected bulk band structure. Only the $\overline{\Gamma} - \overline{\text{Y}}$ part of the surface Brillouin zone and energies $E_{\text{Fermi}} < E < E_{\text{Fermi}} + 3.0$ eV are considered. We find that only one bulk band exists in this range of energies (see, e.g., Fig. 3.13(a)). The

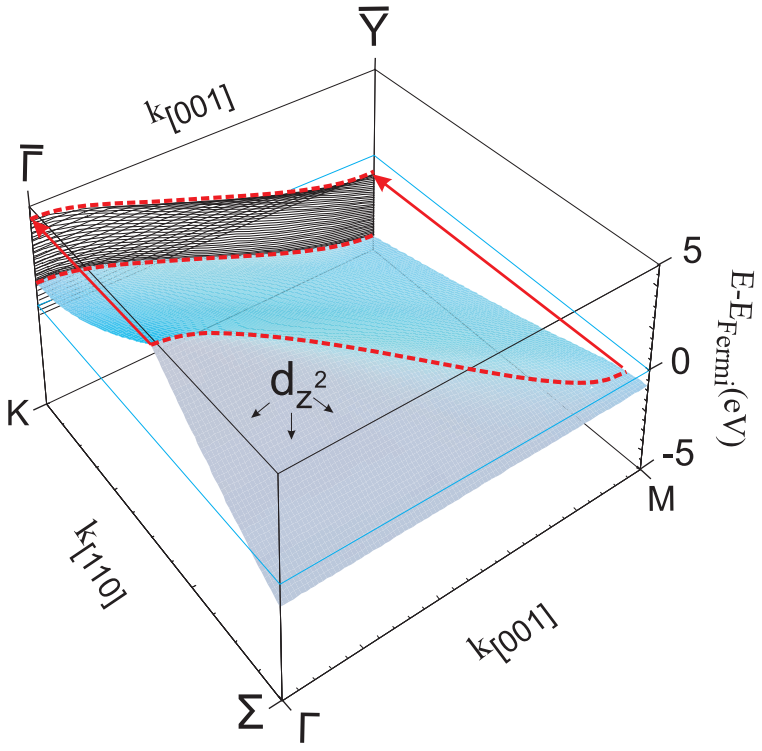


Figure 3.32: Topology of the calculated one-particle band responsible for the formation of the projected bulk band structure along the $\overline{\Gamma} - \overline{\mathrm{Y}}$ $\mathbf{k}_{||}$-path in the vicinity of the Fermi level. The red dashed lines on the surface highlight the positions of extrema along the surface normal ($k_{[110]}$-direction), which causes the increased density of bulk states when projected along the [110] direction (compare the thin black lines obtained by integrating the bulk state along [110]-direction with Fig. 3.15(a)). The thin horizontal blue line indicates the Fermi level.

topology of this bulk band versus the $k_{[110]}$ and $k_{[001]}$ vectors is plotted in Fig. 3.32. The projected bulk band structure (Fig. 3.15(a)) is formed by integrating this band along the surface normal $k_{[110]}$.

From Fig. 3.32 it is immediately clear that the peaks of the projected bulk DOS are due to a three-dimensional bending of the bulk band, and are associated with regions where $d\epsilon(\mathbf{k})/dk_{[110]} = 0$, i.e. where the quasiparticle band goes through a maximum or minimum value along the surface normal (shown as green and red dashed curves, Fig. 3.32)[9]. As mentioned before, however, despite the fact that the dispersion of the bulk state possesses two exterema and consequently gives rise to two peaks in the projected DOS, only one of the peaks shows up in the STM experiments.

In a general case it can be shown that the density of electronic states $g(E)$ is given by (see

[9]The existence of kinks in the bulk density of states has been discovered already several decades ago. Such singularities were first analyzed by the Dutch physicist Léon van Hove for the case of a phonon density of states. These singularities are therefore commonly referred as van Hove singularities [184, 191–194]. Although the discussion of van Hove was focused on singularities in the phonon DOS, the results and conclusions are equally applicable for the case of electronic states.

App. A.3):

$$g(E) = \frac{V}{(2\pi)^3} \sum_i \int_{S_E} \frac{dS_E}{|\nabla \epsilon_i(\mathbf{k})|}, \tag{3.43}$$

where $V$ is the crystal volume, $i$ is the index of the electronic band, $\epsilon_i(\mathbf{k})$ is the dispersion of the quasiparticle in $\mathbf{k}$-space, and $S_E$ is the surface in $\mathbf{k}$-space for which $\epsilon_i(\mathbf{k}) = E$.

From Eq. (3.43) it follows that the integrant increases with decreasing dispersion, and becomes singular where $\nabla \epsilon_i(\mathbf{k}) = 0$. This condition defines a van Hove singularity and the corresponding $\mathbf{k}$ is the critical point. Different types of critical points for van Hove singularities in three-, two- and one-dimensions are discussed elsewhere [192, 195].

In case of a surface the presence of the kinks in the projected bulk DOS is conceptually similar to van Hove singularities. The projection of the three-dimensional bulk electronic structure onto the two-dimensional surface electronic structure effectively yields an integration over the bulk states along the surface normal for each $\mathbf{k}_{||}$, which formally similar to Eq. (3.43). In case of a surface, Eq. (3.43) reduces, therefore, to the one-dimensional case, and the appearance of the kinks in the resulting projected bulk DOS $g_{\mathbf{k}_{||}}(E)$ can be considered as indication of a one-dimensional van Hove singularity where $|\nabla_{k_\perp} \epsilon_i(\mathbf{k})| = 0$.

The above-discussed formation of peaks in the projected bulk band structure is illustrated in Fig. 3.33, where the simplest case of a system consisting of two electron bands is considered. We note, that the enhancement of the projected DOS at the edge of the projected bulk bands is a necessary condition for the formation of projected bulk band pockets, as schematically shown in Fig. 3.33. Since the BBE separates the region of forbidden bulk states from a region of allowed bulk states, the dispersion of the bulk state that is projected onto a surface must necessary possess a global maximum or minimum along the surface normal. The accumulation of the bulk states at the BBE is therefore a completely general phenomenon, that is not restricted to the considered case of a Ag(110) surfaces. We therefore conclude that this mechanism can be employed to facilitate the observation of the projected bulk band edges on other surfaces.

## 3.6 Summary

As presented in this chapter, we have performed an in-depth interpretation of the FT-STM spectra measured on Ag(110) surfaces. Our analysis has proven that local dispersion properties of the bulk electrons can be observed within STM. In order to obtain these results we had to develop the theoretical model for simulating the FT-STM experiments. The model has been implemented into multiscale library S/PHI/nX [37, 38], and can be employed for theoretical analysis of the further FT-STM experiments.

The resulting theoretical FT-STM spectra are in excellent agreement with experimental data. It has been found that in the experimentally relevant range of energies the FT-STM spectrum

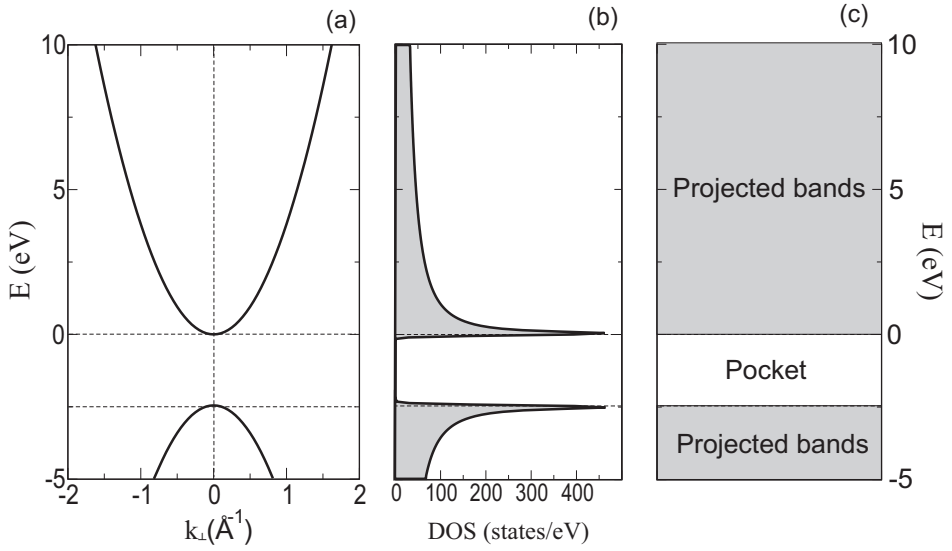


Figure 3.33: Schematic view graph of the projection of bulk electronic bands onto a surface at a given $\mathbf{k}_{||}$ yielding a pocket in the projected band structure and correspondingly an enhancement in the projected DOS at the edge of the pocket. (a) The dispersion of the two electronic bands along the surface normal $k_\perp$ is shown. The higher-lying band dispersion is given by $\epsilon(k_\perp) = \frac{\hbar^2}{2m}k_\perp^2$, where $m$ is the free electron mass. The lower-lying band dispersion is given by $\epsilon(k_\perp) = -2.5$ eV$-\frac{\hbar^2}{2m}k_\perp^2$. (b) Density of states for the band structure shown in (a). (c) Schematic structure of the resulting projected bulk band structure at a given $\mathbf{k}_{||}$.

includes contributions from two surface states dominating the FT-STM spectra, and a nonvanishing contribution stemming from the bulk states. A detailed theoretical analysis of the surface electronic properties showed that an energy gap between the surface states exists, where only bulk states are present. At these energies (between $E = E_{\text{Fermi}} + 0.25$ eV and $E = E_{\text{Fermi}} + 1.70$ eV experimentally, and $E = E_{\text{Fermi}} + 0.50$ eV and $E = E_{\text{Fermi}} + 1.37$ eV theoretically) the bulk states are not screened by surface states. Consequently, at these energies the bulk electronic properties might become accessible for STM.

Indeed, it is shown that the whole continuum of the bulk states contributes to the FT-STM spectrum. The contribution of bulk electrons is of particular importance at those energies where surface states are absent. In agreement with experiment it is found, that the contribution stemming from the edge of the projected bulk band structure (BBE) is superior over the rest of the projected bulk bands. The contribution from the BBE is similar to a (albeit weak) surface state, allowing to detect the topology of the BBE in reciprocal space.

A theoretical analysis allowed for a detailed understanding of this effect. It showed, that not all the bulk states do equally contribute to the simulated FT-STM spectrum. Specifically, only bulk states with $d_{z^2}$-orbital character become relevant for the FT-STM experiments since only these bulk states hybridize with the surface state. The density of these bulk states (DOS) is dramatically

increased at the BBE, leading to a superior role of the BBE signal in FT-STM maps.

The physical effect underlying the increase of the density of bulk states at the BBE is conceptually similar to the appearance of van Hove singularities in the bulk density of states, and is due to a three-dimensional bending of bulk states. The bending might lead to the existence of critical points where the dispersion of a bulk state goes through an extremum along the surface normal, i.e. where $|d\epsilon(\mathbf{k})/dk_{\perp}| = 0$. These critical points in the bulk Brillouin zone result in the appearance of kinks in the surface projected DOS.

The appearance of kinks in the projected bulk DOS is not specific to the Ag(110) surfaces only, but is a general phenomenon. Moreover, the enhancement of the projected DOS at the edge of the projected bulk bands is a necessary condition for the formation of projected bulk band pockets, as schematically shown on Fig. 3.33. This is because at each given $\mathbf{k}_{||}$ the BBE by definition separates a region of the allowed bulk states from a region of forbidden bulk states, which is possible only if the dispersion of the projected bulk state goes through a global maximum or minimum along the surface normal. We argue, therefore, that the high density of projected bulk bands at the BBE might facilitate the observation of projected bulk band edges by STM also on other surfaces.

The model used for FT-STM simulations is based on a high-voltage extension of the widely used Tersoff-Hamann model of the STM. It assumes that surface imperfections act onto the surface wavefunctions like infinite potential barrier. These assumptions allow to significantly reduce the computational demands for simulating FT-STM spectra and to calculate them employing the chemical unit cell of the ideal unperturbed surface.

The surface properties have been calculated invoking a slab approach within plane-wave DFT. With a realistic choice of the plane-wave basis set it has been shown that an accurate description of the vacuum region is limited to several angstrom above the surface. However, larger distances are required to simulate the FT-STM spectrum acquired in the constant current regime. To accomplish this task a new approach has been proposed, that allows to overcome the above mentioned deficiency of the plane-wave basis set and to calculate FT-STM spectrum remaining in that part of the vacuum region where surface wavefunctions are accurately described.

The effect of a limited slab size on the simulated FT-STM spectra, with emphasis on bulk electronic properties, has been discussed. It has been shown that quantum-size effects are crucial and need to be taken into account to get converged theoretical FT-STM spectra. Two different approaches that consistently avoid quantum-size effects in the simulated FT-STM maps have been proposed.

The first approach (Sec. 3.5.4.1) is based on a superposition of FT-STM spectra corresponding to different slab thicknesses, resulting an improved description of the bulk electronic properties. The second approach (Sec. 3.5.4.2) is based on the separation of the FT-STM spectrum into surface and bulk-dependent parts, making it possible to project *ab initio* FT-STM spectra onto a simple model capturing all essential features of the *ab initio* FT-STM spectrum. The parameters of the model are then consistently changed until the converged FT-STM spectrum is obtained.

The resulting FT-STM spectra can be considered as reference for experiments, where the LDOS of a homogeneous surface plays the dominating role, and the tip effects are not essential.

# Chapter 4

# Spin-polarized STM on antiferromagnetic $Mn_3N_2(010)$ surfaces

Nanoscale magnetism is a topic of increasing interest, having potential applications in diverse fields ranging from the development of ultra-fine grained materials to advanced data storage and spin-based electronics. For future development of these fields it is essential to explore properties of new magnetic materials with the highest possible spatial resolution. One of the most powerful magnetic-sensitive techniques that provides insight into magnetic properties of thin films, surfaces and nanostructures is the novel spin-polarized scanning tunneling microscopy (SP-STM) [196]. This microscopy technique offers spin sensitivity combined with the well-known advantage of STM, namely, spatial resolution down to the atomic-scale. A crucial aspect to understand and interpret the experimentally obtained micrographs and to identify the underlying surface structure is the availability of accurate simulation tools to predict the micrographs for a given surface structure.

In a case study on antiferromagnetic $Mn_3N_2(010)$ surface it has been recently shown for the first time that an SP-STM image simultaneously contains both magnetic and chemical information about the surface [197, 198]. The conclusive interrelations between the measured STM images and the actual structure of the magnetic surface was missing. The atomic structure of the surface was not known precisely, e.g. it was not possible to deduce from the measurements whether N atoms remain at the surface, or prefer to desorb from it. The magnetic ordering at the surface was also not well justified: although experiments showed that the surface ordering is antiferromagnetic, there exist various arrangements of the surface magnetic moments that are commensurate with the measured profiles. Furthermore, it was not clear how much the properties of the magnetized STM tip affect the measurements. This set of the unresolved problems indicated that a straightforward interpretation of the detected SP-STM profiles is not possible without a detailed theoretical analysis of the SP-STM experiments.

In order to understand the magnetic STM on $Mn_3N_2(010)$ theoretically, we have performed a detailed *ab initio* study. Our study allows to elucidate the most stable atomic and magnetic configuration of a $Mn_3N_2(010)$ surface, and provides a detailed interpretation of SP-STM experiments on $Mn_3N_2(010)$.

The chapter is organized as follows: In Sec. 4.1 we present a brief introduction into the current state of spin-sensitive STM. The main outcome of recent SP-STM experiments on antiferromagnetic $Mn_3N_2(010)$ surfaces and the motivation for present theoretical research are discussed in Sec. 4.2. In section 4.3 the theoretical approach for finding the most thermodynamically stable atomic and magnetic structure of the surface, and a method for simulating SP-STM images are discussed in detail. The results of the SP-STM simulations on the most stable configuration of a $Mn_3N_2(010)$ surface are presented in Sec. 4.4. The conclusions and a summary of the chapter are given in Sec. 4.5.

## 4.1 Introduction to spin-polarized scanning tunneling microscopy

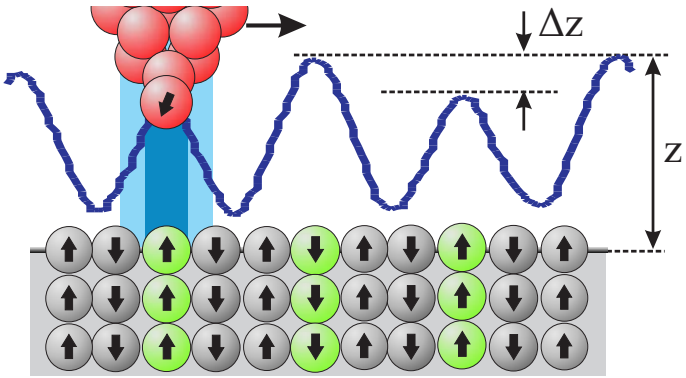


Figure 4.1: Schematics of a SP-STM experiment in the constant-current regime. The modulation of the tip-surface separation $z$ is due to magnetic and nonmagnetic interactions between the magnetically polarized tip and a surface. The measured peak modulation $\Delta z$ is due to magnetic interactions.

The principle of SP-STM is based on the variation of the tunneling current with the angle between the spin of the tip and that of the sample - larger current for parallel orientation and smaller current for antiparallel orientation (see Fig. 4.1). The magnetically-sensitive STM probes are prepared either from bulk ferromagnetic (FM) or antiferromagnetic (aFM) materials, or by coating of a nonmagnetic tip with spin-ordered films. The aFM tips avoid any stray magnetic fields originating from the probe tip and therefore allow the magnetically non-destructive imaging and an investigation of spin structures for magnetically soft samples and superparamagnetic particles [10, 199]. Furthermore, the tip is insensitive to external fields, which allows one to directly access intrinsic sample properties in field dependent studies. On the other hand, the ferromagnetic tips can be magnetized in the required direction, and consequently become sensitive to e.g. in-plane and out-of-plane components of the surface magnetic structure [200].

The first successful application of SP-STM was reported by Wiesendanger *et al.* in 1990 [201],

leading to the first experimental verification of the theoretically predicted antiferromagnetic ordering at Cr(001) surfaces. Since then the atomic-scale SP-STM has been established as a powerful and versatile tool for resolving magnetic structure on surfaces. In 1992 Wiesendanger and co-workers have employed SP-STM to elucidate the spin ordering on (001) facets of magnetide ($Fe_3O_4$) [202]. Lately, Heinze *et al.* reported an atomic-scale magnetic contrast of a Mn monolayer on W(110) surface using atomic-scale SP-STM in constant current (CC) mode [203]. Two years later, Yang *et al.* showed the simultaneous magnetic and nonmagnetic contrast on $Mn_3N_2$(010) [197]. Very recently, Kubetzka *et al.* have applied the same technique to study a single monolayer of Fe on W(001), resolving a long-standing question regarding the magnetic ground state of this system [9]. In 2005 Dreyer and co-workers have used SP-STM to record the morphological and chemical composition of chromium(001) terraces as a function of various stages of surface preparation, and were able to derive the protocols for obtaining a Cr(001) that reveal spin-polarized contrast [204].

SP-STM was used to study a number of nanomagnetic systems with complex noncollinear spin structures, like e.g. magnetic domain walls or magnetic vortexes [10, 13, 14, 199, 200, 205, 206]. Kubetzka *et al.* have performed SP-STM measurements employing ferromagnetic tips sensitive to in-plane and out-of-plane magnetic structure of two monolayers of Fe on W(110) to record and characterize the magnetic stripe domain structure that appears due to the winding 180° Bloch walls [199] (see Fig. 4.2). The internal spin structure of the magnetic vortex cores was directly observed on Fe-islands using aFM tips [10].

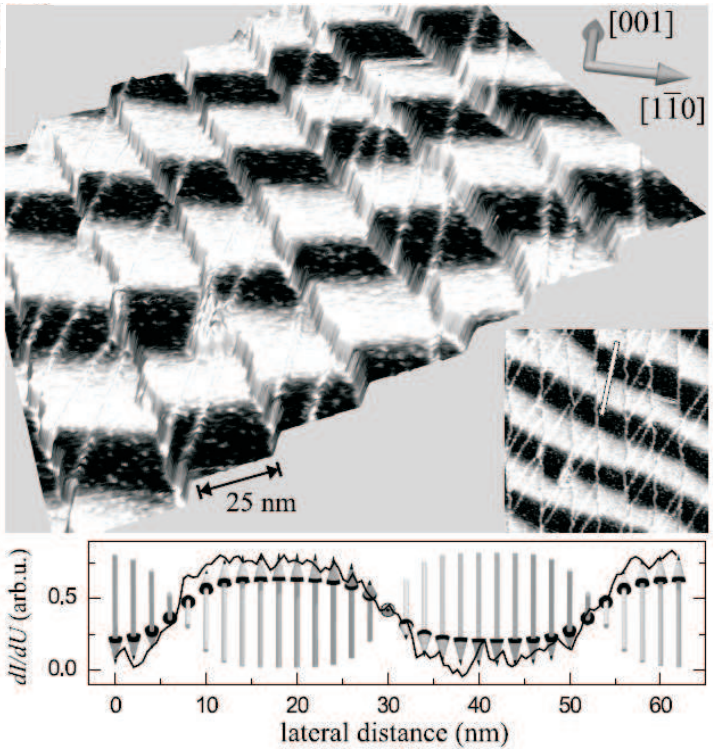


Figure 4.2: Magnetic stripe domains recorded with a ferromagnetic STM tip that is sensitive to the out-of-plane magnetic component on two monolayers of Fe on W(110). The line section is compared to a proposed magnetic configuration (side view). Magnetic domain walls appear alternatively bright and dark. After Kubetzka *et al.* [199].

Eight years after the introduction of SP-STM, this technique has been combined with tunneling spectroscopy (SP-STS) providing access to a spatially, spin and energy-resolved variation of the surface electronic properties [15, 16, 207–213]. For example, SP-STS has been used by Wiesendanger *et al.* [140] to map the energy-dependent

spin polarization of nanoscale ferromagnetic Gd(0001) islands by applying a magnetic field to the sample and measuring the tunneling conductance $dI/dV$ versus bias voltage $V$ in tip-sample parallel and antiparallel configurations. Bode and co-workers employed SP-STS to study electronic and magnetic properties of dislocation lines in a Fe double-layer deposited on a W(110) surface for dislocation lines that are ferromagnetically ordered [15]. In 2005 Bergmann *et al.* used SP-STM/SP-STS for a detailed characterization of magnetic properties of iron on tungsten in the pseudomorphic regime, performing measurements on samples with different coverage and morphology ranging from three-dimensional Fe islands down to the Fe monolayer [12]. One year later, Bergmann and co-workers used variable-temperature SP-STM to measure the reorientation transition temperature of the low-temperature magnetic stripe domain structure on the same system as a function of coverage [11].

Recent time-dependent SP-STS studies even opened the door to studies of magnetic switching phenomena of nanoscale islands and particles being close to the superparamagnetic limit [17].

## 4.2 Motivation for SP-STM theory on $Mn_3N_2$(010) surface

One of the promising candidates for spin-based electronics and high-density magnetic storage devices are transition metal nitride systems. These materials have magnetic properties ranging from ferromagnetic to antiferromagnetic, exhibit very high Curie and Néel temperatures, and very large magnetic moments. Recently, the surface properties of binary nitrides have been explored as model systems employing spin-sensitive STM, with emphasis on the antiferromagnetic $Mn_3N_2$(010) surface [197, 198, 214–218]. Apart from the technological interest, the principle objective of these studies was to elucidate the properties and the potential of the SP-STM technique at the atomic scale to measure atomic-scale properties of magnetically ordered structures.

The bulk atomic and magnetic structures of $Mn_3N_2$ are well known from both theoretical and experimental studies [214, 215, 219–223]. $Mn_3N_2$ has a face-centered tetragonal (fct) rocksalt-type structure, with every third (001)-layer possessing all nitrogen sites vacant (Fig. 4.3). Due to this atomic superstructure the Mn-sublattice in $Mn_3N_2$ crystal is built from two-fold and six-fold coordinated atoms, that are referred hereafter as $Mn_1$ and $Mn_2$, respectively. The presence of the nitrogen-vacancy planes results in a bulk unit cell having lattice parameter $c \approx 12.13$ Å (six atomic layers). Employing neutron diffraction experiments it has been shown that the magnetic moments in bulk $Mn_3N_2$ are directed along the [100] direction, are ordered ferromagnetically within the (001) planes, and layerwise antiferromagnetically along the [001] direction (see Fig. 4.3(b)). The Néel temperature of $Mn_3N_2$ crystals was found to be at 913-927 K.

Using molecular beam epitaxy (MBE), Yang *et al.* have reported the growth of atomically smooth layers of $Mn_3N_2$ with the [001]-axis parallel to the growth surface, which is (010) [214, 215]. Employing nonmagnetic W tips, Yang and co-workers have characterized the atomic structure of $Mn_3N_2$(010) surfaces, revealing an atomic-scale row structure with row spacing $c/2 \sim 6.06$ Å, i.e.

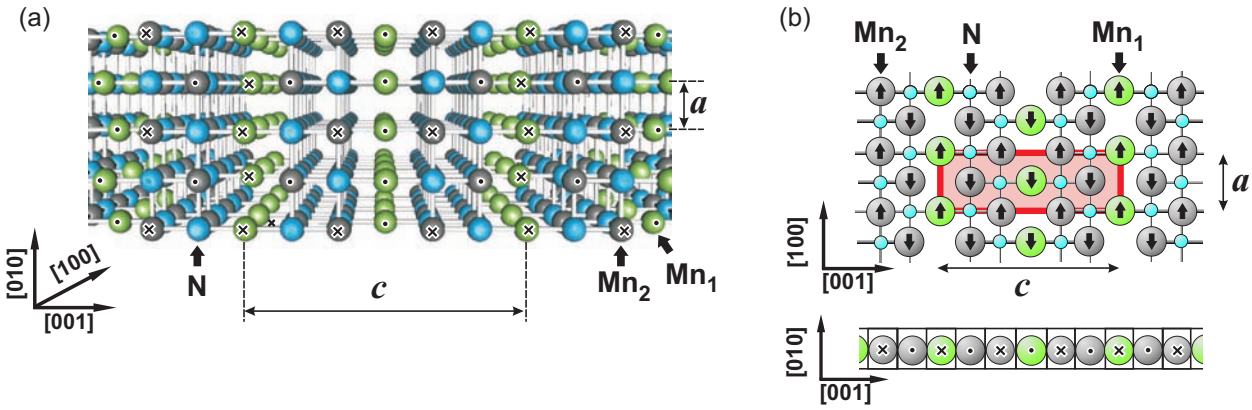


Figure 4.3: (a) Atomic structure of antiferromagnetic $Mn_3N_2$. (b) Top and side view of the bulk-terminated (010) surface of aFM $Mn_3N_2$. The two fold coordinated manganese atoms located in N-vacancy (001)-planes (called $Mn_1$ atoms) are shown as green balls. The six (five) fold coordinated Mn atoms are shown as grey balls. Arrows, dots, and crosses inside the manganese atoms indicate the corresponding local magnetic moments that are parallel to [100].

with the the spacing between N-vacancy planes (Fig. 4.4(a)). With a very sharp tip, they were able to resolve individual Mn atoms, as shown in Fig. 4.4(b). It has been found that the STM image is a perfect match with the Mn atom sublattice shown in Fig. 4.3(b), where the higher and lower maxima correspond to the $Mn_1$ and $Mn_2$ atoms respectively. No traces of nitrogen atoms, however, were detected in spin-averaged corrugation profiles.

Employing magnetized tungsten tips coated with either Mn- or Fe- films on $Mn_3N_2$(010), Yang *et al.* have recently for the first time shown, that the SP-STM images *simultaneously* contain both magnetic and chemical information about the surface [197, 198, 218]. The results of their studies are summarized in Fig. 4.5. Fig. 4.5(a) shows the SP-STM image acquired using a Mn-coated W tip at bias voltage -0.6 V; the corresponding area-averaged corrugation profile is shown in Fig. 4.5(b). Both images clearly indicate a row structure with period $c/2$, similar to the spin-averaged STM image (compare Fig. 4.5(b) and inset in Fig. 4.4(a)). In addition, however, a modulation of the height profiles with period $c$ was clearly observed. Since it can be ruled out that the observed height modulation is due to e.g. charge redistribution and asymmetric $d$-$d$ orbital tunneling [197], this modulation is clearly assigned to the magnetic interactions between the STM tip and the surface.

Assuming that the bulk magnetic symmetry is maintained at the surface, i.e. that the magnetic component of the tunneling current periodically inverses its sign (aFM-modulation), Yang and co-workers [197] presented a straightforward method for separating the magnetic and nonmagnetic components from the SP-STM images. Specifically, they have shown that the nonmagnetic and magnetic component can be extracted from the difference and that (i) the sum of the area-averaged height profile $z(x)$ ($x$ is along [001]) and (ii) exactly the same signal shifted by a period of the non-magnetic component $c/2$ (see Fig. 4.5(b)-(d)). The comparison of the magnetic and nonmagnetic

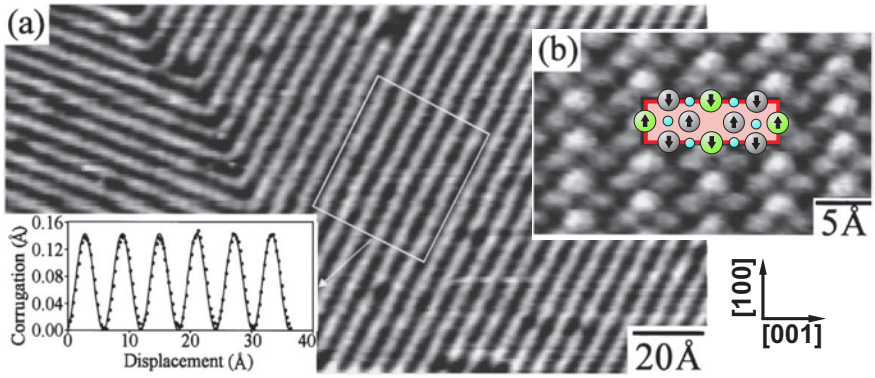


Figure 4.4: (a) Nonmagnetic STM images of the $Mn_3N_2$(010) surface acquired at bias voltage -0.4 V with a tungsten tip. The inset shows the average profile (data points) over the indicated region. The solid line is a sinusoid fitted to the data points. (b) Atomic resolution STM image acquired at bias voltage -0.3 V. The bulk terminated surface is shown for comparison. Figures are adopted from Yang *et al.* [197].

parts of the SP-STM profiles (Fig. 4.5(d)) reveals that the maximum of both contributions is positioned on top of the $Mn_1$ rows. In contrast to the nonmagnetic profiles that have a simple sinus-like shape, the extracted magnetic contributions do not show a layer by layer alternation or a simple sinusoidal form. First, the periodicity of the magnetic modulation is twice as large as that of the nonmagnetic part. Second, the magnetic component reveals a trapezoidal shape.

Recently, it was found that the magnetic contrast on $Mn_3N_2$(010) strongly depends on the bias voltage and at a certain voltage the magnetic amplitude goes to zero and undergoes even an inverse of the contrast (Fig. 4.5(f)) [198]. This reversal is clearly due to a change in the sign of the magnetic term in the tunneling current. Since this term depends on both the tip and surface magnetic properties, the reversal can be caused by either the sample or the tip [218]. Simultaneously, the bias voltage dependence is also found to affect the SP-STM line profile shape. Up to now, however, a straightforward interpretation of the experimental SP-STM profiles, particularly of the magnetic part, was not possible.

First, up to now it was always assumed that the surface magnetic and atomic structure corresponds to a bulk terminated geometry. While the bulk magnetic order is well known [223], the chemical and magnetic structures of $Mn_3N_2$(010) surfaces are not well justified. For instance, even employing an atomically-sharp tip, there are no experimental evidences of nitrogen atoms in the surface layer (see e.g. Fig. 4.4(b)). More importantly, the different magnetic periodicity of the ideal bulk terminated surface and of the measured magnetic component of the SP-STM profile could be an indication of a surface magnetic reconstruction, when magnetic moments of surface Mn atoms are flipped with respect to the orientation of the bulk spins (compare, e.g. the periodicity of the magnetic contrast with the corresponding magnetic structure of the bulk-terminated $Mn_3N_2$(010) surface, Fig. 4.5(d)).

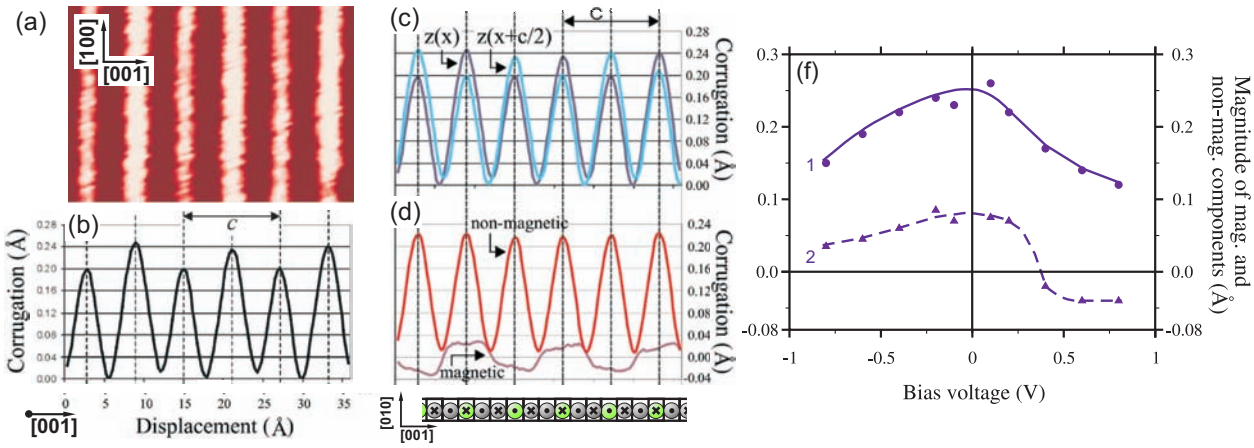


Figure 4.5: (a) Spin-polarized STM image acquired using a Mn-coated tungsten tip at bias voltage -0.6 V. The tip is magnetized in the direction perpendicular to the tip axis, i.e. the SP-STM is sensitive to the in-plane magnetic structure of the surface. (b) Area-averaged SP-STM corrugation line profile $z(x)$ of the whole image of (a), where $x$ is along [001]. (c) Area-averaged $z(x)$ that is shown in (b) (violet curve) and the same corrugation line shifted by a half of the modulation period $c$ $z(x + c/2)$ (blue curve). (d) The resulting nonmagnetic (red) and magnetic line profiles (brown), compared with the side-view of the bulk-terminated $Mn_3N_2(010)$ surface. (f) The magnitude of the magnetic and nonmagnetic component as a function of the bias voltage measured with a Fe-coated W tip. The images are adopted from Refs. [197, 198, 218].

Second, in early studies the theoretical modeling of the SP-STM experiments was based on bulk *ab initio* calculations [197, 216]. While this method provided reasonable agreement with experiments at bias voltage $V_{\text{bias}} = -0.2$ V [197] and for the nonmagnetic part of the STM profiles [216], it completely failed to predict e.g. the inversion of the magnetic contrast as experimentally observed at a bias voltage of +0.4 V (see Fig. 4.5(f)). As mentioned above, since the STM experiments are symmetric with respect to the tip and the surface, the measured contrast inversion might reflect the magnetic structure of the tip, and not of the surface.

In order to understand theoretically the whole set of bias-dependent SP-STM images on $Mn_3N_2(010)$ we have performed a detailed *ab initio* study employing planewave density functional theory, *ab initio* thermodynamics, and a spin-generalized Tersoff-Hamann model for SP-STM (Sec. 2.6.3). First, we determine the most thermodynamically stable magnetic and atomic surface configuration of $Mn_3N_2$ surfaces, as described in Sec. 4.4.5. Based on the identified equilibrium (energetically most stable) structure of $Mn_3N_2(010)$ we first simulate SP-STM profiles employing a featureless model for the STM tip, that allows to separate surface- and tip-driven effects in the experimental SP-STM images (Secs. 4.4.6-4.4.7). A discussion of tip-effects and a comparison of our approach with previous more simplified SP-STM models are presented in Secs. 4.4.8 and 4.4.9 respectively.

## 4.3 Method

### 4.3.1 Real-space description of the vacuum

Under normal tunneling conditions the distance between the outermost tip and the surface atoms is estimated as 5-15 Å. Due to the exponential decay into vacuum a reliable representation of the wavefunctions in this region becomes nontrivial when employing a planewave basis set. Specifically, in planewave slab calculations it is difficult to go beyond $\sim$ 4 Å (see, e.g. Figs. 4.6(b), 4.7(c), 4.8(a), 4.9(a)-(c) and Refs. [4, 224]). To explain the origin of this effect we start with a planewave representation of a Kohn-Sham wavefunction with band index $i$ and wavevector $\mathbf{k}$ (Sec. 2):

$$\psi_{i\mathbf{k}}(\mathbf{r}) = \sum_{\mathbf{G}} C_{i\mathbf{k}}(\mathbf{G}) \exp[\mathrm{i}(\mathbf{G}+\mathbf{k})\cdot\mathbf{r}], \tag{4.1}$$

where $\mathbf{G}$ are reciprocal cell vectors.

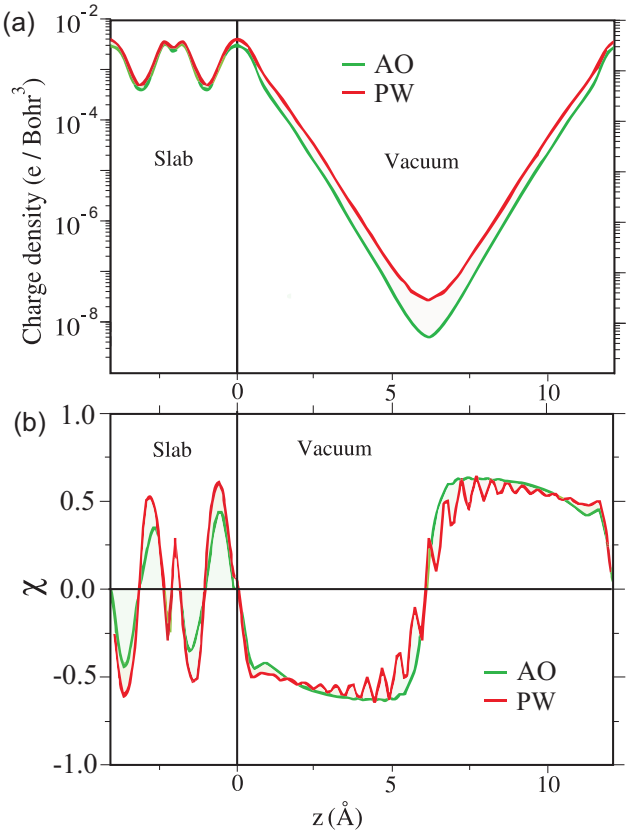


Figure 4.6: Quality of the charge density description in the vacuum region obtained employing a planewave and an atomic orbital basis sets. (a) The $(x, y)$-averaged planewave partial charge density corresponds to an energy window $(E_{\mathrm{Fermi}} - 0.6\ \mathrm{eV}, E_{\mathrm{Fermi}})$ (red curve). The corresponding density in the atomic basis as calculated according to Eq. (4.5) is shown as green curve. The atomic orbital basis set includes the $s$ and $d$ orbitals of all manganese atoms in the slab. This choice provides the best agreement between the planewave and the atomic orbital charge density. The surface is at $z$=0 Å, the back-side of the periodically repeated slab is at $z$=12.35 Å. (b) The $(x, y)$-averaged inverse decay length $\chi$ (see App. A.2 for definition) along the surface normal is calculated for densities shown in (a). Calculations have been performed for a $Mn_3N_2(010)$ slab consisting of 3 atomic layers. The bulk atomic positions are nonrelaxed, the surface geometry corresponds to ideal bulk termination.

For a slab with the surface normal to the $z$-axis Eq. (4.1) can be rearranged as:

$$\psi_{i\mathbf{k}_{||}}(\mathbf{r}) = \sum_{n} \exp\left[\mathrm{i}\left(\mathbf{G}_{||}^{n} + \mathbf{k}_{||}\right)\cdot\mathbf{r}_{||}\right] \sum_{\mathrm{G}_{\perp}} C_{i\mathbf{k}}(\mathbf{G}) \exp\left[\mathrm{i}\mathrm{G}_{\perp}\cdot z\right]. \tag{4.2}$$

Here, $\mathbf{k} = \left(\mathbf{k}_{||}, \mathrm{k}_{\perp}\right)$, $\mathbf{k}_{||}$ belongs to the first surface Brillouin zone. The normal-to-surface component $\mathrm{k}_{\perp}$ of $\mathbf{k}$ in Eq. (4.2) is set to zero because it ceases to be a valid quantum number for a surface. The surface wavefunction is thus described by a superposition of planewaves with wavevectors $\mathbf{G}^{n}_{||} + \mathbf{k}_{||}$ that travel along the surface:

$$\psi_{i\mathbf{k}_{||}}(\mathbf{r}) = \sum_{n} F^{n}_{i\mathbf{k}_{||}}(z)\ \exp\left[\mathrm{i}\left(\mathbf{G}^{n}_{||} + \mathbf{k}_{||}\right) \cdot \mathbf{r}_{||}\right]. \tag{4.3}$$

Here, the amplitude of each planewave is $z$-dependent and is given as:

$$F^{n}_{i\mathbf{k}_{||}}(z) = \sum_{\mathrm{G}_{\perp}} C_{i\mathbf{k}}(\mathbf{G})\ \exp\left[\mathrm{iG}_{\perp} \cdot z\right]. \tag{4.4}$$

From Eq. (4.4) it follows that the real-space function $F^{n}_{i\mathbf{k}_{||}}(z)$ is represented via a corresponding one-dimensional Fourier transformation along the surface normal. The number of planewaves required for an accurate description of $F^{n}_{i\mathbf{k}_{||}}(z)$ is determined by its shape in real space. This shape is step-like due to the sharp transition from a region of high charge density (slab) to a region of extremely low charge density (vacuum). The precise shape of $F^{n}_{i\mathbf{k}_{||}}(z)$ is a system-dependent entity. Typically, however, the number of planewaves required to achieve fully converged slab properties such as, e.g., surface energy, surface geometry, work function *etc.* is much less than that required for an accurate description of $F^{n}_{i\mathbf{k}_{||}}(z)$ at distances exceeding several angstrom above the surface (App. A.2). The origin is a negligible magnitude of the charge density in these regions that does not essentially influences the variational minimization of the total energy, and consequently provides unessential effect on the electronic properties of a slab.

Increasing the size of the planewave basis set to achieve a converged description of the electron charge density at large distances above the surface is computationally highly inefficient or even not feasible (App. A.2). Therefore, we had to develop alternative methods for an improved and efficient description of the slab LDOS in the vacuum region. In the following, two methods will be described. Our first method is based on the expansion of the fully selfconsistent wavefunctions into atomic orbitals:

$$|\psi_{i\mathbf{k}}\rangle = \sum_{\mu} |\mu\rangle \langle\mu|\ \psi_{i\mathbf{k}}\rangle. \tag{4.5}$$

The expansion coefficients $\langle\mu|\ \psi_{i\mathbf{k}}\rangle$ in Eq. (4.5) are calculated in reciprocal space, i.e. as $\sum_{\mathbf{G}} \langle\mu|\mathbf{G}\rangle \langle\mathbf{G}|\psi_{i\mathbf{k}}\rangle$. The surface LDOS is then reconstructed according to Eq. (4.5), but employing a real-space description of the atomic orbitals [217]. This approach allows to get a substantially smoother description of the wavefunctions in the vacuum. This is shown in Fig. 4.6(b), where the inverse decay length (for a definition of the inverse decay length see App. A.2) of the original and the reconstructed slab charge densities are compared. From Fig. 4.6 it is, however, also immediately clear that the projection procedure according to Eq. (4.5) does not provide an accurate description

of the slab charge density. This is observable already within the slab region and becomes more pronounced outside the slab. Here, the discrepancy between the planewave and reconstructed charge densities is more essential, and is manifested by an underestimation of the reconstructed charge densities at all distances above the surface (Fig. 4.6(a)). Such discrepancies are due to the incompleteness of the atomic orbital basis set and cannot be compensated in a fully systematic and consistent manner. This deficiency severely hampers application of this approach in practice.

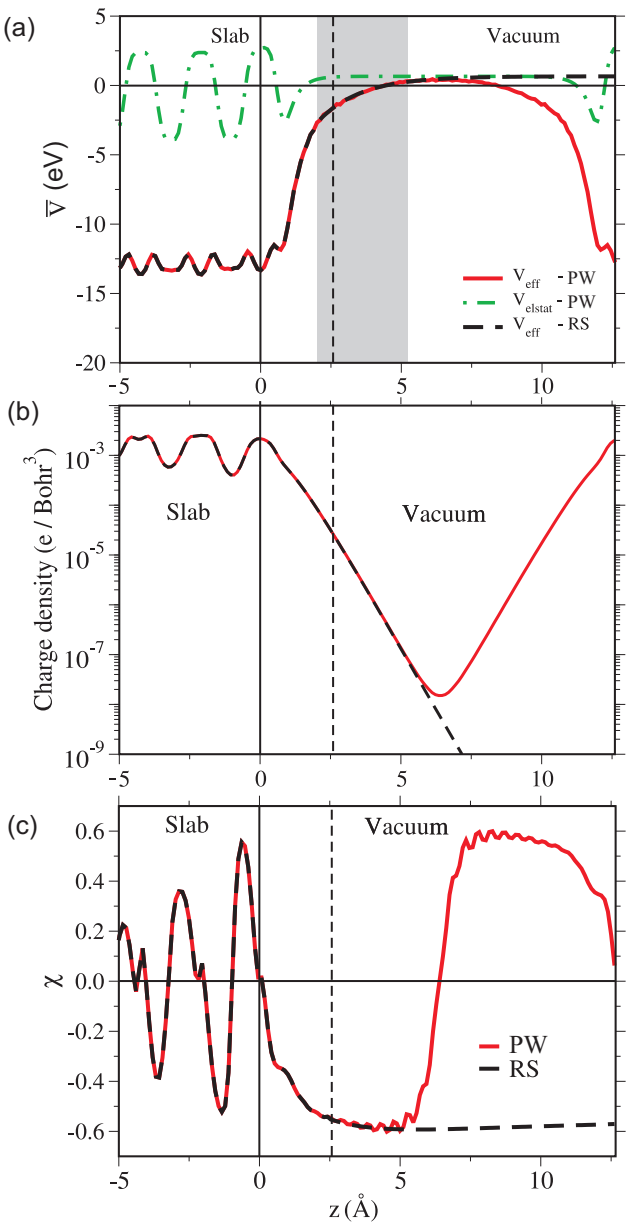


Figure 4.7: (a) $(x, y)$-averaged electrostatic and effective potential for the $Mn_3N_2(010)$ surface along the surface normal. The surface is at $z$=0 Å, the back-side of the image-slab is at $z$=12.8 Å. The self-consistent electrostatic (green dash-dotted curve) and effective (red solid curve) potential are symmetric with respect to $z$=6.4 Å, that is the half-distance between the surface and the back-side of the image-slab. The effective potential employed for the real-space description of the surface charge density is equal to the self-consistent one for $z$ <2.6 Å, and is evaluated according to Eq. (4.9) for $z$ >2.6 Å(black dashed curve). The parameters $A$, $B$ and $C$ in Eq. (4.9) are obtained by fitting a self-consistent effective potential $V_{\text{eff}}$ at distances 2.1 Å< $z$ < 5.1 Å (gray-shaded region), where the electrostatic potential is essentially constant. (b) $(x, y)$-averaged partial charge density calculated in the energy window $(E_{\text{Fermi}} - 0.3 \text{ eV}, E_{\text{Fermi}})$ (solid red curve) with the corresponding density calculated according to Eq. (4.9) (dashed black curve). (c) Quality of the charge density description in the vacuum region obtained employing the planewave and the real-space basis set. The $(x, y)$-averaged inverse decay length $\chi$ along the surface normal is calculated for densities shown in (b). The $Mn_3N_2(010)$ slab employed for these calculations consist of 6 atomic layers. The bulk atomic positions are relaxed, the surface geometry corresponds to the ideal bulk termination.

Therefore, instead of using the projection approach as given by Eq. (4.5), we have employed another method. This approach was first proposed by Heinze and co-workers [224]. According to

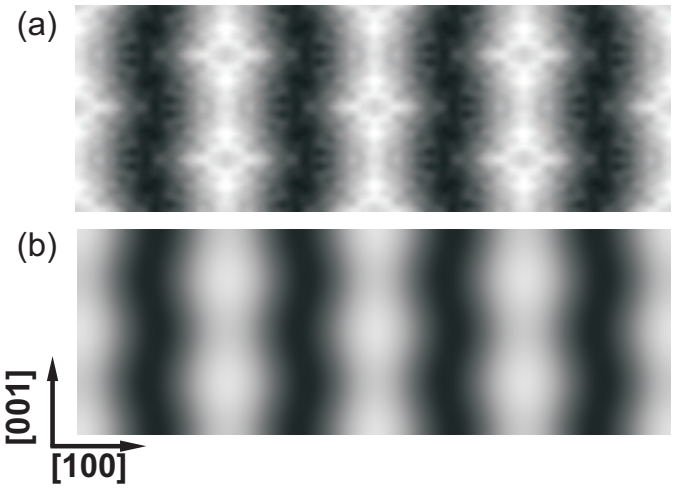


Figure 4.8: Slice of the non-magnetic partial charge density of a $Mn_3N_2(010)$ surface taken 5Å above the surface. (a) Self-consistent charge density. (b) Charge density obtained employing the real-space method. The partial charge density is obtained by integrating over the energy interval $(E_{\mathrm{Fermi}} - 0.3\ \mathrm{eV}, E_{\mathrm{Fermi}})$ and the whole surface Brillouin zone. The $Mn_3N_2(010)$ slab consists of 6 atomic layers. The bulk atomic positions are relaxed, the surface geometry corresponds to an ideal bulk termination. The slices are plotted on the same scale.

this method the function $F^n_{i\mathbf{k}_{||}}(z)$ is represented in the reciprocal-space only within the slab and up to 2-3 Å above the surface, i.e. in the areas of high charge densities, where $F$ is accurately described. For distances larger than some critical value $z_b$ the function $F$ is expanded into basis functions $d^n_{i\mathbf{k}_{||}}(z)$:

$$F^n_{i\mathbf{k}_{||}}(z) = \begin{cases} \sum_{\mathrm{G}_\perp} C_{i\mathbf{k}}(\mathbf{G}) \exp\left[\mathrm{iG}_\perp \cdot z\right] & \text{when } z < z_b, \\ A^n_{i\mathbf{k}_{||}}\, d^n_{i\mathbf{k}_{||}}(z) & \text{otherwise.} \end{cases} \tag{4.6}$$

Here, the function $d^n_{i\mathbf{k}_{||}}(z)$ describes the decay of $F^n_{i\mathbf{k}_{||}}(z)$ along the surface normal and is the exact numerical solution of the one-dimensional Schrödinger equation to the laterally averaged $z$-dependent part of the vacuum effective potential $V_{\mathrm{eff}}(z)$:

$$\left[-\frac{\hbar^2}{2m}\frac{d^2}{dz^2} - \epsilon_{i\mathbf{k}_{||}} + V_{\mathrm{eff}}(z) + \frac{\hbar^2}{2m}\left(\mathbf{k}_{||} + \mathbf{G}^n_{||}\right)^2\right] d^n_{i\mathbf{k}_{||}}(z) = 0. \tag{4.7}$$

The expansion coefficients $A^n_{i\mathbf{k}_{||}}$ in Eq. (4.6) are determined by enforcing the basis function $F^n_{i\mathbf{k}_{||}}(z)$ at the vacuum boundary $z_b$ to be continuous:

$$A^n_{i\mathbf{k}_{||}} = \frac{1}{d^n_{i\mathbf{k}_{||}}(z_{\mathrm{b}})} \sum_{\mathrm{G}_\perp} C_{i\mathbf{k}}(\mathbf{G}) \exp\left[\mathrm{iG}_\perp \cdot z_{\mathrm{b}}\right]. \tag{4.8}$$

The choice of the basis functions to describe $F^n_{i\mathbf{k}_{||}}(z)$ (Eq. (4.6)) is ideally suited to correctly reproduce the behavior in the vacuum region as it already includes the exponential decay of the wavefunctions with respect to the correct potential $V_{\mathrm{eff}}(z)$. Generally, for a known effective potential, it is possible to get exact surface charge densities at arbitrary distances $z$. Below we present

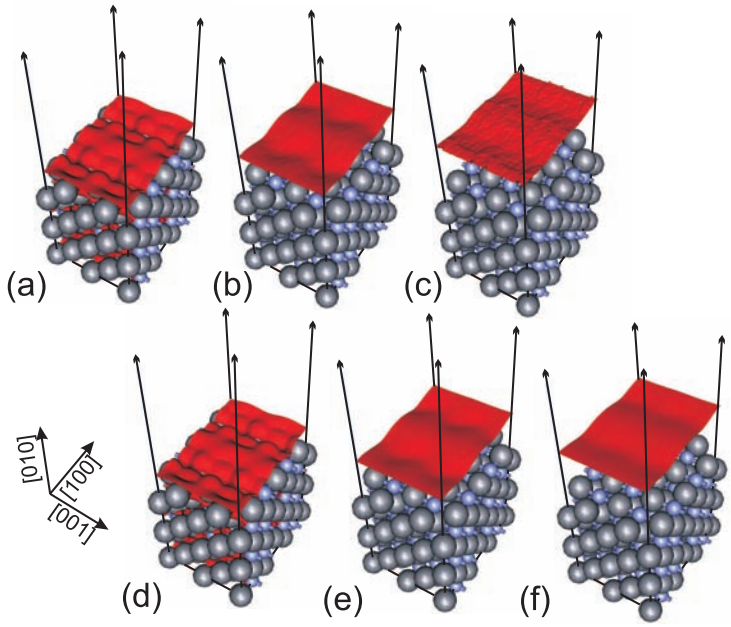


Figure 4.9: Iso-surfaces of the nonmagnetic partial charge density corresponding to thresholds $3 \cdot 10^{-4}$ e/Bohr$^3$, $3 \cdot 10^{-6}$e/Bohr$^3$, and $3 \cdot 10^{-8}$ e/Bohr$^3$. These values correspond to $(x, y)$-averaged $\overline{z}$ ∼1.2 Å, $\overline{z}$ ∼3.5 Å, and $\overline{z}$ ∼ 5.8 Å distance above the surface, respectively. (a)-(c) Self-consistent charge density. (d)-(f) Charge density obtained employing the real-space method. The slab manganese atoms are shown as grey, the nitrogen atoms as blue spheres. The partial charge density corresponds to the energy interval $(E_{\text{Fermi}} - 0.3 \text{ eV}, E_{\text{Fermi}})$. The $Mn_3N_2(010)$ slab is 6 atomic layers thick. The bulk atomic positions are fully relaxed, the surface geometry corresponds to an ideal bulk termination.

the practical approach how to calculate the effective potential at an arbitrary distance above the surface based on slab calculations.

The effective potential experienced by the electrons is composed of an electrostatic and an exchange-correlation part $V_{\text{eff}}(z) = V_{\text{elstat}}(z) + V_{\text{xc}}(z)$. When there is no electric field in the vacuum (i.e., if external fields or inequivalent surface dipoles are absent) the electrostatic potential quickly (typically for $z >$2 Å) converges to a constant value $V_{\text{vac}}$ (Fig. 4.7(a)). In the presence of an electric field an additional linear-dependent term is added: $V_{\text{elstat}}(z) = V_{\text{vac}} + C \cdot z$, where $C$ defines the strength of the electric field.

The dependence of the exchange-correlation part as function of distance $z$ is well known: because the commonly employed exchange-correlation potentials do not provide a complete cancelation of the spurious electron self-interaction contained in the Hartree part, the conventional exchange-correlation functionals provide an exponential instead of a power-law decay[1]. The effective potential in the far-vacuum region can be, therefore, parameterized as:

[1]The discussion of the asymptotic behavior of the exchange-correlation potential is conventionally restricted to an isolated single atom. The same arguments, however, apply to a surface xc-potential [225].

$$V_{\text{eff}}(z)|_{z>z_b} = (V_{\text{vac}} + C \cdot z) + A \exp\left[-B \cdot z\right]. \tag{4.9}$$

Here, the vacuum level $V_{\text{vac}}$ is obtained from a calculation of the work-function, and the parameters $A$, $B$ and $C$ are obtained by fitting Eq. (4.9) to the self-consistent effective potential in the vicinity of the slab. Here, the fitting is done in an area of relatively large charge densities, where the planewave self-consistent potentials are accurate.

The real-space effective potential calculated according to Eq. (4.9) and the corresponding slab charge densities are shown in Fig. 4.7 for the $Mn_3N_2(010)$ surface. The effective potential employed to solve Eq. (4.7) equals to the self-consistent potential for $z - z_{surface} < 2.6$ Å, and is calculated according to Eq. (4.9) at larger distances (Fig. 4.7(a)).

The self-consistent and real-space surface LDOS at different distances above the surface are compared in Figs. 4.7-4.9. Clearly, the self-consistent charge density becomes exceedingly noisy at distances larger than $\sim 2.5$ Å above the surface, making it virtually impossible to perform accurate theoretical STM simulations. In contrast, the real-space method implemented here provides an exact description at all distances.

### 4.3.2 Surface free energy

The accurate determination of the surface free energy by *ab initio* techniques provides a powerful tool in modern theoretical surface science, that allows to determine the hierarchy of stable and metastable surface structures (commonly referred in term of a surface phase diagram), to figure out the equilibrium composition and the geometry of a surface in contact with a given environment, or to suggest experimental conditions required for the growth of a desired surface.

The surface energy is defined as an excess energy (with respect to an ideal bulk crystal) conserved in an interface separating the bulk of a crystal from the surrounding environment. The environment is typically a vapor of constituent atoms described by a temperature $T$ and a pressure $p$ [46]. Since the surface can exchange particles with both the bulk and gas phases (diffusion from the surface to the bulk and vice-versa, adsorption or desorption of adatoms/molecules from the surface), it is not an isolated object, but is affected by its surrounding and should be treated as a constituent part of the coupled bulk-surface-atmosphere complex.

It is generally cumbersome to calculate the free energy of a realistic surface for arbitrary growth conditions. This is because some elementary atomistic processes occurring at surfaces can be strongly kinetically-inhibited, leading to nonequilibrium configurations of a system [226]. The surface energy in this case becomes time-dependent and calculations that explicitly treat the motion of atoms/molecules are required. The problem, however, significantly simplifies when growth temperatures are high enough and/or the surface growth rates are low enough that the bulk-surface-atmosphere subsystems are close to or at the mutual thermodynamic equilibrium (Fig. 4.10). In this case the first principle calculations can be combined with equilibrium thermodynamics. This

approach is commonly termed *ab initio* thermodynamics. The formalism of *ab initio* thermodynamics is presented in this section, closely following the discussion presented by Reuter and Scheffler [227]. For the sake of clarity the discussion is limited to $Mn_3N_2$ surfaces. A generalization to other compounds is, however, obvious.

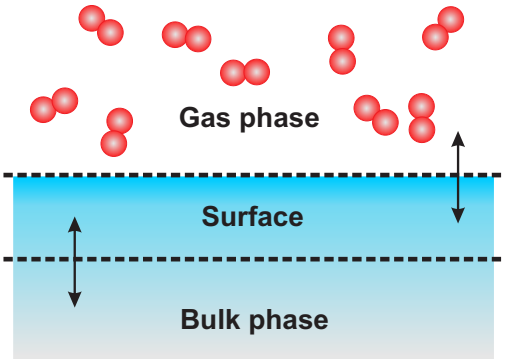


Figure 4.10: Closed thermodynamic system comprised of gas, surface and bulk phases. Under the condition of thermodynamic equilibrium the constituent subsystems are in mutual equilibrium, implying that the chemical potentials of the species are the same in each phase. This allows to decouple the system into gas/surface/bulk subsystems and to treat them separately employing DFT calculations.

Consider a nitrogen atmosphere with constant temperature $T$ and pressure $p$, that is in thermodynamical equilibrium with the $Mn_3N_2$ surface. Constant $T$ and $p$ of the atmosphere imply that it acts as a reservoir, because it can give (take) any amount of nitrogen to (or from) the surface without changing the temperature or pressure. The appropriate thermodynamic potential in this case is the Gibbs free energy $G(T, p, n_N, n_{Mn})$, that also depends on the number of manganese atoms $n_{Mn}$ and nitrogen atoms $n_N$ in the system:

$$G(T, p, n_N, n_{Mn}) = n_N \mu_N(T, p) + n_{Mn} \mu_{Mn}(T, p) + \gamma(T, p) A. \tag{4.10}$$

Here, $\gamma(T, p)$ is the surface free energy per unit area, $A$ is the surface area $A$; $\mu_\alpha$ is the chemical potential of atom $\alpha$ that describes the change in the free energy if the number of atoms of species $\alpha$ changes by $\partial n_\alpha$ under constant temperature, pressure, and the population of other particles [74]:

$$\mu_\alpha(T, p) = \left[ \frac{\partial G(T, p, n_N, n_{Mn})}{\partial n_\alpha} \right]_{T, p, n_\alpha \neq n_\beta}. \tag{4.11}$$

The most stable surface composition and geometry is then the one that minimizes the surface free energy at a given state of environment that is defined through the chemical potentials:

$$\gamma(T, p) = \frac{1}{A} \left[ G(T, p, n_N, n_{Mn}) - n_N \mu_N(T, p) - n_{Mn} \mu_{Mn}(T, p) \right]. \tag{4.12}$$

The chemical potentials of Mn and N enter Eq. (4.12) in a symmetric way. However, since the

thermal equilibrium is established between all constituents of the system, the bulk and atmosphere are also in mutual equilibrium, and Eq. (4.10) can be rewritten for a bulk-atmosphere system as:

$$g^{\text{bulk}}_{\text{Mn}_3\text{N}_2}(T,p) = 3\mu_{\text{Mn}}(T,p) + 2\mu_{\text{N}}(T,p). \tag{4.13}$$

Here and henceforth $g$ denotes the Gibbs free energy per formula unit, and Eq. (4.13) implies that the chemical potentials of the constituent atoms are not independent and coupled by the free energy of bulk $Mn_3N_2$. Hence, only one of the two chemical potentials can be chosen freely. If the surface is modeled with a slab having two equivalent surfaces, a substitution of Eq. (4.13) into Eq. (4.12) gives:

$$\gamma\left(T,p\right) = \frac{1}{2A}\left[G^{\text{slab}}\left(T,p,n_{\text{Mn}},n_{\text{N}}\right) - \frac{1}{3}n_{\text{Mn}}\, g^{\text{bulk}}_{\text{Mn}_3\text{N}_2}(T,p) + \left(\frac{2}{3}n_{\text{Mn}} - n_{\text{N}}\right)\mu_{\text{N}}\left(T,p\right)\right]. \tag{4.14}$$

At any given $T$, $p$ and surface composition the slab free energy $G^{\text{slab}}$ and bulk free energy $g^{\text{bulk}}_{\text{Mn}_3\text{N}_2}$ in Eq. (4.14) are well defined constant values. Therefore, for a stoichiometrically terminated surfaces ($2n_{\text{Mn}} = 3n_{\text{N}}$) the surface free energy $\gamma$ is a constant at arbitrary environment conditions (given by the nitrogen chemical potential), while for a non-stoichiometric case $\gamma$ is a linear function of the nitrogen chemical potential $\mu_{\text{N}}$. Eq. (4.14) implies that positive values of the surface energy define thermodynamically stable surfaces, while negative surface energies indicate that the bulk is unstable versus surface formation and would decompose.

It is important to note, that the physically allowed range of the nitrogen chemical potential is constrained to a certain energy interval. If $\mu_{\text{N}}$ becomes too low (nitrogen-poor condition, that corresponds to low partial pressure of N) all nitrogen atoms leave the sample by desorbing from the surface and the $Mn_3N_2$ crystal decomposes into a solid Mn-phase and $N_2$ gas. To avoid such phase separation the Mn crystallites should be thermodynamically unstable, i.e. the chemical potential of manganese in the system should be lower than that of Mn-bulk:

$$\mu_{\text{Mn}}(T,p) < g^{\text{bulk}}_{\text{Mn}}(T,p), \tag{4.15}$$

where $g^{\text{bulk}}_{\text{Mn}}(T,p)$ is the Gibbs free energy of metallic manganese[2].

On the other hand, the most nitrogen-rich condition can be defined as a point beyond which the amount of nitrogen atoms in the sample is so high that the formation of parasitic nitrogen phases starts. For example, at atmospheric pressures (∼1 bar) the most stable nitrogen phase for temperatures below $T_m = 63$ K is a solid hcp-crystal [229], in temperature range 63 K$< T <$77 K it is a liquid, and at temperatures above $T_c$=77 K it is a gas phase [228]. Obviously, for temperatures lower than $T_c(p)$ the chemical potential of nitrogen in the gas phase is larger than the value actually

[2]The melting temperature of the solid manganese phase is $T_m(1\text{bar}) = 1519$ K [228]. Thus, in the temperature and pressure range we are interested in the manganese always remains in its solid phase, validating the use of Eq. (4.15) at all relevant temperatures $T$ and pressures $p$.

accessible. This allows to get an appropriate and well-defined upper limit of the nitrogen chemical potential at any $T, p$ as:

$$\mu_{\mathrm{N}}(T,p) \leq \frac{1}{2} g^{\mathrm{gas}}_{\mathrm{N_2}}(T,p). \tag{4.16}$$

In order to get lower limit for the Mn and N chemical potentials in the $T, p$-range below the melting point of bulk $Mn_3N_2$, we introduce the free energy of formation for bulk $Mn_3N_2$:

$$\Delta G_f(T,p) = g^{\mathrm{bulk}}_{\mathrm{Mn_3N_2}}(T,p) - 3g^{\mathrm{bulk}}_{\mathrm{Mn}}(T,p) - g^{\mathrm{gas}}_{\mathrm{N_2}}(T,p). \tag{4.17}$$

Combining Eqs. (4.13) and (4.17) with the boundary conditions given by Eqs. (4.15)-(4.16) the thermodynamically allowed range for the nitrogen chemical potential is:

$$\frac{1}{2}\left[\Delta G_f(T,p) + g^{\mathrm{gas}}_{\mathrm{N_2}}(T,p)\right] < \mu_{\mathrm{N}}(T,p) < \frac{1}{2} g^{\mathrm{gas}}_{\mathrm{N_2}}(T,p). \tag{4.18}$$

The lower limit in Eq. (4.18) corresponds to N-poor (Mn-rich) conditions, while the upper one to N-rich (Mn-poor) conditions. In practice, the surface free energies (Eq. (4.14)) are plotted as function of the N chemical potential in the predicted thermodynamically allowed range. Since the chemical potential is fully determined by the temperature $T$ and pressure $p$ of the gas phase, the link between the theoretical phase diagram and experimental conditions is straightforward [88, 227, 230, 231].

The formalism presented up to this point is based on Gibbs free energies of solid/gas phases, that should be related to DFT total energy calculations. The first principles total energies $E^{\mathrm{total}}(V, n_{\mathrm{Mn}}, n_{\mathrm{N}})$ are calculated at a certain volume of the unit cell $V$, and corresponds in a restricted way (neglecting zero point vibrations) to the Gibbs free energy at zero temperature and pressure only:

$$G(0,0,n_{\mathrm{Mn}},n_{\mathrm{N}}) = E^{\mathrm{total}}(V,n_{\mathrm{Mn}},n_{\mathrm{N}}). \tag{4.19}$$

This follows from the general expression for the Gibbs free energy:

$$\begin{aligned} G(T,p,n_{\mathrm{Mn}},n_{\mathrm{N}}) &= E^{\mathrm{total}}(V,n_{\mathrm{Mn}},n_{\mathrm{N}}) + F^{\mathrm{vib}}(T,V,n_{\mathrm{Mn}},n_{\mathrm{N}}) + \\ &+ F^{\mathrm{mag}}(T,V,n_{\mathrm{Mn}},n_{\mathrm{N}}) - TS^{\mathrm{conf}}(T,p,n_{\mathrm{Mn}},n_{\mathrm{N}}) + pV(T,p,n_{\mathrm{Mn}},n_{\mathrm{N}}). \end{aligned} \tag{4.20}$$

Here, $S^{\mathrm{conf}}$ is the configurational entropy, $F^{\mathrm{vib}}(T,V,n_{\mathrm{Mn}},n_{\mathrm{N}})$ is the vibrational Helmholtz free energy:

$$F^{\mathrm{vib}}(T,V,n_{\mathrm{Mn}},n_{\mathrm{N}}) = E^{\mathrm{vib}}(T=0,V,n_{\mathrm{Mn}},n_{\mathrm{N}}) - TS^{\mathrm{vib}}(T,V,n_{\mathrm{Mn}},n_{\mathrm{N}}), \tag{4.21}$$

where $E^{\mathrm{vib}}$ and $S^{\mathrm{vib}}$ are the energy (including zero point vibrations) and entropy contribution due all vibrational modes of the system. $S^{\mathrm{mag}}(T,V,n_{\mathrm{Mn}},n_{\mathrm{N}})$ in Eq. (4.20) is the magnetic Helmholtz free energy due to all kind of magnetic excitations that are expressed in terms of energy (residual

or zero point entropy) and entropy terms similar to Eq. (4.21).

For solid phases, the order of the pressure term in Eq. (4.20) can be estimated from a simple dimensional analysis, that results into contribution of $\sim 10^{-3}$ meV/Å$^2$ to the surface free energy [68, 227]. This contribution is negligible compared to the actually calculated surface energies of the $Mn_3N_2$ surface. For well-ordered crystals and surfaces ($S^{\text{conf}} = 0$) this leaves only vibrational and magnetic entropy contributions in Eq. (4.20) that are typically assumed to be negligible [74, 88, 230, 231]. The Gibbs free energy for a slab and bulk systems is then:

$$G(T, p, n_{\text{Mn}}, n_{\text{N}}) \approx E^{\text{total}}(V, n_{\text{Mn}}, n_{\text{N}}). \tag{4.22}$$

In contrast to solid/liquid phases, the temperature and pressure terms are significant for the gas phase, such as a gas of $N_2$ molecules [74]. Consequently, these terms can not be neglected. For a nitrogen gas, however, the $pV$ term in Eq. (4.20) is always smaller than the entropy contribution [88, 228]. Disregarding the Helmholtz free energy contribution and the $pV$ term for nitrogen gas provides, therefore, the upper limit of the nitrogen chemical potential:

$$\left[g^{\text{gas}}_{\text{N}_2}(T, p)\right]_{\text{max}} \approx \frac{1}{2} E^{\text{total}}_{\text{N}_2}, \tag{4.23}$$

where $E^{\text{total}}_{\text{N}_2}$ is the total energy of a free isolated $N_2$-molecule at $T = 0$ K.

It is noteworthy that DFT calculations typically provide more accurate results for extended systems than for isolated atoms or molecules [227]. It is therefore suitable to rewrite Eq. (4.18) such that it does not explicitly include atomic or molecular quantities:

$$\frac{1}{2}\left[g^{\text{bulk}}_{\text{Mn}_3\text{N}_2}(0,0) - 3g^{\text{bulk}}_{\text{Mn}}(0,0)\right] < \mu_{\text{N}}(T, p) < \frac{1}{2}\left[g^{\text{bulk}}_{\text{Mn}_3\text{N}_2}(0,0) - 3g^{\text{bulk}}_{\text{Mn}}(0,0)\right] - \frac{1}{2}\Delta G_f(T, p). \tag{4.24}$$

In this formulation the lower boundary (nitrogen-poor limit) is a safe reference that is solely defined by bulk and slab quantities. Although the chemical potential of $N_2$ does not explicitly enter Eq. (4.24), $\Delta G_f(T, p)$ in the right-hand side of Eq. (4.24) depends on the free energy of the $N_2$ molecule:

$$\Delta G_f(T, p) \approx g^{\text{bulk}}_{\text{Mn}_3\text{N}_2}(0,0) - 3g^{\text{bulk}}_{\text{Mn}}(0,0) - g^{\text{gas}}_{\text{N}_2}(T, p). \tag{4.25}$$

Eqs. (4.23) and (4.25) imply that $\Delta G_f(0,0)$ corresponds to the largest thermodynamically allowed range accessible for the nitrogen chemical potential. The calculated $\Delta G_f(0,0)$ is typically in reasonable agreement with experimental values due to the DFT error cancelation in Eq. (4.17) [227]. In some cases, however, the mismatch between the calculated and experimental formation free energies is significant. This leads to ill-defined theoretical boundaries of $\mu_{\text{N}}$ and might alter the calculated phase diagram [88]. To prevent such situations the calculated formation energies $\Delta G_f(0,0)$ should be compared with experimental values, and, if needed, the predicted range should be cor-

rected[3].

It is important to note that the above described boundaries for $\mu_N(T,p)$ are theoretically well defined limits, yet they only represent an estimate of the truly accessible range of the nitrogen chemical potential. Therefore, in the following we include in the resulting surface phase diagrams also regions some tens of an eV outside the nitrogen-rich and nitrogen-poor boundaries.

## 4.4 Results

### 4.4.1 Choice of Pseudopotentials

Properly constructed pseudopotentials present a rather marginal approximation and allow for an accurate description of the valence electrons over the entire chemically relevant range of systems [43]. Ideally, pseudopotential calculations allow to adequately reproduce the corresponding all-electron counterpart. For most of the elements (like, e.g., nitrogen) such a high accuracy of the pseudopotential is combined with its softness, i.e. with relatively low computational cost. For some of the chemical elements (like, e.g., $3d$-metals), however, the all-electron results can be precisely reproduced only at unrealistic computational costs. In this situation it is essential to find an acceptable compromise between the computational demands and the accuracy of the pseudopotential, as discussed in this section for Mn. The discussion is made for a pseudoatom generated with the PBE exchange-correlation functional. The same arguments apply if LDA is used, i.e. both LDA and PBE pseudopotentials are generated employing an identical set of parameters.

We generate the Mn pseudopotential taking its atomic ground state as a reference. We have found, that the ground state of an isolated Mn atom does not correspond to the configuration $[\mathrm{Ar}]3d^5 4s^2$ as conventionally given in textbooks. In fact, transferring part of the $4s$ electrons to the $3d$ orbital, i.e. hybridizing the $s$ and $d$ electrons, leads to (i) a change of the energy splitting between $d$ and $s$ eigenenergies, and (ii) can reduce the total energy of a Mn atom (see Fig. 4.11(a)). The occupancy state that minimizes the total energy is $[\mathrm{Ar}]3d^{5.655}4s^{1.345}$ (see Fig. 4.11(b)).

We focus now on the description of the $3d$ orbital, since it is the most localized valence shell of Mn (see Fig. 4.12(a)). This orbital essentially defines the computational cost and the quality of the pseudopotential. A high degree of $3d$ localization also implies that the Mn pseudopotential should be generated employing the Troullier-Martins scheme because Hamann-pseudopotentials would need by far too many planewaves [102].

A reasonable compromise between the computational cost and the accuracy was found at a cutoff radius $r_d^{\mathrm{ps}}$=2.3 Bohr for the $d$-orbital. The cutoff radius for the nonlinear core-correction (nlcc) is $r_{\mathrm{cut}}^{\mathrm{core}}$=1.0 Bohr. The $3d$ Troullier-Martins pseudowavefunction, however, has a substantially different shape compared to its all-electron counterpart: its maximum is shifted to a larger radius,

[3] In cases when experimental calorimetry data are not available the theoretical errorbar in the formation energy can be *roughly* estimated from a comparison of the $\Delta G_f(0,0)$ calculated employing local (LDA) and gradient-corrected (GGA) exchange-correlation functionals (see, e.g., Ref. [88]).

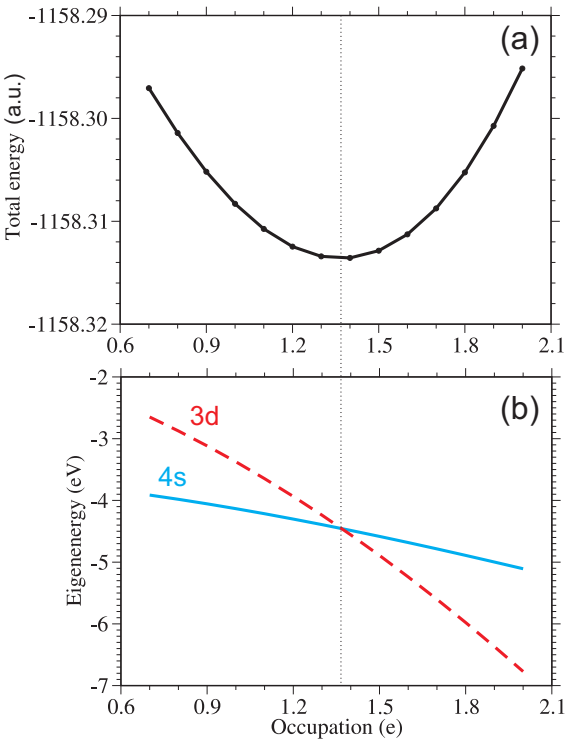


Figure 4.11: (a) Total energy of an isolated manganese atom calculated with an all-electron DFT versus the occupation of the 4$s$ orbital. The occupation of this orbital is changed by a transfer of part of an electron from the 4$s$ to the 3$d$ orbital. (b) Corresponding eigenenergies of 4$s$ and 3$d$ orbitals. PBE exchange-correlation is used, the cutoff radii of the pseudopotential are $r_s^{\rm ps}$=2.3 Bohr, $r_p^{\rm ps}$=2.4 Bohr, $r_d^{\rm ps}$=2.3 Bohr.

as can be seen in Fig. 4.12(a). The discrepancy can be reduced by choosing a smaller $r_d^{\rm ps}$. The required computational cost increases, however, tremendously: while for $r_d^{\rm ps}$=2.3 Bohr it is sufficient to use a planewave energy cutoff 50 Ry, $r_d^{\rm ps}$=1.5 Bohr would require 100 Ry, and $r_d^{\rm ps}$=1.3 Bohr more than 200 Ry. The latter cutoff energies are hardly feasible and completely diminish the advantages of a low-cost pseudopotential approach. At the same time, $r_{\rm cut}^{\rm core}$=1.0 Bohr is found to be fully converged and provides an accurate description of the full-potential core density for radii larger than 0.5 Bohr (see Fig. 4.12(b)).

To quantify the accuracy of the pseudopotential in the atomic calculations we consider the spin-polarization energy. This energy is defined as the difference between the total energy of a spin-polarized and a spin-neutral atom $E_{\rm total}^{\rm spin} - E_{\rm total}^{\rm nospin}$. For an all-electron atom the spin-polarization energy is -4.3 eV. This energy differs by 0.4 eV from that of a pseudo atom with $r_d^{\rm ps}$=2.3 Bohr and $r_{\rm cut}^{\rm core}$=1.0 Bohr (see Tab. 4.1) for the reason discussed above. We note here, that from Tab. 4.1 it follows that $r_{\rm cut}^{\rm core}$=1.0 Bohr is indeed a converged nlcc-radius, and that nlcc is absolutely necessary for Mn. Moreover, for $r_d^{\rm ps}$ = 1.0 Bohr or less, the spin-polarization energy approaches the all-electron result.

The cutoff radii for an $s$ orbital providing an accurate description for $r < 1.8$ Bohr is $r_s^{\rm ps}$=2.3 Bohr, and for an unoccupied $p$ shell $r_p^{\rm ps}$=2.4 Bohr[4].

[4]The reference energy employed in generating the Mn $p$-pseudopotential is -1 eV. The $p$-wavefunction is generated for an ionized $Mn^{+1}$ ion in the $3d^{5.655}4s^{0.045}4p^{0.3}$ state. The local component for a fully-separable Mn pseudopotential is $s$.

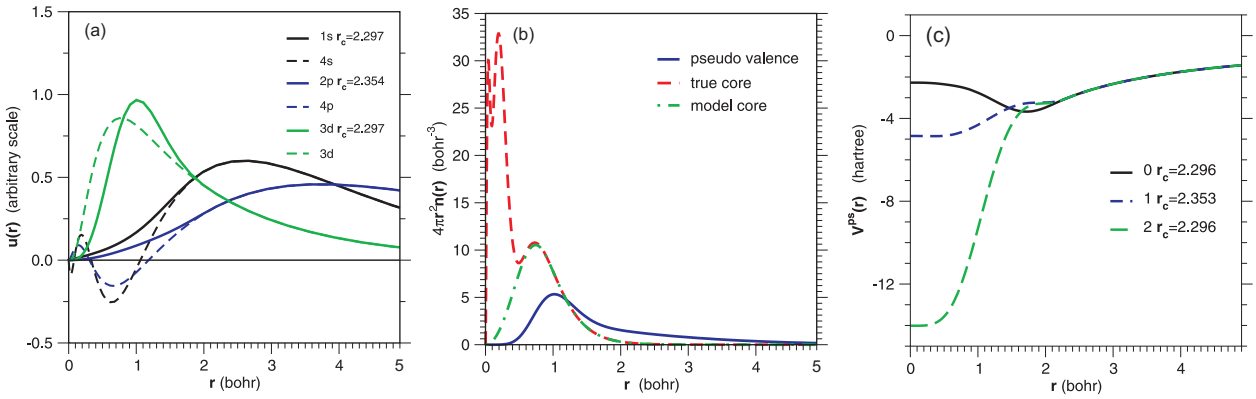


Figure 4.12: (a) Radial part of the all-electron and the pseudopotential wavefunctions calculated for an isolated Mn atom in equilibrium state. (b) Corresponding all-electron and pseudopotential charge densities, including the model-core density employed in a nonlinear core correction. (c) Radial part of the Mn pseudopotential. PBE exchange-correlation is employed. The cutoff radii of the pseudopotential are $r_s^{\rm ps}$=2.3 Bohr, $r_p^{\rm ps}$=2.4 Bohr, $r_d^{\rm ps}$=2.3 Bohr, $r_{\rm cut}^{\rm core}$=1.0 Bohr.

In contrast to Mn, the nonlinear core-correction is not required to construct a nitrogen pseudopotential [88, 232]. The chosen radii $r_s^{\rm ps}$=1.45 Bohr, $r_p^{\rm ps}$=1.45 Bohr, and $r_d^{\rm ps}$=1.45 Bohr ensure a perfect agreement between pseudoatom and full-potential wavefunctions (see Fig. 4.13)[5].

In addition we have verified that the transferability of the Mn and N pseudopotentials, i.e. their ability to perform in different chemical environments. We have therefore applied the test scheme proposed Gonze, analyzing logarithmic derivatives of the semilocal and fully separable pseudopotentials, and performing a spectral test of the pseudo and all-electron eigenenergies. For a detailed explanation of these tests see Refs. [43, 102]. The performance of the generated pseudopotentials in molecular and bulk calculations has been verified by a comparison to previous *ab initio* studies and to available experimental data in Secs. 4.4.2-4.4.4.

### 4.4.2 Properties of the $N_2$ molecule

In order to verify the accuracy of the N pseudopotential we have calculated the binding and vibrational properties of an isolated $N_2$ molecule. These computations are also essential to get the upper range of the experimentally accessible chemical potential of a nitrogen atom, as e.g. later needed to construct the $Mn_3N_2(010)$ surface phase diagram (see Sec. 4.4.5).

The calculated binding energy, the equilibrium bond length, and the frequency of the fundamental vibrational mode of the $N_2$ molecule are listed in Table 4.2. The binding energy is the energy difference between the total energy of the $N_2$ molecule and that of the isolated constituent nitrogen atoms $E_{\rm b} = E_{\rm tot}^{\rm N_2} - 2E_{\rm tot}^{\rm N-atom}$. Vibrational properties of $N_2$ are obtained from the total energy versus bond length curve $E_{\rm tot}^{\rm N_2}(d)$, that was calculated by varying the bond length in a range of ±10%

[5]The reference energy employed for $d$-pseudopotential is the eigenvalue of the $p$-state. The $d$-wavefunction is generated for an ionized $N^{+1}$ atom in the $3s^{1.5}4p^{0.0}4d^{0.5}$ state. The local component of the pseudopotential is $d$.

| $r_{\text{core}}^{\text{cut}}$ | $r_d^{\text{ps}}$ | $E_{\text{total}}^{\text{spin}}$(a.u.) | $E_{\text{total}}^{\text{nospin}}$(a.u.) | $E_{\text{total}}^{\text{spin}} - E_{\text{total}}^{\text{nospin}}$(eV) |
|---|---|---|---|---|
| none | 2.3 | -13.95486 | -13.65970 | -8.03 |
| 1.8 | 2.3 | -15.26518 | -15.04516 | -5.99 |
| 1.6 | 2.3 | -16.36410 | -16.16642 | -5.38 |
| 1.4 | 2.3 | -18.31905 | -18.13905 | -4.90 |
| 1.2 | 2.3 | -20.06334 | -19.88987 | -4.72 |
| 1.0 | 2.3 | -21.88791 | -21.71584 | -4.68 |
| 0.5 | 2.3 | -26.79048 | -26.61828 | -4.69 |
| 0.5 | 1.0 | -27.87220 | -27.71049 | -4.40 |
| all-electron | | -1158.47053 | -1158.31358 | -4.27 |

Table 4.1: Dependence of the spin-polarization energy on the cutoff radius of the $d$-orbital $r_d^{\text{ps}}$ and the cutoff radius of the nonlinear core-correction $r_{\text{core}}^{\text{cut}}$. The occupations of the $s$ and $d$ orbitals correspond to the atomic equilibrium (5.655 and 1.345, respectively), the $p$-orbital is unoccupied. PBE exchange-correlation is used.

around the experimental equilibrium bond length (1.10 Å). Assuming that the molecule behaves like a quantum harmonic oscillator (quasiharmonic approximation) the fundamental vibrational frequency can be expressed as:

$$\omega = \sqrt{\frac{k}{m_{\text{r}}}}, \tag{4.26}$$

where $\omega = 2\pi\nu$ is the angular frequency, $\nu$ is the vibrational frequency, $k$ is the bond length constant, and $m_{\text{r}}$ is the reduced mass of the molecule. $k$ is found by fitting the theoretical $E_{\text{tot}}^{\text{N}_2}(d)$ curve to the equation of the classical harmonic oscillator $E(d) = \frac{1}{2}k(d - d_0)^2$, where $d_0$ is the theoretical equilibrium bond length. The conversion from the units of Hertz to units of wavelength, as widely used when presenting spectroscopic data was done by:

$$\nu[\text{cm}^{-1}] = \frac{2\pi c}{\omega}. \tag{4.27}$$

Here $c$ is the light velocity.

The present results are in good agreement with previous calculations: the deviations of the calculated equilibrium bond length and the vibrational frequency from those of the full-potential method is less than 0.1% and 1.5%, respectively. The calculated binding energy is overestimated by about 0.25 eV/atom compared to all-electron results. This error is attributed to the overlapping core regions of nitrogen pseudoatoms, which is caused by the short bond length of a $N_2$ dimer and the chosen pseudopotential cutoff radii $r_{s,p,s}^{\text{cut}} = 1.45$ Bohr. Decreasing $r_{s,p,s}^{\text{cut}}$ improves the performance of the N pseudopotential [232], but would require a planewave cutoff much larger than 50 Ry (the scale set by the Mn $3d$ states) and consequently much costlier computations. We consider this overlap error as acceptable because it does not affect any results of this chapter. Specifically, it has essentially negligible effect on the calculated phase diagram of $Mn_3N_2(010)$ surface, since for

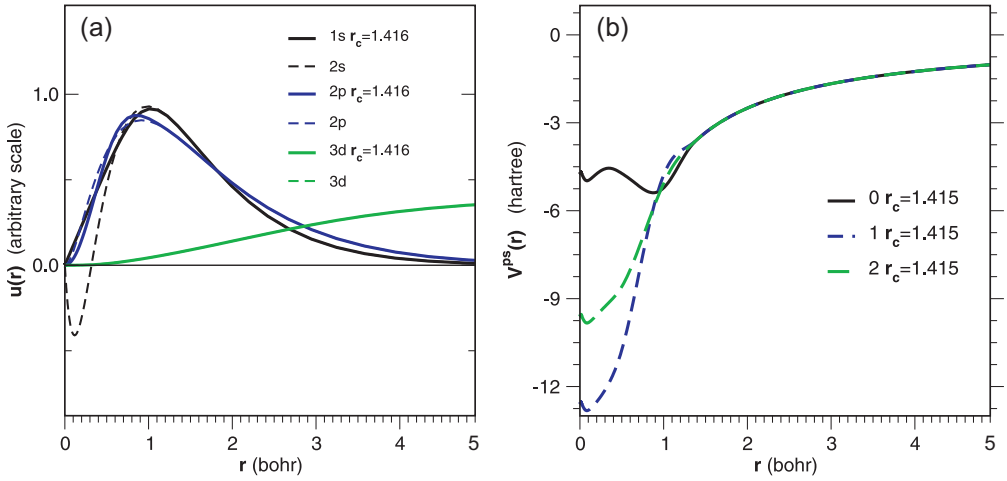


Figure 4.13: (a) Radial part of all-electron and pseudopotential wavefunctions calculated for isolated nitrogen atom. (b) Radial part of the N pseudopotentials. PBE exchange-correlation is employed, cutoff radii of the pseudopotential are $r_s^{\mathrm{ps}}$=1.45 Bohr, $r_p^{\mathrm{ps}}$=1.45 Bohr, $r_d^{\mathrm{ps}}$=1.45 Bohr.

the system $Mn_3N_2$ considered here the interatomic distances are about 3.78 Bohr, thus exceeding the critical distance of 3.74 Bohr for which the Mn and N cores start to overlap.

Compared to LDA, PBE leads to slightly lower vibrational frequencies and smaller binding energies, which are closer to experiment. Compared to experiment the calculated binding energies are overestimated by 3% and 13% using PBE and LDA, respectively.

Concluding, from Table 4.2 it follows that the chosen settings for the pseudopotentials reliably describe properties of $N_2$ molecule and provides results that are in good agreement with previous theoretical studies.

### 4.4.3 Properties of bulk Mn

The chemical potential of manganese in the bulk ground state is an essential property for the construction of the $Mn_3N_2(010)$ surface phase diagram (see, e.g., Eqs. (4.24)-(4.25)). Since it is not feasible to construct a Mn normconserving pseudopotential that would exactly reproduce the full-potential calculations at reasonable computational cost (see Sec. 4.4.1), it is crucial to verify whether and if the employed norm-conserving pseudopotential (NCPP) provides accurate results when physical properties of extended systems are calculated. For this reasoning we study here the stability of manganese in its simple cubic crystalline phases and compare results with available *ab initio* and experimental data.

The properties of bulk Mn are intensively studied both theoretically and experimentally [235–237]. $\alpha$-Mn, the most stable polymorph under normal conditions of temperature and pressure has an exotic crystal structure consisting of 58 atoms in a cubic unit cell with a complex noncollinear antiferromagnetic configuration [235]. $\beta$-Mn exists in the temperature interval between 1000 and

| Reference | XC | Method | $d$(Bohr) | $E_b$(eV) | $\nu$(cm$^{-1}$) |
|---|---|---|---|---|---|
| This work | LDA | NCPP | 2.06 | -11.21 | 2398 |
| Ref. [88] | LDA | NCPP | 2.06 | -11.71 | 2363 |
| Ref. [233] | LDA | NCPP | 2.08 | -11.59 | 2384 |
| Ref. [232] | LDA | NCPP | 2.06 | -11.90 | 2372 |
| Ref. [232] | LDA | FP-LAPW | 2.08 | -11.72 | 2399 |
| Ref. [234] | LDA | USPP | 2.10 | -11.33 | 2465 |
| This work | PBE | NCPP | 2.06 | -10.17 | 2324 |
| Ref. [88] | PBE | NCPP | 2.06 | -10.66 | 2331 |
| Ref. [233] | PWII | NCPP | 2.10 | -10.24 | 2332 |
| Ref. [232] | PBE | NCPP | 2.08 | -10.83 | 2325 |
| Ref. [232] | PBE | FP-LAPW | 2.08 | -10.64 | 2355 |
| Ref. [234] | PW91 | USPP | 2.10 | -10.56 | 2351 |
| Experiment[a] | | | 2.08 | -9.91[b] | 2360 |

[a] Taken from Ref. [232]

[b] Including the zero point vibrational energy gives a value of -9.76 eV

Table 4.2: Calculated bond length $d$, frequency of the fundamental mode $\nu$, and binding energy $E_b$ for an $N_2$ molecule employing LDA and GGA exchange-correlation functionals. The zero-point vibrational energies of the molecule are not included. The properties of the $N_2$ molecule and of the isolated nitrogen atom are calculated employing a planewave energy cutoff of 50 Ry and a single **k**-point with relative coordinates (0.25,0.25,0.25); the unit cell is cubic with lattice parameter 20 Bohr. The calculated parameters are converged with respect to the planewave cutoff energy and the size of the unit cell. NCPP stands for norm-conserving pseudopotentials, USPP for ultrasoft pseudopotentials, FP-LAPW for the full-potential linear augmented planewave method.

1368 K and is simple cubic with twenty atoms per unit cell. At temperatures exceeding 1368 K manganese transforms to fcc $\gamma$-phase, and above 1406 K to bcc $\delta$-Mn [236].

Because of the enormous computational effort we do not explicitly calculate the properties of $\alpha$- and $\beta$-Mn, but focus on the much simpler cubic phases of bulk manganese, namely, on $\gamma$-Mn (fcc), $\delta$-Mn (bcc) and $\epsilon$-Mn (hcp). We note here that the energy difference between $\alpha$-Mn and the most stable among $\gamma$-, $\delta$-, and $\epsilon$-Mn has been calculated by Hafner and co-workers [238] and is less than 0.1 eV. We have verified that including this energy difference in the calculation of the chemical potential of bulk Mn does not affect any conclusion of this study. This provides a strong justification for restriction of the ground state of manganese to cubic crystalline phases.

For each structure (fcc, hcp, and bcc) we have computed the total energy and the local magnetic moments as function of volume. Nonmagnetic (NM), ferromagnetic (FM) and antiferromagnetic (aFM, magnetic moments alternate layer-wise along the [001] axis) states are considered. The position of the minimum in the energy vs volume curve gives the equilibrium lattice constant and the curvature at the minimum is related to the bulk modulus at equilibrium. The ground-state properties have been obtained from a fit of the total energies computed at a series of fixed volumes to a Murnaghan equation of state (see App. A.4). The calculations are performed employing a

planewave energy cutoff of 50 Ry, a Monkhorst-Pack mesh with 6x6x6 folding (18 **k**-points in the irreducible wedge of the Brillouin zone (IBZ)) for fcc- and bcc-structures, and 8x8x5 (60 **k**-points in the IBZ) for the hcp-phase. These parameters ensure a convergence of the total energy better than 2 meV/atom.

The calculated structural, cohesive and magnetic properties of the energetically most favorable $\gamma$-, $\delta$- and $\epsilon$-Mn phase are listed in Table 4.3.

Our pseudopotential calculations in LDA agree with ultrasoft pseudopotential (USPP) (Ref. [239]) and full-potential (FP) LMTO (Ref. [237]) total energy calculations, indicating that the nonmagnetic hcp-phase has the lowest energy among the three structures considered here. The structural energy difference between the aFM fcc-phase and NM hcp-phase is only 18 meV, and between the FM bcc and NM hcp-phase 150 meV. In agreement with results of USPP and FP-LMTO studies, for each crystal structure the total energy difference between the NM, FM, and aFM phase is in the range of the few meV/atom. This implies that the various magnetic states for $\gamma$-, $\delta$- and $\epsilon$-Mn are energetically almost degenerate. This explains the difference between our ground-state phases (FM for bcc, aFM for fcc), USPP (NM for bcc, NM for fcc) and FP-LMTO (NM for bcc, aFM for fcc). For the equilibrium atomic volume $V_0$, all phases are in the range between 10.83 and 10.93 Å$^3$. For the same quantities FP-LMTO and USPP give 10.05-10.16 Å$^3$, i.e. predict an about 3% smaller equilibrium lattice constants than the norm-conserving pseudopotential used in this work. Despite the atomic volumes predicted with by NCPP are closer to experiment, LDA gives too small equilibrium volumes and cannot predict an aFM ordering for the ground state of fcc-Mn when compared with experimental results.

A similar agreement between NCPP and USPP calculations is found when GGA is used. The results are summarized in Table 4.3. For both methods, the comparison of LDA and GGA calculations demonstrates that the gradient correction lifts the energy degeneracy of various magnetic phases, and leads to a strong magnetovolume effect (see, e.g., Fig. 4.15(a)-(d)). The origin of the magnetovolume effect is in the occupation of antibonding orbitals of the majority spins and the depletion of the bonding states of the minority spins [239]. For all crystal structures this leads to a stabilization of the aFM-ordering in the ground state.

We find that GGA increases the equilibrium volumes and decreases the calculated bulk moduli. This agrees with the well-known tendency of GGA to reduce the bond strength, to stabilize magnetic ordering, and to produce substantially larger magnetovolume effects than the purely local LDA [239–241]. Both NCPP and USPP indicate that an increase of the equilibrium volume is more pronounced for the magnetic phases, while the structural energy differences between the nonmagnetic states are very little affected by nonlocal exchange-correlation corrections. This implies that aFM ordering arises almost entirely from the energy gain in the magnetic rather than in the structural energy contributions.

Similar to LDA, NCPP in GGA predicts somewhat overestimated equilibrium lattice constants (by about 3% larger) compared to the corresponding USPP total energy calculations. Because both

| | Structure | Phase | $\Delta H$(meV) | $V_0$(Å$^3$/atom) | $a_0$(Å) | $B_0$(Mbar) | $\lvert m_0\rvert$ ($\mu_B$) |
|---|---|---|---|---|---|---|---|
| This work (NCPP) | | | | | | | |
| LDA | hcp | NM | -18 | 10.83 | 2.492 | 2.98 | 0.0 |
| | bcc | FM | 131 | 10.84 | 2.789 | 2.28 | 0.6 |
| | fcc | aFM | 0 | 10.94 | 3.524 | 1.87 | 0.7 |
| PBE | hcp | aFM | 190 | 12.35 | 2.595 | 1.16 | 1.9 |
| | bcc | aFM | 18 | 14.95 | 3.103 | 0.44 | 3.6 |
| | fcc | aFM | 0 | 13.33 | 3.764 | 0.90 | 2.9 |
| Reference [239] (USPP) | | | | | | | |
| LDA | hcp | NM | -40 | 10.08 | 2.425 | 3.13 | 0.0 |
| | bcc | NM | 130 | 10.16 | 2.729 | 3.10 | 0.0 |
| | fcc | NM | 0 | 10.12 | 3.433 | 3.10 | 0.0 |
| PW92 | hcp | aFM | 100 | 11.08 | 2.502 | 1.00 | 0.8 |
| | bcc | aFM | 120 | 13.80 | 3.022 | 0.60 | 3.2 |
| | fcc | aFM | 0 | 12.19 | 3.653 | 0.95 | 2.4 |
| Reference [237] (FP-LMTO) | | | | | | | |
| LDA | hcp | NM | -54 | 10.05 | 2.431 | | 0.0 |
| | bcc | NM | 82 | 10.05 | 2.719 | | 0.0 |
| | fcc | aFM | 0 | 10.05 | 3.426 | | 0.2 |
| Reference [238] (PAW) | | | | | | | |
| PW92 | $\alpha$-Mn | aFM-NCL | 0 | 11.08 | | 1.88 | |
| | $\beta$-Mn | FI | 63 | 10.84 | | 2.69 | |
| | hcp | NM | 61 | 10.72 | 3.500 | 2.46 | 0.0 |
| | fcc | aFM | 67 | 11.16 | 3.547 | 1.44 | 1.6(2.3)[a] |
| Ref. [238] | | | Experiment[b] | | | | |
| | $\alpha$-Mn | aFM-NCL | | 12.05 | | | |
| | $\beta$-Mn | FI | | 12.44 | | | |
| | fcc | aFM | | 12.95 | 3.728 | | 2.4 |

[a] Calculated at the experimental atomic volume

[b] Values obtained by an extrapolation of the high-temperature data to room temperature

Table 4.3: Structural, cohesive, and magnetic properties of the energetically most favorable phases of fcc, bcc, and hcp Mn calculated in LDA and GGA. $\Delta H$ is the enthalpy difference with respect to the aFM fcc-phase, $V_0$ is the atomic equilibrium volume, $a_0$ is the equilibrium lattice constant, $B_0$ is the bulk modulus, and $m_0$ is the atomic moment. Theoretical results obtained employing norm-conserving pseudopotentials (NCPP) are compared with full-potential linear muffin-tin orbitals (FP-LMTO), ultrasoft pseudopotentials (USPP), and projected-augmented waves (PAW) *ab-initio* calculations.

sets of calculations provide essentially identical magnetovolume curves (see, e.g., Fig. 4.15(b),(d) for $\gamma$-Mn), the equilibrium magnetic moments calculated with NCPP are larger than the corresponding USPP counterparts. Compared to experimental data on quenched $\gamma$-Mn, NCPP and USPP correctly predict aFM $\gamma$-Mn as ground state; the corresponding lattice constant is overestimated (underestimated) by 1% (2%), and the calculated magnetic moment is 0.5 $\mu_B$ (0.0 $\mu_B$) larger than the respective experimental value.

In contrast to pseudopotential calculations and in disagreement with experiment, the ground state predicted in PAW study (Ref. [238]) is nonmagnetic hcp-Mn. This phase is by about 8 meV lower than the aFM fcc-phase (see Table 4.3). At the same time, all-electron and pseudopotential methods provide essentially identical results for magnetic volume as a function of volume, and description of aFM and FM phases (see, e.g., results for $\gamma$-Mn on Fig. 4.15). The nonmagnetic phase calculated with NCPP and USPP is less favorable compared to the all-electron calculations. Similar to LDA, the equilibrium lattice constants predicted with pseudopotential methods are larger than the all-electron counterparts, and therefore are closer to experiment (see Table 4.3).

According to Hafner and co-workers [238], the difference between the all-electron and pseudopotential calculations can be traced back to an isotropic contribution of the gradient terms to the internal pressure arising mostly from the region where valence- and core electrons and spin densities overlap. In this region, the difference between the all-electron and pseudodensities becomes important - the effect is larger for the magnetic terms because the spin densities tend to be more localized. As discussed in Sec. 4.4.1, this difference cannot be eliminated by nonlinear core corrections, it can be made to disappear only by choosing a very hard pseudopotential requiring also a very extended basis set.

While qualitatively the norm-conserving and ultrasoft pseudopotentials yield identical results in both GGA and LDA, NCPP consistently predicts larger equilibrium volumes for all Mn phases. For magnetically ordered states this results in slightly larger values of the magnetic moments for manganese atoms (see Table 4.3). This behavior improves the agreement between calculated and experimental equilibrium lattice constants (about -5%(+1%) in LDA (GGA) employing norm-conserving pseudopotentials versus -13%(-2%) with USPP for aFM $\gamma$-Mn), but simultaneously indicates that NCPP performs poorer than USPP when compared to all-electron total energy calculations (-8% and -5% for LDA and GGA, respectively).

The minor quantitative difference between the NCPP and USPP calculations appears due to different generation schemes employed to construct the pseudopotentials. While norm-conserving pseudopotentials are generated using one reference energy per orbital, the USPP are generated taking advantage of the Vanderbilt approach [97], that uses a second reference energy in the construction of the factorized pseudopotential. This approach considerably improves the transferability and allows for increased cut-off radii without compromising the accuracy [242][6]. In other words,

[6]Because of the implementation obstacles only a few authors have tried to work out norm-conserving Vanderbilt pseudopotentials. For details see Ref. [242] and references therein.

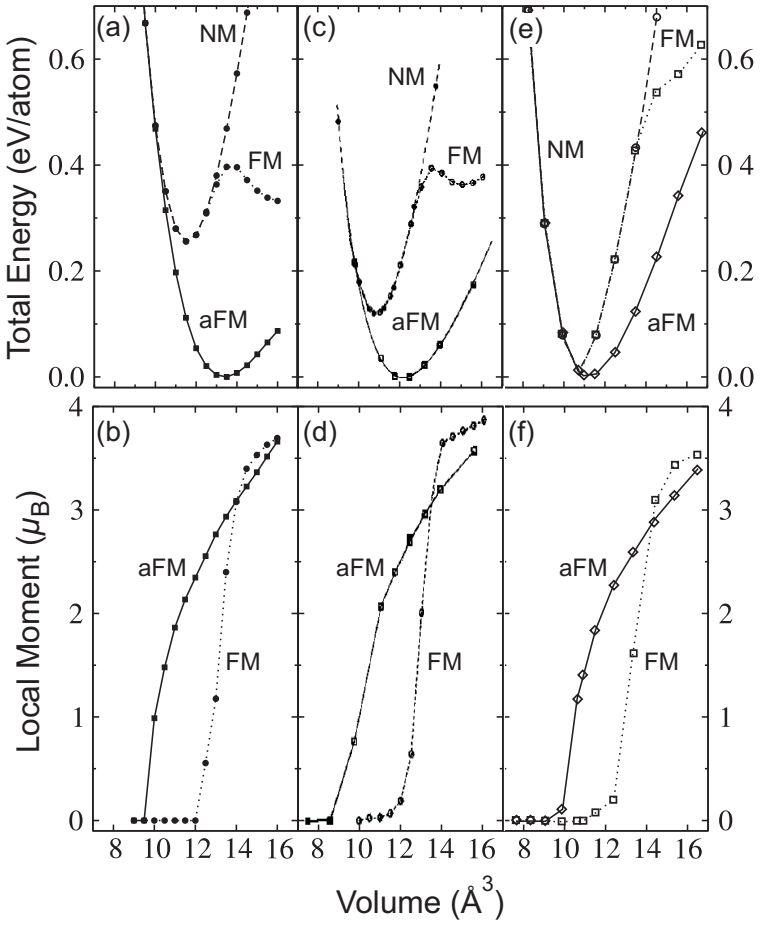


Figure 4.14: Total energy and magnetic moments as a function of atomic volume for nonmagnetic (NM), ferromagnetic (FM), and antiferromagnetic (aFM) phase of fcc Mn calculated in the GGA. The energy is given relative to the ground state energy. (a)-(b) Calculated with norm-conserving pseudopotentials (this work), (c)-(d) calculated employing ultra-soft pseudopotentials (Ref. [239]), and (e)-(f) PAW (Ref. [238]).

despite the cutoff radii of the *d*-component being similar for NCPP (2.3 Bohr) and USPP (2.2 Bohr), USPP provides a slightly better quantitative agreement with all-electron studies.

In summary, we have shown that the norm-conserving manganese pseudopotential used in this study provides a perfect agreement with previously reported pseudopotential calculations with respect to the stability and the magnetic phases of bulk Mn. Results of pseudopotential calculations are reasonably close to that of all-electron studies, especially in describing the stability of the magnetic ordering in a Mn-crystal and magnetovolume effects. Quantitatively, the Mn norm-conserving pseudopotential predicts equilibrium lattice parameters that are closer to experiment when compared to previous *ab initio* studies. It has been shown that a correct prediction of the Mn ground state is possible only by employing the GGA exchange-correlation functional.

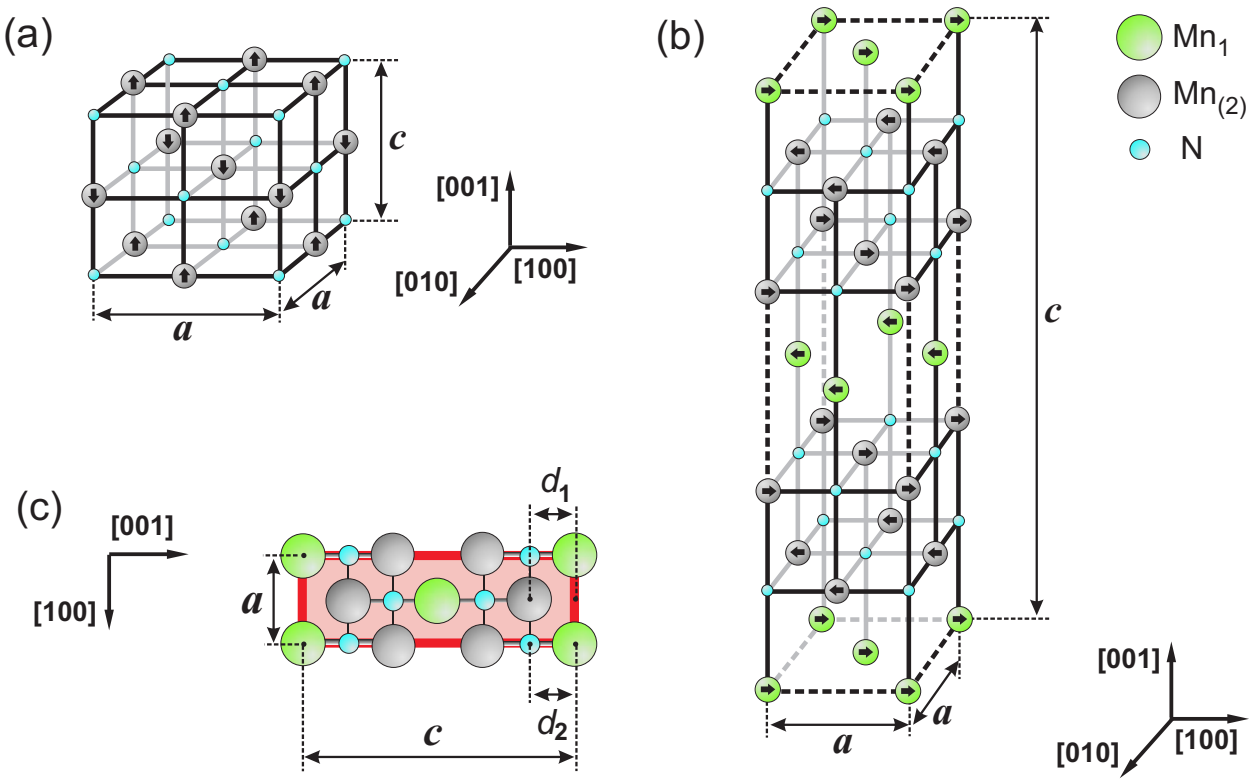


Figure 4.15: Crystalline and magnetic structure of ground-state (a) $\theta$-MnN (MnN) and (b)-(c) $\eta$-MnN ($Mn_3N_2$). Solid lines schematically indicate the bonds between atoms. The arrows in the shaded circles indicate the orientation of the magnetic moments. $Mn_1$ marks two-fold coordinated, $Mn_2$ five-fold coordinated manganese atoms.

### 4.4.4 Properties of bulk Mn-N at high N content

Manganese nitride is known to form different bulk phases, including the $\theta$-phase (MnN), the $\eta$-phase ($Mn_3N_2$), the $\zeta$-phase ($Mn_5N_2$, $Mn_2N$, and $Mn_2N_{0.86}$), and the $\epsilon$-phase ($Mn_4N$) [214, 215, 221–223, 243]. Both structural and magnetic measurements have been reported for most of these phases, with particular emphasize on the $\theta$-, $\eta$-, and $\epsilon$-phase. $\epsilon$-MnN at room temperature is known to have a ferrimagnetic fcc-type structure with Mn atoms occupying the eight corner sites and the six face-centered sites and the N atom located at an interstitial site at the body center [244]; the reported Curie temperature is 738 K [220]. Increasing the Mn content stabilizes the antiferromagnetically ordered hexagonal close packed $\zeta$-phase. The latter has a Néel temperature of 301 K [220, 244–246].

The crystal structures for both N-rich $\theta$-MnN and $\eta$-MnN are known to have a NaCl-type face-centered-tetragonal (fct) structure at room temperature (see Fig. 4.15). For $\eta$-$Mn_3N_2$, the measured Mn:N composition ratio matches very well with the ideal Mn:N ratio of 3:2. Nitrogen vacancies in $Mn_3N_2$ preferentially incorporate into every third (001) plane of manganese atoms, resulting in an ordered vacancy superlattice with two- and five-fold coordinated Mn. Neutron diffraction

studies have established that $Mn_3N_2$ is antiferromagnetic with the bulk magnetic moments oriented perpendicular to the tetragonal $c$ axis. These moments are ferromagnetic within (001) planes and are layerwise antiferromagnetic along [001]. The Néel temperature of $Mn_3N_2$ is 913-927 K.

The crystalline structure of $\theta$-MnN is very similar to that of $Mn_3N_2$ (see Fig. 4.15). The ideal Mn:N composition ratio for $\theta$-MnN is 1:1, while major experimental studies established that the actual ratio is close to 6:5. The $\theta$-phase is therefore frequently referred to as $Mn_6N_5$ or $Mn_6N_{5+x}$. There are, however, essentially no evidences that $Mn_6N_5$ is phase that supports a superstructure of nitrogen vacancies. Instead, the deviation from the 1:1 ratio only indicates the presence of N-vacancies that are randomly incorporated into octahedral lattice sites [247]. $\theta$-MnN is antiferromagnetic, with spins aligned parallel in (001) planes but with the direction of magnetization switching from one plane to the next. At low and ambient temperatures the Mn magnetic moments are tilted at 23° relative to the tetragonal $c$ axis, and become parallel to the axis above 550 K before the magnetization disappears at a Néel temperature of 600 K.

Despite numerous experimental studies on Mn-N compounds stimulated by the technological importance of manganese nitrides, very little is known about this class of materials from electronic structure calculations. We are aware only of one *ab initio* study by Lambrecht *et al.* [223], who analyzed the magnetic interactions and the crystalline structure of nitrogen-rich MnN phases, namely, the $\theta$- and $\eta$-phase employing the full-potential linear muffin-tin orbitals (FP-LMTO) approach. To crosscheck our calculations with the previously performed theoretical study we have focused, therefore, not only on the $Mn_3N_2$ phase relevant for this study, but also on $\theta$-MnN.

The calculated structural, cohesive, and magnetic properties of bulk $\theta$-MnN are shown in Table 4.4. Only collinear arrangements of magnetic moments are studied. The space of possible collinear antiferromagnetic configurations has been restricted to the experimentally reported layerwise alternating order (see Fig. 4.15(a)), and is compared with ferromagnetic and nonmagnetic states of MnN. The employed cutoff energy is 50 Ry, the bulk Brillouin zone is sampled using a 3x3x3 Monkhorst-Pack mesh (18 **k**-point in the irreducible wedge of the Brillouin zone (IBZ)).

Both LDA and GGA provide very similar results and correctly predict the aFM-state as the ground state of $\theta$-MnN. The next favorable spin-state is ferromagnetic, while the nonmagnetic phase is found to be unstable with respect to a decomposition into bulk-Mn and $N_2$. The aFM equilibrium lattice parameter $a_0$ is underestimated (overestimated) by about -1% (+2%) compared to the experimental value when LDA (GGA) is used. In agreement with experiment we find that the total energy of $\theta$-MnN is reduced by a tetragonal distortion of the unit cell with $c_0/a_0 < 1$. Corresponding magnetic moments of Mn are 2.94 $\mu_B$ and 3.54 $\mu_B$ for LDA and GGA, respectively.

In contrast to our results, the full-potential calculations of Lambrecht *et al.* predict a FM $\theta$-MnN as the ground state. This discrepancy with experiment is due to a strong underestimation of the lattice constant (by about 3%) [223]. This underestimation is a well known tendency of LDA and becomes more severe in transition metals and their compounds. Lambrecht and co-workers speculated that LDA underestimates correlation effects and the trends towards magnetism due to

| | Phase | $\Delta H$(meV) | $a_0$(Å) | $c_0/a_0$ | $E_{\rm coh}$(eV) | $E_f$(eV) | $B_0$(Mbar) | $\lvert m_0\rvert$ ($\mu_B$) |
|---|---|---|---|---|---|---|---|---|
| This work (NCPP) | | | | | | | | |
| LDA | NM | 453 | 4.044 | 1.000 | -10.21 | 0.01 | 3.79 | 0.00 |
| | FM | 60 | 4.129 | 1.000 | -10.61 | -0.38 | 2.36 | 2.73 |
| | aFM | 0 | 4.165 | 0.990 | -10.67 | -0.44 | 2.35 | 2.94 |
| PBE | NM | 1043 | 4.118 | 1.000 | -7.34 | 0.89 | 3.12 | 0.00 |
| | FM | 112 | 4.312 | 1.000 | -8.27 | -0.05 | 1.56 | 3.64 |
| | aFM | 0 | 4.315 | 0.985 | -8.39 | -0.16 | 1.90 | 3.54 |
| Reference [223] (FP-LMTO) | | | | | | | | |
| LDA | NM | 270 | 3.967 | 1.000 | -11.1 | | | 0.00 |
| | FM | -2 (69)[a] | 4.035 | 1.000 | -11.4 | | | 3.15 |
| | aFM | 0 | 4.086 | 0.978 | -11.4 | | 2.62 | 3.30 |
| Experiment (300 K) | | | | | | | | |
| Ref. [222] | aFM | | 4.256 | 0.984 | | | | |
| Ref. [215] | aFM | | 4.22 | 0.976 | | | | |
| Ref. [221][b] | aFM | | 4.219 | 0.979 | | | | 3.31 |

[a] Calculated at experimental atomic volume

[b] Data for $Mn_6N_{5.26}$

Table 4.4: Structural, cohesive and magnetic properties of bulk nonmagnetic (NM), ferromagnetic (FM) and antiferromagnetic (aFM) MnN. $\Delta H$ is the enthalpy difference with respect to the aFM phase, $V_0$ is the atomic equilibrium volume, $a_0$ is the equilibrium lattice constant, $B_0$ is the bulk modulus, and $m_0$ is the atomic magnetic moment. Theoretical results obtained employing norm-conserving pseudopotentials (NCPP) are compared with available experimental data and full-potential linear muffin-tin orbital (FP-LMTO) *ab initio* calculations.

an inadequate treatment of the LDA for the fairly narrow *d*-bands.

To improve the agreement with experiment Lambrecht *et al.* [223] performed FP-LMTO calculations at the experimental lattice constant rather than at the calculated value. Under these conditions full-potential calculations correctly assign the lowest energy spin-state to aFM (see Table 4.4). We note here, that such a rather crude approximation is not needed in our study. In fact, our current LDA and GGA calculations provide upper and the lower boundaries for the equilibrium lattice parameters and the corresponding magnetic moments. Both also accurately treat magnetic interactions in $\theta$-MnN.

We now focus on the $\eta$-phase of MnN. The crystalline and magnetic structure of the most stable bulk $Mn_3N_2$ is shown in Fig. 4.15(b)-(c). The calculated structural and magnetic properties of $\eta$-MnN are given in Table 4.5. The employed cutoff energy is 50 Ry, the bulk Brillouin zone is sampled using a 3x1x3 Monkhorst-Pack mesh (6 **k**-points in the IBZ). We analyze only the antiferromagnetic spin structure which is the stable according to experiment (see, e.g., Fig. 4.15(b)). We did not perform explicit calculations to derive the magnetic phase diagram for bulk $Mn_3N_2$ because similar calculations have been reported by Lambrecht *et al.*. Assuming the experimental lattice parameters they have computed the stability of various spin-states for bulk $Mn_3N_2$, including 6 different aFM,

| | This work (NCPP) | | Ref. [223] (FP-LMTO) | Refs. [214, 215, 219, 221, 222] |
|---|---|---|---|---|
| | LDA | PBE | LDA | Experiment |
| $a_0$(Å) | 4.058 | 4.265 | 4.077 | 4.21 |
| $c_0/a_0$ | 2.891 | 2.901 | 2.825 | 2.88 |
| $d_1(c_0)$ | 0.165 | 0.156 | 0.178 | 0.167 |
| $d_2(c_0)$ | 0.161 | 0.165 | 0.159 | 0.160 |
| $E_{\mathrm{coh}}$(eV) | -26.33 | -20.47 | | |
| $E_f$(eV) | -1.21 | -0.87 | | |
| $\lvert m_1\rvert$ ($\mu_{\mathrm{B}}$) | 2.67 | 3.55 | 3.0[a] | 3.38 or 3.75 |
| $\lvert m_2\rvert$ ($\mu_{\mathrm{B}}$) | 2.70 | 3.61 | 2.8[a] | 3.65 or 3.47 |

[a] Calculated at experimental atomic volume

Table 4.5: Structural relaxation results for aFM bulk $Mn_3N_2$. $a_0$ and $c_0$ are the equilibrium lattice constants, $d_1$ and $d_2$ are the relative coordinates of the relaxed $Mn_2$ atoms (see Fig. 4.15(b)-(c)), $E_{\mathrm{coh}}$ and $E_f$ are the cohesive and formation energy of $Mn_3N_2$ per chemical formula, $|m_1|$ and $|m_2|$ are the atomic magnetic moments of $Mn_1$ and $Mn_2$, respectively. NCPP stands for a norm-conserving pseudopotential, FP-LMTO for the full-potential linear muffin-tin orbital method.

FM and NM configurations. These results are in perfect agreement with experiment; the magnetic structure shown in Fig. 4.15(b) is found to be the lowest energy configuration of bulk $Mn_3N_2$ (about 150 meV/Mn lower than FM and 80 meV/Mn lower than the next energetically preferred aFM configuration).

Similar to $\theta$-MnN, our LDA and GGA calculations predict upper and lower boundaries for the lattice parameters $a$ and $c$, and the magnetic moments $m_1$ and $m_2$ of the two-fold coordinated ($Mn_1$) and five-fold coordinated ($Mn_2$) manganese atoms respectively. Indeed, the calculated equilibrium lattice parameter $a_0$ is underestimated (overestimated) by about 4% (1%) compared to experiment, while the mismatch between the theoretical and the experimental $c_0/a_0$ ratio is less than 1%. Besides the $c/a$ ratio and the lattice constant $a$, there are two intercellular structural degrees of freedom $d_1$ and $d_2$ to relax. These correspond to the vertical distance (along [001]) between $Mn_1$ and $Mn_2$ ($d_1$), and the $Mn_1$-N distance $d_2$, which are indicated in Fig. 4.15(c). Ideal bulk positions correspond to $d_1 = d_2 = 1/6 = 0.167$ of the lattice parameter $c$. Again, LDA and GGA predict a qualitatively similar structures, where both $d_1$ and $d_2$ are reduced compared to the ideal positions. This distortion can be interpreted as a contraction of the Mn-Mn and Mn-N distance between the Mn-N double layer. This finding agrees with experiment, where it is known that $d_1$ remains essentially unchanged and $d_2$ is reduced.

Both LDA and GGA predict qualitatively the same magnetic structure of $Mn_3N_2$, indicating that $|m_1| < |m_2|$ (see Table 4.5). Our theoretical study allows, therefore, to resolve the uncertainty of neutron powder diffraction experiments of Leinweber *et al.* [221], where neutron diffraction patterns suggest equally probable magnetic structures with either (i) $m_1$=3.75 $\mu_{\mathrm{B}}$ and $m_2$=3.47 $\mu_{\mathrm{B}}$ or (ii) $m_1$=3.38 $\mu_{\mathrm{B}}$ and $m_2$=3.65 $\mu_{\mathrm{B}}$ (see, e.g., Table 4.5). Both LDA and GGA total energy

calculations suggest the magnetic structure (ii) to be more favorable.

Our *ab initio* calculations for $Mn_3N_2$ disagree in some points with the results reported by Lambrecht *et al.* Specifically, in their study a relaxation of the internal coordinates yields an increase of the $d_1$ coordinate compared to the ideal position (decrease in our study), and predicts that the magnetic moment $m_1$ is slightly larger than $m_2$ (opposite to our results). Since our calculations provide systematically better agreement with experiment for $\theta$-MnN, we assume that this trend holds for $\eta$-MnN as well and consider our calculations to be more accurate.

In summary, we have shown that our total energy calculations are in very good agreement with experiment for both bulk $\theta$- and bulk $\eta$-MnN, particularly in describing the magnetic interactions in Mn-N compounds. This provides a firm basis for computing the phase diagram of the magnetic $Mn_3N_2(010)$ surface, as discussed in detail in the next section.

### 4.4.5 Stability of stoichiometric and nonstoichiometric $Mn_3N_2(010)$ surfaces versus magnetic reconstructions

In all previous STM studies on $Mn_3N_2(010)$ surfaces it was assumed that the surface magnetic and atomic structure corresponds to that of the ideal bulk-terminated case (see Sec. 4.2 and discussion there for more details). This assumption, however, has never been justified neither experimentally nor theoretically. In fact, a reasonable first assumption would be that the experimentally observed periodicity of the magnetic STM images should correspond to that of the Mn surface magnetic moments. For a bulk terminated surface this would result in a ↑↓↑↓↑↓-pattern along the [100] axis, i.e. in a modulation with period $c_0/3$ (see, e.g., Fig. 4.16(a)). In contrast to this expectation, the actually measured magnetic contribution to the SP-STM images shows a ↑↑↑↓↓↓-pattern that corresponding to a periodic signal with period $c_0$ [197, 198, 214, 217, 218]. The increase in the periodicity by a factor of three may indicate that the $Mn_3N_2(010)$ surface undergoes a magnetic reconstruction by flipping the magnetic moments of some Mn-rows in the top-most surface layer. Furthermore, even employing extremely sharp nonmagnetized STM tips yielding atomically resolved images, allowed not to discriminate whether nitrogen atoms are present in the surface layer [216]. Before starting STM simulations it is, therefore, crucial to identify the most stable magnetic and atomic structure of the $Mn_3N_2(010)$ surface. This task is accomplished in this chapter assuming that the $Mn_3N_2(010)$ surface is in thermodynamic equilibrium allowing to employ the formalism presented in Sec. 4.3.2.

In the following we consider all possible configurations of surface Mn magnetic moments that (i) are commensurate with a $c_0$ magnetic periodicity along the [100] direction and (ii) result in a homogeneous distribution of magnetic moments along the [001] axis; these requirements follow from the experimental magnetic STM profiles (see, e.g., Fig. 4.23). Condition (ii) implies that the magnetic moments of the surface manganese atoms should be flipped in a row-wise manner, with rows being parallel to [001]. We have found that conditions (i) and (ii) are fulfilled for five different magnetic configurations. These are schematically shown in Fig. 4.16(a)-(e). First, a ↑↑↑↓↓↓-pattern

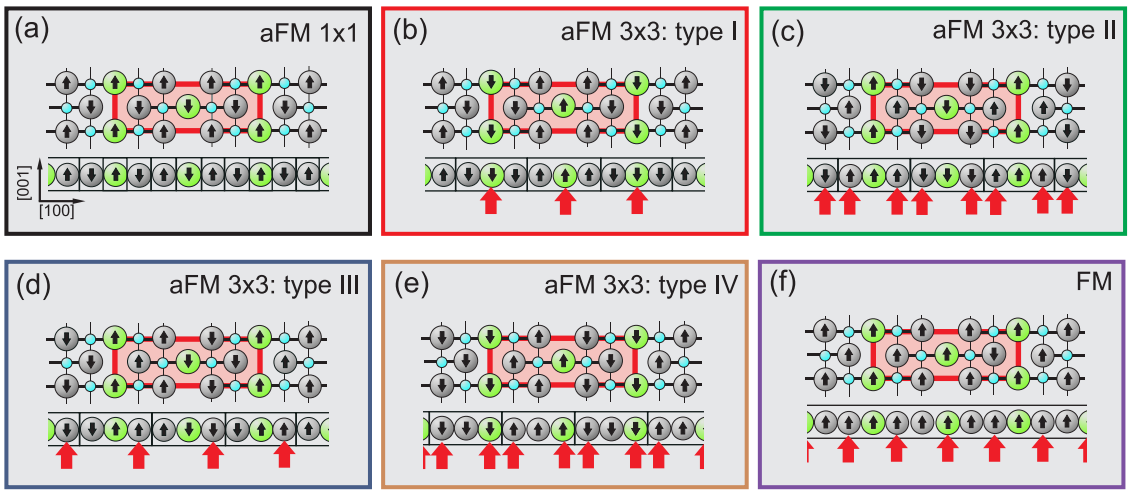


Figure 4.16: Magnetic structure of (a) an antiferromagnetic bulk terminated surface with a ↑↓↑↓↑↓ pattern created by local magnetic moments of Mn atoms along [100], (b)-(e) antiferromagnetic magnetically reconstructed surfaces that result in a ↑↑↑↓↓↓ pattern, and (f) ferromagnetic magnetically reconstructed $Mn_3N_2(010)$. The top and side surface view of the top-most layers are shown for each magnetic configuration. Surface rows of magnetically flipped Mn atoms as compared to the aFM 1x1 configuration are highlighted by red arrows.

can be realized with a bulk-terminated magnetic structure assuming that either $Mn_1$ or $Mn_2$ rows do not significantly contribute to the measured STM image (Fig. 4.16(a)). Another possibility is to flip the magnetic moments of Mn-rows such that the resulting magnetic structure yields ↑↑↑↓↓↓-configuration. This case can be realized by flipping rows of $Mn_1$, $Mn_2$, or simultaneously $Mn_1$ and $Mn_2$ atoms (see Fig. 4.16(b)-(e)). All other configurations of surface magnetic moments would result in either a too small or a too large period of the magnetic structure. To estimate the strength of magnetic interactions at the surface we have also considered a configuration with ferromagnetic orientation of Mn moments in the top-most layer (Fig. 4.16(f)).

For each magnetic state of the $Mn_3N_2(010)$ surface we have calculated two atomic structures, with and without nitrogen atoms in the top-most layer. The latter mimics a situation where all surface nitrogen atoms are desorbed.

The stability of the different surface structures is estimated from a comparison of the corresponding surface energies. These are calculated employing the slab approach and the methodology described in Sec. 4.3.2 (see, e.g., Eq. (4.13)). The total energy of a $Mn_3N_2(010)$ slab is calculated using a planewave energy cutoff of 50 Ry. The surface Brillouin zone (SBZ) is sampled according to the Monkhorst-Pack scheme, with 3 **k**-points in the irreducible wedge of the SBZ. The chemical potentials of Mn and N in $N_2$, bulk Mn, and bulk $Mn_3N_2$ are given in Sec. 4.4.2, Sec. 4.4.3, and Sec. 4.4.4 respectively. To verify the effect of exchange-correlation functionals both LDA and PBE calculations are performed.

The accuracy of the slab calculations versus the slab and vacuum thickness is shown in Fig. 4.17.

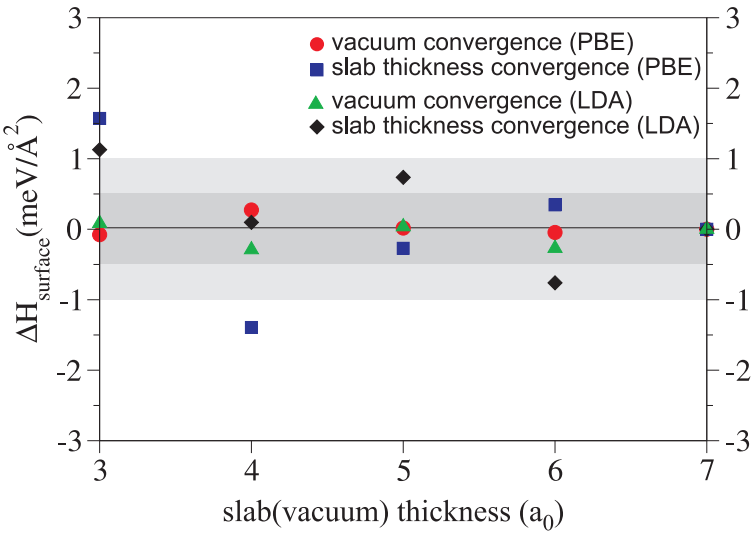


Figure 4.17: Energies of the stoichiometric magnetically nonreconstructed $Mn_3N_2(010)$ surface as a function of the slab thickness and vacuum separation. The thickness is given in units of the interlayer spacing along the surface normal, i.e. in multiplies of the lattice constant $a_0$. The surface energies for the slab thickness convergence are shown relative to that for a slab thickness of $7a_0$ separated by a $3a_0$ thick vacuum region, that is assumed to be converged. The corresponding values for the vacuum separation convergence are $5a_0$ and $7a_0$, respectively. Red dots and blue squares correspond to the vacuum and slab convergence employing the PBE exchange-correlation functional, green triangles and black diamonds - to that employing the LDA exchange-correlation parametrization respectively. The bulk atomic structure of $Mn_3N_2$ is fully relaxed.

Both LDA and PBE show a fast convergence with respect to the vacuum thickness: already for a vacuum with thickness larger than $3a_0$ the errorbar of the surface energy is less than $\pm 0.5$ meV/Å$^2$. The interaction between the two surfaces of the slab via the bulk region is stronger, resulting in a slightly slower convergence versus slab thickness. For slabs thicker than 4 atomic layers the errorbar of the surface energy is less than $\pm 0.5$ meV/Å$^2$ in PBE, and $\pm 1.0$ meV/Å$^2$ in LDA. Therefore, to compute the phase diagrams of $Mn_3N_2(010)$, we employ slabs having thickness of 5 atomic layers and a vacuum separation of $3a_0$.

First, we estimate the strength and importance of the magnetic interactions only. To do so we have first calculated the phase diagram of magnetically reconstructed $Mn_3N_2(010)$ surfaces for the same surface geometry, corresponding to the ideal nonrelaxed bulk-terminated atomic structure. The energy differences in this case are due to different exchange interactions between the magnetic moments of Mn atoms. The calculated surface phase diagrams in LDA and PBE are shown on Fig. 4.18(a) and Fig. 4.19(a) respectively. Both LDA and GGA predict that the magnetically nonreconstructed surface is most stable among the considered structures. The calculated surface energy is 89 meV/Å$^2$ and 55 meV/Å$^2$, respectively. Despite of the fact that LDA and GGA predict a slightly different ordering of the magnetically reconstructed $Mn_3N_2(010)$ surfaces, they both

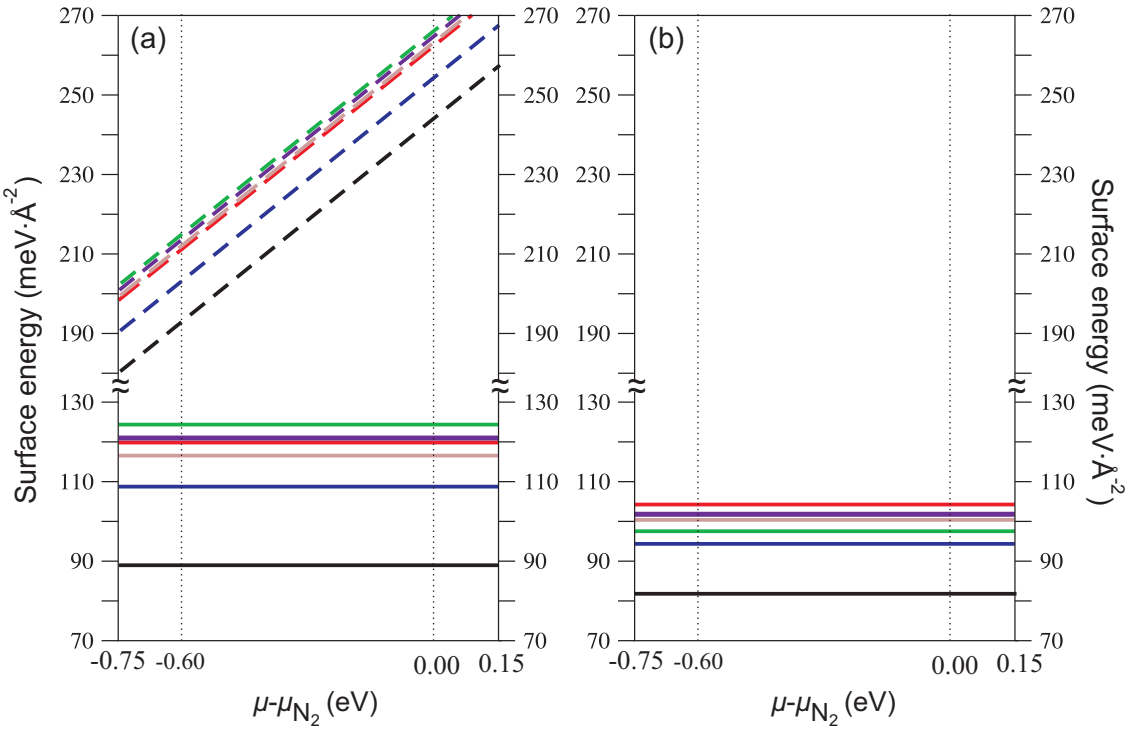


Figure 4.18: Phase diagram of magnetically reconstructed $Mn_3N_2(010)$ surface calculated in LDA for (a) a surface with an ideal bulk-terminated structure and (b) an atomically relaxed surface. Colors correspond to color-coding of different surface structures in Fig. 4.16. Solid lines correspond to stoichiometric magnetically reconstructed surfaces, dashed lines correspond to nonstoichiometric magnetically reconstructed surfaces where nitrogen atoms are desorbed. The effect of the surface atomic relaxation is not considered on N-free surfaces due to the large energy splitting between the stoichiometric and the corresponding non-stoichiometric surfaces. Bulk atomic relaxation has been fully taken into account.

indicate that the magnetic reconstructions increase the surface energy by at least 20 meV/Å$^2$. It is also noticeable that the desorption of nitrogen atoms from the surface significantly increases the surface energy by at least 50 meV/Å$^2$. This renders N-deficient surfaces to be thermodynamically unstable versus any considered $Mn_3N_2(010)$ surface with stoichiometric termination.

In Figs. 4.18(b) and 4.19(b) we show the calculated phase diagram of the magnetically reconstructed $Mn_3N_2(010)$ surfaces with and without surface nitrogen atoms when atomic relaxations are taken into account. We fully relax the top-most and the first sub-surface layer; the slab total energy calculations are interrupted when the surface energies are converged to less than 0.02 meV/Å$^2$. Because of the large energy splitting (about 100 meV/Å$^2$) between the most stable surface termination and the corresponding N-free counterpart we do not consider the effect of the surface atomic relaxations on N-free surfaces in LDA[7].

[7]This is a valid approach because atomic relaxations on $Mn_3N_2(010)$ reduce the surface energies by less than 30 meV/Å$^2$ (see Figs. 4.18-4.19), that is far too less to stabilize N-free surfaces.

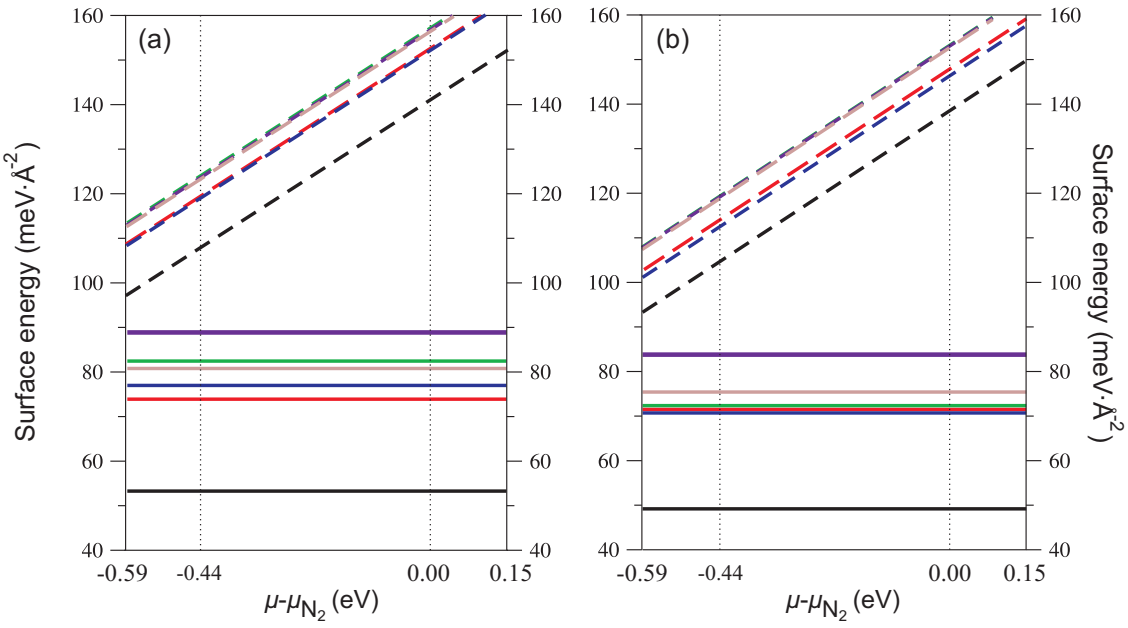


Figure 4.19: Phase diagram of the magnetically reconstructed $Mn_3N_2(010)$ surfaces calculated in PBE for (a) a surface with an ideal bulk-terminated structure and (b) atomically relaxed surface. Colors correspond to the color-coding of the various surface structures shown in Fig. 4.16. Solid lines correspond to stoichiometric magnetically reconstructed surfaces, dashed lines correspond to nonstoichiometric magnetically reconstructed surfaces where nitrogen atoms are desorbed. The bulk atomic structure of $Mn_3N_2$ is fully relaxed.

We find that relaxation of atomic positions does not significantly affect the calculated phase diagram of a $Mn_3N_2(010)$ surface. Indeed, for all surface configurations the surface energy is reduced by less than 30 meV/Å$^2$. The relaxation effect is smallest for the magnetically nonreconstructed surfaces (reduction by about 5 meV/Å$^2$), and is largest for the magnetically reconstructed surfaces (reduction by about 10-30 meV/Å$^2$). Although the energy difference between the most stable bulk-terminated and next surface phase decreases by ∼25% due to atomic relaxations, both LDA and GGA indicate that the antiferromagnetic magnetically nonreconstructed $Mn_3N_2(010)$ configuration is thermodynamically most stable. The surface energy of this surface structure is at least 15 meV/Å$^2$ smaller than that of any other considered surface.

The calculated structural relaxation data of the bulk-terminated $Mn_3N_2(010)$ surface are summarized in Table 4.6. Qualitatively, LDA and GGA predict similar relaxation patterns, with an inward relaxation of surface $Mn_1$ and an outward relaxation of surface $Mn_2$ atoms. For nitrogen atoms the results are similar, with the only difference that LDA predicts an outward, GGA a slight inward relaxation of the N-atoms at the surface. Quantitatively, LDA calculations predict a relaxation of the atomic positions by a maximum of 9%, while PBE predicts significantly smaller values that do not exceed 4%.

Our calculations nicely demonstrate the value of *ab initio* calculations for a correct interpreta-

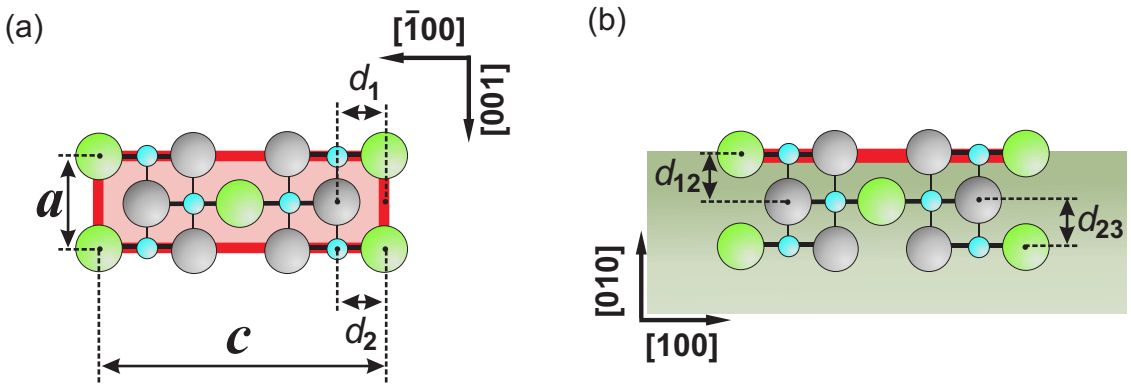


Figure 4.20: (a) Top and (b) side view on $Mn_3N_2(010)$ surface.

| | | LDA | | PBE | |
|---|---|---|---|---|---|
| | | top-layer | sub-surface layer | top-layer | sub-surface layer |
| $Mn_1$ | $d_{12}$ (%) | -6.25 | | -3.13 | |
| | $d_{23}$ (%) | | -1.91 | | -2.59 |
| $Mn_2$ | $d_1$ (%) | 8.49 | 1.27 | 3.80 | 0.41 |
| | $d_{12}$ (%) | 1.87 | | 0.86 | |
| | $d_{23}$ (%) | | 1.70 | | 0.32 |
| N | $d_2$ (%) | -2.51 | 0.14 | -0.66 | 0.22 |
| | $d_{12}$ (%) | 4.29 | | -0.80 | |
| | $d_{23}$ (%) | | -0.26 | | -2.93 |

Table 4.6: Calculated atomic relaxations of the aFM $Mn_3N_2(010)$ surface in LDA and PBE (see Fig. 4.20 for a definition of the structure parameters). The surface is modeled with by a 5 atomic layers thick slab. The bulk atomic structure of $Mn_3N_2$ is fully relaxed.

tion of experimental STM images. Indeed, experimentally it was shown that on STM images with atomic resolution $Mn_1$ atoms appear brighter than $Mn_2$ atoms. This holds at positive and negative bias voltages [216]. It was interpreted as a structural effect that is due to an outward relaxation of $Mn_1$ atoms. This assumption was used in all $Mn_3N_2(010)$ STM simulations employing the ILDOS model [197, 214, 216, 218]. In contrast to this assumption, our *ab initio* LDA and PBE calculations consistently show that $Mn_1$ atoms relax inward, and that the $Mn_2$ atoms relax outward. We conclude from this, that the experimentally observed superiority of the $Mn_1$ over $Mn_2$ atoms is an electronic rather than a structural effect.

In summary, we have found that the atomically relaxed bulk-terminated surface structure is thermodynamically most stable configuration of the $Mn_3N_2(010)$ surface among all possible magnetic and atomic structures commensurate with the SP-STM experiments. This conclusion is independent on the type of the exchange-correlation employed (LDA or PBE), validating that this surface structure is a valid basis for the subsequent *ab initio* STM simulations described in Secs. 4.4.6-4.4.9.

### 4.4.6 Spin-compensated STM simulations on the $Mn_3N_2(010)$ surface

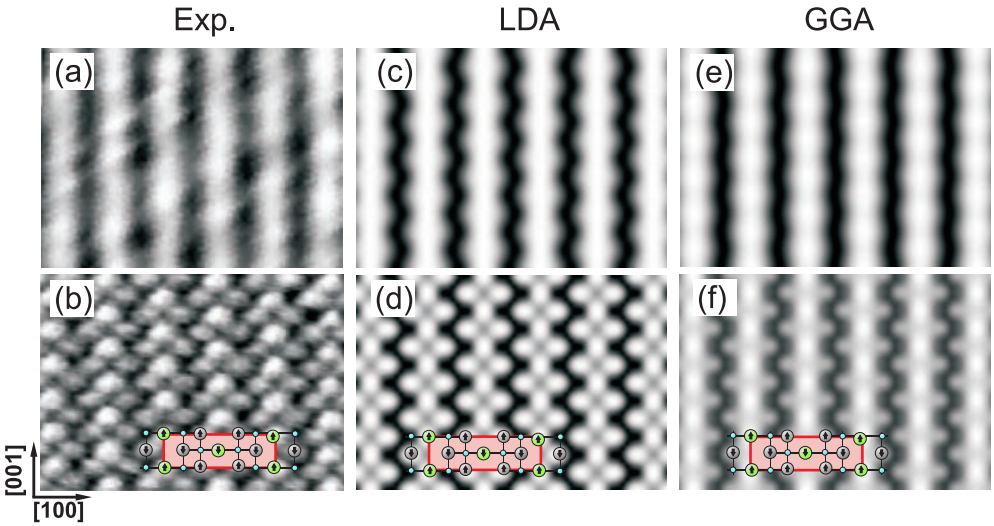


Figure 4.21: Constant-current STM images on $Mn_3N_2(010)$ obtained employing nonmagnetic tips at -0.4 V bias voltage. Experimental STM maps are acquired employing (a) atomically obtuse and (d) atomically sharp tips [218]. Simulated STM images without atomic resolution calculated with (b) LDA and (c) PBE exchange-correlation functionals are obtained within the Tersoff-Hamann model at an averaged tip-surface separation of 5 Å. Atomically-resolved theoretical STM maps are calculated at an averaged tip-surface separation of 2 Å in (e) LDA and (f) PBE. The theoretical bulk and surface atomic positions are completely relaxed, the slabs are 6 layers thick.

Despite of the fact that the Tersoff-Hamann (TH) method being a widely used approach for simulating STM images, it relies on assumption of specific tip properties. Specifically, the TH-model assumes that the STM tip is electronically featureless, with a single *s*-like atom in the tip apex. While in most situations the TH-approach provides satisfactory agreement with experiment, in some cases more complicated tip models are known to be necessary [4]. In this section we check the accuracy and reliability of the example of the TH-model for $Mn_3N_2(010)$ surface, focusing on the conventional spin-compensated mode of STM in the constant current regime.

We compare our simulated STM maps with corresponding experimental images, that were recently reported by Smith *et al.* [218]. Employing different magnetically neutral tungsten tips Smith and co-workers have provided both a normal STM images of the $Mn_3N_2(010)$ surface (Fig. 4.21(a)) and an atomically resolved STM, where it is clearly possible to distinguish surface $Mn_1$ and $Mn_2$ atoms (Fig. 4.21(b)). The corresponding simulated STM images are shown in Fig. 4.21(c)-(f). In the simulations we employed both LDA (Fig. 4.21(c)-(d)) and PBE (Fig. 4.21(e)-(f)) to estimate the effect of the exchange-correlation functional.

Our calculations indicate that the TH-approach provides a virtually perfect agreement with experiment when simulating STM images without atomic resolution. Figs. 4.21(a),(c),(e) are essentially identical, showing a stripe-like structure of the STM maps, where bright stripes are located

on top of the $Mn_1$ atomic rows.

It is not possible, however, to obtain the theoretical counterpart of the sharp-tip experimental image (Fig. 4.21(b)) in the framework of the Tersoff-Hamann approach, unless we assume in our simulations an unrealistically short tip-surface separation of less than 2.5 Å. Although the theoretical STM images obtained at such a short tip-surface distance of 2 Å (Figs. 4.21(d),(f)) are in very good agreement with the atomically-resolved experimental profile (Fig. 4.21(b)), these simulations are not reliable (see also discussion in Sec. 2.6.2). At such small separations between the tip and the surface the mutual interactions become so significant that the tip can no longer be treated as a small perturbation to the surface. Indeed, it has been shown that both the tip and the atomic surface structure beneath the tip can be significantly modified at small (less than 4 Å) tip-surface separations [248]. Second, even assuming that tip and surface structures remain unchanged, it is known that the Tersoff-Hamann approach may become inaccurate for tip-surface distances shorter than $\sim 4$ Å due to a modification of the surface potential barrier [113]. Nevertheless, we speculate that similar STM images could be obtained employing "electronically sharp" tip models with, e.g., dominating $d_{z^2}$- or $p_z$-orbital character, that are more localized in space when compared with the simple isotropic $s$-like single atom tip model. We leave, however, the problem of atomically-resolved STM simulations on $Mn_3N_2(010)$ out of scope of this study, since none of the so-far reported spin-polarized STM images on $Mn_3N_2(010)$ was atomically-resolved.

In summary, we have shown that employing Tersoff-Hamann approach it is possible to accurately simulate normal (without atomic resolution) STM images on $Mn_3N_2(010)$ surfaces, although the method fails to reproduce atomically-resolved STM images. This implies that the TH-simulations on $Mn_3N_2(010)$ correspond to obtuse STM tips. Since all experimental spin-polarized STM images on $Mn_3N_2(010)$ do not show atomic resolution, we are confident that the TH-method provides a good approximation to simulate SP-STM maps.

### 4.4.7 Bias-dependent SP-STM simulations of $Mn_3N_2(010)$ surfaces employing the Tersoff-Hamann approach

In this section we present a detailed theoretical analysis of spin-polarized STM images. In the first place we strive to clarify to which extend SP-STM images characterize the properties of a $Mn_3N_2(010)$ surface, e.g., whether the magnetic contrast reversal and/or the subtle variation in the shape of the magnetic spatially-resolved profiles is a surface-induced effect, or whether they are related to the STM tip.

To analyze the SP-STM experiments, we model the bias-dependent profiles using the spin-generalized Tersoff-Hamann approach (see Eq. (2.119) and Sec. 2.6.3 for details) and assuming a constant tip density of states, as was done, e.g., in Refs. [16, 249, 250]. In these studies Fe tips having constant polarizations over the range from -0.5 eV to +0.5 eV of $\sim$40% have been assumed.

In the present study we employ a model tip with an *effective* magnetic polarization $P_t = 15\%$[8].

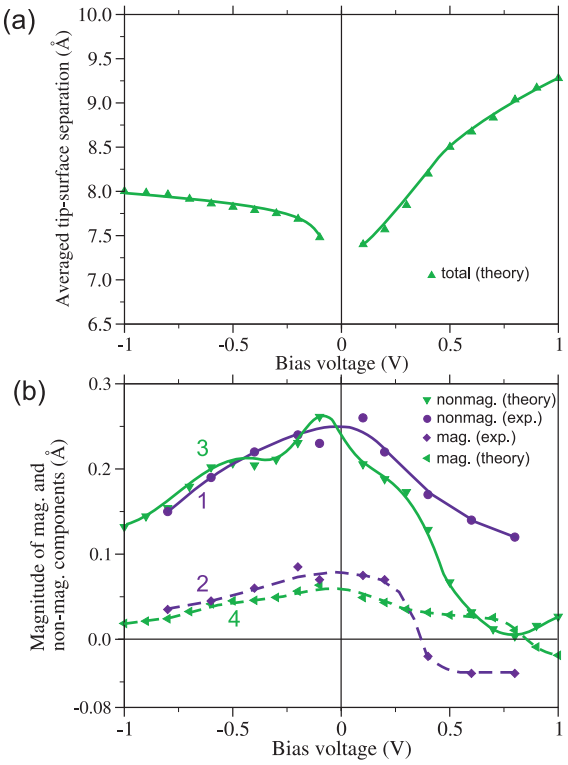


Figure 4.22: (a) Simulation of the averaged tip-surface separation versus applied bias voltage. (b) The magnitude of the magnetic component (purple diamonds - experiment; green triangles left - theory) and the nonmagnetic component (purple circles - experiment; green triangles down - theory). The fitted solid and dashed curves 1-2 (blue - experiment) and solid and dashed curves 3-4 (green - theory) are shown as a guide to the eye. LDA exchange-correlation is employed.

The influence of the exchange-correlation functionals on the STM images is estimated by performing two series of calculations employing either the spin-LDA [67, 72] or the spin-PBE approximations [251], and by cross-checking the obtained results. We find that both functionals provide qualitatively similar SP-STM profiles. Quantitatively, however, LDA and PBE calculations are significantly different. For instance, LDA predicts an inversion of the magnetic contrast at a bias voltage $\sim +0.8$ V. This value is twice as large as the corresponding experimentally observed value. In contrast, PBE shows an encouraging agreement with experiment (compare, e.g., Fig. 4.22 with Fig. 4.25, curves 3 and 4). We also recall here that, in contrast to LDA, the spin-PBE approximation correctly predicts the ground-state of bulk-Mn (see Sec. 4.4.3). Furthermore, PBE calculations are also superior with respect to the calculated lattice parameters and internal atomic coordinates for bulk $Mn_3N_2$ [214] (see Sec. 4.4.4). We will therefore restrict our theoretical analysis on SP-STM simulations employing the spin-PBE approximation.

We turn now to a detailed comparison of the theoretical and experimental SP-STM images.

[8]We define an effective tip polarization $P_t = \frac{m^t}{n^t}\cos(\theta')$, where $\theta' = \theta(\mathbf{R}_t) = \text{const}$ is the angle between the magnetization axis of the tip $\mathbf{e}^t_M$ and that of the surface $\mathbf{e}^s_M$ (see Eqs. (2.119)-(2.122)). The electronic properties of the $Mn_3N_2(010)$ surface that enter Eqs. (2.120)-(2.122) are calculated employing slabs that are 6 atomic layers thick, with fully relaxed bulk and surface atomic positions (see Secs. 4.4.4-4.4.5). To ensure convergence of the SP-STM corrugation maps with respect to the **k**-point sampling a 12x4x1 Monkhorst-Pack mesh has been used. An accurate description of the surface wavefunctions even at large distances above the surface is accomplished by employing a real-space description of the vacuum (Sec. 4.3.1).

The experimental results are summarized in Fig. 4.23(a-e,k-o), where we show sets of experimental constant-current mode SP-STM images acquired on exactly the same location of the $Mn_3N_2(010)$ surface under different bias voltages. In contrast to the nonmagnetic STM images discussed in the previous Sec. 4.4.6, the spin-sensitive STM images do not resolve the individual $Mn_1$ and $Mn_2$ atoms; this is common for all of the experimental spin-polarized STM images on this surface reported so-far. It suggests, that the magnetic tips are less sharp than a single atom non-magnetic tip [198].

The [100]-averaged height profiles are shown below each image. The profiles are shown on an identical scale, so that the height modulation of the rows as well as the overall corrugation can be clearly observed. From Fig. 4.23(a-e,k-o) it follows that there are distinct variations of the SP-STM line profile as function of energy. Several key points can be made: First, the overall corrugation magnitude is largest at the smallest bias magnitudes. Second, the magnetic modulation reaches a maximum of $\sim$ 0.04 Å at a bias voltage $V_{\rm bias}$=-0.1 V. Third, the magnetic modulation is clearly observed at all energies except at $V_{\rm bias}$ $\sim$+0.4 V, where it becomes very small. In fact and as the fourth key point, at $V_{\rm bias}$ $\sim$+0.4 V, the modulation undergoes a reversal. This magnetic contrast reversal becomes evident when counting the number of "high peaks" and "low peaks". For $V_{\rm bias}$ <0.4 V, there are two high peaks (indicated by upward red arrows in Fig. 4.23) and 3 low peaks, whereas for $V_{\rm bias}$ >0.4 V, there are 3 high peaks and 2 low peaks.

By adding and subtracting, for a given SP-STM image, the averaged line profile and shifting the same line profile by half the magnetic period (equal to $c_0/2$), it is possible to separate the magnetic and non-magnetic components from the total SP-STM experimental height profiles. Such a procedure for separating magnetic and nonmagnetic contribution was introduced and validated by Yang *et al.*. A detailed explanation is given elsewhere [197]. The results of this separation are shown in Fig. 4.24(a-e,k-o) for each image corresponding to Fig. 4.23(a-e,k-o), respectively. The separated SP-STM line profiles clearly indicate that the non-magnetic component has a smooth sinusoid-like shape with period $c_0/2$ at all bias voltages.

On the other hand, the magnetic component has a shape which varies with the value and sign of the applied bias. While to first-order, the magnetic profile shape is roughly sinusoidal, at many voltages within the range from -0.8 V to +0.2 V the magnetic profile shows a distinctly trapezoid-like shape. This feature shows clearly, for example, between -0.6 V and -0.2 V in Fig. 4.24. At positive voltages greater than 0.2 V, the trapezoidal shape is not evident; a more rounded profile is observed. At $V_{\rm bias}$ $\sim$0.4 V the magnetic line profile is nearly flat, and a contrast reversal occurs close to this voltage.

Fig. 4.23(f-j,p-t) shows simulated spatially-resolved SP-STM images. The change of the averaged tip-surface separation versus applied bias voltage, that is dictated by the constant tunneling current regime, is shown in Fig. 4.25(a).

The simulations have been performed for a surface region identical to the experimental one (Fig. 4.23(a-e,k-o)). Overall, we find a remarkable qualitative agreement between simulated and

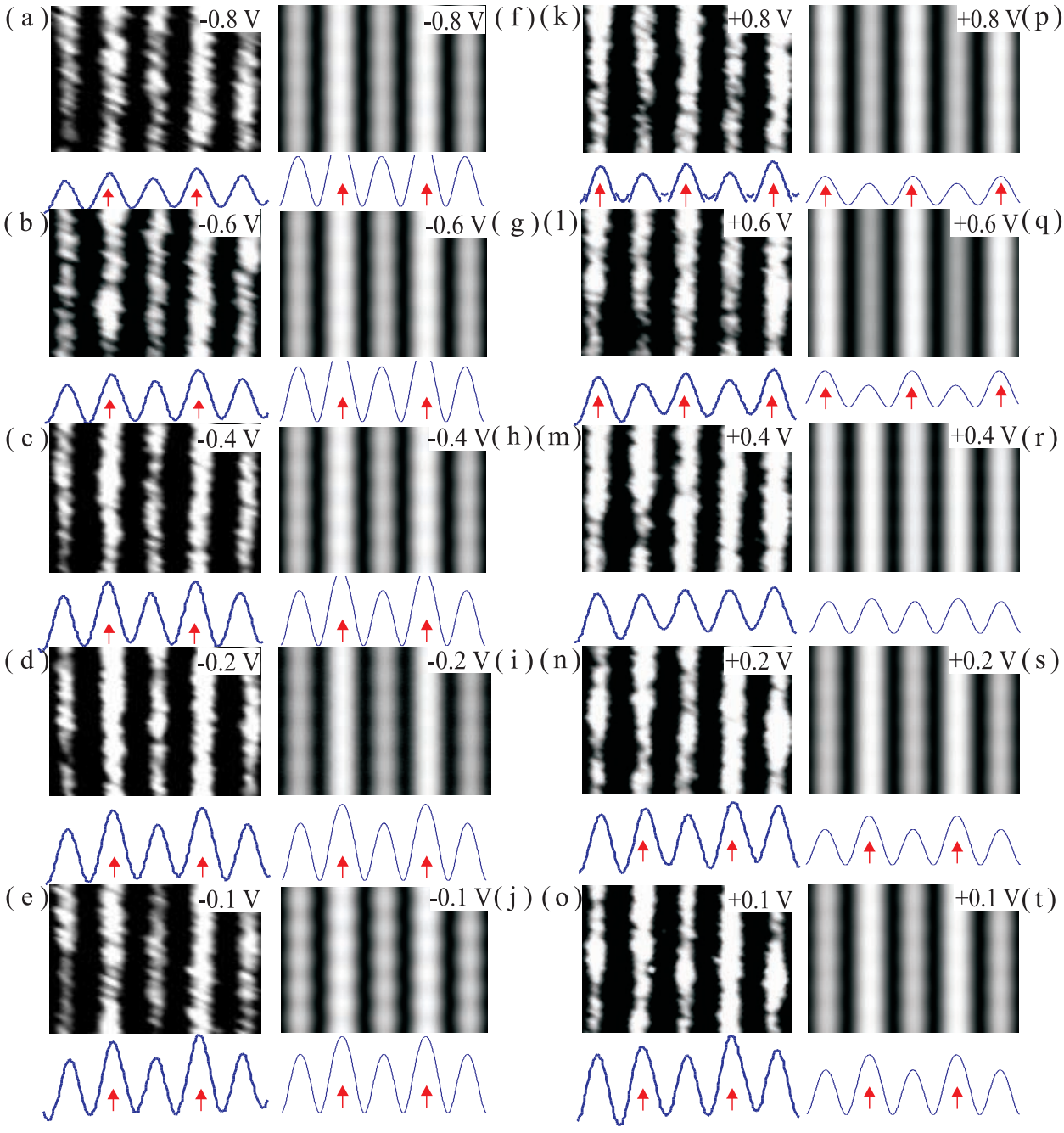


Figure 4.23: Experimental and theoretical SP-STM images. (a)-(e),(k)-(o) A series of SP-STM images acquired using a Fe-coated W tip with corresponding height line profiles. The bias voltage ranges from -0.8 to +0.8 V, and the tunneling current is $I_t$=0.3 nA. (f)-(j),(p)-(t) Corresponding theoretical images calculated using spin-polarized DFT and assuming a tip with constant DOS. All line are plotted for an identical scale. The maximum height profile magnitude is 0.28 Å. PBE exchange-correlation is employed.

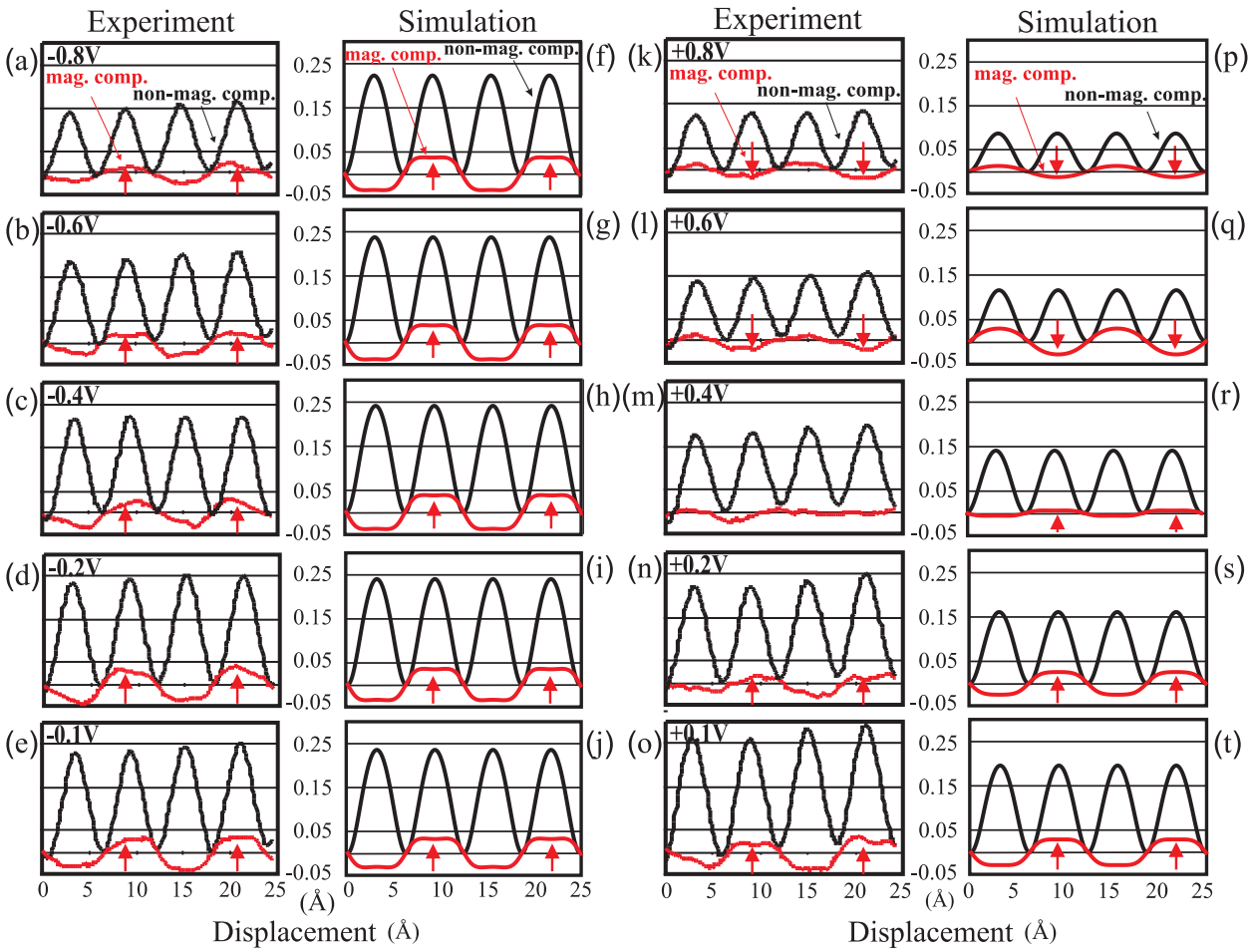


Figure 4.24: Resulting magnetic and nonmagnetic height profiles. (a)-(e),(k)-(o) Experimental nonmagnetic and magnetic profiles. (f)-(j),(p)-(t) Corresponding theoretical nonmagnetic and magnetic height profiles calculated using the Tersoff-Hamann model. A tip with constant DOS and a tip polarization of 15% have been assumed. PBE exchange-correlation is employed.

experimental SP-STM images: it is clearly apparent that both simulated and experimental images show a magnetic contrast at all bias voltages with a contrast reversal occurring at $V_{\text{bias}}$ near +0.4 V. Moreover, at positive bias voltages the overall corrugation of the simulated profiles is largest at small bias magnitudes, whereas it is smaller at larger bias magnitudes, in agreement with experiment. A similar behavior is observed at negative biases, with the exception for bias magnitudes smaller than 0.2 V (0.3 V), where the overall corrugation of the measured (simulated) profiles increases with increasing $|V_{\text{bias}}|$.

Similar to experiment, we have also separated the magnetic and non-magnetic components from the total SP-STM theoretical height profiles. Fig. 4.24(f-j,p-t) are the height profiles corresponding to the simulated SP-STM images shown in Fig. 4.23(f-j,p-t), respectively. Comparing the non-magnetic profiles with the experimental ones, we find that both agree well showing a simple sinusoid-

like form. The magnetic profiles are also in perfect agreement with experiment over the whole range of biases between -0.8 V and +0.8 V. Even the shape of the simulated magnetic profiles is in remarkable agreement with experiment, being trapezoidal below +0.4 V and more rounded above this value.

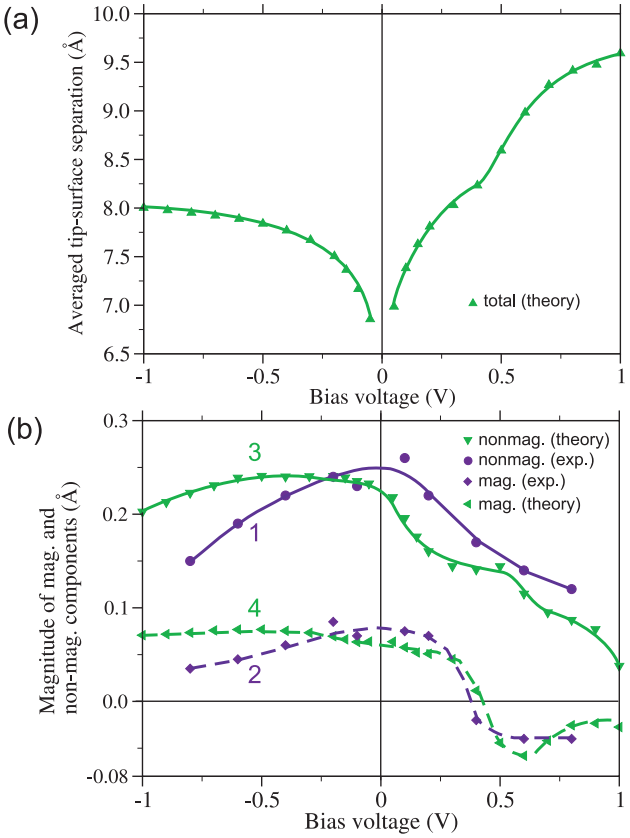


Figure 4.25: (a) Simulation of the averaged tip-surface separation versus applied bias voltage. (b) The magnitude of the magnetic component (purple diamonds - experiment; green triangles left - theory) and the nonmagnetic component (purple circles - experiment; green triangles down - theory). The fitted solid and dashed curves 1-2 (blue - experiment) and solid and dashed curves 3-4 (green - theory) are shown to guide the eye. PBE exchange-correlation is employed.

The experimental and theoretical magnetic and non-magnetic line profile magnitudes (peak to valley) are plotted versus $V_{\text{bias}}$ in Fig. 4.25(b). Clearly, the magnitudes of the experimental non-magnetic contributions (curve 1) are maximum at small voltage, whereas they get smaller at larger magnitudes of the voltage. The exception from this behavior is the magnitude of the non-magnetic profile at -0.1 V, that is smaller than that at -0.2 V. For the experimental magnetic component (curve 2), the sign change can be clearly seen at +0.4 V, indicating the change of polarity of the magnetic contrast. SP-STM simulations are in overall perfect qualitative agreement with experiment and capture all essential experimental features. The magnitudes of the theoretical nonmagnetic contribution (curve 3) show a similar bias dependence, smoothly decreasing with an increase of the bias magnitude; in agreement with experiment the exception from this behavior is at small negative biases. Quantitatively the magnitudes of the simulated nonmagnetic profiles are slightly underestimated at positive biases, and overestimated at negative ones, with largest deviation at $V_{\text{bias}}$=-0.8 V. Regarding the magnetic contribution, we find that simulations and measurements closely agree with each other, both qualitatively and quantitatively.

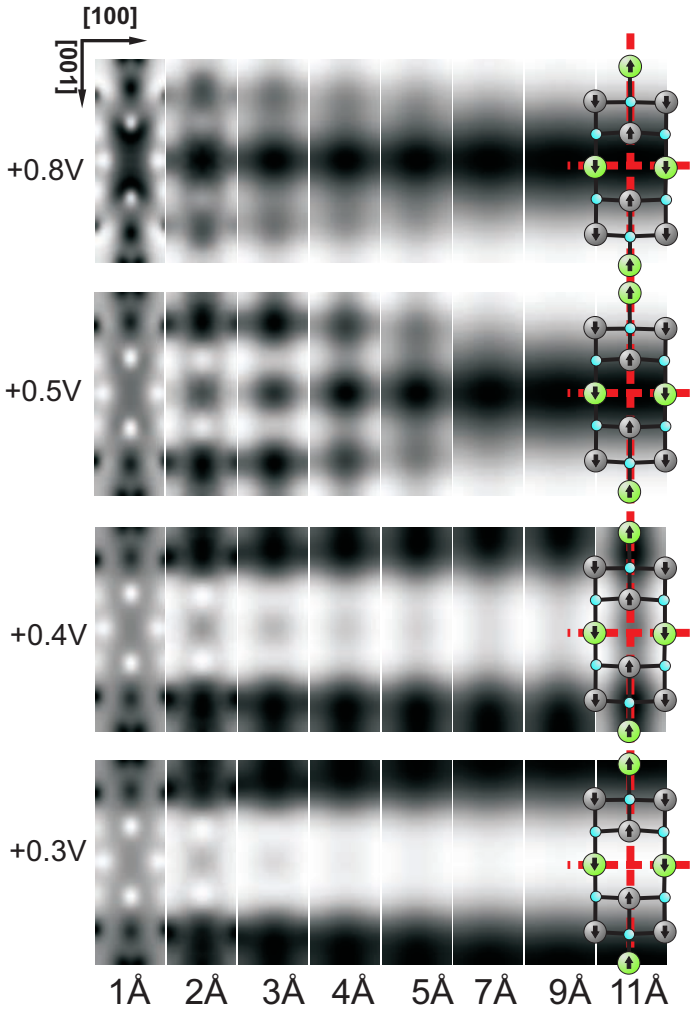


Figure 4.26: Evolution of the calculated surface spin-LDOS versus applied bias voltage (vertical axis) at different distances above the surface (horizontal axis). Bright and dark regions correspond to spin-up and spin-down densities, respectively. The position of the top surface atoms is schematically shown on the plot with the largest tip-surface separation of 11 Å. Arrows inside $Mn_1$ and $Mn_2$ atoms indicate their total magnetic moment; nitrogen atoms are shown as small balls. The dashed lines along the (001) and (100) directions correspond to the position of the (100) and (001) crosssection planes shown in Fig. 4.30. PBE exchange-correlation is employed.

From a comparative analysis of the simulated and experimental data presented in Figs. 4.23-4.25 it follows, that even employing the simplest Tersoff-Hamann tip with constant DOS it is possible to reproduce the whole set of experiments, with fairly good agreement for the magnetic part of the SP-STM profiles. As a side remark we note here, that a better quantitative agreement for the non-magnetic part (being out of the scope of the current study) would be achieved if precise information regarding the experimental tip geometrical and electronic properties were available (see also the discussion in Sec. 4.4.6).

Since the simulated profiles correspond to an electronically featureless tip, i.e. depend only on the surface electronic properties, we conclude that the experimentally observed magnetic contrast reversal can be adequately described solely in terms of the surface electronic structure.

Fig. 4.26 shows a density plot of the surface spin-LDOS corresponding to different applied bias voltages. Only positive voltages relevant to the magnetic contrast reversal are presented. First, comparing the magnetic LDOS in the energy range between +0.3 V and +0.8 V, it becomes clear that the magnetic contrast undergoes a reversal due to the change of the surface electronic

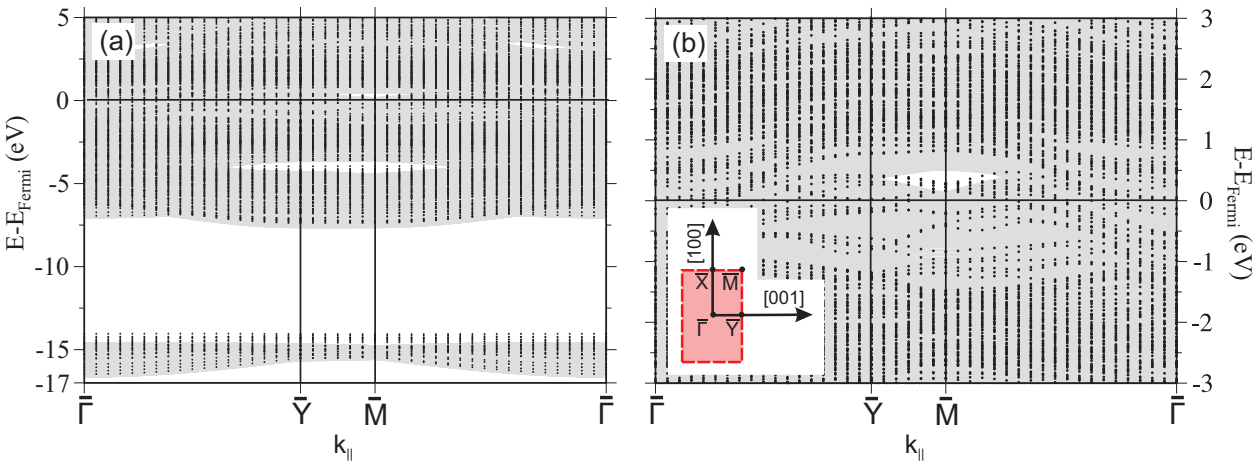


Figure 4.27: Electronic band structure of the $Mn_3N_2(010)$ surface. The gray-shaded regions indicate the projected bulk bands from bulk calculations, the black dots - the slab electronic states. PBE exchange-correlation is employed.

properties: while at +0.3 V the spin-up density accumulates in the vicinity of the $Mn_1 \downarrow$ rows (see Fig. 4.26), at +0.8 V this region is clearly dominated by the spin-down density. For biases close to +0.4 V, there is an apparent dependence of the surface magnetic LDOS on the distance above the surface. Specifically, at +0.5 V the inverse of the magnetic contrast occurs at ∼4 Å above the surface: for distances smaller than ∼4 Å the magnetic LDOS behaves similar to that at +0.3 V, but above this distance the magnetic profile is essentially like the one at ∼+0.8 V. For +0.4 V the corresponding contrast reversal occurs at ∼11 Å. Therefore, the voltage at which the magnetic contrast reversal occurs can slightly vary depending on the actual tip-surface separation.

To elucidate the origin of the magnetic contrast reversal we now turn to the electronic properties of the $Mn_3N_2(010)$ surface, focusing on the vicinity of the Fermi level. The surface bulk band structure is shown in Fig. 4.27. The corresponding density of the slab electronic states projected onto the atomic orbitals is shown in Figs. 4.28-4.29.

First, from Fig. 4.28(a)-(b) it follows that the electronic states of nitrogen do not significantly affect the properties of $Mn_3N_2$ in the vicinity of the Fermi level. In fact, the *s*-states of the nitrogen atoms essentially contribute only in the energy range from $E_{\text{Fermi}} - 17$ eV to $E_{\text{Fermi}} - 13$ eV, while the *p*-character can be recognized below $E_{\text{Fermi}} - 4$ eV (*p*-states). Close to the Fermi level the density of nitrogen electronic states is significantly lower than that of the manganese. Second, the majority and minority spin channels of nitrogen are practically symmetric, yielding a very small magnetization of this species. This implies that nitrogen atoms cannot be responsible for an inversion of the magnetic contrast, and consequently can be disregarded in the following analysis.

The electronic properties of $Mn_1$ and $Mn_2$ atoms are very similar, and are substantially defined by the *d*-electrons when considering energies close to the Fermi level. A characteristic feature of the Mn *d*-electrons is their splitting into nonsymmetric spin-up and spin-down channels due to

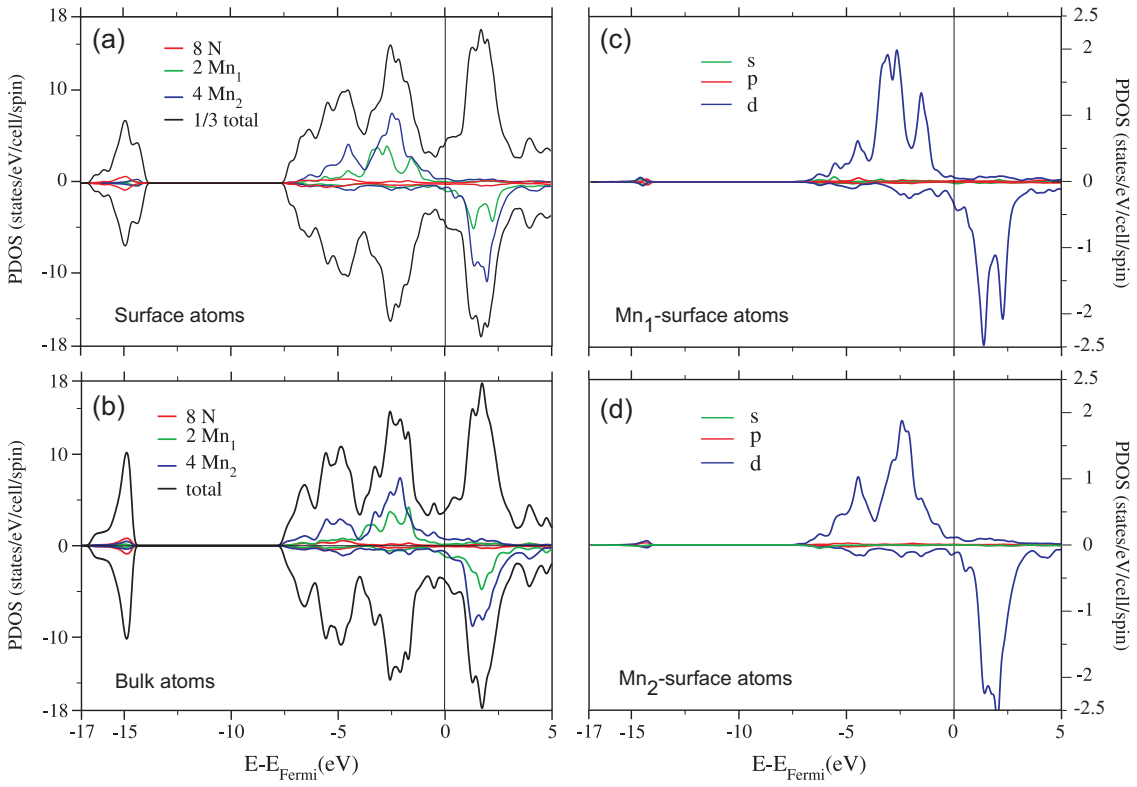


Figure 4.28: Density of electronic states projected onto (a) Mn and N atoms in the top-most layer of $Mn_3N_2(010)$, and onto (b) Mn and N atoms in the $Mn_3N_2$ bulk. (c)-(d) Orbital-resolved density of states projected onto surface $Mn_1$ and $Mn_2$ atoms respectively. PBE exchange-correlation is employed.

exchange interactions. The splitting is about 5 eV, resulting in a substantial magnetic moment of the manganese species. The center of mass for the spin-up channel is shifted by $\sim 2.5$ eV below the Fermi level, and protrudes by about 2 eV into the region of the unoccupied electronic states for spin-down $d$-electrons (Fig. 4.28(c)-(d)). The density of $sp$-electrons at the Fermi level is relatively low. We conclude, therefore, that electronic properties of $Mn_3N_2$ are to major extend defined by the $d$-states of the Mn atoms only. Consequently only these electronic states are responsible for the variation of the magnetic SP-STM profiles.

On Fig. 4.29 we zoom into the projected density of manganese $d$-states, restricting to the $d_{yz}$, $d_{xz}$, and $d_{z^2}$ orbitals. The $d_{x^2-y^2}$ and $d_{xy}$ orbitals are not relevant for STM because they are strongly localized in the surface plane[9]. Furthermore, we focus on the electronic states above $E_{\mathrm{Fermi}}$, because they determine the inverse of the magnetic contrast. First, for the $Mn_1$ atoms, we find that the spin-density contribution of minority (with respect to the total magnetic moment of the corresponding atom) type substantially dominates over the majority electrons. Within the minority channel $d_{xz}$-electrons prevail over the contribution stemming from the $d_{yz}$- and $d_{z^2}$-orbitals. Such

[9]We define the $x$,$y$,$z$ axis being parallel to the [100],[001],[010] crystallographic axis, respectively.

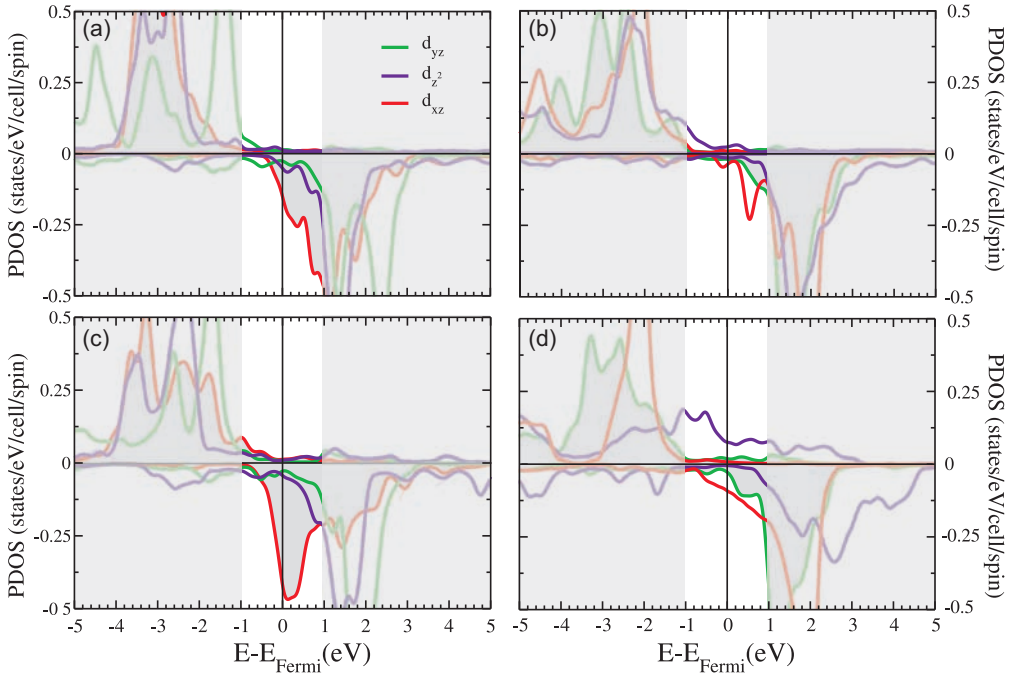


Figure 4.29: (a)-(b) Orbital-resolved density of electronic states projected onto bulk and surface $Mn_1$ atoms respectively. (c)-(d) The corresponding profile for the $Mn_2$ atoms. Only $d$-orbitals that are relevant for the STM simulations ($d_{xz}$, $d_{yz}$, and $d_{z^2}$) are shown. PBE exchange-correlation is employed.

ranking remains unchanged at positive energies up to $E_{\text{Fermi}}$+1 eV, implying that the $Mn_1$ atoms cannot be responsible for the magnetic contrast reversal (Fig. 4.29(a)-(b)). This conclusion is somewhat unexpected, because the inverse of the magnetic contrast occurs on top of [100]-rows of $Mn_1$ atoms (see e.g. Fig. 4.26).

In contrast to $Mn_1$, there is an evident change of the dominating spin-contribution versus bias voltage for the $Mn_2$ atoms. We consider only the variation of the $d_{yz}$ and $d_{z^2}$ orbitals as being responsible for the magnetic contrast reversal. This is because, by definition of a $d_{xz}$-orbital, the major fraction of $Mn_2$ $d_{xz}$-electrons is spatially localized on top of [100]-rows of $Mn_2$, and therefore cannot significantly influence the distribution of the spin-density above $Mn_1$ (see e.g. Figs. 4.23(k-t), 4.26).

As can be seen from Figs. 4.29, 4.26, 4.30, at small positive bias voltages the $Mn_2$ atoms mainly exhibit majority $d_{z^2}$-character. These $d_{z^2}$ orbitals are clearly distinguishable, e.g., in Fig. 4.26 as intense spots located on top of the $Mn_2$ atoms at $\sim 1-2$ Å above the surface, and in Fig. 4.30(c). Since the $Mn_2$-$Mn_1$-$Mn_2$ rows of surface atoms are row-wise aFM, the minority contribution of the $Mn_1$ atoms has the same sign as the majority contributions of the surrounding $Mn_2$ atoms. The overlap of the minority $d_{xz}$ lobes of $Mn_1$ atoms with the majority $d_{z^2}$ lobes of the surrounding $Mn_2$ atoms results, therefore, in a $(\uparrow\uparrow\uparrow)(\downarrow\downarrow\downarrow)$ pattern at all distances above the surface, as shown at

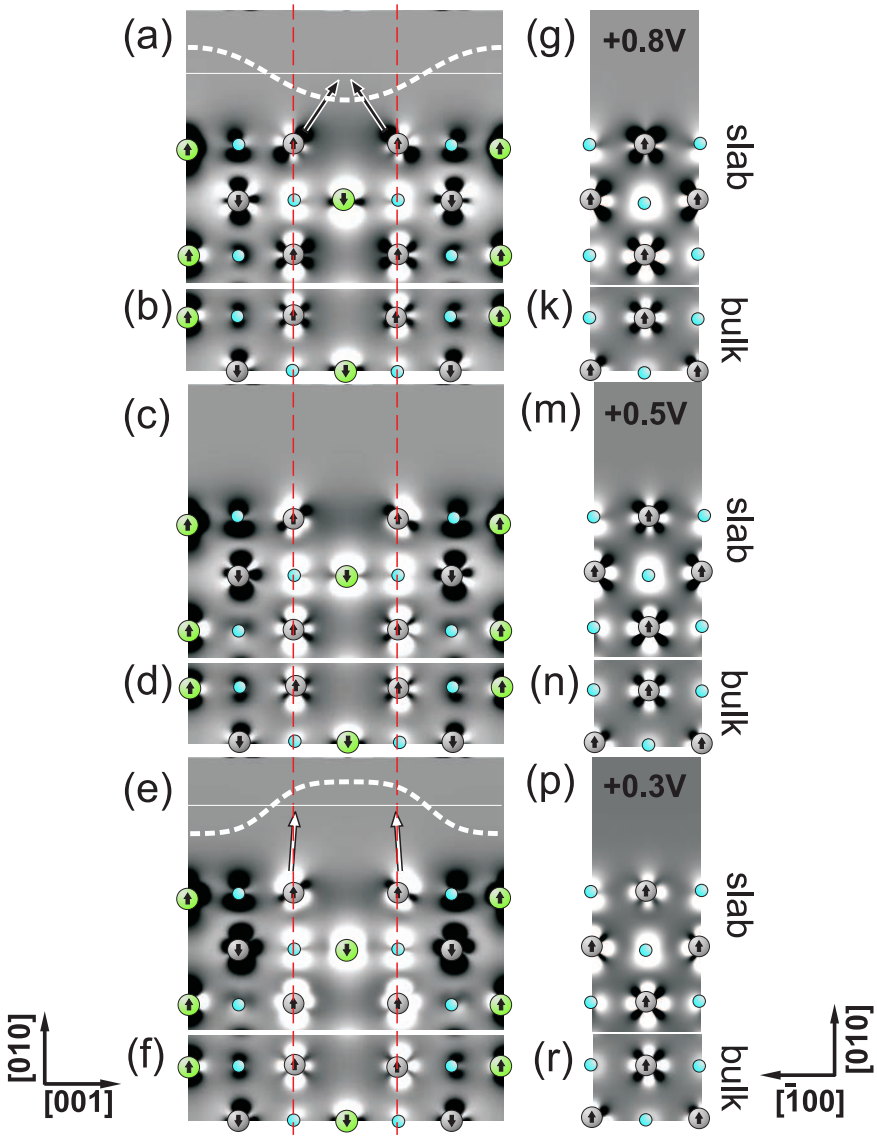


Figure 4.30: Evolution of the calculated surface and bulk spin density with change of the bias voltage. Cross sections of the surface spin density in the (100) plane correspond to bias voltages +0.8 V (a), +0.5 V (c), and +0.3 V (e). The corresponding cross sections in the (001) plane are shown in (g), (m), and (p), respectively. The position of the cross sections with respect to the surface unit cell is depicted in Fig. 4.26 as a vertical (for the (100) plane) and the horizontal (for the (001) plane) dashed lines. The corresponding cross sections of the bulk spin density are shown in (b), (d), (f) for the (001) plane, and in (k), (n), and (r) for the (100) plane respectively. Arrows inside the $Mn_1$ and $Mn_2$ atoms indicate their total magnetic moments; nitrogen atoms are shown as small balls. Bright and dark regions correspond to spin-up and spin-down densities correspondingly. Vertical dashed lines indicate rows of $Mn_2$ atoms that effectively screen the contribution of $Mn_1$ atoms which are located in the middle. The black arrows in (a) highlight the minority $d_{yz}$ character of $Mn_2$ atoms that dominate the surface spin-LDOS at +0.8 V, resulting in the rounded shape (schematically shown as a white dashed curve) of the spin-LDOS profile. The white arrows in (e) highlight the dominating majority $d_{z^2}$ character of $Mn_2$ atoms, that determines the trapezoidal shape (schematically shown as a white dashed curve) of the surface spin-LDOS. PBE exchange-correlation is employed.

+0.3 V in Fig. 4.26.

As the bias voltage $V_{\text{bias}}$ increases, the spin character of the $Mn_2$ atoms evolves smoothly from majority $d_{z^2}$ to minority $d_{yz}$ character. This can be seen in Fig. 4.30 at +0.5 and +0.8 V, where the minority $d_{yz}$ orbital lobes become more prominent. These lobes tend to overlap each other above hollow sites of the neighboring $Mn_1$ row. At sufficiently large bias voltages, the minority $d_{yz}$ of the $Mn_2$ atoms effectively screens the minority $d_{xz}$ of the $Mn_1$ atoms and becomes the dominating feature in the surface spin-LDOS. This is manifested by the appearance of high spin-density features on the hollow sites in the $Mn_1$ rows (see, e.g., the spin-LDOS at +0.8 V in Fig. 4.26), and leads to an inversion of the magnetic pattern, e.g., from (↑↑↑) to (↓↓↓) and vice versa. The magnetic contrast reversal at the $Mn_3N_2(010)$ surface is, therefore, caused by the smooth change from majority to minority $d$-orbitals of the $Mn_2$ atoms in the energy resolved DOS above the Fermi level. At sufficiently large positive biases, this leads to an effective (↓↓↓)(↑↑↑) magnetic pattern with underlying ($Mn_2$↑$Mn_1$↓$Mn_2$↑)($Mn_2$↓$Mn_1$↑$Mn_2$↓) rows.

It is not a coincidence that the shape change in the magnetic line profile from trapezoidal to rounded, observed both in experiment and theory, occurs at about the same bias voltage as the magnetic contrast reversal, namely at $V_{\text{bias}} + 0.4$ V. In fact, the transition in the line profile shape can also be explained by the change from majority to minority $d$-orbitals. As can be seen from Fig. 4.30, at +0.3 V the majority $d_{z^2}$ orbital lobes of the two $Mn_2$ surface atoms are relatively far apart, leading to the trapezoidal-like line profile shape. However, with increasing bias voltage (i.e., as seen at +0.5 and +0.8 V), the minority $d_{yz}$ orbital lobes become more prominent and, since they are spatially closer together, lead to a more rounded line profile.

As a concluding remark, we note that the aforementioned smooth change from majority $d_{z^2}$ to minority $d_{yz}$ electronic character for $Mn_2$ atoms at the surface is dictated by the underlying aFM bulk structure. This can be seen by comparing of the surface and bulk projected density of states (Fig. 4.29(b) and 4.29(d)) and is also shown in Fig. 4.30. There, an increase of the bias leads to essentially identical changes in $d_{z^2}$ and $d_{yz}$-electrons for surface and bulk $Mn_2$ atoms[10]. In this way, the observed inversion of the magnetic contrast at the surface is a direct consequence of the underlying bulk electronic structure.

[10]The same applies to $Mn_2$ $d_{xz}$-electrons, although the correlation between the corresponding surface and bulk electronic states is less obvious. Indeed, as can be seen in Fig. 4.30, for large bias voltages (Fig. 4.30(a)) the minority $d_{xz}$-character at the surface is stronger when compared to that for bulk atoms. At the same time, the situation is inverse when considering smaller biases (Fig. 4.30(a)). Considering Fig. 4.29(b),(d), we see clear differences between the bulk and surface PDOS for the minority $d_{xz}$ states. While the bulk contribution smoothly increases with increasing energy, the surface counterpart shows pronounced wiggles. Specifically, focusing on the energies between $E_{\text{Fermi}}$ and $E_{\text{Fermi}}+1$ eV, we can localize a clear peak in the surface PDOS at about $E_{\text{Fermi}}$+0.5 eV. Despite the fact that there is a pocket in the projected bulk band structure (between $E_{\text{Fermi}}$+0.1 eV and $E_{\text{Fermi}}$+0.5 eV; Fig. 4.27), this peak is no evidence for a surface state. In fact, there exists a set of peaks between $\sim E_{\text{Fermi}} - 0.5$ eV and $\sim E_{\text{Fermi}} + 3.5$ eV. We find that in this energy window (i) the peaks are homogeneously distributed along the energy axis, (ii) the number of peaks smoothly increases when the slab thickness is increased, (iii) the energy alignment of the peaks depends on the slab thickness, (iv) the intensity of each peak smoothly decreases when increasing the slab thickness, and (v) the relaxation of surface atomic positions does not significantly affect the magnitude, or the position of each peak. From the above we conclude that these peaks are likely due to a finite thickness of the slab, resulting in a discretization of the bulk $d_{xz}$ states.

In summary, we have analyzed the bias-dependent magnetic profiles obtained by SP-STM on the $Mn_3N_2(010)$ surface. Particularly, we have shown that a polarization reversal occurs and that the magnetic contrast and magnetic line profile shape vary with the bias voltage. Based on our spin-polarized DFT calculations, we have performed simulations of the SP-STM experiments employing a featureless STM tip model. Our theoretical results are in very good agreement with the measured profiles and allow an in-depth interpretation of the observed reversal of the magnetic contrast as a surface-driven, rather than tip-driven, effect. Moreover, the change in the line profile shape, as well as the magnetic contrast reversal, are explained in terms of a smooth change from majority to minority spin *d*-orbitals in the bulk band structure.

### 4.4.8 Effect of tip properties on the simulated SP-STM images

It is well known that properties of an STM tip can significantly influence STM images [4, 174, 176, 248, 252–254]. In some cases it is not even possible to achieve a quantitative agreement between theory and experiment unless the STM tip is considered as a complex nanoscale object on the *ab initio* level [4, 248, 252, 253].

Within the Tersoff-Hamann approach the tip is treated as electronically featureless with constant density of states, with a single atom in the tip apex, and assuming that the tip electronic properties are dominated by a *s*-like angular momentum contribution. Furthermore, in case of a spin-polarized tip, it is assumed that spin-up and spin-down electrons possess identical scattering properties in the vacuum region (Sec. 2.6.3). Such an idealized tip provides a major advantage to construct STM profiles solely in terms of the surface electronic properties.

Evidently, the properties of realistic tips might significantly deviate from that of the Tersoff-Hamann model. This applies to both the electronic properties and the atomic structure of the STM tips: the tip apex may consist of several atoms, that might be arranged in facets or have even a more complex geometry [4]. Even though the convolution of all electronic states near the Fermi level in many cases shows radial symmetry, the electronic properties of the tip may be dominated by *p*- or *d*-like orbitals [252]. Moreover, the dominating electronic character might even change with energy. Although the agreement between the Tersoff-Hamann SP-STM images and experimental profiles is excellent in this study (Sec. 4.4.7), it is crucial to examine how and to which extend the simulated SP-STM images are modified when employing more realistic models of an STM tip.

To theoretically mimic a realistic tip one has to introduce assumptions regarding the tip atomic structure. The model tip structure should be chosen such that it agrees to the highest possible degree to the experimental counterpart. For instance, the experimental STM tip prepared by deposition of Mn onto a tungsten tip can be modeled as a Mn atom deposited on a W(100) surface [4, 252]. Explicit *ab initio* calculations are then performed to get the ground-state electronic and relaxed atomic structure of such a complex tip. Finally, the STM images are calculated employing Eqs. (2.108)-(2.109), i.e., by an explicit convolution of the surface and the tip wavefunctions. Despite the fact that such an approach treats the tip on the same level of accuracy as the surface,

it possesses several disadvantages. First, such an explicit approach still relies on the assumption of a specific tip structure. The full atomic structure at the tip apex, however, is in general unknown and may even change within scanning a single STM picture. Second, the interpretation of the simulated STM images is not straightforward, because the electronic properties of a realistic tip are coupled with the tip geometry. Therefore, a separation of the tip effects into electronic-driven and structure-driven parts is not feasible. Third, an explicit treatment of realistic tip models on an *ab initio* level is computationally extremely demanding.

Instead of an explicit treatment of the tip according to Eqs. (2.108)-(2.109) we employ here a much simpler approach. This approach, expressed in Eq. (2.119), is similar to Tersoff-Hamann model, and it is based on the assumption of a single apex atom tip with a spherically symmetric wavefunction. According to Eq. (2.119), and in contrast to the Tersoff-Hamann approach, the tip is no longer electronically featureless: the electronic structure of the tip is included via an energy-dependent density of the tip eigenstates (see Eqs. (2.108)-(2.109)). Thereby, Eq. (2.119) allows to derive to what extend the final SP-STM images depend on the electronic properties of the STM tip. Employing Eq. (2.119), we have performed three sets of bias-dependent SP-STM simulations on the $Mn_3N_2(010)$ surface employing different tip models. These models roughly correspond to a Fe-tip, a Mn-covered tungsten tip, and a tip with constant density of states (CDOS). The magnetic moments of the tip and of the surface are assumed to be collinear at all bias voltages for all three tip models. The energy-dependent DOS for the Fe- and the Mn-tips have been extracted from *ab initio* studies by Heinze *et al.* [203, 224], assuming that the DOS of the apex atom at the Fe-tip *roughly* corresponds to the DOS of a surface Fe atom on a ferromagnetically ordered Fe(110) surface [224]. For the Mn-tip we assume that the DOS of the apex atom *roughly* corresponds to the DOS of an atom in an antiferromagnetically ordered Mn-monolayer on a W(100) substrate [203]. The energy-dependent DOS for Fe, Mn, and the CDOS tips are shown in Fig. 4.31. We emphasize, that despite we use results of the first-principles calculations to mimick the electronic properties of the Mn- and Fe-tip, our tip models are not meant to accurately reproduce realistic Fe and Mn tips and should be regarded only as a rough approximation to estimate the effect of tip properties on STM.

In order to estimate the effect of the tip geometry we compare an atomically sharp tip (a single atom in the tip apex) with an atomically obtuse tip. The latter is modeled by an atomic configuration where the apex atoms are located at the corners of a square being parallel to the surface (see inset in Fig. 4.31(b)). The area occupied by the tip apex is defined by the interatomic distance $d$ along the edges of the square. To separate electronic and geometric effects, we assume for simplicity that the apex atoms do not interact with each other. In other words, each atom contributes to the tunneling current according to Eq. (2.119), and the total STM current is simply the sum of the contributions from all apex atoms. Using this 4-atom-tip we estimate the influence of the tip blurness on the nonmagnetic and magnetic parts of the total SP-STM profile.

The results of the STM simulations employing atomically sharp tip models are summarized in

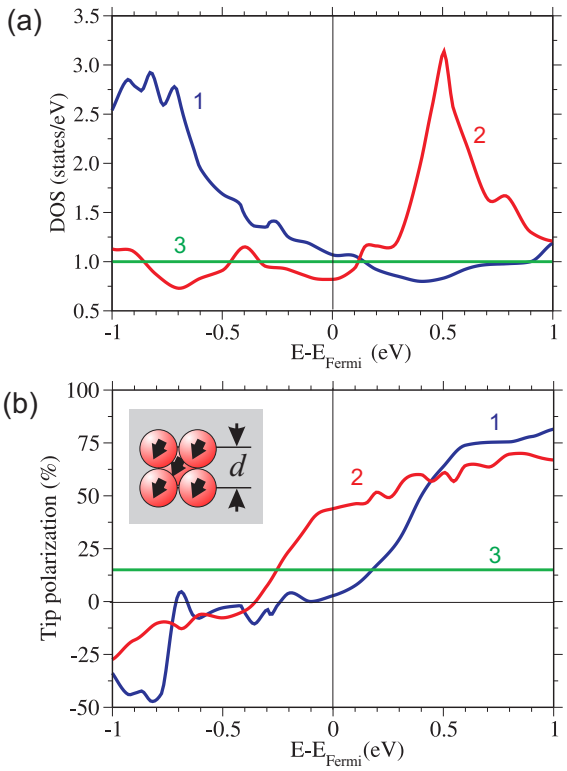


Figure 4.31: (a) DOS and (b) magnetic polarization of the model Fe-tip (curves 1), Mn-tip (curves 2) and CDOS (curves 3). The data for the Fe-tip is taken from Ref. [224], for the Mn-tip from Ref. [203]. The inset in (b) schematically shows a top-view of the atomic structure of the model 4-atom-tip: the atoms sit at the corners of a square with length $d$, and lie in a plane parallel to the surface.

Fig. 4.32, where we show the magnitude of the nonmagnetic and magnetic profiles versus the bias voltage for CDOS, Mn and Fe tips. The tunneling current in all cases is chosen to provide the same averaged tip-surface separation at bias voltage -0.1 V for all tips. The shape and periodicity of the SP-STM images are not influenced when employing different tip models, and consequently are not shown here. From Fig. 4.32 is follows, that the electronic properties of the STM tip very differently affect the magnetic and nonmagnetic parts of SP-STM images. For nonmagnetic contribution, all three tip models provide very similar results, particularly at positive bias voltages. For negative biases the Fe and CDOS tips provide essentially identical magnitudes of the nonmagnetic profile up to about -0.6 V. At negative biases (up to about -0.9 V) the predicted magnitude of the nonmagnetic component using the Mn-tip is slightly smaller than that for the Fe- and CDOS-tips. This is due to larger tip-surfaces separations for Mn-tip model. In turn, these larger tip-surfaces separations at negative biases is due to the huge amplitude of the magnetic contribution, predicted for Mn and Fe tips (Fig. 4.32). Summarizing, the electronic properties of the tip do not significantly modify the nonmagnetic profile, especially in the range of small biases, and result in minor quantitative differences of the predicted magnitudes of the nonmagnetic component.

In contrast to the nonmagnetic part, the magnetic contribution is significantly affected by the electronic properties of the tip. From Fig. 4.32(b) it follows, e.g., that the Fe-tip detects essentially no magnetic contrast at a positive bias, mainly due to the very low magnetic polarization below the Fermi level of this tip (see Fig. 4.31(b)). At negative biases, the Fe-tip model predicts huge

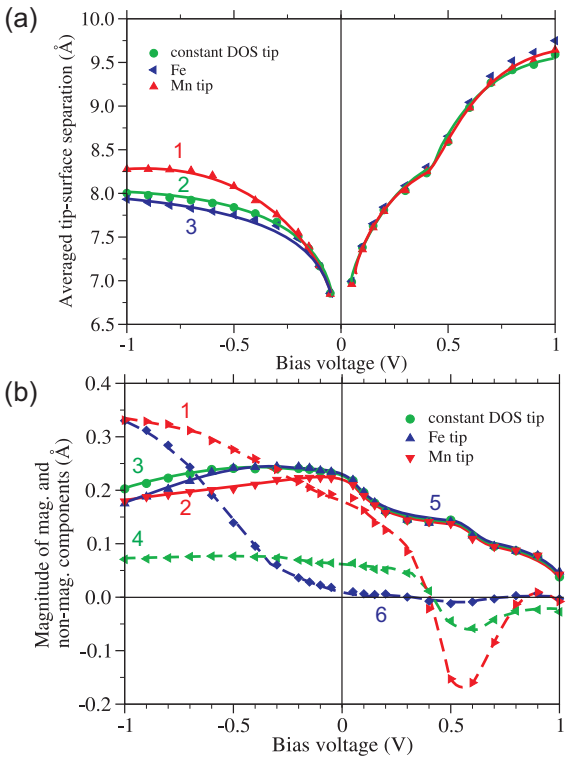


Figure 4.32: Effect of the tip electronic properties on the SP-STM in the single atom tip geometry. (a) Simulated averaged tip-surface separation versus applied bias voltage assuming a Mn-tip (curve 1), a constant DOS tip (curve 2) and a Fe-tip (curve 3). (b) The magnitude of the nonmagnetic component (green circles - constant DOS tip; blue triangles up - Fe tip; red triangles down - Mn tip) and the magnetic component (green triangle left - constant DOS tip; blue diamonds - Fe tip; red triangles right - Mn tip). Fitted solid curves 1-3 (nonmagnetic) and dashed curves 4-6 (magnetic) are shown as a guide to the eye. PBE exchange-correlation is employed.

(compared to the CDOS-tip) magnitudes of the magnetic corrugation at biases below -0.5 V. This can be understood from the high spin-polarization of this tip at energies ∼+0.5 eV above the Fermi level. For the Mn-tip an inversion of the magnetic contrast is predicted not only at a bias voltage of about +0.4 V, but also at +0.8 V. We therefore conclude that the behavior of the magnetic profile with bias voltage might qualitatively change when varying the chemical nature of the tip. From Figs. 4.31-4.32 we deduce, therefore, that within the frame of our model the tip electronic properties are essential for the magnetic part of the SP-STM image, while of minor importance for the nonmagnetic constituent.

We now focus on the impact of the tip geometry on SP-STM simulations. In Fig. 4.33 we summarize bias-dependent SP-STM simulations obtained using an electronically featureless tip (CDOS-model) and employing an atomically sharp tip (curves 1-2) or atomically obtuse tips. The latter are characterized by side length $d = 1.6$ Å, $d = 1.8$ Å, and $d = 2.0$ Å within the 4-atom-tip model. Similar to the case of electronically different STM tips, we require that the tunneling current provides the same averaged tip-surface separation at bias voltage -0.1 V for all tips. From Fig. 4.33 it follows that the tip-surface separation vs. bias voltage remains essentially unchanged for both single-atom and 4-atom-tips. The same applies to the magnetic part of the STM image: the impact of the tip geometry on this component is negligible. The magnitude of the nonmagnetic part, however, smoothly decreases when using more obtuse tips, i.e. when increasing $d$. The origin of this behavior can be understood as follows: Atomically obtuse tips essentially smoothen the SP-

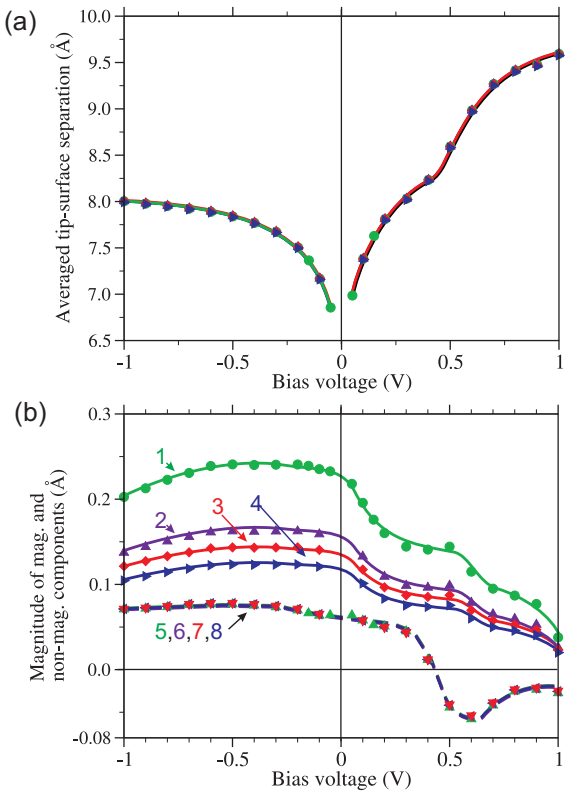


Figure 4.33: Effect of the tip geometry on the SP-STM. (a) Theoretical averaged tip-surface separation versus applied bias voltage. (b) The magnitude of nonmagnetic component (green circles - single atom tip; purple triangles up - $d$=1.6 Å; red diamonds - $d$=1.8 Å; blue triangles left - $d$=2.0 Å) and magnetic component (green triangle up - single atom tip; purple triangles left - $d$=1.6 Å; red triangles down - $d$=1.8 Å; blue squares - $d$=2.0 Å). Fitted solid curves 5-8 (nonmagnetic) and dashed curves 1-4 (magnetic) are shown to guide eye. PBE exchange-correlation is employed.

STM image, i.e., they result in a lower resolution of the STM by averaging the STM image over the area of the tip apex. Obviously, this has a larger impact on the contributions having a higher spatial resolution, i.e., in our case the nonmagnetic component. In contrast to the nonmagnetic contrast, the magnetic corrugation is not affected because it already has a large periodicity $c_0 \sim 12$ Å that is larger than $d$, and is therefore not blurred further (see, e.g. Fig. 4.24).

In summary, we have estimated the impact of the electronic and geometrical properties of the STM tip onto simulated SP-STM images. Employing a simplified tip model based on the transfer-Hamiltonian formalism and the assuming a radially symmetric tip wavefunctions, we have shown that the magnetic part of the SP-STM images might be significantly influenced by the tip electronic properties; the nonmagnetic part is much less sensitive with respect to the electronic properties of the tip. In contrast, the tip geometry predominantly affects the resolution of the STM. Consequently it is more important for the nonmagnetic part, and has therefore much less impact onto the magnetic contribution, mainly because it has a lower spatial resolution when compared to the nonmagnetic component of the SP-STM.

### 4.4.9 Comparison of the Tersoff-Hamann and the ILDOS model for SP-STM simulations

In their early studies Yang and co-workers [197, 216] simulated the spin-polarized STM images on $Mn_3N_2(010)$ using a simplified theoretical approach that relies on the transfer-Hamiltonian formalism (see Secs. 2.6.1-2.6.3), but does not require any explicit surface calculations. It has been shown that employing this approach it is possible to correctly predict not only the shape of the spatially resolved magnetic and nonmagnetic components [197], but also to accurately reproduce bias-dependent atom-resolved STM images obtained using nonmagnetic STM tips [216]. Despite of this encouraging success it turned out, however, that the method (referred throughout this text as ILDOS model, with ILDOS standing for integrated local density of states) fails to predict the magnetic contrast reversal that has been detected in spin-polarized STM experiments (see, e.g., Sec. 4.4.7 and Ref. [198] for details). The origin of this failure was not understood. To shed light onto this problem and to figure out the reliability and limitations of the ILDOS method, which would be an interesting and computationally much less demanding approach to perform SP-STM simulations, we have performed a detailed comparison between the simulated bias-dependent SP-STM images obtained employing accurate Tersoff-Hamann approach with corresponding images acquired within the ILDOS model.

Both, the Tersoff-Hamann and the ILDOS model are based on the same expression Eq. (2.119), giving the tunneling current in terms of the (local) densities of electronic states of the tip and of the surface. To introduce the ILDOS approach it is instructive to reformulate Eq. (2.119) as:

$$I(\theta, \mathbf{R}_\mathrm{t}, V_\mathrm{bias}) \propto n^\mathrm{t} \check{n}^\mathrm{s}(\mathbf{R}_\mathrm{t}, V_\mathrm{bias}) + m^\mathrm{t} \check{m}^\mathrm{s}(\mathbf{R}_\mathrm{t}, V_\mathrm{bias}) \cos\theta(\mathbf{R}_\mathrm{t}, V_\mathrm{bias}). \tag{4.28}$$

Here, it is assumed that the magnetic $m^\mathrm{t}$ and nonmagnetic $n^\mathrm{t}$ tip DOS is a constant and independent on the bias energy. $\theta(\mathbf{R}_\mathrm{t}, V_\mathrm{bias})$ is the angle between the magnetization axis of the tip and of the surface at the tip position $\mathbf{R}_\mathrm{t}$ and bias voltage $V_\mathrm{bias}$. $\check{n}^\mathrm{s}$ and $\check{m}^\mathrm{s}$ are the nonmagnetic and magnetic integrated LDOS of the surface, given as:

$$\check{n}^\mathrm{s}(\mathbf{R}_\mathrm{t}, V_\mathrm{bias}) = \int dE g_v(E) n^\mathrm{s}(\mathbf{R}_\mathrm{t}, E), \tag{4.29}$$

and

$$\check{m}^\mathrm{s}(\mathbf{R}_\mathrm{t}, V_\mathrm{bias}) = \int dE g_v(E) m^\mathrm{s}(\mathbf{R}_\mathrm{t}, E). \tag{4.30}$$

The function $g_v(E)$ in Eqs. (4.29)-(4.30), the nonmagnetic LDOS $n^\mathrm{s}(\mathbf{R}_\mathrm{t}, E)$, and the magnetic LDOS $m^\mathrm{s}(\mathbf{R}_\mathrm{t}, E)$ are defined in Sec. 2.6.3 (Eqs. (2.120)-(2.122)).

Yang and co-workers have simplified Eqs. (4.28)-(4.30) further, and mapped the spatially-resolved surface ILDOS to a set of the atomic moments, i.e. to point-like objects that are placed onto atomic positions and are characterized by the corresponding space integrated nonmagnetic

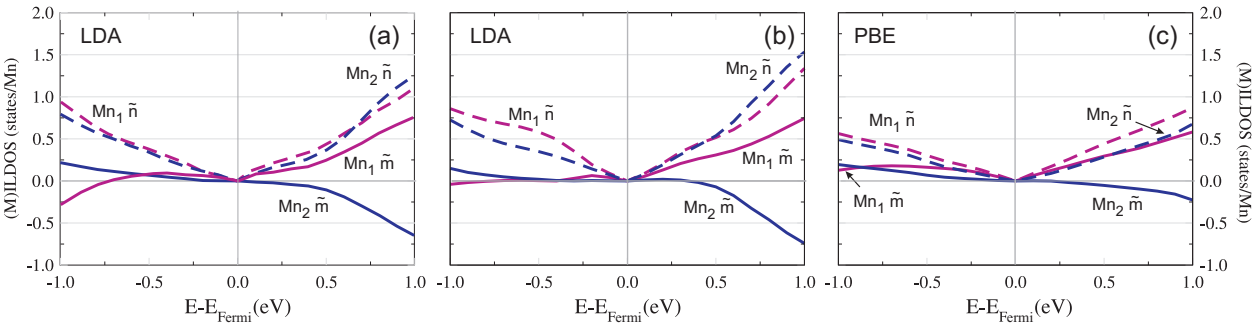


Figure 4.34: Nonmagnetic and magnetic integrated local density of states (ILDOS) of surface manganese atoms on $Mn_3N_2(010)$ as function of energy calculated (a) in LDA by Lambrecht *et al.* [223], (b) in LDA (this work) and (c) in PBE exchange-correlation functional (this work). Bulk atomic positions are fully relaxed.

and magnetic ILDOS, as:

$$\tilde{n}^{\mathrm{s}}(\mathbf{R}_i, V_{\mathrm{bias}}) = \int_{\Omega} d\mathbf{r}\, S(\mathbf{R}_i, \mathbf{r}) \check{n}^{\mathrm{s}}(\mathbf{r}, V_{\mathrm{bias}}), \tag{4.31}$$

$$\tilde{m}^{\mathrm{s}}(\mathbf{R}_i, V_{\mathrm{bias}}) = \int_{\Omega} d\mathbf{r}\, S(\mathbf{R}_i, \mathbf{r}) \check{m}^{\mathrm{s}}(\mathbf{r}, V_{\mathrm{bias}}). \tag{4.32}$$

The integrations in Eqs. (4.31)-(4.32) are performed over the unit cell $\Omega$, and $S(\mathbf{R}_i, \mathbf{r}) = (\exp\left[\frac{|\mathbf{R}_i - \mathbf{r}| - r_{\mathrm{mt}}}{w_{\mathrm{mt}}}\right] + 1)^{-1}$ is a Fermi-like function that mimics the atomic muffin-tin sphere placed around an atom located at $\mathbf{R}_i$; $r_{\mathrm{mt}}$ defines the radius of the muffin-tin sphere, $w_{\mathrm{wt}}$ defines the tails decay of the sphere boundaries. Assuming that all atoms have a radially symmetric distribution of the (spin) charge density and identical scattering properties in the vacuum region, Yang *et al.* have derived from Eq. (4.28) a simplified expression for the tunneling current:

$$I(\mathbf{R}_{\mathrm{t}}, V_{\mathrm{bias}}) \propto \sum_i \left[ n^{\mathrm{t}} \tilde{n}^{\mathrm{s}}(\mathbf{R}_i, V_{\mathrm{bias}}) + m^{\mathrm{t}} \tilde{m}^{\mathrm{s}}(\mathbf{R}_{\mathrm{t}}, V_{\mathrm{bias}}) \right] \cos\theta_i e^{-2\kappa|\mathbf{R}_{\mathrm{t}} - \mathbf{R}_i|}. \tag{4.33}$$

According to Eq. (4.33) the tunneling current is proportional to the exponentially weighted sum over the surface nonmagnetic and magnetic atomic moments $i$. The contribution of the subsurface and bulk atoms in this model can be neglected due to the exponential term in Eq. (4.33). Moreover, because the ILDOS of the nitrogen atoms is by at least a factor of 5 smaller than that for Mn atoms, it is sufficient to consider only $Mn_1$ and $Mn_2$ atoms [197, 223].

Yang *et al.* have used Eq. (4.33) to simulate SP-STM images assuming that $\theta_i$ and the ratio between $n^{\mathrm{t}}$ and $m^{\mathrm{t}}$ are constants, and taking the vacuum decay parameter $\kappa = 1.14$ Å$^{-1}$ (corresponding to a work function of 5 eV). Values for $\check{n}^{\mathrm{s}}$ and $\check{m}^{\mathrm{s}}$ were obtained from the first-principles calculations by Lambrecht and co-workers [197, 223] for antiferromagnetically ordered bulk $Mn_3N_2$ (see Fig. 4.34(a)). Because of a lack of explicit surface *ab initio* calculations the surface atomic

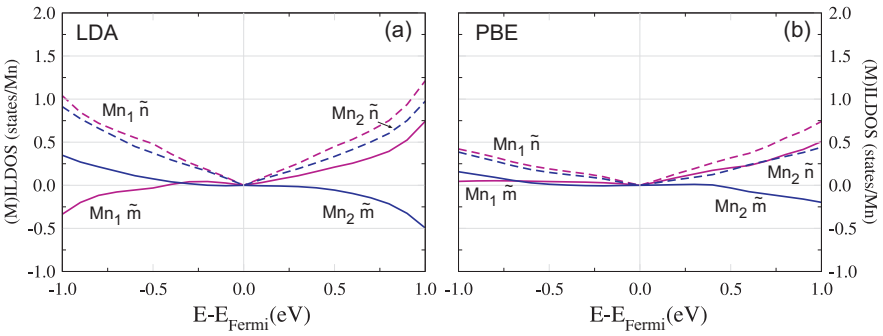


Figure 4.35: Nonmagnetic and magnetic integrated local density of states (ILDOS) of surface manganese atoms on $Mn_3N_2(010)$ as a function of energy calculated in (a) LDA and (b) PBE exchange-correlation functional. Bulk and surface atomic positions are fully relaxed.

geometry was speculated. Specifically, from an analysis of the experimental STM images it was assumed that the surface $Mn_1$ atoms are relaxed outward by about $\sim 0.1$ Å with respect to the surface plane. As mentioned in the beginning of this section, this method provided excellent agreement with respect to the shape of the magnetic and nonmagnetic line-profile on the $Mn_3N_2(010)$ surface, but failed to reproduce the inverse of the magnetic contrast. Because the ILDOS of the surface manganese atoms shows essentially no difference from the respective ILDOS for bulk species (compare Fig. 4.34(b)-(c) with Fig. 4.35(a)-(b)), this failure is not due to the wrong prefactors $\check{n}^{\mathrm{s}}$ and $\check{m}^{\mathrm{s}}$ employed by Yang *et al.*

In Fig. 4.36 we compare the magnitudes of the magnetic and nonmagnetic components of SP-STM profiles as function of the bias voltage simulated using Eq. (4.28) with corresponding results obtained with Eq. (4.33). In both sets of simulations we assume an effective tip polarization $P_{\mathrm{t}} = \frac{m^{\mathrm{t}}}{n^{\mathrm{t}}} \cos\theta_i = 15\%$. The ILDOS are calculated for surface Mn atoms. The bulk and surface geometries are identical in both cases, and correspond to the fully relaxed structure calculated in PBE (see Secs. 4.4.4-4.4.5 for details). The simulations are performed in the constant current mode of the STM. The values of the tunneling current for ILDOS and Tersoff-Hamann models are chosen to provide a tip-surface separation of 7 Å at bias -0.1 V (Fig. 4.36(a)).

From Fig. 4.36(a)-(b) it follows that the ILDOS and the Tersoff-Hamann model predict essentially different SP-STM images, although both methods show the same periodicity of the magnetic pattern. The periodicity is twice that of the nonmagnetic corrugation, and agrees with the periodicity of the nonmagnetic part (see e.g. Fig. 4.37). According to these results the ILDOS approach has a number of severe simulations: First, the ILDOS model tends to quantitatively disagree with the Tersoff-Hamann simulations in the whole range of the studied bias voltages. Specifically, it underestimates the magnitude of the corrugation pattern by a factor 3 to 8, particularly at negative biases. Noteworthy, that the magnitude of the nonmagnetic corrugation is underestimated stronger when compared with that of the magnetic component. This leads to a wrong ratio between simulated nonmagnetic and magnetic corrugations. According to Fig. 4.36(a) this cannot be explained

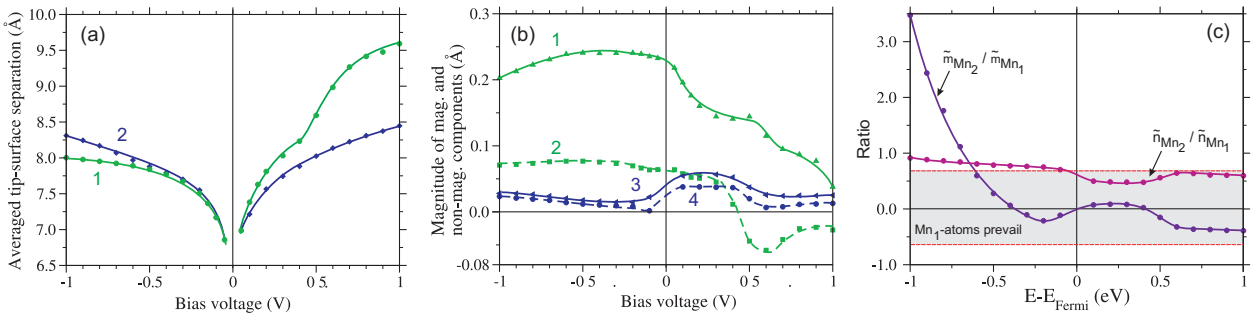


Figure 4.36: (a) Theoretical averaged tip-surface separation versus applied bias voltage calculated within the spin-polarized Tersoff-Hamann model (curve 1) and the ILDOS model (curve 2). (b) The magnitude of the magnetic component (blue triangle left - Tersoff-Hamann; blue circles - ILDOS) and of the nonmagnetic component (green triangle up - Tersoff-Hamann; green squares - ILDOS). Fitted solid and dashed curves (1 and 2-Tersoff-Hamann, 3 and 4-ILDOS model) are shown to guide the eye. (c) Ratio of the nonmagnetic and magnetic ILDOS of surface $Mn_1$ and $Mn_2$ atoms versus energy. The PBE exchange-correlation functional is used.

in terms of significantly different tip-surface separations between the ILDOS and Tersoff-Hamann simulations. Indeed, at negative biases the corresponding tip-surface separations differ by at most 0.03 Å; at positive biases the ILDOS approach provides systematically smaller tip-surface separations when compared to the Tersoff-Hamann method. Because the magnitude of the nonmagnetic corrugations is typically decreased when moving away from the surface, the smaller tip-surface separations should result in a larger magnitude of the corrugation for the ILDOS model. However, this is not the case (Fig. 4.36(b)). We conclude, therefore, that a systematic underestimation of the nonmagnetic corrugation is an intrinsic shortcoming of the ILDOS approach.

A more significant drawback of the ILDOS model is its inability to correctly reproduce SP-STM images on a qualitative level. Even disregarding the quantitative discrepancies, the ILDOS STM line-profiles at negative biases are not consistent with that of the Tersoff-Hamann model (Fig. 4.37). As follows from Fig. 4.37(c)-(d) the nonmagnetic part in the ILDOS simulations turns out to be shifted by a half-period, i.e., the maximum of the nonmagnetic corrugation is on-top of the $Mn_2$-rows instead of the $Mn_1$-rows as predicted by Tersoff-Hamann approach and observed in experiments. This phase shift can be explained in terms of the prevailing contribution due to either $Mn_1$ or $Mn_2$ species in Eq. (4.33). We have found that at commonly employed tip-surface distances (between 5 Å and 10 Å) the contribution due to the $Mn_1$ atoms becomes dominating when the ratio between the (non)magnetic ILDOS of $Mn_2$ and $Mn_1$ does not exceed a critical value $\lambda_{21} \simeq 0.65$ (Fig. 4.36(c)). This implies that $Mn_2$ prevails over $Mn_1$ in the nonmagnetic STM image at negative biases. At positive biases, however, the situation is inverse since $\tilde{n}_{\mathrm{Mn}_2}/\tilde{n}_{\mathrm{Mn}_1}$ is below $\lambda_{21}$. This leads to the correct phase of the nonmagnetic contribution.

We also note qualitative discrepancies between the ILDOS and the Tersoff-Hamann model in the description of the magnetic part. As can be seen e.g. in Fig. 4.36(b), the ILDOS model is

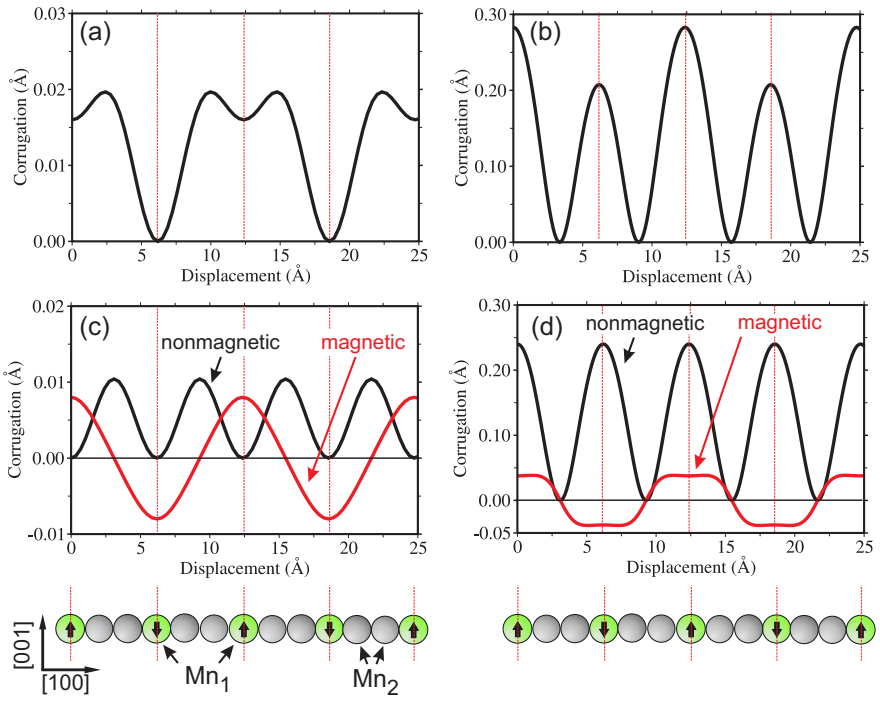


Figure 4.37: (a)-(b) Total SP-STM profiles and (c)-(d) separated magnetic and nonmagnetic components calculated employing the ILDOS-model ((a),(c)) and the spin-polarized Tersoff-Hamann approach ((b),(d)) at bias voltage -0.4 V on the $Mn_3N_2(010)$ surface. Line-profiles are obtained by averaging over the two-dimensional corrugation patterns along the [001] direction. The averaged tip-surface separation is 7.8 Å, and a tip with a constant effective magnetic polarization of 15% is assumed. PBE exchange-correlation is employed. The arrows inside the atoms indicate the sign of the magnetic moment as determined by the ILDOS at bias voltage $V_{\text{bias}}$ -0.4 V.

not able to reproduce the magnetic contrast reversal at bias +0.4 V. Similar to the analysis of the nonmagnetic line-profiles, this failure can be explained in terms of the interrelation between the magnetic ILDOS of $Mn_2$ and $Mn_1$ atoms. From Fig. 4.36(c) it follows that $Mn_1$ atoms prevail over $Mn_2$ at bias voltages above -0.7 V. Since the magnetic ILDOS of the $Mn_1$ species does not undergo a sign reversal between -1 V and +1 V, and $\tilde{m}_{\text{Mn}_2}$ and $\tilde{m}_{\text{Mn}_1}$ have the same sign below -0.7 V (see Fig. 4.35(b)), the ILDOS approach predicts no change of the magnetic contrast.

In order to analyze the origin for discrepancy between the ILDOS and Tersoff-Hamann simulations, we have studied in detail the spatially resolved LDOS that defines the STM image in the Tersoff-Hamann simulations (see e.g. Eq. (4.28)). We focus on the magnetic contribution to the SP-STM image. Fig. 4.38 shows a cross-section through the spin-LDOS along the [001] axis (b) and [100] axes (c) and (d) for a bias voltage $V_{\text{bias}}$ =-0.4 V. For the following discussion we focus on the $Mn_1$ and $Mn_2$ surface atoms highlighted with red in Fig. 4.38. From the ILDOS, which integrates the spin-density over a sphere around the Mn nucleus, these atoms are found to have an integrated spin-up moment (positive $\tilde{m}_{\text{Mn}_1}$) at the considered bias. The dominance of the spin-up density can be nicely seen in Fig. 4.38(c). However, what can be also seen in this figure and in Fig. 4.38(b)

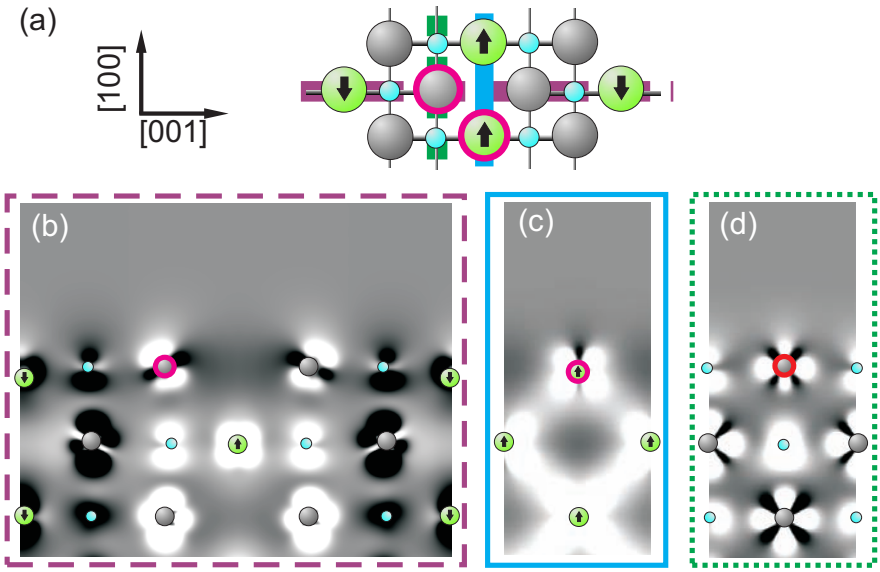


Figure 4.38: Schematic view of the atomic and magnetic structure of the $Mn_3N_2(010)$ top surface layer. The arrows inside the atoms indicate the sign of the magnetic moment as determined by the ILDOS at bias voltage $V_{bias}$ -0.4 V. (b)-(d) show contour plots of the magnetic LDOS for the case of $V_{bias}$=-0.4 V, where bright and dark regions correspond to spin-up and spin-down densities respectively. The density plots shown are the cross-sections through the surface layer along the [001] axis (b) and the [100] axis (c, d). Horizontal and vertical bars of (a) show cross-section position of (b)-(d) correspondingly. Spin-densities on (b)-(d) are plotted on the same scale. PBE exchange-correlation is employed.

is that in the region probed by the STM tip (i.e. 5-10 Å above the surface) the spin-density is negative. Thus, in an STM image, and at this bias, this atom would appear to be spin-down despite of the fact that the ILDOS for this atom is spin up. Regarding the $Mn_2$ atom we find a similar discrepancy between the LDOS and ILDOS: the ILDOS calculations indicate that $Mn_2$ atoms are essentially spin-neutral and consequently do not contribute to the magnetic corrugation. Figs. 4.38(b) and (d) show, however, that $Mn_2$ atoms possess a complex spatial distribution of the spin-density. In Tersoff-Hamann simulations, the spin-up lobes of the $Mn_2$ atoms dominate in the magnetic contrast, and completely screen the spin-down contribution from the $Mn_1$ atoms that are located between [100] rows of $Mn_2$. Although the ILDOS and the Tersoff-Hamann simulations provide qualitatively similar magnetic line-profiles (compare Fig. 4.37(c) and (d)), this agreement is accidental and leads to a wrong interpretation of the STM images within the ILDOS model. We conclude that the ILDOS spherical atom superposition is generally not suitable for SP-STM simulations, because it averages the spatial distribution of the spin-LDOS and consequently cannot account for the appearance of strongly directed orbitals at the surface atoms. This feature, however, is crucial for an accurate simulation of SP-STM corrugation patterns.

In summary, we have compared the SP-STM images simulated employing the Tersoff-Hamann approach and the simpler ILDOS model, that has been a popular model to simulate STM images on

$Mn_3N_2(010)$. We have shown that and explained why the ILDOS model fails to reproduce results of the Tersoff-Hamann simulations both on a quantitative and qualitative level. The reasons for the discrepancy were tracked back and demonstrated to be a consequence of the overly simplified spatial averaging used in the ILDOS approach.

## 4.5 Summary

In summary, we have developed an *ab initio* based tool to theoretically predict and analyze bias-dependent micrographs obtained by SP-STM on surfaces exhibiting nanomagnetism. The method has been implemented into our multiscale library S/PHI/nX [37, 38], and can be used in the future for simulating spin-sensitive STM micrographs. The model is based on the transfer-Hamiltonian formalism that treats the STM tip as a weak perturbation, and assumes that the tip wavefunctions have dominant radial symmetry ($s$-like tip). Planewave norm-conserving pseudopotential DFT as implemented in ABINIT [86, 87] and S/PHI/nX [37, 38] are used to yield the atomic and electronic properties of the surfaces. The applicability and predictive power of the approach have been demonstrated for the antiferromagnetic $Mn_3N_2(010)$ surface. The theoretical results have been found in excellent agreement with measured profiles and allowed an in-depth interpretation of all major effects such as the magnetic contrast reversal and even of subtle details affecting the specific shape of the line profile.

Specifically, we have performed detailed SP-STM simulations on the thermodynamically most stable magnetic and atomic surface reconstructions of $\eta$-MnN(010). The latter was elucidated within the framework of *ab initio* thermodynamics, by figuring out the surface configuration that has the lowest surface free energy among all possible magnetic and surface geometries that are commensurate with the periodicity of the experimental magnetic STM profiles. The accuracy of the calculations, emphasizing also details regarding the construction of an accurate norm-conserving pseudopotential and the importance of the local and gradient-corrected parameterizations for the exchange-correlation functional, are presented.

The bias-dependent spin-sensitive STM simulations were performed on the most thermodynamically stable surface configuration, that turned out to be the atomically relaxed bulk terminated surface. Based on our spin-polarized DFT calculations, we have performed simulations of the SP-STM experiments employing a featureless STM tip model. Our theoretical results are in very good agreement with measured profiles. An in-depth analysis allowed us to interpret the observed reversal of the magnetic contrast as a surface-driven, rather than a tip-driven, effect. Moreover, the change in the line profile shape, as well as the magnetic contrast reversal, are each explained in terms of a smooth change from majority to minority spin $d$-orbitals.

The effect of the tip properties, including the geometrical and electronic effects, are analyzed in SP-STM simulations that roughly mimic Fe and Mn tips. Our simulations imply that the magnetic contribution of the SP-STM image is essentially sensitive to the electronic properties of the STM

tip, i.e., to the chemical nature of the tip. The tip geometry, however, is found to be less critical to predict magnetic profiles. In contrast, the nonmagnetic STM current is significantly affected by the specific tip geometry, but exhibits only a low sensitivity with respect to the electronic properties of the tip.

Our SP-STM simulations were also compared with a previous more simplistic STM model. This model was employed in early studies for the calculating SP-STM images on $Mn_3N_2(010)$. The limitations of the model with respect to accuracy and predictive power are demonstrated.

# Chapter 5

# Summary

The goal of this work was to provide an in-depth understanding of a new generation of scanning tunneling microscopy experiments. These experiments were performed on nonmagnetic and magnetic surfaces employing different regimes of the STM: the spectroscopy-mode on nonmagnetic low-index noble-metal surfaces, and the spin-sensitive mode on magnetic transition-metal nitride surfaces. A strong motivation for the present study was that despite the obvious importance from both technological and fundamental points of view of the new STM scanning modes, critical problems remained unsolved and hindered an understanding of the experimental data. We have developed a variety of *ab initio* tools to theoretically predict and analyze (i) Fourier-Transformed STM images on terraced metallic surfaces, and (ii) bias-dependent micrographs obtained by SP-STM on surfaces exhibiting nanomagnetism. All STM-relevant schemes discussed below were implemented into the multiscale library S/PHI/nX [37, 38]. The methods developed and implemented are general and can be applied to accurately predict and analyze in the future STM images on various magnetic and nonmagnetic metallic surfaces.

The theoretical analysis of the Fourier-Transformed STM experiments was focused on acquiring dispersion properties of electrons at the surfaces. In these experiments, performed on a terraced Ag(110) surface, the dispersion of a weak signal behaving similar to surface electronic states has been observed on-top of the projected bulk band edge. The origin of this signal was not well understood, but it was speculated that the signal is due to bulk electrons. While experimentally it was not possible to confirm or withdraw this speculation, a clearcut answer was considered to be crucial: if the observed description was due to bulk electrons it would for the first time demonstrated that the range of physical phenomena accessible by STM can be extended to *local* dynamical properties of *bulk* electrons. In order to address this fundamental question, we have developed extensive theoretical tools and applied them on an experimental prototype surface - the Ag(110) surface. Specifically, we combined an *ab initio* DFT description of the surface with the widely used transfer-Hamiltonian model for STM. A plane-wave basis set was used in the DFT calculations, since it provides an exact asymptotic description (within the framework of the DFT)

of the surface wavefunctions in the vacuum region being probed by STM. ABINIT and S/PHI/nX program packages were employed for DFT simulations.

To simulate the theoretical counterpart of the experimental FT-STM spectrum, we had to introduce several assumptions to make the problem computationally feasible. Careful tests were performed to prevent a loss in accuracy. Specifically, instead of an explicit reproduction of the experimental FT-STM maps on terraced surfaces, we have developed an implicit approach that treats surface steps as ideally reflecting walls. The model further assumes an *s*-like electronically featureless STM tip with a single atom at the tip apex (Tersoff-Hamann approach). This approach allowed a dramatic reduction of the computational complexity since it requires explicit *ab initio* calculations only for the smallest (chemical) unit cell of the ideal unperturbed surface. The calculated and highly converged electronic properties for the bare Ag(110) surface revealed new features in the surface band structure compared to a previous *ab initio* study and are in perfect agreement with previously reported photoemission spectra.

A challenge in performing the simulations was to obtain an accurate description of the surface wavefunctions at $5 - 15$ Å above the surface, imposed by the constant-current mode in FT-STM experiments. Within a realistic setting of the plane-wave basis set, however, an accurate wavefunction description is limited to about $4 - 5$ Å. We have, therefore, developed and implemented a new approach that allows, without any additional calculations, to overcome the above mentioned deficiency of the plane-wave basis set, and to calculate qualitatively accurate FT-STM spectrum. Finally, due to the slab-supercell approach used for modeling the surface, we had to pay special attention to spurious quantum-size effects. Two different approaches that correct for the quantum-size effects in the simulated FT-STM maps have been proposed.

The resulting simulated FT-STM spectra are in excellent agreement with experimental data, implying that the theoretical model captures all essential experimental effects. Based on this approach we were able to theoretically demonstrate that the source of the albeit weak signal are indeed bulk electrons. Our subsequent analysis allowed for a detailed understanding of this effect. In particular, we were able to explain why only a fraction of the bulk electrons that are located on-top of the bulk band edge (BBE) have been detected in experiments. We show, that while all bulk states contribute to the FT-STM map, this contribution is essentially negligible everywhere except for the BBE, where the density of the bulk states is dramatically increased. The physical effect underlying this increase is conceptually similar to the appearance of van Hove singularities in the density of states, and is due to the three-dimensional bending of bulk states. In conclusion of this part, we showed that such an enhancement of the projected DOS at the edge of the projected bulk bands is a necessary condition for the formation of the projected bulk band pockets. We therefore expect, that the high density of the projected bulk bands at the BBE might facilitate the observation of the projected bulk band edges by STM on other metallic surfaces, and is not limited to a particular case of a Ag(110) surface.

The second experimental STM mode for which we developed and applied theoretical analysis

tools was spin-polarized STM (SP-STM). As model system we studied here the magnetically-ordered transition-metal nitride surface $Mn_3N_2(010)$. Transition-metal nitrides are of primary technological interest, in view of potential applications in spin-based electronics and data-storage. The SP-STM on the $Mn_3N_2(010)$ has for the first time *simultaneously* detected both nonmagnetic and magnetic surface properties, i.e. these experiments are also essential from the methodological point of view. Although SP-STM images clearly elucidated antiferromagnetic order of the surface atomic moments, at the beginning of the thesis several unresolved questions remained. First, there were several possible magnetic configurations of the surface commensurate with the measured magnetic profile. This implies that a surface magnetic reconstruction might occur, and the periodicity of the measured magnetic corrugation reflects that of the reconstructed surface. Even more, not only the magnetic configuration, but also the atomic structure of the surface had not been characterized in detail - only the heavy transition-metal atoms could be resolved experimentally, while the relatively small nitrogen atoms were not detected. Unfortunately, no experimental studies were available to resolve the actual termination of the $Mn_3N_2(010)$ surface. Second, there was an apparent dependence of the measured magnetic profiles on the applied bias voltage, manifested in an inversion of the magnetic contrast at +0.4 V, and a qualitative change of the profile-shape occurring at nearly the same voltage. It was not clear, however, whether these changes reflect properties of surface, or whether they are influenced by the STM tip.

To resolve the above described questions, we started with a determination of the thermodynamically most stable $Mn_3N_2(010)$ surface structure. The latter was identified within the framework of *ab initio* thermodynamics, by figuring out the surface configuration that has the lowest surface free energy among all possible magnetic and surface geometries that are commensurate with the experimentally observed periodicity. The accuracy of the DFT calculations, with specific emphasis on the construction of accurate norm-conserving pseudopotentials and the importance of the local and gradient-corrected parametrizations for exchange-correlation functional, was discussed. The most stable configuration was found to be the atomically relaxed bulk-terminated surface.

In order to simulate the SP-STM images on bulk-terminated $Mn_3N_2(010)$ surface we have employed the spin-generalized transfer-Hamiltonian formalism, assuming that the tip wavefunctions have dominant radial symmetry ($s$-like tip). A real-space description of the vacuum region was found to be essential in our case, and was implemented into S/PHI/nX. The theoretical results have been found in excellent agreement with the measured profiles and allowed an in-depth interpretation of all major effects such as the magnetic contrast reversal and even of subtle details affecting the specific shape of the line profile. The observed reversal of the magnetic contrast is explained as a surface-driven, rather than a tip-driven, effect. Moreover, both the change in the shape of the line profile, and the magnetic contrast reversal, are explained in terms of a smooth change from majority to minority spin Mn $d$-orbitals.

Finally, we have studied the effect of the tip properties (both electronic and geometrical) on the simulated SP-STM images. Our simulations imply that the magnetic contribution of a SP-STM

image is essentially sensitive to electronic properties of the STM tip, while the tip geometry is less critical for magnetic profiles. The inverse holds for the nonmagnetic STM current, that is significantly affected by the specific tip geometry, but reveals a low sensitivity with respect to the electronic properties of the tip.

# Appendix A

## A.1 Effect of the surface relaxation on the simulated FT-STM spectrum

The surface band structure of Ag(110) changes only slightly upon relaxation. Specifically, a relaxation slightly shifts the $S_2$ surface state by 0.05 eV upwards, and does essentially not change the position of the $S_3$ state (by less than 0.01 eV).

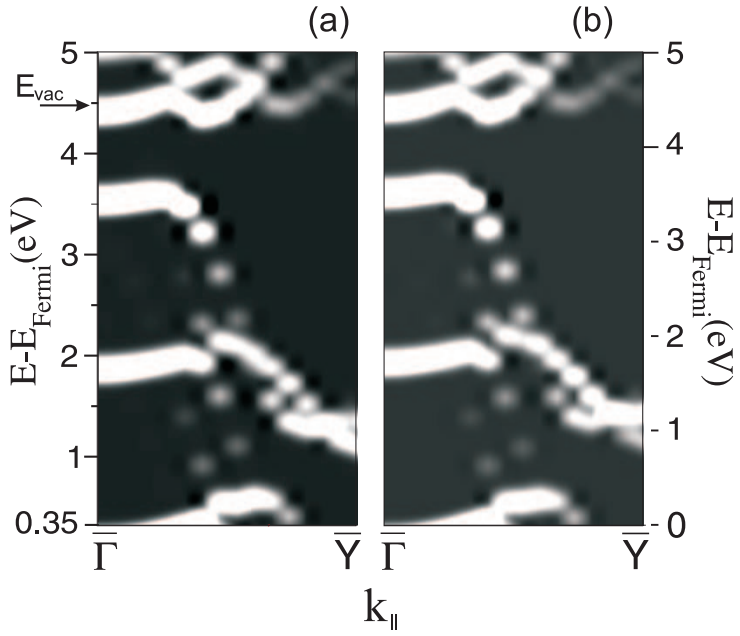


Figure A.1: Effect of the surface relaxation on the FT-STM spectrum. (a) FT-STM spectrum calculated on a nonrelaxed ideal bulk-terminated surface and (b) the surface with a fully relaxed surface geometry. The arrow shows the theoretically determined vacuum energy. The slab is 9 atomic layers thick.

We have checked whether and how surface relaxation affects the simulated FT-STM spectrum. A comparison of the FT-STM spectrum calculated for the ideal bulk terminated atomic structure (Fig. A.1(a)) with that for the relaxed atomic structure (Fig. A.1(b)) shows that the surface relax-

ation has little effect on the FT-STM spectra of the Ag(110) surfaces and can be safely neglected.

## A.2 Accuracy of the vacuum description for the Ag(110) surface

We have found that the quality of the LDOS description in the vacuum can be accurately estimated by an analysis of a single function $k_{\text{eff}}$, that we call the effective inverse vacuum decay length. We introduce $k_{\text{eff}}(z)$ as follows: in the one-dimensional case a wavefunction in the vacuum region can be described as:

$$\psi(z) = \psi(0)\, \exp(-kz), \tag{A.1}$$

where $k$ is the inverse vacuum decay length [112], and $z$ is the distance along the surface normal (the surface is located at $z = 0$). In the three-dimensional case the surface wavefunction at distance $z$ over the surface can be written as [119]:

$$\psi_{i\mathbf{k}_{||}}(z) \propto \sum_{\mathbf{G}} a_{i\mathbf{G}}\left(\mathbf{k}_{||}\right) \exp\left[-k\left(\mathbf{k}_{||}+\mathbf{G}\right) z\right]. \tag{A.2}$$

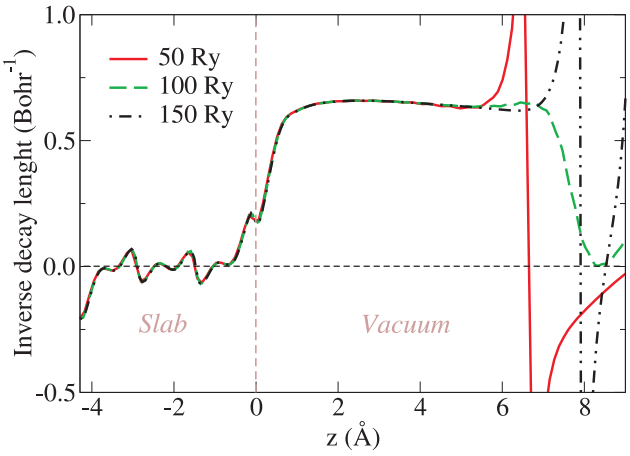


Figure A.2: Basis set dependence of the inverse vacuum decay length (see Eq. (A.1)) for the total valence charge density: the $(x, y)$-averaged inverse vacuum decay length is shown for the Ag(110) surface along the surface normal ($z$-axis). The surface plane is at $z = 0$ Å. A 3x4 Monkhorst-Pack $\mathbf{k}$-point mesh is used to sample the first surface Brillouin zone. The slab is 4 atomic layers thick.

Here $k\left(\mathbf{k}_{||}+\mathbf{G}\right)$ is the inverse vacuum decay length for the wavevector $\mathbf{k}_{||}+\mathbf{G}$, $\mathbf{G}$ is a reciprocal lattice vector and $a_{i\mathbf{G}}\left(\mathbf{k}_{||}\right)$ are the planewave expansion coefficients. From Eq. (A.2) it follows that in the general case the three-dimensional wavefunction $\psi_{i\mathbf{k}_{||}}$ decays into the vacuum following a complex relation, that cannot be cast to simple exponential decay as characteristic for the one-dimensional case. For large values of $z$, however, the contributions with smallest inverse decay lengths $k\left(\mathbf{k}_{||}+\mathbf{G}\right)$ start to dominate, and Eq. (A.2) can be approximated by Eq. (A.1) with an

*effective* inverse vacuum decay length $k_{\text{eff}}$. On Fig. A.2 we plot $k_{\text{eff}}$ calculated for the total valence charge density in case of the Ag(110) surface. First we focus on the curve that corresponds to a completely converged (with respect to the lattice constant, bulk modulus and surface energy) wavefunction basis set, i.e. the one with a cutoff energy 50 Ry. Depending on the $k_{\text{eff}}$ behavior, the vacuum can be split into three different regions. Namely, for $z < 2$ Å the effective decay length exhibits a pronounced nonlinear character, due to the superposition of multiple components with different inverse decay lengths (Eq. (A.2)). Within the second region 2 Å$< z < 5$ Å the effective inverse decay length remains essentially constant, i.e., at these distances only a few exponents with similar inverse decay lengths are essential (Eq. (A.2)). Significant deviations from this constant value are observed for $z > 5$ Å, where $k_{\text{eff}}$ undergoes a pronounced change in both magnitude and sign. These deviations characterize the region where the surface LDOS is spoiled.

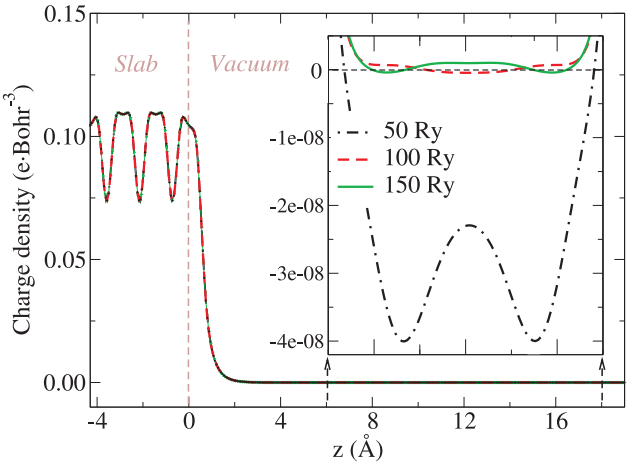


Figure A.3: Basis set dependence of the electronic total charge density decay into the vacuum: the $(x, y)$-averaged density is shown for the Ag(110) surface and along the surface normal ($z$-axis). The surface plane is at $z = 0$ Å. A 3x4 Monkhorst-Pack **k**-point mesh is used to sample the surface Brillouin zone. The slab is 4 atomic layers thick.

The origin of the limited description of the surface LDOS is the existence of a negative charge density region in the vacuum region $z > 6$ Å (Fig. A.3). These negative charge densities are not physical, and are caused by (i) a *finite* planewave basis set used for wavefunction expansions and (ii) a negligible magnitude of the LDOS at large distances above the surface, resulting in practically zero sensitivity of the Hamiltonian solvers to this region since they are based on an energy minimization.

In order to check the convergence of the maximum distance $z_{\text{max}}$ at which the surface LDOS is still accurately described with respect to the basis set size, we have tested the vacuum region for higher values of the cutoff energy, namely, for 100 Ry and 150 Ry (Figs. A.2-A.3). Clearly, a larger basis set provides a more accurate description of the vacuum. The maximum tip-sample separation increases up to $z_{\text{max}} \sim 5.8$ Å in the case of 100 Ry, and up to $z_{\text{max}} \sim 6.5$ Å in the case of 150 Ry

cutoff energy.

In summary, employing a converged (with respect to atomic, lattice geometry and surface energy) planewave basis set for a Ag(110) surface, the maximum tip-sample separation at which wavefunctions are still accurately described is $z_{\max} \sim 5$ Å. A further increase of $z_{\max}$ is possible by increasing the planewave basis set. However, this approach is strongly limited by its computational demands.

## A.3 General expression for the density of electronic states

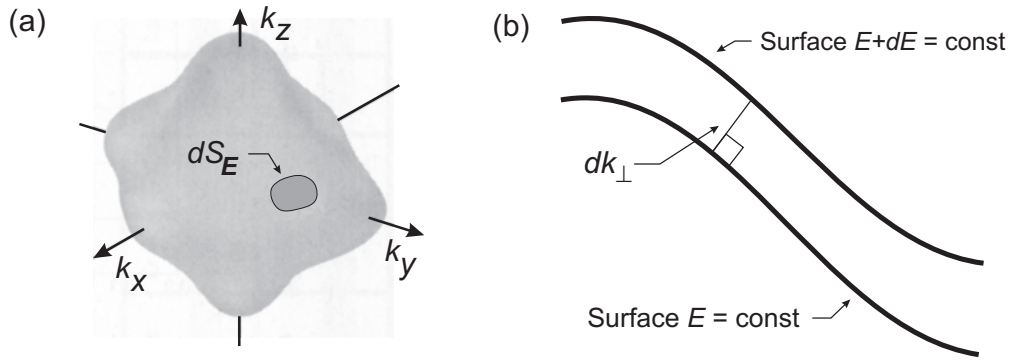


Figure A.4: (a) Surface of constant energy for a quasiparticle state $\epsilon_i(\mathbf{k})$ in $\mathbf{k}$-space. An element of the surface area is denoted as $dS_E$. (b) The quantity $dk_\perp$ is the perpendicular distance between two constant energy surfaces $S_E$ and $S_{E+dE}$ in $\mathbf{k}$-space.

The density of electronic states is a quantity frequently used to characterize an electronic band structure and to interpret experimental data. The density of states counts the number of allowed electronic states at an energy $E$, and is defined as [194]:

$$g(E) = \sum_{i\mathbf{k}} \delta(E - \epsilon_i(\mathbf{k})), \tag{A.3}$$

where the summation is performed over all electronic bands of the first Brillouin zone. Instead of performing a summation over all allowed $\mathbf{k}$-points we assign to each $\mathbf{k}$-point the volume $(2\pi)^3/V$, where $V$ is the crystal volume, and rearrange Eq. (A.3) to:

$$g(E) = \frac{V}{(2\pi)^3} \sum_i \int_{BZ} \delta(E - \epsilon_i(\mathbf{k}))d\mathbf{k}. \tag{A.4}$$

From Eq. (A.4) the number of allowed quasiparticle states for which the energies are between $E$ and $E + dE$ can be expressed as [184]:

$$g(E)dE = \frac{V}{(2\pi)^3} \sum_i \int_{shell} d\mathbf{k}. \tag{A.5}$$

Here the integral is extended over the volume of the shell in **k**-space that is bounded by the two surfaces on which the quasiparticle energies are constant and equal to $E$ and $E + dE$, respectively.

An evaluation of the volume of the shell in Eq. (A.5) is not straightforward. Let us define $S_E$ as the surface in **k**-space for which $\epsilon_i(\mathbf{k}) = E$. $dS_E$ denotes the element of area of this surface, as it is shown on Fig. A.4(a). The element of the volume between the constant energy surfaces $S_E$ and $S_{E+dE}$ can be written as $dV_{\text{shell}} = dS_E\, dk_\perp$, where $dk_\perp$ is the perpendicular distance between these surfaces (see Fig. A.4(b)). The integral in Eq. (A.5) can be rearranged as:

$$\int_{\text{shell}} d\mathbf{k} = \int_{S_E} dS_E\, dk_\perp. \tag{A.6}$$

For each state $\epsilon_i(\mathbf{k})$ the gradient $\nabla\epsilon_i(\mathbf{k})$ is normal to the surface of constant energy. The difference in energy between the two surfaces connected by $dk_\perp$ can be written then as:

$$|\nabla\epsilon_i(\mathbf{k})| dk_\perp = dE. \tag{A.7}$$

Employing Eq. (A.7) the element of the volume can be expressed as:

$$dS_E\, dk_\perp = dS_E \frac{dE}{|\nabla\epsilon_i(\mathbf{k})|}. \tag{A.8}$$

Substituting Eq. (A.8) into Eq. (A.5) gives us:

$$g(E)dE = \frac{V}{(2\pi)^3} \sum_i \int_{S_E} \frac{dS_E}{|\nabla\epsilon_i(\mathbf{k})|} dE. \tag{A.9}$$

From this expression the result for the density of states is obtained by dividing both parts by $dE$:

$$g(E) = \frac{V}{(2\pi)^3} \sum_i \int_{S_E} \frac{dS_E}{|\nabla\epsilon_i(\mathbf{k})|}. \tag{A.10}$$

## A.4 Murnaghan's equation of state

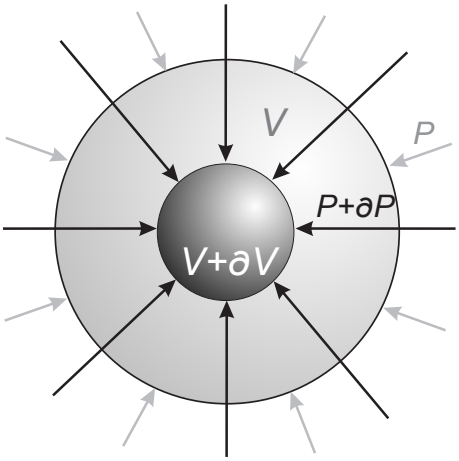


Figure A.5: The bulk modulus describes the change in volume when the pressure on it changes: $B(P) = -V\left(\frac{\partial P}{\partial V}\right)_T$.

The bulk modulus $B$ describes the resistance of a material to a change of its volume. It is defined as the ratio of the change in hydrostatic pressure acting on a volume to the uniform dilatation:

$$B(P) = -V\left(\frac{\partial P}{\partial V}\right)_T. \tag{A.11}$$

From Eq. (A.11) the bulk modulus pressure derivative is given by:

$$B'(P) = -\frac{\partial}{\partial P}\left(V\frac{\partial P}{\partial V}\right)_T. \tag{A.12}$$

Experimentally, it has been found that $B'$ changes little with pressure. Assuming constant $B'(P)$ one can write:

$$B(P) = B_0 + B_0'P, \tag{A.13}$$

where $B_0'$ and $B_0$ are the values of $B'$ and $B$ at $P = 0$, respectively. Equating Eq. (A.13) with Eq. (A.11) and integrating the results gives:

$$P(V) = \frac{B_0}{B_0'}\left(\left(\frac{V_0}{V}\right)^{B_0'} - 1\right), \tag{A.14}$$

where $V_0$ corresponds to system volume $V$ at zero pressure. Substituting Eq. (A.14) into $E = E(V_0) - \int PdV$ results in the equation of state for energy, known as Murnaghan's equation of state [255]:

$$E(V) = E(V_0) + \frac{B_0V}{B_0'(B_0'-1)}\left[B_0'\left(1 - \frac{V_0}{V}\right) + \left(\frac{V_0}{V}\right)^{B_0'} - 1\right]. \tag{A.15}$$

Eq. (A.15) is often used to fit the calculated total energy versus volume data in order to obtain the equilibrium volume $V_0$, the equilibrium total energy $E(V_0)$, the bulk modulus $B_0$, and its derivative $B_0'$.

# Bibliography


[1] G. Binnig and H. Rohrer, "Scanning tunneling microscopy - from birth to adolescence", *Reviews of Modern Physics* **59**, 615 (1987).

[2] Ch. Gerber and H. P. Lang, "How the doors to the nanoworld were opened", *Nature Nanotechnology* **1**, 3 (2006).

[3] H. C. Manoharan, C. P. Lutz, and D. M. Eigler, "Quantum mirages formed by coherent projection of electronic structure", *Nature* **403**, 512 (2000).

[4] W. A. Hofer, A. S. Foster, and A. L. Shluger, "Theories of scanning probe microscopes at the atomic scale", *Reviews of Modern Physics* **75**, 1287 (2003).

[5] M. F. Crommie, C. P. Lutz, and D. M. Eigler, "Confinement of Electrons to Quantum Corrals on a Metal Surface", *Science* **262**, 218 (1993).

[6] E. J. Heller, M. F. Crommie, C. P. Lutz, and D. M. Eigler, "Scattering and absorption of surface electron waves in quantum corrals", *Nature* **369**, 464 (1994).

[7] G. A. Fiete and E. J. Heller, "Colloquium: Theory of quantum corrals and quantum mirages", *Reviews of Modern Physics* **75**, 933 (2003).

[8] J. I. Pascual, J. Gómez-Herrero, D. Sánchez-Portal, and H.-P. Rust, "Vibrational spectroscopy on single $C_{60}$ molecules: The role of molecular orientation", *Journal of Chemical Physics* **117**, 9531 (2002).

[9] A. Kubetzka, P. Ferriani, M. Bode, S. Heinze, G. Bihlmayer, K. von Bergmann, O. Pietzsch, S. Blügel, and R. Wiesendanger, "Revealing Antiferromagnetic Order of the Fe Monolayer on W(001): Spin-Polarized Scanning Tunneling Microscopy and First-Principles Calculations", *Physical Review Letters* **94**, 087 204 (2005).

[10] A. Wachowiak, J. Wiebe, M. Bode, O. Pietzsch, M. Morgenstern, and R. Wiesendanger, "Direct Observation of Internal Spin Structure of Magnetic Vortex Cores", *Science* **298**, 577 (2002).

[11] K. von Bergmann, M. Bode, and R. Wiesendanger, "Coverage-dependent spin reorientation transition temperature of the Fe double-layer on W(110) observed by scanning tunneling microscopy", *Journal of Magnetism and Magnetic Materials* **305**, 279 (2006).

[12] K. von Bergmann, M. Bode, A. Kubetzka, O. Pietzsch, and R. Wiesendanger, "Spin-polarized scanning tunneling microscopy: Insight into magnetism from nanostructures to atomic scale spin structures", *Microscopy Research and Technique* **66**, 61 (2005).

[13] K. von Bergmann, S. Heinze, M. Bode, E. Y. Vedmedenko, G. Bihlmayer, S. Blügel, and R. Wiesendanger, "Observation of a Complex Nanoscale Magnetic Structure in a Hexagonal Fe Monolayer", *Physical Review Letters* **96**, 167 203 (2006).

[14] L. Berbil-Bautista, S. Krause, T. Hänke, M. Bode, and R. Wiesendanger, "Spin-polarized scanning tunneling microscopy through an adsorbate layer: Sulfur-covered Fe/W(110)", *Surface Science* **600**, L20 (2006).

[15] M. Bode, K. von Bergmann, O. Pietzsch, A. Kubetzka, and R. Wiesendanger, "Spin-polarized scanning tunneling spectroscopy of dislocation lines in Fe films on W(110)", *Journal of Magnetism and Magnetic Materials* **304**, 1 (2006).

[16] M. Bode, M. Getzlaff, and R. Wiesendanger, "Spin-Polarized Vacuum Tunneling into the Exchange-Split Surface State of Gd(0001)", *Physical Review Letters* **81**, 4256 (1998).

[17] M. Bode, O. Pietzsch, A. Kubetzka, and R. Wiesendanger, "Shape-Dependent Thermal Switching Behavior of Superparamagnetic Nanoislands", *Physical Review Letters* **92**, 067 201 (2004).

[18] L. Bürgi, H. Brune, O. Jeandupeux, and K. Kern, "Quantum coherence and lifetimes of surface-state electrons", *Journal of Electron Spectroscopy and Related Phenomena* **109**, 33 (2000).

[19] W. A. Hofer, A. J. Fisher, G. P. Lopinski, and R. A. Wolkow, "Benzene on silicon: combining STM experiments with first principles studies", *Surface Science* **482-485**, 1181 (2001).

[20] D. M. Eigler and E. K. Schweizer, "Positioning single atoms with a scanning tunnelling microscope", *Nature* **344**, 524 (1990).

[21] T. Müller-Reichert, H.-J. Butt, and H. Gross, "STM of metal embedded and coated DNA and DNA-protein complexes", *Journal of Microscopy* **182**, 169 (1996).

[22] J. Hwang, Th. Timusk, and J. P. Carbotte, "Scanning-tunnelling spectra of cuprates", *Nature* **446**, E3 (2007).

[23] M. Chiao, "Superconductivity: Are we there yet?" *Nature Physics* **3**, 148 (2007).

[24] S. Gemming and G. Seifert, "Nanocrystals: Catalysts on the edge", *Nature Nanotechnology* **2**, 21 (2007).

[25] J. I. Pascual, J. Gómez-Herrero, C. Rogero, A. M. Baró, D. Sánchez-Portal, E. Artacho, P. Ordejón, and J. M. Soler, "Seeing molecular orbitals", *Chemical Physics Letters* **321**, 78 (2000).

[26] A. Bachtold, M. Henny, C. Terrier, C. Strunk, C. Schönenberger, J.-P. Salvetat, J.-M. Bonard, and L. Forró, "Contacting carbon nanotubes selectively with low-ohmic contacts for four-probe electric measurements", *Applied Physics Letters* **73**, 274 (1998).

[27] M. S. Fuhrer, J. Nygård, L. Shih, M. Forero, Y.-G. Yoon, M. S. C. Mazzoni, H. J. Choi, J. Ihm, S. G. Louie, A. Zettl, and P. L. McEuen, "Crossed Nanotube Junctions", *Science* **288**, 494 (2000).

[28] P. A. Lewis, C. E. Inman, F. Maya, J. M. Tour, J. E. Hutchison, and P. S. Weiss, "Molecular Engineering of the Polarity and Interactions of Molecular Electronic Switches", *Journal of the American Chemical Society* **127**, 17 421 (2005).

[29] http://stm2.nrl.navy.mil/ lwhitman/spiral.html.

[30] B. R. Bennett, B. V. Shanabrook, P. M. Thibado, L. J. Whitman, and R. Magno, "Stranski-Krastanov growth of InSb, GaSb, and AlSb on GaAs: structure of the wetting layers", *Journal of Crystal Growth* **175-176**, 888 (1997).

[31] C. Toumey, "The man who understood the Feynman machine", *Nature Nanotechnology* **2**, 9 (2007).

[32] A. J. Heinrich, C. P. Lutz, J. A. Gupta, and D. M. Eigler, "Molecule Cascades", *Science* **298**, 1381 (2002).

[33] S.-W. Hla, "Molecular machines: Reinventing the wheel", *Nature Nanotechnology* **2**, 82 (2007).

[34] L. Grill, K.-H. Rieder, F. Moresco, G. Rapenne, S. Stojkovic, X. Bouju, and C. Joachim, "Rolling a single molecular wheel at the atomic scale", *Nature Nanotechnology* **2**, 95 (2007).

[35] K. Takayanagi, Y. Tanishiro, M. Takahashi, and S. Takahashi, "Structural analysis of Si(111)-7×7 by UHV-transmission electron diffraction and microscopy", *Journal of Vacuum Science and Technology A: Vacuum, Surfaces, and Films* **3**, 1502 (1985).

[36] www.princeton.edu/ kahnlab/images/Si111.html.

[37] S. Boeck, A. Dick, Ch. Freysoldt, F. Grzegorzewski, T. Hammerschmidt, L. Ismer, and L. Lymperakis, *SFHIngX - User's guide*, www.sxlib.de (2003).

[38] S. Boeck *et al.*, www.sxlib.de.

[39] E. Schödinger, "Die Erfüllbarkeit der Relativitätsforderung in der klassischen Mechanik", *Annalen der Physik* **77**, 325 (1925).

[40] J. Grotendorst, S. Blügel, and D. Marx, *Computational Nanoscience: Do It Yourself!* (Forschungszentrum Jülich, 2006).

[41] D. D. Koelling and B. N. Harmon, "A technique for relativistic spin-polarized calculations", *Journal of Physics C: Solid State Physics* **10**, 3107 (1977).

[42] L. A. Hemstreet, C. Y. Fong, and J. S. Nelson, "First-principles calculations of spin-orbit splittings in solids using nonlocal separable pseudopotentials", *Physical Review B* **47**, 4238 (1993).

[43] M. Fuchs and M. Scheffler, "Ab initio psudopotentials for electronic structure calculations of poly-atomic systems using density-functional-theory", *Computer Physics Communications* **119**, 67 (1999).

[44] M. Born and R. Oppenheimer, "Zur Quantentheorie der Molekeln", *Annalen der Physik* **84**, 457 (1927).

[45] U. Rössler, *Solid State Theory: An Introduction* (Springer, 2004).

[46] A. Groß, *Theoretical Surface Science. A Microscopic Perspective* (Springer, Berlin, 2003).

[47] B. Grabowski, *Ab initio based free-energy surfaces: Method development and application to aluminum and iron*, Master's thesis, University of Paderborn (2005).

[48] M. Scheffler and K. Reuter, "Lecture notes on Solid State Theory", (Berlin, 2003).

[49] G. Baym, *Lectures on Qunatum Mechanics* (Benjamin/Cummings, Merlo Park, 1973).

[50] D. R. Hartree, "Some relations between the optical spectra of different atoms of the same electronic structure. II. Aluminium-like and copper-like atoms." *Proceedings of the Cambridge Philosophical Society* **24**, 328 (1928).

[51] V. A. Fock, "Näherungsmethode zur Lösung des quantenmechanischen Mehrkörperproblems", *Zeitschrift für Physik* **61**, 126 (1930).

[52] Chr. Møller and M. S. Plesset, "Note on an Approximation Treatment for Many-Electron Systems", *Physical Review* **46**, 618 (1934).

[53] B. O. Roos, P. R. Taylor, and P. E. M. Siégbahn, "A complete active space SCF method (CASSCF) using a density matrix formulated super-CI approach", *Chemical Physics* **48**, 157 (1980).

[54] A. Szabo and N. Ostlund, *Modern Quantum Chemistry* (Dover Publications, New York, 1989).

[55] R. J. Bartlett, "Coupled-cluster approach to molecular structure and spectra: a step toward predictive quantum chemistry", *The Journal of Physical Chemistry* **93**, 1697 (1989).

[56] K. Raghavachari and J. B. Anderson, "Electron correlation effects in molecules", *The Journal of Chemical Physics* **100**, 12 960 (1996).

[57] I. Levine, *Quantum Chemistry* (Prentice-Hall, New Jersey, 2000).

[58] W. M. C. Foulkes, L. Mitas, R. J. Needs, and G. Rajagopal, "Quantum Monte Carlo simulations of solids", *Reviews of Modern Physics* **73**, 33 (2001).

[59] R. G. Parr and W. Yang, *Density-Functional Theory of Atoms and Molecules* (Oxford University Press, 1994).

[60] L. H. Thomas, "The calculation of atomic fields", *Proceedings of the Cambridge Philosophical Society* **23**, 542 (1927).

[61] E. Fermi, "Un metodo statistico per la determinazione di alcune priorieta dell'atome", *Atti Reale Accademia Nazionale Dei Lincei* **6**, 602 (1927).

[62] E. Fermi, "Eine statistische Methode zur Bestimmung einiger Eigenschaften des Atoms und ihre Anwendung auf die Theorie des periodischen Systems der Elemente", *Zeitshcrift für Physik* **48**, 73 (1928).

[63] S. Blügel, G. Gompper, and K. Erik, *Computational Condensed Matter Physics* (Forschungszentrum Jülich, 2006).

[64] P. Hohenberg and W. Kohn, "Inhomogeneous electron gas", *Physical Review* **136**, B864 (1964).

[65] W. Kohn and L. J. Sham, "Self-Consistent Equations Including Exchange and Correlation Effects", *Physical Review* **140**, A1133 (1965).

[66] D. M. Ceperley and B. J. Alder, "Ground State of the Electron Gas by a Stochastic Method", *Physical Review Letters* **45**, 566 (1980).

[67] J. P. Perdew and A. Zunger, "Self-interaction correction to density-functional approximations for many-electron systems", *Physical Review B* **23**, 5048 (1981).

[68] J. Rogal, *Stability, Composition and Function of Palladium Surfaces on Oxidizng Environments: A First-Principles Statistical Mechanics Approach*, Ph.D. thesis, Free University Berlin (2006).

[69] A. D. Becke, "Density-functional exchange-energy approximation with correct asymptotic behavior", *Physical Review A* **38**, 3098 (1988).

[70] J. P. Perdew, "Density-functional approximation for the correlation energy of the inhomogeneous electron gas", *Physical Review B* **33**, 8822 (1986).

[71] Ch. Lee, W. Yang, and R. G. Parr, "Development of the Colle-Salvetti correlation-energy formula into a functional of the electron density", *Physical Review B* **37**, 785 (1988).

[72] J. P. Perdew and Y. Wang, "Accurate and simple analytic representation of the electron-gas correlation energy", *Physical Review B* **45**, 13 244 (1992).

[73] J. P. Perdew, K. Burke, and M. Ernzerhof, "Generalized Gradient Approximation Made Simple", *Physical Review Letters* **77**, 3865 (1996).

[74] L. Lymperakis, *Ab-Initio Based Multiscale Calculations Of Extended Defects In And On Group III - Nitrides*, Ph.D. thesis, Paderborn University (2005).

[75] U. von Barth and L. Hedin, "A local exchange-correlation potential for the spin polarized case", *Journal of Physics C: Solid State Physics* **5**, 1629 (1972).

[76] W. Kohn, A. Savin, and C. A. Ullrich, "Hohenberg-Kohn theory including spin magnetism and magnetic fields", *International Journal of Quantum Chemistry* **100**, 20 (2004).

[77] K. Capelle and G. Vignale, "Nonuniqueness of the Potentials of Spin-Density-Functional Theory", *Physical Review Letters* **86**, 5546 (2001).

[78] H. Eschrig and W. E. Pickett, "Density functional theory of magnetic systems revisited", *Solid State Communications* **118**, 123 (2001).

[79] S. H. Vosko, L. Wilk, and M. Nusair, "Accurate spin-dependent electron liquid correlation energies for local spin density calculations: a critical analysis", *Canadian Journal of Physics* **59**, 1200 (1980).

[80] J. P. Perdew, J. A. Chevary, S. H. Vosko, K. A. Jackson, M. R. Pederson, D. J. Singh, and C. Fiolhais, "Atoms, molecules, solids, and surfaces: Applications of the generalized gradient approximation for exchange and correlation", *Physical Review B* **46**, 6671 (1992).

[81] J. P. Perdew, J. A. Chevary, S. H. Vosko, K. A. Jackson, M. R. Pederson, D. J. Singh, and C. Fiolhais, "Erratum: Atoms, molecules, solids, and surfaces: Applications of the generalized gradient approximation for exchange and correlation", *Physical Review B* **48**, 4978 (1993).

[82] M. C. Payne, M. P. Teter, D. C. Allan, T. A. Arias, and J. D. Joannopoulos, "Iterative minimization techniques for ab initio total-energy calculations: molecular dynamics and conjugate gradients", *Reviews of Modern Physics* **64**, 1045 (1992).

[83] N. W. Ashcroft and N. D. Mermin, *Solid State Physics* (Itps Thomson Learning, 1976).

[84] D. J. Chadi and M. L. Cohen, "Special Points in the Brillouin Zone", *Physical Review B* **8**, 5747 (1973).

[85] H. J. Monkhorst and J. D. Pack, "Special points for Brillouin-zone integrations", *Physical Review B* **13**, 5188 (1976).

[86] X. Gonze, J.-M. Beuken, R. Caracas, F. Detraux, M. Fuchs, G.-M. Rignanese, L. Sindic, M. Verstraete, G. Zerah, F. Jollet, M. Torrent, A. Roy, M. Mikami, Ph. Ghosez, J.-Y. Raty, and D. C. Allan, "First-principles computation of material properties: the ABINIT software project", *Computational Materials Science* **25**, 478 (2002).

[87] X. Gonze, G.-M. Rignanese, M. Verstraete, J.-M. Beuken, Y. Pouillon, R. Caracas, F. Jollet, M. Torrent, G. Zerah, M. Mikami, Ph. Ghosez, M. Veithen, J.-Y. Raty, V. Olevano, F. Bruneval, L. Reining, R. Godby, G. Onida, D. R. Hamann, and D. C. Allan, "A brief introduction to the ABINIT software package", *Zeitschrift für Kristallographie* **220**, 558 (2005).

[88] A. L. da Rosa, *Density-Functional Theory Calculations on Anti-Surfactants at Gallium Nitride Surfaces*, Ph.D. thesis, Technical University Berlin (2003).

[89] V. Heine, *The Pseudopotential Concept* (Academic Press, New York, 1970).

[90] U. von Barth and C. D. Gelatt, "Validity of the frozen-core approximation and pseudopotential theory for cohesive energy calculations", *Physical Review B* **21**, 2222 (1980).

[91] R. O. Jones and O. Gunnarsson, "The density functional formalism, its applications and prospects", *Review of Modern Physics* **61**, 689 (1989).

[92] J. P. Perdew and K. Burke, "Comparison shopping for a gradient-corrected density functional", *International Journal of Quantum Chemistry* **57**, 309 (1996).

[93] D. R. Hamann, M. Schlüter, and C. Chiang, "Norm-Conserving Pseudopotentials", *Physical Review Letters* **43**, 1494 (1979).

[94] G. P. Kerker, "Non-singular atomic pseudopotentials for solid state applications", *Journal of Physics C: Solid State Physics* **13**, L189 (1980).

[95] G. B. Bachelet, D. R. Hamann, and M. Schlüter, "Pseudopotentials that work: From H to Pu", *Physical Review B* **26**, 4199 (1982).

[96] D. Vanderbilt, "Optimally smooth norm-conserving pseudopotentials", *Physical Review B* **32**, 8412 (1985).

[97] D. Vanderbilt, "Soft self-consistent pseudopotentials in a generalized eigenvalue formalism", *Physical Review B* **41**, 7892 (1990).

[98] N. Troullier and J. Martins, "A straightforward method for generating soft transferable pseudopotentials", *Solid State Communications* **43**, 613 (1990).

[99] N. Troullier and J. L. Martins, "Efficient pseudopotentials for plane-wave calculations", *Physical Review B* **43**, 1993 (1991).

[100] S. Goedecker, M. Teter, and J. Hutter, "Separable dual-space Gaussian pseudopotentials", *Physical Review B* **54**, 1703 (1996).

[101] C. Hartwigsen, S. Goedecker, and J. Hutter, "Relativistic separable dual-space Gaussian pseudopotentials from H to Rn", *Physical Review B* **58**, 3641 (1998).

[102] Martin Fuchs and Evgeny Penev, "Exercise E1 on "Workshop on application of density-fuctional-theory in condensed matter physics, surface physics, chemistry, engineering and biology", Berlin, 21-30 July 2003: "Constructing pseudopotentials with the Program fhi98PP"", (2003).

[103] G. A. D. Briggs and A. J. Fisher, "STM experiment and atomistic modelling hand in hand: individual molecules on semiconductor surfaces", *Surface Science Reports* **33**, 1 (1999).

[104] Y. Meir and N. S. Wingreen, "Landauer formula for the current through an interacting electron region", *Physical Review Letters* **68**, 2512 (1992).

[105] M. Büttiker, Y. Imry, R. Landauer, and S. Pinhas, "Generalized many-channel conductance formula with application to small rings", *Physical Review B* **31**, 6207 (1985).

[106] J. Bardeen, "Tunnelling from a many-particle point of view", *Physical Review Letters* **6**, 57 (1961).

[107] R. Wiesendanger and H.-J. Güntherodt, *Scanning Tunneling Microscopy III* (Springer, 1993).

[108] S. Blügel, "Theorie der Rastertunnelmikroskopie", (lecture notes).

[109] A. D. Gottlieb and L. Wesoloski, "Bardeen's tunnelling theory as applied to scanning tunnelling microscopy: a technical guide to the traditional interpretation", *Nanotechnology* **17**, R57 (2006).

[110] J. B. Pendry, A. B. Pretre, and B. C. H. Krutzen, "Theory of the scanning tunnelling microscope", *Journal of Physics: Condensed Matter* **3**, 4313 (1991).

[111] G. Hörmandinger, "Imaging of the Cu(111) surface state in scanning tunneling microscopy", *Physical Review B* **49**, 13 897 (1994).

[112] C. Chen, *Introduction to Scanning Tunneling Microscopy* (Oxford University Press, 1993).

[113] W. A. Hofer, J. Redinger, A. Biedermann, and P. Varga, "Limits of perturbation theory: first principles simulations of scanning tunneling microscopy scans on Fe(100)", *Surface Science* **466**, L795 (2000).

[114] N. D. Lang, "Vacuum tunneling current from an adsorbed atom", *Physical Review Letters* **55**, 230 (1985).

[115] N. D. Lang, "Theory of Single-Atom Imaging in the Scanning Tunneling Microscope", *Physical Review Letters* **56**, 1164 (1986).

[116] M. Tsukada, K. Kobayashi, and S. Ohnishi, "First-principles theory of the scanning tunneling microscopy simulation", *Journal of Vacuum Science and Technology A: Vacuum, Surfaces, and Films* **8**, 160 (1990).

[117] K. Kobayashi and M. Tsukada, "Simulation of scanning tunneling microscope image based on electronic states of surface/tip system", *Journal of Vacuum Science and Technology A: Vacuum, Surfaces, and Films* **8**, 170 (1990).

[118] W. A. Hofer and J. Redinger, "Scanning tunneling microscopy of binary alloys: first principles calculation of the current for PtX (100) surfaces", *Surface Science* **447**, 51 (2000).

[119] J. Tersoff and D. R. Hamann, "Theory of the scanning tunneling microscope", *Physical Review B* **31**, 805 (1985).

[120] C. J. Chen, "Theory of scanning tunneling spectroscopy", *Journal of Vacuum Science and Technology A: Vacuum, Surfaces, and Films* **6**, 319 (1988).

[121] C. J. Chen, "Microscopic view of scanning tunneling microscopy", *Journal of Vacuum Scince and Technology A: Vacuum, Surfaces, and Films* **9**, 44 (1991).

[122] H. J. Reittu, "Analysis of spin-dependent tunnelling of electrons in solid state structures using the transfer-Hamiltonian method", *Journal of Physics: Condensed Matter* **9**, 10 651 (1997).

[123] D. Wortmann, S. Heinze, Ph. Kurz, G. Bihlmayer, and S. Blügel, "Resolving Complex Atomic-Scale Spin Structures by Spin-Polarized Scanning Tunneling Microscopy", *Physical Review Letters* **86**, 4132 (2001).

[124] R. J. Hamers, "Atomic-Resolution Surface Spectroscopy with the Scanning Tunneling Microscope", *Annual Review of Physical Chemistry* **40**, 531 (1989).

[125] R. J. Hamers and U. K. Köhler, "Determination of the local electronic structure of atomic-sized defects on Si(001) by tunneling spectroscopy", *Journal of Vacuum Science and Technology A* **7**, 2854 (1989).

[126] R. M. Feenstra, W. A. Thompson, and A. P. Fein, "Real-space observation of $\pi$-bonded chains and surface disorder on Si(111)2×1", *Physical Review Letters* **56**, 608 (1986).

[127] J. D. Fuhr, A. Saúl, and J. O. Sofo, "Scanning Tunneling Microscopy Chemical Signature of Point Defects on the $MoS_2$(0001) Surface", *Physical Review Letters* **92**, 026 802 (2004).

[128] R. M. Feenstra, Joseph A. Stroscio, and A. P. Fein, "Tunneling spectroscopy of the Si(111)2×1 surface", *Surface Science* **181**, 295 (1987).

[129] G. Binnig, K. H. Frank, H. Fuchs, N. Garcia, B. Reihl, H. Rohrer, F. Salvan, and A. R. Williams, "Tunneling Spectroscopy and Inverse Photoemission: Image and Field States", *Physical Review Letters* **55**, 991 (1985).

[130] G. Binnig, H. Rohrer, F. Salvan, Ch. Gerber, and A. Baro, "Revisiting the 7×7 reconstruction of Si(111)", *Surface Science* **157**, L373 (1985).

[131] R. S. Becker, J. A. Golovchenko, D. R. Hamann, and B. S. Swartzentruber, "Real-Space Observation of Surface States on Si(111) 7×7 with the Tunneling Microscope", *Physical Review Letters* **55**, 2032 (1985).

[132] J. I. Pascual, Z. Song, J. J. Jackiw, K. Horn, and H.-P. Rust, "Visualization of surface electronic structure: Dispersion of surface states of Ag(110)", *Physical Review B* **63**, 241 103(R) (2001).

[133] M. P. Everson, R. C. Jaklevic, and Weidian Shen, "Measurement of the local density of states on a metal surface: Scanning tunneling spectroscopic imaging of Au(111)", *Journal of Vacuum Science & Technology A* **8(5)**, 3662 (1990).

[134] A. Yazdani, B. A. Jones, C. P. Lutz, M. F. Crommie, and D. M. Eigler, "Probing the Local Effects of Magnetic Impurities on Superconductivity", *Science* **275**, 1767 (1997).

[135] W. Chen, V. Madhavan, T. Jamneala, and M. F. Crommie, "Scanning Tunneling Microscopy Observation of an Electronic Superlattice at the Surface of Clean Gold", *Physical Review Letters* **80**, 1469 (1998).

[136] M. Preisinger, J. Moosburger-Will, M. Klemm, S. Klimm, and S. Horn, "Atomic-scale imaging and spectroscopy of the $V_2O_3$ (0001) surface: Bulk versus surface effects", *Physical Review B* **69**, 075 423 (2004).

[137] J. Li, W.-D. Schneider, R. Berndt, O. R. Bryant, and S. Crampin, "Surface-State Lifetime Measured by Scanning Tunneling Spectroscopy", *Physical Review Letters* **81**, 4464 (1998).

[138] R. Berndt, J. Li, W.D. Schneider, and S. Crampin, "Surface-state linewidth from scanning tunnelling spectroscopy", *Applied Physics A* **69**, 503 (1999).

[139] N. Nilius, M. Kulawik, H.-P. Rust, and H.-J. Freund, "Defect-induced gap states in $Al_2O_3$ thin films on NiAl(110)", *Physical Review B* **69**, 121 401 (2004).

[140] R. Wiesendanger, M. Bode, and M. Getzlaff, "Vacuum-tunneling magnetoresistance: The role of spin-polarized surface states", *Applied Physics Letters* **75**, 124 (1999).

[141] A. Yamasaki, W. Wulfhekel, R. Hertel, S. Suga, and J. Kirschner, "Spin-polarized scanning tunneling spectroscopy study of Fe nanomagnets on W(001)", *Journal of Applied physics* **95**, 7025 (2004).

[142] O. Pietzsch, A. Kubetzka, M. Bode, and R. Wiesendanger, "Spin-Polarized Scanning Tunneling Spectroscopy of Nanoscale Cobalt Islands on Cu(111)", *Physical Review Letters* **92**, 057 202 (2004).

[143] J. E. Hoffman, K. McElroy, D.-H. Lee, K. M Lang, H. Eisaki, S. Uchida, and J. C. Davis, "Imaging Quasiparticle Interference in $Bi_2Sr_2CaCu_2O_8 + \delta$", *Science* **297**, 1148 (2002).

[144] Y. Hasegawa and Ph. Avouris, "Direct observation of standing wave formation at surface steps using scanning tunneling spectroscopy", *Physical Review Letters* **71**, 1071 (1993).

[145] Ph. Avouris, I.-W. Lyo, R. E. Walkup, and Y. Hasegawa, "Real space imaging of electron scattering phenomena at metal surfaces", *Journal of Vacuum Science & Technology B* **12**, 1447 (1994).

[146] L. Petersen, P. T. Sprunger, Ph. Hofmann, E. Lægsgaard, B. G. Briner, M. Doering, H.-P. Rust, and A. M. Bradshaw, F. Besenbacher, and E. W. Plummer, "Direct imaging of the two-dimensional Fermi contour: Fourier-transform STM", *Physical Review B* **57**, R6858 (1998).

[147] L. Petersen, Ph. Hofmann, E.W. Plummer, and F. Besenbacher, "Fourier Transform-STM: determining the surface Fermi contour", *Journal of Electron Spectroscopy and Related Phenomena* **109**, 97 (2000).

[148] K. Kanisawa, M. J. Butcher, H. Yamaguchi, and Y. Hirayama, "Imaging of Friedel Oscillation Patterns of Two-Dimensionally Accumulated Electrons at Epitaxially Grown InAs(111) A Surfaces", *Physical Review Letters* **86**, 3384 (2001).

[149] K. von Bergmann, M. Bode, A. Kubetzka, M. Heide, S. Blügel, and R. Wiesendanger, "Spin-Polarized Electron Scattering at Single Oxygen Adsorbates on a Magnetic Surface", *Physical Review Letters* **92**, 046 801 (2004).

[150] J. Li, W.-D. Schneider, and R. Berndt, "Local density of states from spectroscopic scanning-tunneling-microscope images: Ag(111)", *Physical Review B* **56**, 7656 (1997).

[151] L. Bürgi, O. Jeandupeux, H. Brune, and K. Kern, "Probing Hot-Electron Dynamics at Surfaces with a Cold Scanning Tunneling Microscope", *Physical Review Letters* **82**, 4516 (1999).

[152] O. Jeandupeux, L. Bürgi, A. Hirstein, H. Brune, and K. Kern, "Thermal damping of quantum interference patterns of surface-state electrons", *Physical Review B* **59**, 15 926 (1999).

[153] L. Bürgi, L. Petersen, H. Brune, and K. Kern, "Noble metal surface states: deviations from parabolic dispersion", *Surface Science* **447**, L157 (2000).

[154] L. Vitali, P. Wahl, M. A. Schneider, K. Kern, V. M. Silkin, E. V. Chulkov, and P. M. Echenique, "Inter- and intraband inelastic scattering of hot surface state electrons at the Ag(1 1 1) surface", *Surface Science* **523**, L47 (2003).

[155] J. I. Pascual, A. Dick, M. Hansmann, H.-P. Rust, J. Neugebauer, and K. Horn, "Bulk Electronic Structure of Metals Resolved with Scanning Tunneling Microscopy", *Physical Review Letters* **96**, 046 801 (2006).

[156] L. Bürgi, O. Jeandupeux, A. Hirstein, H. Brune, and K. Kern, "Confinement of Surface State Electrons in Fabry-Pérot Resonators", *Physical Review Letters* **81**, 5370 (1998).

[157] M. Hansmann, J. I. Pascual, G. Ceballos, H.-P. Rust, and K. Horn, "Scanning tunneling spectroscopy study of Cu(554): Confinement and dimensionality at a stepped surface", *Physical Review B* **67**, 121 409 (2003).

[158] P. M. Echenique, R. Berndt, E. V. Chulkov, Th. Fauster, A. Goldmann, and U. Höfer, "Decay of electronic excitations at metal surfaces", *Surface Science Reports* **52**, 219 (2004).

[159] M. Schmid, S. Crampin, and P. Varga, "STM and STS of bulk electron scattering by subsurface objects", *Journal of Electron Spectroscopy and Related Phenomena* **109**, 71 (2000).

[160] K. Højrup Hansen, J. Gottschalck, L. Petersen, B. Hammer, E. Lægsgaard, F. Besenbacher, and I. Stensgaard, "Surface waves on NiAl(110)", *Physical Review B* **63**, 115 421 (2001).

[161] M. H. Jung, T. Ekino, Y. S. Kwon, and T. Takabatake, "Tunneling spectroscopy of $RTe_2$ (R=La, Ce) and possible coexistence between charge-density waves and magnetic order", *Physical Review B* **63**, 035 101 (2000).

[162] D. Drakova and G. Doyen, "Theory of scanning tunneling spectroscopy on Pd(111)", *Surface Science* **352-354**, 698 (1996).

[163] G. Doyen and D. Drakova, "Theoretical aspects of scanning tunneling microscopy, scpectroscopy and atomic force microscopy on clean metal surfaces", *Progress in Surface Science* **54**, 249 (1997).

[164] W. J. Kaiser and R. C. Jaklevic, "Scanning tunneling microscopy study of metals: Spectroscopy and topography", *Surface Science* **181**, 55 (1987).

[165] B. Koslowski, C. Dietrich, and P. Ziemann, "Studying the bulk band structure of niobium by scanning tunneling spectroscopy", *Surface Science* **557**, 255 (2004).

[166] L. Petersen, P. Laitenberger, E. Lægsgaard, and F. Besenbacher, "Screening waves from steps and defects on Cu(111) and Au(111) imaged with STM: Contribution from bulk electrons", *Physical Review B* **58**, 7361 (1998).

[167] J. I. Pascual, unpublished.

[168] K.-M. Ho, B. N. Harmon, and S. H. Liu, "Surface-State Contribution to the Electroreflectance of Noble Metals", *Physical Review Letters* **44**, 1531 (1980).

[169] A. Goldmann, V. Dose, and G. Borstel, "Empty electronic states at the (100), (110), and (111) surfaces of nickel, copper, and silver", *Physical Review B* **32**, 1971 (1985).

[170] W. Altmann, V. Dose, and A. Goldmann, "Momentum-resolved bremsstrahlung isochromat spectroscopy of silver surfaces", *Zeitschrift für Physik B* **65**, 171 (1986).

[171] B. Reihl, R. R. Schlittler, and H. Neff, "Unoccupied Surface State on Ag(110) as Revealed by Inverse Photoemission", *Physical Review Letters* **52**, 1826 (1984).

[172] K. Stokbro, U. Quaade, and F. Grey, "Electric field effects in scanning tunneling microscope imaging", *Applied Physics A* **66**, S907 (1998).

[173] A. Selloni, P. Carnevali, E. Tosatti, and C. D. Chen, "Voltage-dependent scanning-tunneling microscopy of a crystal surface: Graphite", *Physical Review B* **31**, 2602 (1985).

[174] N. Li , M. Zinke-Allmang, and H. Iwasaki, "A re-examination of scanning tunneling spectroscopy for its practical application in studies of surface electronic structures", *Surface Science* **554**, 253 (2004).

[175] M. F. Crommie, "Observing electronic scattering in atomic-scale structures on metals", *Journal of Electron Spectroscopy and Related Phenomena* **109**, 1 (2000).

[176] V. A. Ukraintsev, "Data evaluation technique for electron-tunneling spectroscopy", *Physical Review B* **53**, 11 176 (1996).

[177] L. Petersen, L. Bürgi, H. Brune, F. Besenbacher, and K. Kern, "Comment on "Observation of two-dimensional Fermi contour of a reconstructed Au(111) surface using Fourier transform scanning tunneling microscopy" by D. Fujita, K. Amemiya, T. Yakabe, H. Nejoh, T. Sato, M. Iwatsuki [Surf. Sci. 423 (1999) 160]", *Surface Science* **443**, 154 (1999).

[178] N. D. Lang, "Spectroscopy of single atoms in the scanning tunneling microscope", *Physical Review B* **34**, 5947 (1986).

[179] A. W. Dweydari and C. H. B. Mee, *Physica Status Solidi A* **17**, 247 (1973).

[180] A. W. Dweydari and C. H. B. Mee, *Physica Status Solidi A* **27**, 223 (1975).

[181] S. Narasimhan and M. Scheffler, "A model for the thermal expansion of Ag(111) and other metal surfaces", *Zeitschrift für Physikalische Chemie* **202**, 253 (1997).

[182] J. Xie, S. de Gironcoli, S. Baroni, and M. Scheffler, "First-principles calculation of the thermal properties of silver", *Physical Review B* **59**, 965 (1999).

[183] D. R. Lide and H. P. R. Frederikse, *Handbook of Chemistry and Physics* (CRC Press, 1995).

[184] C. Kittel, *Introduction to Solid State Physics* (John Wiley and Sons, 2004).

[185] A. Nduwimana, X. G. Gong, and X. Q. Wang, "Relative stability of missing-row reconstructed (110) surfaces of noble metals", *Applied Surface Science* **219**, 129 (2003).

[186] R. Smoluchowski, "Anisotropy of the Electronic Work Function of Metals", *Physical Review* **60**, 661 (1941).

[187] C. L. Fu and K. M. Ho, "External-charge-induced surface reconstruction on Ag(110)", *Physical Review Letters* **63**, 1617 (1989).

[188] D. F. Shriver and P. W. Atkins, *Inorganic Chemistry* (Oxford university Press, 2001).

[189] R. A. Bartynski and T. Gustafsson, "Experimental study of surface states on the (110) faces of the noble metals", *Physical Review B* **33**, 6588 (1986).

[190] A. Gerlach, G. Meister, R. Matzdorf, and A. Goldmann, "High-resolution photoemission study of the $\overline{\mathrm{Y}}$ surface state on Ag(110)", *Surface Science* **443**, 221 (1999).

[191] L. Van Hove, "The Occurrence of Singularities in the Elastic Frequency Distribution of a Crystal", *Physical Review* **89**, 1189 (1953).

[192] F. Bassani and G. P. Parravicini, *Electronic States and Optical Transitions in Solids* (Pergamon Press, 1975).

[193] O. Madelung, *Introduction to Solid-State Theory* (Springer, Berlin, 1996).

[194] U. Rössler, *Solid State Theory: An Introduction* (Springer, Berlin, 2004).

[195] E. Kaxiras, *Atomic and Electronic Structure of Solids* (Cambridge University Press, 2003).

[196] R. Wiesendanger, "Introduction: Fifteen years of spin-polarized scanning tunneling microscopy", *Microscopy Research and Technique* **66**, 59 (2005).

[197] H. Yang, A. R. Smith, M. Prikhodko, and W. R. L. Lambrecht, "Atomic-Scale Spin-Polarized Scanning Tunneling Microscopy Applied to $Mn_3N_2(010)$", *Physical Review Letters* **89**, 226 101 (2002).

[198] R. Yang, H. Yang, A. R. Smith, A. Dick, and J. Neugebauer, "Energy-dependent contrast in atomic-scale spin-polarized scanning tunneling microscopy of $Mn_3N_2$ (010): Experiment and first-principles theory", *Physical Review B* **74**, 115 409 (2006).

[199] A. Kubetzka, M. Bode, O. Pietzsch, and R. Wiesendanger, "Spin-Polarized Scanning Tunneling Microscopy with Antiferromagnetic Probe Tips", *Physical Review Letters* **88**, 057 201 (2002).

[200] M. Bode, E. Y. Vedmedenko, K. von Bergmann, A. Kubetzka, P. Ferriani, S. Heinze, and R. Wiesendanger, "Atomic spin structure of antiferromagnetic domain walls", *Nature Materials* **5**, 477 (2006).

[201] R. Wiesendanger, H.-J. Güntherodt, G. Güntherodt, R. J. Gambino, and R. Ruf, "Observation of vacuum tunneling of spin-polarized electrons with the scanning tunneling microscope", *Physical Review Letters* **65**, 247 (1990).

[202] R. Wiesendanger, I. V. Shvets, D. Bürgler, G. Tarrach, H. J. Güntherodt, J. M. D. Coey, and S. Gräser, "Topographic and Magnetic-Sensitive Scanning Tunneling Microscope Study of Magnetite", *Science* **255**, 583 (1992).

[203] S. Heinze, M. Bode, A. Kubetzka, O. Pietzsch, X. Nie, S. Blügel, and R. Wiesendanger, "Real-Space Imaging of Two-Dimensional Antiferromagnetism on the Atomic Scale", *Science* **288**, 1805 (2000).

[204] M. Dreyer, J. Lee, C. Krafft, and R. Gomez, "(Towards) Spin-polarized scanning tunneling microscopy of NiFe films on a chromium(001) single crystal: Growth and electronic structure of Permalloy", *Journal of Applied Physics* **97**, 10E703 (2005).

[205] M. Bode, R. Ravlicacute, M. Kleiber, and R. Wiesendanger, "Growth and magnetism of Fe on Cr(001): a spin-polarized scanning tunneling spectroscopy and magnetic force microscopy study", *Applied Physics A: Materials Science & Processing* **80**, 907 (2005).

[206] S. Krause, L. Berbil-Bautista, T. Hänke, F. Vonau, M. Bode, and R. Wiesendanger, "Consequences of line defects on the magnetic structure of high anisotropy films: Pinning centers on Dy/W(110)", *Europhysics Letters* **76**, 637 (2006).

[207] M. Kleiber, M. Bode, R. Ravlić, and R. Wiesendanger, "Topology-Induced Spin Frustrations at the Cr(001) Surface Studied by Spin-Polarized Scanning Tunneling Spectroscopy", *Physical Review Letters* **85**, 4606 (2000).

[208] O. Pietzsch, A. Kubetzka, M. Bode, and R. Wiesendanger, "Real-Space Observation of Dipolar Antiferromagnetism in Magnetic Nanowires by Spin-Polarized Scanning Tunneling Spectroscopy", *Physical Review Letters* **84**, 5212 (2000).

[209] M. Bode, S. Heinze, A. Kubetzka, O. Pietzsch, M. Hennefarth, M. Getzlaff, R. Wiesendanger, X. Nie, G. Bihlmayer, and S. Blügel, "Structural, electronic, and magnetic properties of a Mn monolayer on W(110)", *Physical Review B* **66**, 014 425 (2002).

[210] O. Pietzsch, A. Kubetzka, M. Bode, and R.Wiesendanger, "Spin-Polarized Scanning Tunneling Spectroscopy of Nanoscale Cobalt Islands on Cu(111)", *Physical Review Letters* **92**, 057 202 (2004).

[211] T. K. Yamada, A. L. Vázquez de Parga, M. M. J. Bischoff, T. Mizoguchi, and H. van Kempen, "Evaluation of sample spin-polarization from spin-polarized scanning tunneling spectroscopy experiments", *Microscopy Research and Technique* **66**, 93 (2005).

[212] J. Prokop, A. Kukunin, and H. J. Elmers, "Spin-polarized scanning tunneling microscopy and spectroscopy of ultrathin Fe/Mo(110) films using W/Au/Co tips", *Physical Review B* **73**, 014 428 (2006).

[213] F. Meier, K. von Bergmann, P. Ferriani, J. Wiebe, M. Bode, K. Hashimoto, S. Heinze, and R. Wiesendanger, "Spin-dependent electronic and magnetic properties of Co nanostructures on Pt(111) studied by spin-resolved scanning tunneling spectroscopy", *Physical Review B* **74**, 195 411 (2006).

[214] H. Yang, H. Al-Brithen, A. R. Smith, J. A. Borchers, R. L. Cappelletti, and M. D. Vaudin, "Structural and magnetic properties of $\eta$-phase manganese nitride films grown by molecular-beam epitaxy", *Applied Physics Letters* **78**, 3860 (2001).

[215] H. Yang, H. Al-Brithen, E. Trifan, D. C. Ingram, and A. R. Smith, "Crystalline phase and orientation control of manganese nitride grown on MgO(001) by molecular beam epitaxy", *Journal of Applied Physics* **91**, 1053 (2002).

[216] H. Yang, R. Yang, A. R. Smith, and W. R. L. Lambrecht, "Atomic-scale structure of $\eta$-phase $Mn_3N_2(010)$ studied by scanning tunneling microscopy and first-principles theory", *Surface Science* **548**, 117 (2004).

[217] A. R. Smith, R. Yang, H. Yang, W. R. L. Lambrecht, A. Dick, and J. Neugebauer, "Aspects of spin-polarized scanning tunneling microscopy at the atomic scale: experiment, theory, and simulation", *Surface Science* **561**, 154–170 (2004).

[218] A. R. Smith, R. Yang, H. Yang, A. Dick, J. Neugebauer, and W. R. L. Lambrecht, "Recent advances in atomic-scale spin-polarized scanning tunneling microscopy", *Microscopy Research and Technique* **66**, 72 (2005).

[219] G. Kreiner and H. Jacobs, "Magnetische struktur von $\eta$-$Mn_3N_2$", *Journal of Alloys and Compounds* **183**, 345 (1992).

[220] M. Tabuchi, M. Takahashi, and F. Kanamaru, "Relation between the magnetic transition temperature and magnetic moment for manganese nitrides $MnN_y$ ($0<y<1$)", *Journal of Alloys and Compounds* **210**, 143 (1994).

[221] A. Leineweber, R. Niewa, H. Jacobs, and W. Kockelmann, "The manganese nitrides $\eta$-$Mn_3N_2$ and $\theta$-$Mn_6N_{5+x}$: nuclear and magnetic structures", *Journal of Materials Chemistry* **10**, 2827 (2000).

[222] K. Suzuki, T. Kaneko, H. Yoshida, Y. Obi, H. Fujimori, and H. Morita, "Crystal structure and magnetic properties of the compound MnN", *Journal of Alloys and Compounds* **306**, 66 (2000).

[223] W. R. L. Lambrecht, M. Prikhodko, and M. S. Miao, "Electronic structure and magnetic interactions in MnN and $Mn_3N_2$", *Physical Review B* **68**, 174 411 (2003).

[224] S. Heinze, S. Blügel, R. Pascal, M. Bode, and R. Wiesendanger, "Prediction of bias-voltage-dependent corrugation reversal for STM images of bcc (110) surfaces: W(110), Ta(110), and Fe(110)", *Physical Review B* **58**, 16 432–16 445 (1998).

[225] C.-O. Almbladh and U. von Barth, "Exact results for the charge and spin densities, exchange-correlation potentials, and density-functional eigenvalues", *Physical Review B* **31**, 3231 (1985).

[226] K. Reuter, C. Stampfl, and M. Scheffler, *Handbook of Materials Modelling, Part A. Methods* (Springer, Berlin, 2005), chap. Ab initio atomistic thermodynamics and statistical mechanics of surface properties and functions, pp. 149–234.

[227] K. Reuter and M. Scheffler, "Composition, structure, and stability of $RuO_2(110)$ as a function of oxygen pressure", *Physical Review B* **65**, 035 406 (2002).

[228] D. R. Lide, *CRC Handbook of Chemistry and Physics* (CRC Press, 2005).

[229] T. A. Scott, "Solid and liquid nitrogen", *Physics Reports* **27**, 89 (1976).

[230] J. E. Northrup and J. Neugebauer, "Indium-induced changes in GaN(0001) surface morphology", *Physical Review B* **60**, R8473 (1999).

[231] C. G. Van de Walle and J. Neugebauer, "Structure and energetics of nitride surfaces under MOCVD growth conditions", *Journal of Crystal Growth* **248**, 8 (2003).

[232] M. Fuchs, J. L. F. Da Silva, C. Stampfl, J. Neugebauer, and M. Scheffler, "Cohesive properties of group-III nitrides: A comparative study of all-electron and pseudopotential calculations using the generalized gradient approximation", *Physical Review B* **65**, 245 212 (2002).

[233] C. Stampfl and C. G. Van de Walle, "Density-functional calculations for III-V nitrides using the local-density approximation and the generalized gradient approximation", *Physical Review B* **59**, 5521 (1999).

[234] A. Zoroddu, F. Bernardini, P. Ruggerone, and V. Fiorentini, "First-principles prediction of structure, energetics, formation enthalpy, elastic constants, polarization, and piezoelectric constants of AlN, GaN, and InN: Comparison of local and gradient-corrected density-functional theory", *Physical Review B* **64**, 045 208 (2001).

[235] A. C. Lawson, A. C. Larson, M. C. Aronson, S. Johnson, Z. Fisk, P. C. Canfield, J. D. Thompson, and R. B. Von Dreele, "Magnetic and crystallographic order in $\alpha$-manganese", *Journal of Applied Physics* **76**, 7049 (1994).

[236] D. Hobbs, J. Hafner, and D. Spišák, "Understanding the complex metallic element Mn. I. Crystalline and noncollinear magnetic structure of $\alpha$-Mn", *Physical Review B* **68**, 014 407 (2003).

[237] J. X. Zheng-Johansson, O. Eriksson, B. Johansson, L. Fast, and R. Ahuja, "Comment on "Stability and the equation of state of $\alpha$-manganese under ultrahigh pressure"", *Physical Review B* **57**, 10 989 (1998).

[238] J. Hafner and D. Hobbs, "Understanding the complex metallic element Mn. II. Geometric frustration in $\beta$-Mn, phase stability, and phase transitions", *Physical Review B* **68**, 014 408 (2003).

[239] M. Eder, J. Hafner, and E. G. Moroni, "Structural, electronic, and magnetic properties of thin Mn/Cu(100) films", *Physical Review B* **61**, 2000 (2000).

[240] T. Asada and K. Terakura, "Generalized-gradient-approximation study of the magnetic and cohesive properties of bcc, fcc, and hcp Mn", *Physical Review B* **47**, 15 992 (1993).

[241] E. G. Moroni, G. Kresse, and J. Hafner, and J. Furthmüller, "Ultrasoft pseudopotentials applied to magnetic Fe, Co, and Ni: From atoms to solids", *Physical Review B* **56**, 15 629 (1997).

[242] G. Kresse and J. Hafner, "Norm-conserving and ultrasoft pseudopotentials for first-row and transition elements", *Journal of Physics: Condensed Matter* **6**, 8245 (1994).

[243] K. Suzuki, Y. Yamaguchi, T. Kaneko, H. Yoshida, Y. Obi, H. Fujimori, and H. Morita, "Neutron Diffraction Studies of the Compounds MnN and FeN", *Journal of the Physical Society of Japan* **70**, 1084 (2001).

[244] F. Lihl, P. Ettmayer, and A. Kuzelnigg, "Neutron Diffraction Studies of the Compounds MnN and FeN", *Zeitschrift für Metallkunde* **53**, 715 (1962).

[245] M. Mekata, J. Haruna, and H. Takaki, "Neutron Diffraction Study of Antiferromagnetic $Mn_2N$", *Journal of the Physical Society of Japan* **25**, 234 (1968).

[246] M. N. Eddine, E. F. Bertaut, and M. Maunaye, "Structure cristallographique de $Mn_2N_{0.86}$", *Acta Crystallographica Section B* **33**, 2696 (1977).

[247] M. $\overline{\text{O}}$tsuka, Y. Hanawa, and S. Nagakura, "Crystal Structure and Phase Transition of $Mn_6N_5$ Studied by Electron Diffraction", *Physica Status Solidi (a)* **43**, K127 (1977).

[248] W. A. Hofer, A. J. Fisher, R. A. Wolkow, and P. Grütter, "Surface Relaxations, Current Enhancements, and Absolute Distances in High Resolution Scanning Tunneling Microscopy", *Physical Review Letters* **87**, 236 104 (2001).

[249] R. Wiesendanger, M. Bode, and M. Getzlaff, "Vacuum-tunneling magnetoresistance: The role of spin-polarized surface states", *Applied Physics Letters* **75**, 124 (1999).

[250] P. M. Tedrow and R. Meservey, "Spin Polarization of Electrons Tunneling from Films of Fe, Co, Ni, and Gd", *Physical Review B* **7**, 318 (1973).

[251] J. P. Perdew, K. Burke, and Y. Wang, "Generalized gradient approximation for the exchange-correlation hole of a many-electron system", *Physical Review B* **54**, 16 533 (1996).

[252] W. A. Hofer, J. Redinger, and R. Podloucky, "Modeling STM tips by single absorbed atoms on W(100) films: 3d and 4d transition-metal atoms", *Physical Review B* **64**, 125 108 (2001).

[253] W. A. Hofer and A. J. Fisher, "Determining surface magnetization and local magnetic moments with atomic scale resolution", *Surface Science Letters* **515**, L487 (2002).

[254] W. A. Hofer and A. J. Fisher, "Signature of a Chemical Bond in the Conductance between Two Metal Surfaces", *Physical Review Letters* **91**, 036 803 (2003).

[255] F. D. Murnaghan, "The Compressibility of Media under Extreme Pressures", *Proceedings of the National Academy of Sciences* **30**, 244 (1944).

## List of Publications

- A. R. Smith, R. Yang, H. Yang, W. R. L. Lambrecht, A. Dick, and J. Neugebauer, "Aspects of spin-polarized scanning tunneling microscopy at the atomic scale: experiment, theory, and simulation", *Surface Science* **561**, 154 (2004).

- A. R. Smith , R. Yang, H. Yang, A. Dick, J. Neugebauer, and W. R. L. Lambrecht, "Recent advances in atomic-scale spin-polarized scanning tunneling microscopy", *Microscopy Research and Technique* **66**, 72 (2005).

- J. I. Pascual, A. Dick, M. Hansmann, H.-P. Rust, J. Neugebauer, and K. Horn, "Bulk Electronic Structure of Metals Resolved with Scanning Tunneling Microscopy", *Physical Review Letters* **96**, 046801 (2006).

- R. Yang, H. Yang, A. R. Smith, A. Dick, and J. Neugebauer, "Energy-dependent contrast in atomic-scale spin-polarized scanning tunneling microscopy of $Mn_3N_2$ (010): Experiment and first-principles theory", *Physical Review B* **74**, 115409 (2006).